SLAC-219
UC-34d
(T/E)

CHARMED MESON PRODUCTION AND DECAY PROPERTIES AT THE $\psi(3770)^*$

Rafe Hyam Schindler

Stanford Linear Accelerator Center
Stanford University
Stanford, California 94305

May 1979

Prepared for the Department of Energy
under contract number DE-AC03-76SF00515

Printed in the United States of America. Available from the National Technical Information Service, U.S. Department of Commerce, 5285 Port Royal Road, Springfield, VA 22161. Price: Printed Copy $9.25; Microfiche $3.00.

---

* Ph.D dissertation.

CHARMED MESON PRODUCTION AND DECAY

PROPERTIES AT THE $\psi(3770)$

Rafe Hyam Schindler, Ph.D.
Stanford University, 1979

A remeasurement of the resonance near $E_{cm} = 3.77$ GeV in the e^+e^- annihilation is presented. The properties of the resonance are used to deduce branching fractions of charmed mesons into hadronic final states. Several previously unseen decay modes are reported. Decays into Cabibbo suppressed final states are observed. The inclusive properties of D meson decays are studied, including strangeness and charged particle multiplicity. The semileptonic branching fractions for D^0 and $D^{\mp}$ are measured, providing a determination of the relative lifetimes of these particles.

ACKNOWLEDGEMENTS

It stands without question that no part of this work would be possible without the combined efforts of all the members of the SLAC/LBL Mark II Collaboration. I owe much of my later education to the groundwork established while working in the original SLAC/LBL (Mark I) Collaboration.

For education, guidance, and inspiration through these five years, I must single out my advisor, Roy Schwitters.

Special achnowledgement is due Willy Chinowsky, Dave Johnson, George Trilling, and Henri Zaccone for their essential contributions to the development of the algorithms and techniques presented in Chapter III. Similarly, I would expecially like to acknowledge the work and help of Gary Feldman on the analysis presented in Chapter V.

For the many useful discussions that helped in understanding the theoretical interpretation of the analysis presented, I would particularly like to thank Fred Gilman and David Miller.

Finally, I feel it is essential for me to thank all those both inside and outside the collaboration for the very useful educational discussions and help they have provided. Names here are certainly unnecessary.

TABLE OF CONTENTS

Appendices Page

I. INTRODUCTION

WHERE DOES CHARM STAND?

In 1974, the discovery of the first member of the ψ family of narrow resonances[1] in two vastly different experiments ushered in a new era in high energy physics. These mesons were unlike all previously discovered particles for they had both large masses (> 3 GeV/c^2) and extremely narrow widths (e.g., 67 and 228 KeV for $\psi(3095)$ and $\psi(3684)$, respectively) compared to the tens and hundreds of MeV's characterizing most previously discovered heavy mesons. The interpretation of these new states was that of a bound system of quark and anti-quark, each carrying the new quantum number "charm". Their extreme narrowness or long lives implied highly suppressed decays to ordinary hadrons, wherein the new quantum number was lost.[2]

The need for charm as first postulated by Bjorken, Glashow, Iliopoulos, and Maiani,[3] came long before the ψ discoveries, as did its natural incorporation in the Weinberg-Salam model[4] which has been successful so far in presenting a unified description of weak and electromagnetic interactions. These theories were motivated by several experimental observations which the current theory of the time (3-quarks) was unable to account for. Measurements of the $K_S^o - \bar{K}_L^o$ mass difference, the general absence of first order strangeness changing neutral currents, and of the suppression of certain second order weak processes such as $K_L^o \to \mu^+\mu^-$ and $K^+ \to \pi^+\nu\bar{\nu}$, all lent support to the model and the hidden effect of charm in calculations of the expected experimental rates associated with these processes. The measurements (in particular the $K_S^o - K_L^o$ mass difference) provided the first early estimates of the charmed quark mass of a few GeV/c^2.[5] This, of course, suggested that the first charmed particles to appear would be several GeV/c^2 in mass. Within several years ($\sim$ 1973) evidence for the charm hypothesis came in a perhaps more direct form, from the first experiments measuring electron and positron annihilation cross sections into non-quantum electrodynamic (QED) final states. In these experiments,[5] the total hadronic cross section was compared to the QED process $e^+e^- \rightarrow \mu^+\mu^-$ and the ratio (denoted R) measured as a function of center-of-mass energy. The quantity R is used because the lowest order process involves the annihilation of the e^+e^- pair into a virtual photon, and the photon's re-emergence as another particle-antiparticle pair. These final state pointlike particles or fermions may be either lepton pairs (meaning light particles) such as e^+e^- and $\mu^+\mu^-$ or quark and antiquark pairs ($q\bar{q}$). All of these processes occur at a rate which scales like the square of the electric charge of the fermion type produced. In this picture, hadrons emerge in the final state when a $q\bar{q}$ pair is produced in the annihilation, and each quark "dresses" itself with other quarks from the vacuum.

Therefore, R, which measures the total hadron production rate relative to the simple $\mu^+\mu^-$ process, should remain approximately constant with center-of-mass energy, as long as no new final state fermion pairs appear. It was a large apparent rise in R between 3 and 4 GeV that first suggested that a threshold for production of a new species of fermion had been crossed (see Fig. 1). The precise size of the rise is determined by the properties of the fermion (charge and color), and suggested that a new quark rather than a lepton was being

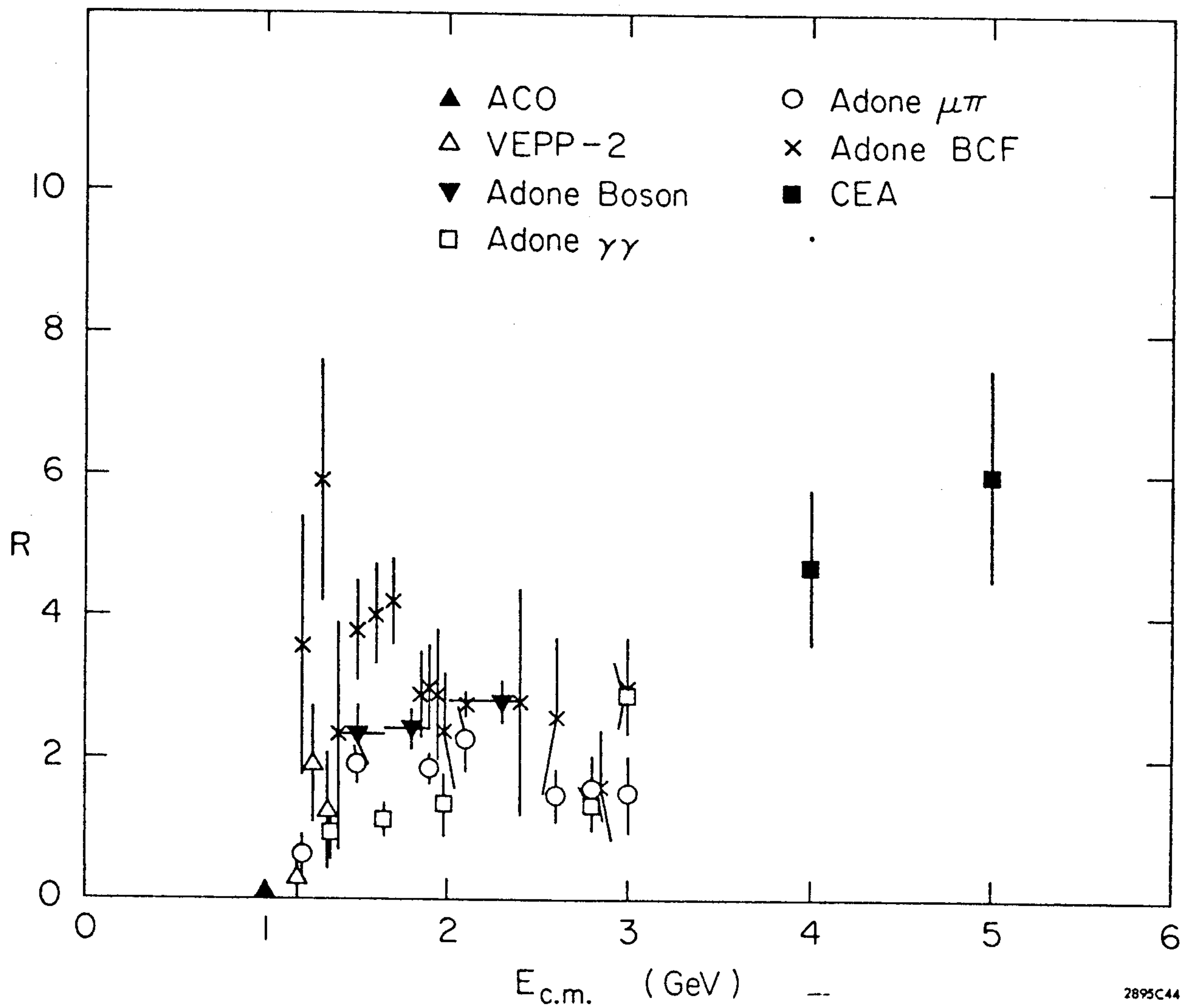

Fig. 1. Results for R for the early detectors (see Schwitters *et al.*, Ref. 5).

produced. A quantitative discrimination by this technique would have to wait however until the next generation of detectors and storage rings were built (see Schwitters et al., Ref. 5).

Within the framework of the theory, the new property or "flavor" charm was to be conserved in electromagnetic and strong interactions, thus leading Gaillard, Lee and Rosner [6] to propose prior to discovery a "new" spectroscopy of charmed particles in analogy of the scheme of SU(3), which was highly successful in predicting both the existence and properties of strange and non-strange mesons, baryons, and their associated resonances.[7] Some of the predicted properties follow. Ordinary mesons of the "old" spectroscopy (the conventional quark model based on SU(3) symmetry) consisted of pairs of the light u,d,s quarks and antiquarks while baryons were triplets of these quarks. In the new spectroscopy, the fourth charmed quark (c) could also be used in these combinations. Thus, charmed mesons would consist of a light quark plus charmed quark forming an isodoublet ($c\bar{u}$, $c\bar{d}$) denoted (D^o, D^+) or an isosinglet state ($c\bar{s}$) denoted F^+. In addition, singlet states of $c\bar{c}$ could form, which are now identified with the ψ family of vector mesons. In addition to the mesons, complex multiplets of baryon states containing either one, two or three charmed quarks would exist. The number of baryonic combinations are large, with for example the lowest lying 20-multiplet ($\frac{1}{2}^+$) containing twelve new charmed baryons in addition to the eight old baryons (proton, neutron, lambda,...). Each of the meson and baryon states within the quark model could exist in excited states of the quark configuration (in analogy to the energy levels of ordinary atoms), and which could then cascade down through either pion or γ-ray emission. Thus for example, the $c\bar{c}$ states might show a level structure with intermediate states in various spin and orbital angular momentum configurations, while $c\bar{q}$ mesons could come in pseudoscalar or vector form (spin 1), the latter corresponding to an alignment of quark spins. Because charm is to be conserved in strong and electromagnetic interactions, the lowest lying states containing net charm would generally loose their charm through a weak decay to a final state containing a strange particle. [6]

At this writing, the experimental evidence for this picture of charm is overwhelming and even somewhat difficult to summarize. In addition to the observations [1] of narrow $c\bar{c}$ resonances and level structure, broader resonances such as the $\psi(3770)$ which lie above charm meson threshold and presumably decay strongly to charmed D mesons have been observed in e^+e^- annihilation. [8] In the realm of charmed mesons, several distinct decay modes of the D^+ and D^o as well as their excited states have been directly observed in e^+e^- annihilation, [10] neutrino induced charged current reactions, [11] as well as in pp interactions. [12] The evidence for observation of the F^+ state is still sparce, with only six FF* candidate events produced in e^+e^- annihilation [13] with the subsequent decay $F^+ \rightarrow \eta\pi^+$, and possible signals seen in $\eta 3\pi$, and $\eta 5\pi$ invariant mass plots at approximately the same mass (2030 GeV/c^2). [14] Limits on F^+ production in another experiment in e^+e^- annihilation have also been reported [15] consistent with the observations of the Ref. 13. Finally, evidence for the existence of charmed baryons has been rapidly increasing with several significant observations of what appears to be the weak decays of the lowest lying state Λ_c (the cud quark combination) into several different channels ($\Lambda\pi$, $\Lambda 3\pi$, $pK\pi$, pK^o,....). These measurements have been made in e^+e^- annihilation, [15] neutrino interactions, [16] pp interactions, [17] and in photoproduction. [18]

While all these measurements have been of predominently hadronic final states, the semileptonic decays of charmed particles have been measured through their lepton signiture in a number of experiments in e^+e^- annihilations [19] as well as in neutrino interactions. [11]

Thus at present, a reasonably consistent picture for the existence of charm emerges experimentally, with many of the expected final states being observed. The questions which still remain concern the details of the decay processes of the mesons and baryons and the interesting question of charmed particle lifetimes.

MOTIVATION AND GOALS

The measurements discussed in the previous section have basically provided undeniable evidence supporting the existence of charmed particles, however, the picture as a whole falls far short of being complete. Much of the detailed work measuring the decay properties of charmed particles has only been started and the majority of the work comes predominently from the handful of e^+e^- annihilation experiments mentioned. The motivation of this thesis is then clear. It is necessary to repeat some of the early measurements of D decay properties wherever improvements can be made either from hardware, statistics, or the understanding of systematic uncertainties. It is also important to attempt to add new measurements which have direct implication to the theory in question.

In this light, the specific goals which have been sought can be summarized here:

(1) A remeasurement of the $\psi(3770)$ resonance both to resolve ambiguities in previously reported results [8,9] as well as to provide a single consistent measurement of the charm production cross section needed for other measurements presented here.

(2) To repeat measurements of D meson hadronic branching fractions with smaller statistical and systematic errors. To search for new decay modes in hadronic channels. The addition of the large solid angle calorimeter will provide improved acceptance for decay modes involving π^o (see Scharre et al., Ref. 9).

(3) To accumulate a large sample of D mesons which can be used to study the inclusive properties of D decays such as strangeness and charged particle multiplicity. In particular, previous measurements of strangeness in D decays,[20] suggested the possibility of significant deviations from the simple theoretical expectations.[6]

(4) To try to measure the relative lifetime of D^+ and D^o through their semileptonic decays. Evidence has been reported [15,21] that the lifetimes of the two species may be quite different. Tagged events provide a direct means of studying the inclusive electron distributions for D^+ and D^o separately, thus measuring their relative semileptonic branching ratios. These numbers can be combined with

theoretical estimates for partial widths to obtain an estimate of the absolute lifetimes.

REFERENCES

1. Aubert, J. J. et al., Phys. Rev. Lett. 33, 1404 (1974).

   Augustin, J. E. et al., Phys. Rev. Lett. 33, 1406 (1974).

2. De Rujula, A., Glashow, S. L., Phys. Rev. Lett. 34, 43 (1975).

3. Bjorken, J. D., Glashow, S. L., Phys. Rev. Lett. 11, 255 (1964).

   Glashow, S. L., Iliopoulos, J., Maiani, L., Phys. Rev. D2, 1285 (1970).

4. Weinberg, S., Phys. Rev. Lett. 19, 1264 (1976).

   Salam, A., in Elementary Particle Theory, (Ed. by Almquist and Wiksells, Stockholm, 1969) p. 367.

5. A good theoretical discussion is given in Gaillard, M. and Lee, B., Phys. Rev. D10, 897 (1974). Some of the interesting early experiments are: Carithers, W., et al., Phys. Rev. Lett. 31, 1025 (1973) ($K^o_S - K^o_L$ mass difference); Aronson, S. et al., Phys. Rev. Lett. 29, 1057 (1970) ($K^o_L \to \mu^+\mu^-$); Cable, G. D. et al., Phys. Rev. D8, 3807(1973) ($K^+ \to \pi^+ \nu\bar{\nu}$); Litke, A. et al., Phys. Rev. Lett. 30, 1189 (1973) (an early e^+e^- cross section); Schwitters, R. F., and Strauch, K., Ann. Rev. Nucl. Sci. 26, 89 (1976) (an excellent review of e^+e^- physics).

6. Gaillard, M. K., Lee, B. W., and Rosner, J. L., Rev. of Mod. Phys., Vol. 47, No. 2 (1975).

7. For an excellent review see Gilman, F., Proceedings of the SLAC Summer Institute of Particle Physics (Edited by M. Zipf), 1978.

8. Rapidis, P. et al., Phys. Rev. Lett. 39, 1301 (1977).

   Bacino, W. et al., Phys. Rev. Lett. 40, 526 (1977).

9. Goldhaber, G. _et al_., Phys. Rev. Lett. _37_, 255 (1976).
Peruzzi, I. _et al_., Phys. Rev. Lett. _39_, 1301 (1977).
Scharre, D. L. _et al_., Phys. Rev. Lett. _40_, 74 (1978).

10. For an excellent review see Feldman, G. J., Stanford Linear Accelerator Preprint, SLAC-PUB-2068 (1977).

11. Baltay, C. _et al_., Phys. Rev. Lett. _39_, 62 (1977) and _41_, 73 (1978).

12. Drijard, D. _et al_., Phys. Lett. _81B_, 250 (1979).

13. Brandelik, R. _et al_., Z. Physik C, Particles and Fields _1_, 233 (1979).

14. Richard, F., _Proceedings of the International Symposium on Lepton and Photon Interactions_, Fermilab (1979).

15. Luth, V., _Proceedings of the International Symposium on Lepton and Photon Interactions_, Fermilab (1979).

16. Cazzoli, E. G. _et al_., Phys. Rev. Lett. _34_, 1125 (1975).
Cnops,A. M. _et al_., Phys. Rev. Lett. _42_, 197 (1979).
Baltay, C. _et al_., Phys. Rev. Lett. _42_, 1721 (1970).
Angelini, C. _et al_., CERN-EP 79-44 (8 May 1979, submitted to Phys. Lett.

17. Drijard, D. _et al_., Phys. Lett. _85B_, 452 (1970).
Giboni, K. L. _et al_., _ibid_, 437.
Lockman, W. _et al_., _ibid_. 443.

18. Knapp, B. _et al_., Phys. Rev. Lett. _37_, 882 (1976).

19. Brandelik, R. _et al_., Phys. Lett. 70B, 397 (1977).
Feller, J. M. _et al_., Phys. Rev. Lett. _40_, 274 (1978).

20. Vuillemin, V. *et al.*, Phys. Rev. Lett. **41**, 1149 (1978).

21. Kirkby, J., and Reeder, D., *Proceedings of the International Symposium on Lepton and Photon Interactions*, Fermilab (1979).

II. APPARATUS

INTRODUCTION

The Mark II detector was installed in the West Pit of the e^+e^- storage ring SPEAR at SLAC during the winter of 1977 - 78. Data were collected for this thesis during blocks of running in May 1978 (780 nb^{-1}), February 1979 (2070 nb^{-1}) and March 1979 (430 nb^{-1}). The following is a brief description of SPEAR and its characteristics during the running times at the $\psi(3770)$.

SPEAR

The SPEAR ring (see Figure 1) stores counter-rotating bunches of positrons and electrons in a single beam pipe and magnetic lattice. The ring is filled alternately with positrons and electrons from the SLAC two mile long linear accelerator to a current of about 11 mA per beam at the $\psi(3770)$. The filling time averages about 15 minutes, and storage is optimally about 2.5 hours; the latter is determined to maximize luminosity given the average fill times and beam decay rate. At fixed energies below 4.5 GeV, the ring can be filled in "topoff" mode, which doesn't require dumping the beams. Average fill times are reduced to ~5 minutes.

Four radio frequency cavities supply energy to the beam making up for the synchrotron losses. The average loss per electron varies as E_b^4 and amounts to about 36 KeV/turn at the $\psi(3770)$. In single bunch per beam operation, the electrons and positrons collide at 1/280th of the rf frequency or 1.28 MHz (every 780 ns) at two intersection points around the ring. The luminosity for SPEAR below 6.4 GeV is

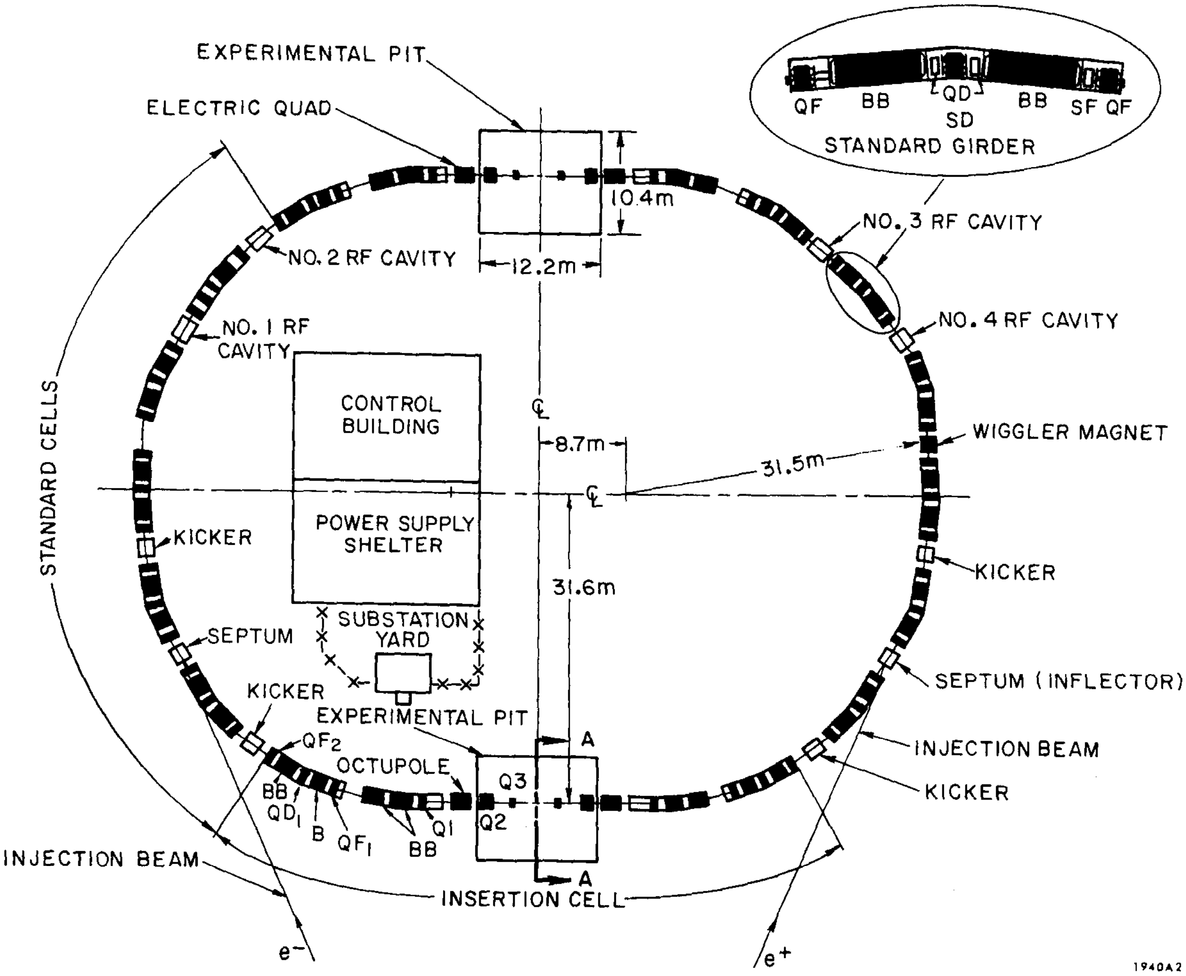

Fig. 1. SPEAR storage ring in February 1979.

given by:

$$\mathscr{L}_{peak} \approx 10^{31} \left(\frac{E_{beam}}{3.2}\right)^4 \ cm^{-2}\ sec^{-1}$$

$$\mathscr{L}_{avg} \approx \begin{cases} \tfrac{1}{2}\ \mathscr{L}_{peak} & \text{in topoff mode} \\ \tfrac{1}{4}\ \mathscr{L}_{peak} & \text{otherwise} \end{cases} \qquad (1)$$

At the $\psi(3770)$, $\mathscr{L}_{avg} = 6 \times 10^{29}\ cm^{-2}\ sec^{-1}$ or $50\ nb^{-1}$/day. During actual running $70\ nb^{-1}$/day was achieved. At this luminosity and energy the average trigger rate is about 1 Hz, with hadronic events occurring every 75 seconds.

The beam bunches at SPEAR have approximately Gaussian shapes whose RMS widths in mm are:

$$\sigma_x = 0.6\ (E_b\ /2.2) \qquad \sigma_y = 0.04\ (E_b\ /2.2) \qquad \sigma_z = 32$$

where E_b is the beam energy in GeV. The horizontal width σ_x is the result of direct synchrotron radiation loss coupling to the betatron oscillations in the bending plane. The vertical width is dominated by coupling to the horizontal oscillations, but has additional contributions from synchrotron losses during the rf acceleration phase. The longitudinal width σ_z is also the result of quantum fluctuations from synchrotron radiation; it is weakly energy dependent. Quantum fluctuations introduce a natural spread in the beam energy with the dependence:[1]

$$\sigma_\varepsilon \approx 3.5 \times 10^{-4}\ (E_b)^2\ (GeV) \qquad (2)$$

At the $\psi(3770)$ this amounts to about $\pm\,1.2$ MeV/beam. The ring energy calibration is performed using detailed knowledge of the magnetic fields and orbit geometry. The 36 bending magnets were all previously measured in series with a reference magnet. During running the reference magnet, still in series with the dipoles, is sampled continuously by a flip coil. The relative field error is expected to be less than .05% . The equilibrium orbit circumference is measured after minimizing orbit deviations read by 24 position monitors around the ring. The energy is thus determined by the rf cavity frequency, the magnetic field, and the orbit circumference with an error of approximately .1% . This is comparable to the beam's energy spread. During the last two weeks of the 1979 data taking, an 18 kg, 7 pole "wiggler" magnet was tested at SPEAR.[2] The wiggler is able to improve luminosities by blowing up the dimensions of the beam, allowing up to 13 mA current/beam to be stored before the beam-beam limit is achieved. Peak luminosities of $2.6-2.8 \times 10^{30}$ cm^{-1} sec^{-1} were obtained. By "topping off" every 75 minutes, an average luminosity over a fill of 2.2×10^{30} cm^{-2} sec^{-1} was obtained, allowing data collection at ~ 100 nb^{-1}/day.

MARK II DETECTOR

The Mark II magnetic detector was designed as a general purpose magnetic detector suitable for a broad range of studies at SPEAR and PEP (see Figures 2 and 3). Over a 30 GeV range in center of mass energy, the MKII can simultaneously perform measurements on inclusive particle production, the dynamics of jet structure, the identification of new exclusive states, and the detailed structure of the total cross section. The MKII has significant advantages previous detectors in its trigger design, neutral particle detection and time-of-flight

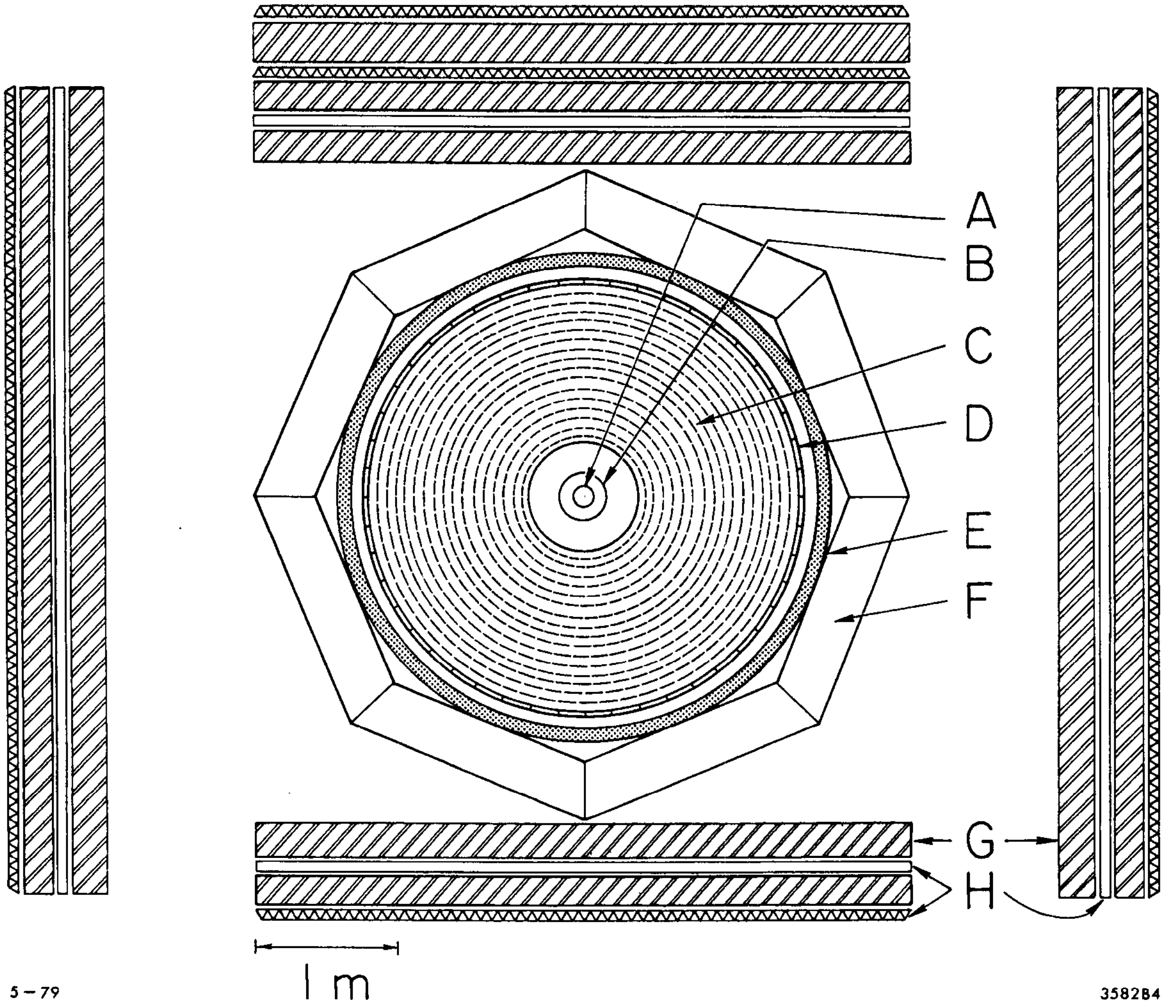

Fig. 2. Mark II Detector (End View):

A) Beam Pipe

B) Pipe Counters

C) Drift Chambers

D) TOF Counters

E) Magnet Coil

F) Liquid Argon Calorimeter Module

G) Bottom Flux — Return and Side Hadron Absorber

H) Muon Proportional Tubes

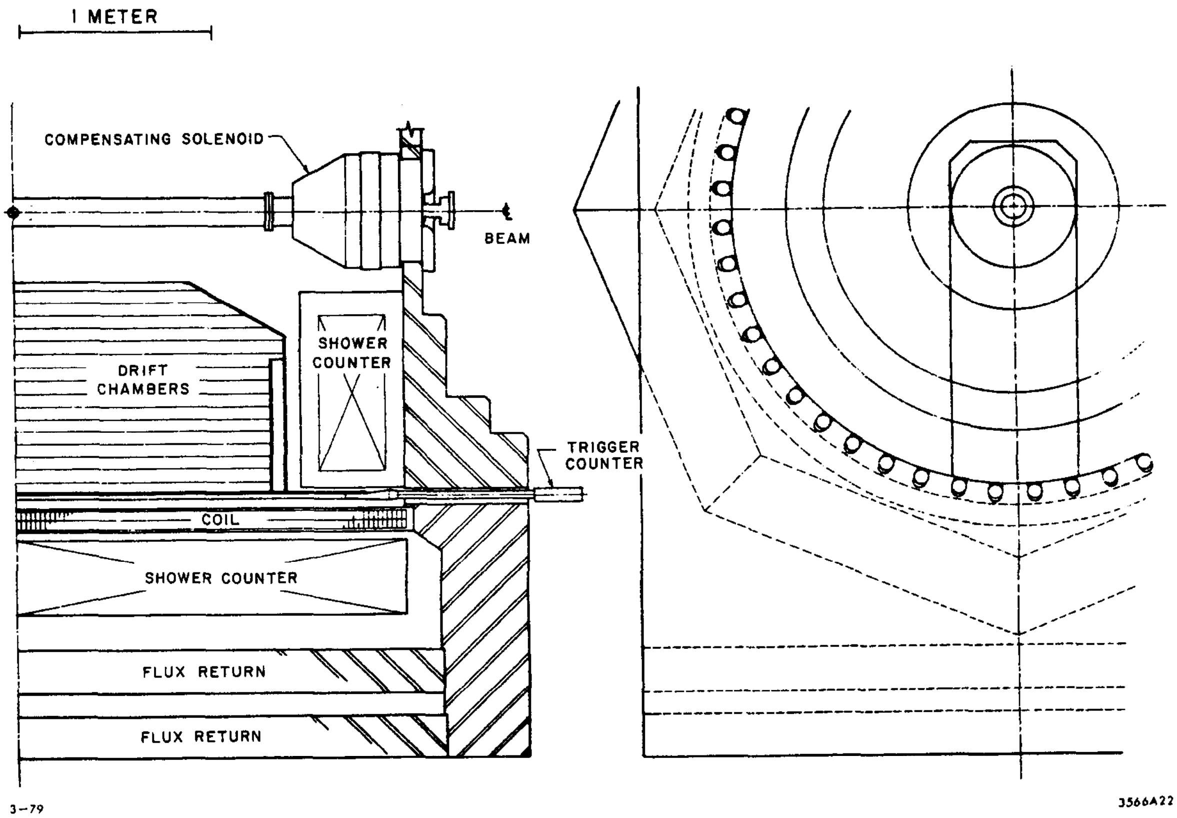

Fig. 3. Mark II Detector (Side View).

resolution. At higher center of mass energies, the improved resolution of the charged particle tracking chambers becomes important.

In the next sections each detector subsystem and its performance is described in detail. I have excluded a discussion of the endcap region for it is not relevant to the results presented in the later chapters. Table I is a summary of the material transversed by a particle from the interaction point up to the muon detection system.

Beam Pipe and Pipe Counter

The vacuum chamber surrounding the interaction region (IR) is a 6 mil thick stainless steel pipe with ± 4 mm corrugations. It is 1.5 m in length, and has a 7.7 cm radius. Ion pumps placed at ± 1 meter from the IR provide about 10^{-9} torr vacuum (see Figure 4).

Surrounding the beam pipe are two concentric cylinders of scintillator each formed of two half cylinders. They are 6.4 mm thick and 81 cm long, with inner surfaces located at 11 and 12.5 cm radially outward. Each of the four half cylinders are viewed by a lucite light pipe on one end, leading out ($\sim$ 1.5 m) to a photomultiplier tube beyond the magnet. The adjacent hemi-cylinders are placed in coincidence for the primary trigger and cover $\sim$ 96 % of 4π.

Drift Chamber

Beyond the pipe counter is a 15 cm air gap followed by a .3 cm thick clear Lexan window constituting the inner gas seal of the drift chamber. Details of the drift chamber are contained in the following section.

The drift chamber provides charged particle tracking with a mean spacial resolution of $\sim$ 220 μm, over $\sim$ 85 % of 4π. $\delta p/p$ is about 1 % at 1 GeV (ignoring multiple scattering). To achieve this, there are

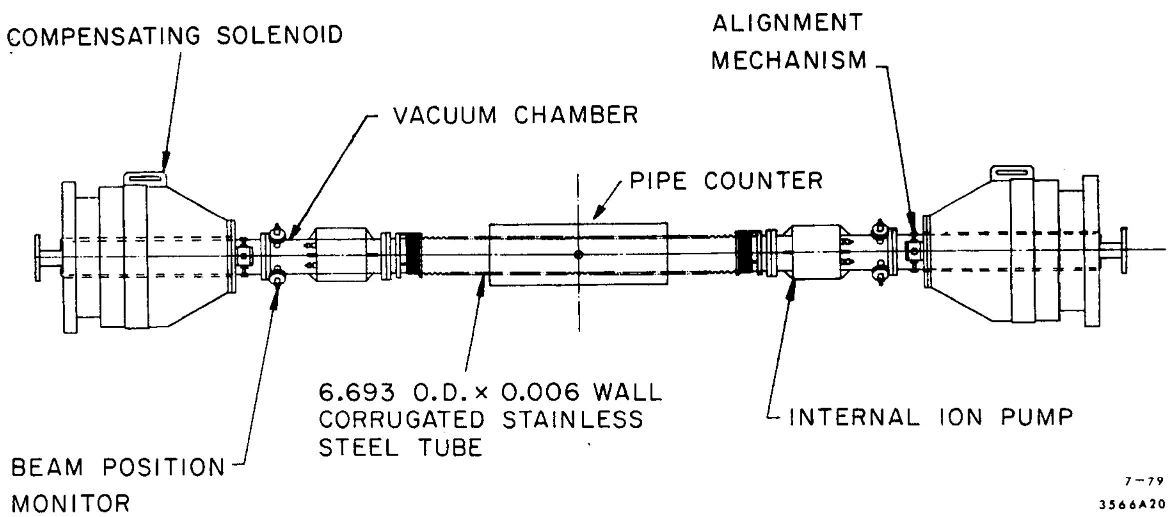

Fig. 4. Beam Pipe (Side View).

TABLE I

Materials in Flight Path

Object	Mean Radius (cm)	Thickness (cm)	Mass (mgm/cm^2)	Energy loss (MeV)	Radiation Length ($\times 10^{-3}$)
Vacuum Chamber	8.0	0.021	162	0.2	12
Pipe Counter Assembly	12.1	3.8	1566	3.0	38
Air Space	28.1	28.3	36	0.0	1
Lexan Window	37.3	0.32	381	0.7	9
Drift Chamber Gas and Wires	94.0	113.0	207	0.5	9
Outer Can	150.6	0.64	1715	2.8	71
TOF Counters	152.4	2.6	2735	5.8	64
Coil to First TR Plane	155.0	--	--	50.4	1250
TR Plane to LA Stack	182.4	--	--	4.8	150
LA Stack	191.4	--	--	230.0	14000

sixteen concentric cylindrical layers of wires, of which six lie along the beam and magnetic field axis, and ten lie at $\pm 3^{\circ}$ stereo angle to this axis. The wires are in a common gas volume with no other material present, thus presenting less than .01 X_0 for scattering. The vertex can be reconstructed to about .5 mm radially and 5 mm axially. Using beam position information, $\delta p/p$ is reduced to ~ .5% at 1 GeV.

Time of Flight Counters

The drift chamber's outer aluminum can is .64 cm thick and has a radius of 1.51 meters. Directly outside its fiberglass wrappings are mounted 48 scintillators of approximate dimension 135.5" × 8.0" × 1.0". These are made of Pilot F, and are viewed at each end by 2" XP2230 photomultipliers, attached to the scintillator by 47." × 1.75" lucite rods. Each phototube is housed in an iron cylinder to shield against the residual magnetic field. In addition, each counter has a 10 m long fiber optic attached at its center. These are coupled to the output of a N_2 flashtube which is pulsed at high voltage to provide isochronous calibration signals of 1.8 ns risetime and 10 ns duration on each counter.

The output of each phototube is split with 20% going to an ADC and 80% to a discriminator, latch and 12 bit TDC. A set of time-compensated signals are provided at a fixed time relative to the beam crossing, and are employed in the primary and secondary trigger. The ADC is used to correct the TDC for variations in pulse height which introduce time slewing.

The system is calibrated in part online by use of the flasher. This is done every ~ 8 hours and provides counter-counter alignment to about 100 ps. Further refinements are applied offline by minimizing the variation of predicted and measured times for each counter, for a sample (~ 7 days running time) of reconstructed Bhabha and muon pair events. The resolution of the system is determined to be ~ 270 ps for the "calibration" sample and ~ 300 ps for hadrons (see Figures 5 and 6). The use of TOF for charged particle identification will be discussed further in Chapter V. It is found that $\sim 97\%$ of tracks heading for a TOF counter will be reconstructed with a valid time. About 6% of all tracks have a second track in the same counter. One of the times is usually recoverable, with its resolution degraded to ~ 480 ps.

Magnet Coil and Flux Return

Immediately beyond the TOF counters is the coil of the solenoid magnet. The main characteristics are summarized in Table II. The 4.16 kilogauss field produced by the ~ 1.4 r.l. aluminum coil is returned through two upper and two lower steel slabs shown in Figure 2. These flux returns are ~ 23 cm thick and carry about 10 kg; their thickness being chosen principally for the muon/pion separation rather than flux handling. In addition to the solenoid, two compensating coils are needed to reduce the longitudinal field integral on the beam line to zero (these are shown in Figures 3 and 4). This prevents the solenoid from introducing a coupling of the vertical and horizontal beam oscillations.

The entire magnet was assembled and later mapped with a Hall probe, before moving to SPEAR. The longitudinal field B_z within the drift chamber volume was found to be constant within $\sim 1.4\%$ of its

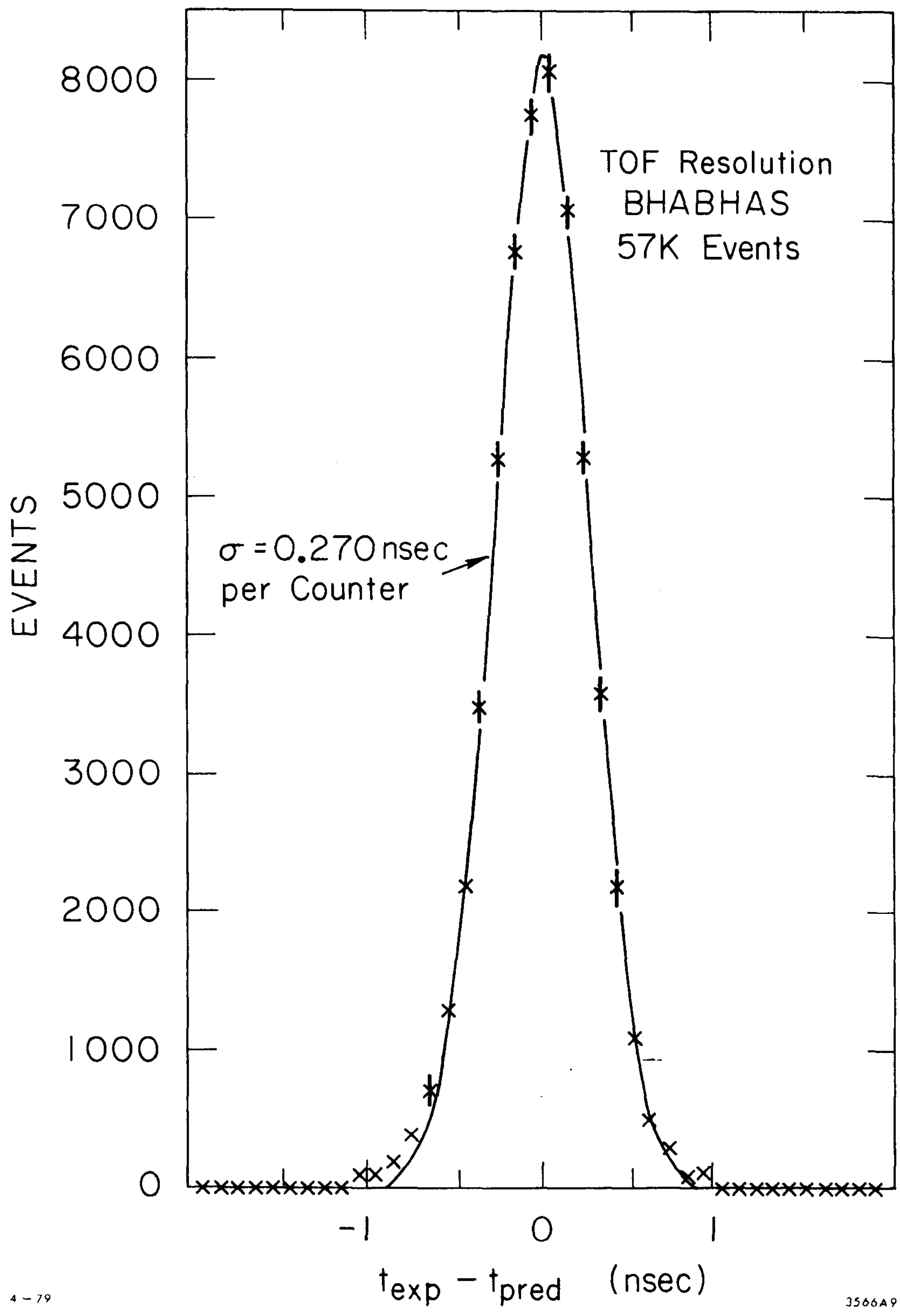

Fig. 5. Difference of measured TOF and predicted TOF for Bhabha-scattered electrons, showing TOF resolution.

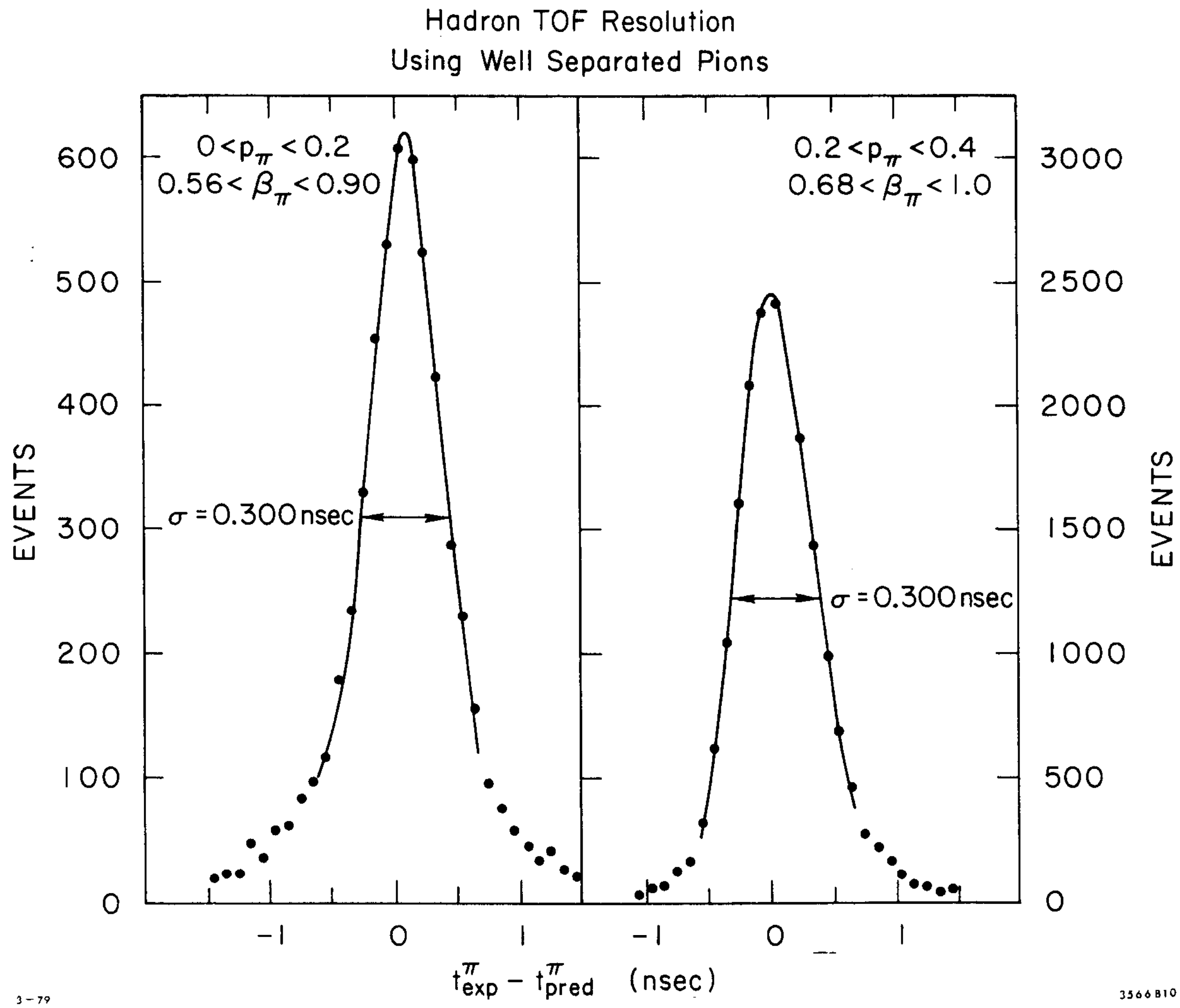

Fig. 6. Difference of measured TOF and predicted TOF for pions, showing typical TOF resolution for hadrons.

TABLE II

Main Coil Details	
Inner Diameter	= 125 in. = 3.18 m
Length	= 164-1/4 in. = 4.18 m
Number of Turns	= 336
Conductor - Material	= Aluminum (63% IACS) 99.9%
Conductor - Dimension	= 1.75 in. × 0.95 in. R = 10.58 μΩ/ft
Conductor - Water Hole	= 0.50 in. × 0.40 in.
Conductor - Total Length	= 11,388 ft
Resistance at Mean Temperature	= 0.121 Ω
Number of Water Passages	= 28 (double) 6 turns per single passage
Flow	= 316 GPM at 200 psi
Compensator Details	
Number of Compensators	= 2
Inner Diameter	= 7-1/16 in.
Length	= 23-1/4 in.
Number of Turns	= 168
Conductor - Material	= Copper
Conductor - Overall Dimensions	= 0.800 in. × 0.800 in.
Conductor - Water Hole	= 0.375 in. diam
Resistance	= 0.0115 Ω
Flow	= 30 GPM at 200 psi
Operating Characteristics	
Main Field	= 5 kG (nominal) uniform ±1.5% over volume of chambers
Current	= 5000 A (design values)
Voltage	= 732 V = 608 V (main) + 114 V (comp) + 10 V (bus)
Operation at SPEAR	= 4.16 kG at 4000 A

mean value of 4.620 kG. The radial field B_r varied from ~ 0 Gauss at the center of the magnet, to ~ 102 Gauss near the compensators. A small variation (δB_z) in B_z was found in the region $\phi = 320 \pm 15^0$. δB_z ranges from ~ 5 to ~ 20 Gauss as r moves from 0 inches to 58 inches. No z dependence was observed. It is speculated that the fluctuation is the result of the cooling water outlets in that area. For offline tracking, a polynomial fit in z and r is done to the B_z field map averaging over ϕ, outside the 320^0 region discussed above. The scale of the polynomial is set continuously by an NMR probe within the solenoid volume. Since axial symmetry is assumed, B_r is obtained from B_z directly. The fit reproduces the field within .028% axially and deviates ~ 1.5 Gauss radially. The overall systematic field error is $\sim .2\%$.

Lead-Liquid Argon Shower Counters

Immediately beyond the coil is the inner wall of the common vacuum jacket for eight liquid argon calorimeter modules. These "barrel" modules cover $\sim 69\%$ of 4π sr. Each module is an 18 layer sandwich of 2 mm thick lead and 3 mm liquid argon gaps. At normal incidence, there are 14 X_0 of material. Alternate layers of the sandwich are lead strips, 3.7, 5 and 7.4 cm wide, running in θ, ϕ and 45^0 directions, allowing spacial resolution of the showers.

Each module is a sealed and super-insulated capsule which has liquid N_2 cooling pipes attached to its back face. The modules are slowly cooled with LN_2 to $\sim 89^0$K, then argon liquid is introduced. Directly in front of the lead stack are two 8 mm trigger gaps. The strips between these gaps are read out, to determine if any preconversion in the coil has occurred, allowing an energy correction to be made. To reduce the number of channels to ~ 360/module, the strips are grouped internally in depth and in width. Table III shows the scheme

TABLE III

Plane	Coordinate		Width (cm)	Number of Channels per Module
1	ϕ	TRIGGER GAP	3.7	36
2	ϕ		3.7	38
3	θ		3.7	100
4	u		5.0	56
5	ϕ			
6	θ			
7	u			
8	ϕ			
9	θ			
10	u			
11	ϕ		3.7	40
12	θ			
13	θ		7.4	52
14	θ			
15	ϕ			
16	ϕ			
17	ϕ		3.7	40
18	ϕ			
19	ϕ			
			total	362

of ganging and the coordinates read out. The charge collected on the strips from a shower is preamplified and integrated over ~ 460 ns by a SHAM module (Sample and Hold Analog Module). The analog signals are then passed through an ADC and read out (see Refs. 3 and 4). The analog-to-digital conversion, readout and calibration are analogous to the drift chamber's scheme described in the next section.

The liquid argon detector is calibrated using non-radiating Bhabhas (i.e., measured momentum close to the beam energy) and cosmic rays. The trigger gaps are adjusted for cosmics to read just to the minimum dE/dx loss (1.6 cm $\times$ 2.11 MeV/cm). The energy scale of the lead/argon stack is determined using normally incident Bhabhas and muon pairs which are minimum-ionizing at the trigger gaps. The energy in the stack is scaled to be the measured momentum (in the drift chamber) less an estimate for back leakage and coil loss (equal to coil dE/dx plus an average radiative loss in the coil and trigger gaps). A shower Monte Carlo is then used to determine the functional form for other incident energies, angles and the measured energy in the trigger gap. At normal and non-normal incidence, the Monte Carlo was checked against the measured values and the two agreed well.

Using tracked Bhabhas, the energy resolution for electrons in the calorimeter is (see Fig. 7):

$$\delta E/E = 11.5\% \,/\, \sqrt{E(\mathrm{GeV})} \quad .$$

The measured detection efficiency for photons is shown in Fig. 8. The efficiency is measured using decays of the $\Psi(3095)$. In particular, two channels are selected by missing mass to the charged tracks:

$$\psi \rightarrow \pi^{+}\pi^{-}\pi^{0} \text{ and } \psi \rightarrow \pi^{+}\pi^{-}\pi^{+}\pi^{-}\pi^{0} \quad .$$

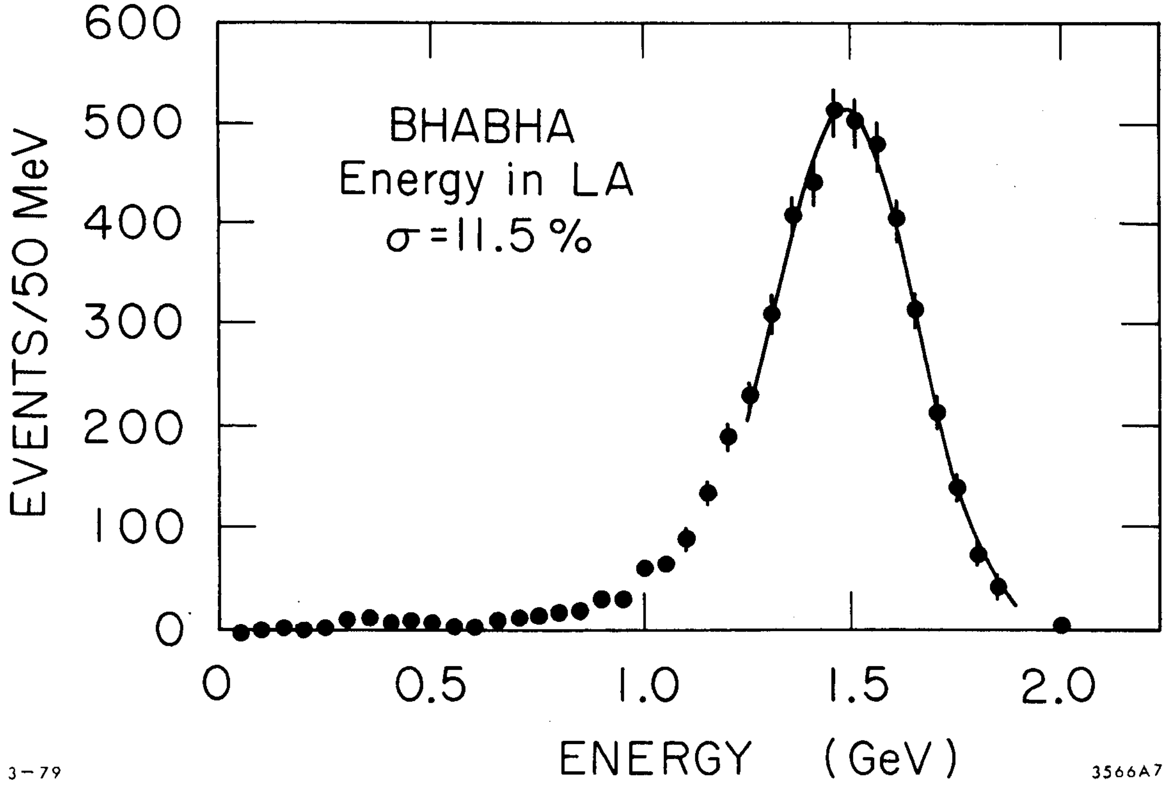

Fig. 7. Energy resolution for Bhabha-scattered electrons in the liquid argon calorimeter. The tail results from initial and final state radiation.

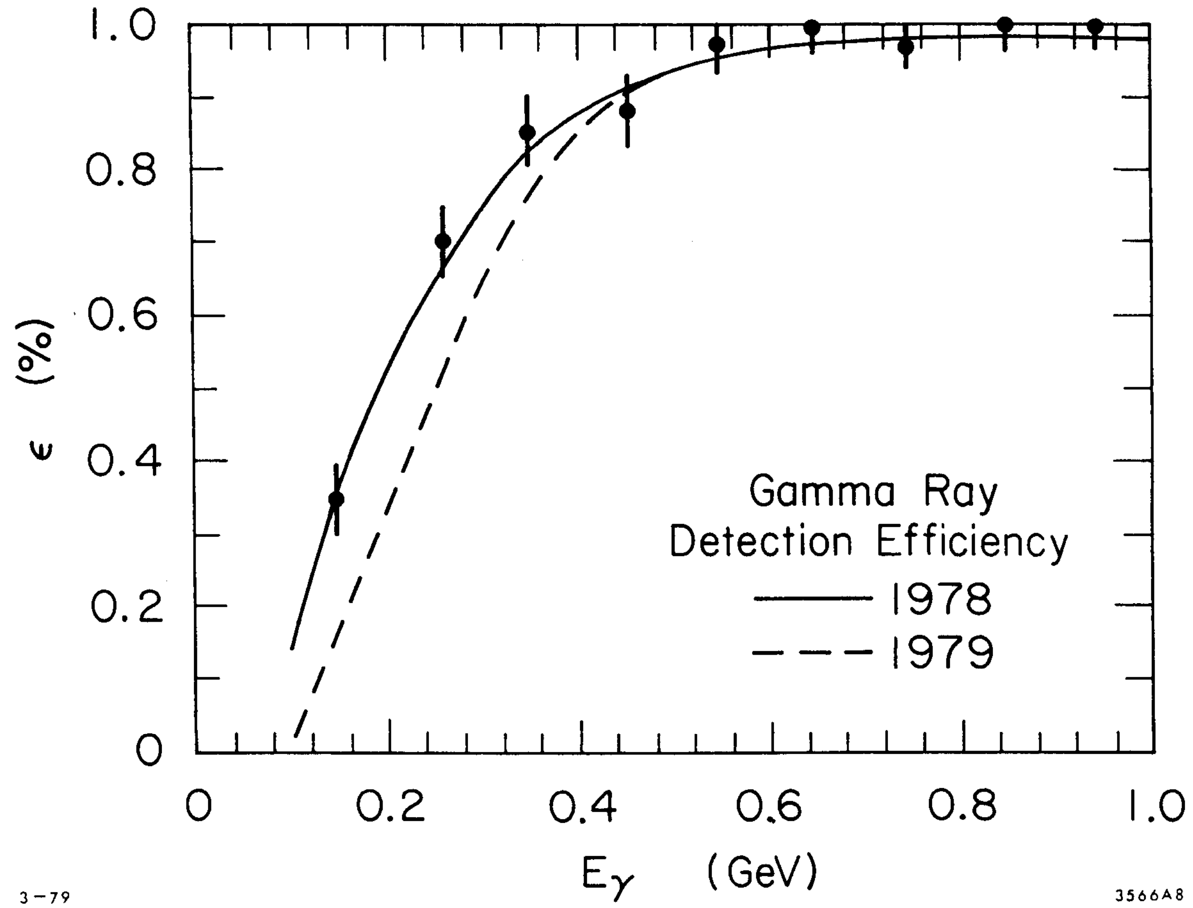

Fig. 8. Detection efficiency for γ-rays. The curves are a Monte Carlo shower calculation.

In events where there is at least one photon with energy greater than 300 MeV, a two constraint fit is performed (using the ψ mass and the π^0 mass). The second photon is searched for in the appropriate cone ($\sim 9^o$) determined by the fit. These efficiencies agree well with a shower Monte Carlo calculation (the curves in Fig. 8). The resolution of photon energies can be measured by the pulls in these fitted events. The resolution is degraded by the coil (1.36 r.l.) to about $14\% / \sqrt{E}$ for photons, and deviates below ~ 600 MeV from this parametrization.

Muon System

The muon detection system contains planes of triangular-shaped proportional tubes interspersed among layers of steel. The full system is shown in Figure 2. Table IV, below, shows solid angle covered for the two groups of data used in this thesis:

TABLE IV

Muon System Depth and Solid Angle

Layer	$\langle\text{Depth}\rangle_{\text{c.m.}}$	1978(% 4π)	1979(% 4π)	Cutoff(MeV/c)
1	47	27	61	700
2	70	26	48	900
3	101	--	30	1100

Particles are identified as muons if they are detected within a predicted region (for multiple scattering) about an extrapolated drift chamber track, and if they pass through the iron to a specific depth. The backgrounds arise from K and π decays. The actual misidentification is reduced somewhat, as a result of the good drift chamber resolution, which tends to terminate tracks at decay kinks. Pion misidentification, measured using multiprong ψ decays, is shown in Fig. 9 for the 1978 configuration.

Trigger Logic

The trigger scheme for the MKII features a two level system with small dead-time and good suppression of backgrounds due to cosmics and beam gas. The primary trigger logic consists of a coincidence between the pipe counter (PIPE) segments, a beam crossing signal (BEAMX) and a drift chamber majority signal (DCM). The pipe counter was discussed in the previous section. BEAMX is a signal derived from a pickup ~ 50 meters upstream (e^- side). This signal is placed in coincidence with an rf timing pulse, to avoid confusion with positrons arriving later. The pickup signal goes through a circuit which provides time compensation for different beam currents. To reduce cosmic background, PIPE and BEAMX are in tight coincidence (~ 5 ns). DCM is a signal derived from the OR of a subset of drift chamber layers (each with one or more cells hit), and is available ~ 430 ns after BEAMX. DCM usually requires ≥ 4 of 9 layers to be hit. In certain running conditions, TOF majority (one or more time-compensated latches) can be added to the primary trigger.

At moderate beam energies $\left(\text{such as } \psi(3770)\right)$ the BEAMX $\cdot$ PIPE yields ~ 20 kHz rates, which is reduced to $\leq .1$ kHz by DCM. The primary trigger decision is made within ~ 600 ns of BEAMX, allowing ~ 200 ns for the resetting and clearing of all the hardware before the next beam crossing.

When the primary trigger is satisfied, the secondary trigger is activated and all clear and reset signals are aborted. At the same time, the autonomous hardware begins digitizing data (TOF TDC's and

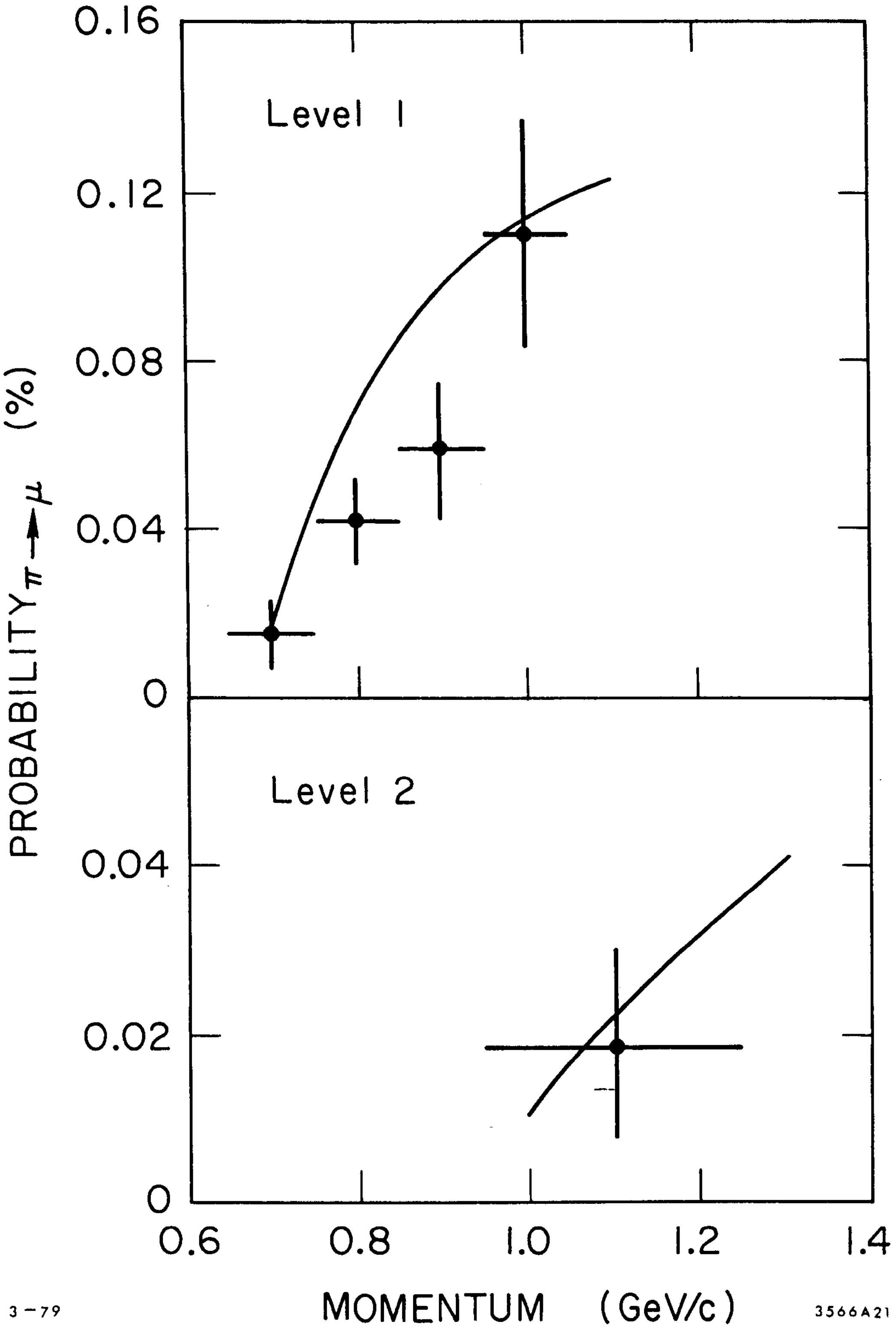

Fig. 9. Pion misidentification rate for muon system.

ADC's, BADC's on TACS and SHAMS). The secondary trigger logic is described in detail in Ref. 4. Its basic function is to search for and count charged track candidates in the drift chamber. It contains two major parts:

(1) A set of 24 "curvature" modules, each of which searches the set of drift chamber hits (in six axial and 4 stereo layers) for alignments within its mask of definite curvature range. The definition of up to three track types is allowed (e.g., Type A means ≥ 4 axial hits out of six in a curvature mask).

(2) A track counter module which collates the curvature module outputs into a trigger decision (e.g., a valid trigger is ≥ 1 A and ≥ 1 B type track).

The curvature modules and track counter are programmable. Since the curvature modules work in parallel, the entire secondary logic takes only ~ 30 μs. The resulting secondary trigger rate is about 1 Hz at the $\psi(3770)$. Most of the $\psi(3770)$ data was taken with a "1½" particle trigger, meaning one A track (four to six axial hits in a road) and one B track (three to five hits in a road, in the inner five layers), and two or more A tracks. Given a drift chamber efficiency of 96%/layer (average), the 1½ particle secondary trigger efficiency is $\geq$ (.997) (.999).

If the secondary trigger is satisfied, the read-in procedure begins. For the largest systems, the drift chamber and liquid argon, this amounts to reading out the memory of the BADC in each of 12 crates, once digitization is completed. This time varies depending on the number of channels that fire; it is typically 30 ms for about 1000 channels. The raw data, amounting to ~ 1200 words, is written on magnetic tapes. At the end of the readout, the electronics are cleared and set up for the next event. Typical deadtimes amount to ~ 3% . The computer used for readout was a Σ5, which was replaced in 1979 by a VAX780. These larger machines are able to analyze asynchronously a sample of the events written on tape. This allows a monitoring of the detector at all times.

<u>The Drift Chamber Inner Detector</u>

I detail here the construction and operational properties of the drift chamber. Further information is available in Ref. 6. The basic theory of drift chambers can be found in numerous references.[7]

(i) <u>Mechanical and geometry</u>

The dimensions of the 16-layer cylindrical drift chamber are shown in Fig. 10. The outer cylindrical can is made of six 6.25 mm aluminum plates which are fiberglass wrapped for torsion relief. These plates hold the endplates apart, thus taking up the wire tension. The inner cylinder is 3.2 mm thick, clear polycarbonate plastic (Lexan), which allows visual inspection of the chamber interior and provides a gas seal. The endplates are a composite of flat aluminum hexcel (7.62 cm thick) and a solid aluminum conical plate. The hexcel part is shaped as an anulus and faced off on both surfaces with twelve pie-shaped aluminum plates (1.59 mm thick) which have been precision drilled (~ 50 μm) with the wire-hole pattern (see Fig. 11). Wires for the outer eight layers are held by these hexcel plates. The inner eight layers of wires are supported by a truncated "cone", rolled of 6.35 mm thick aluminum, with a rim on the larger diameter end which holds two of the eight layers.

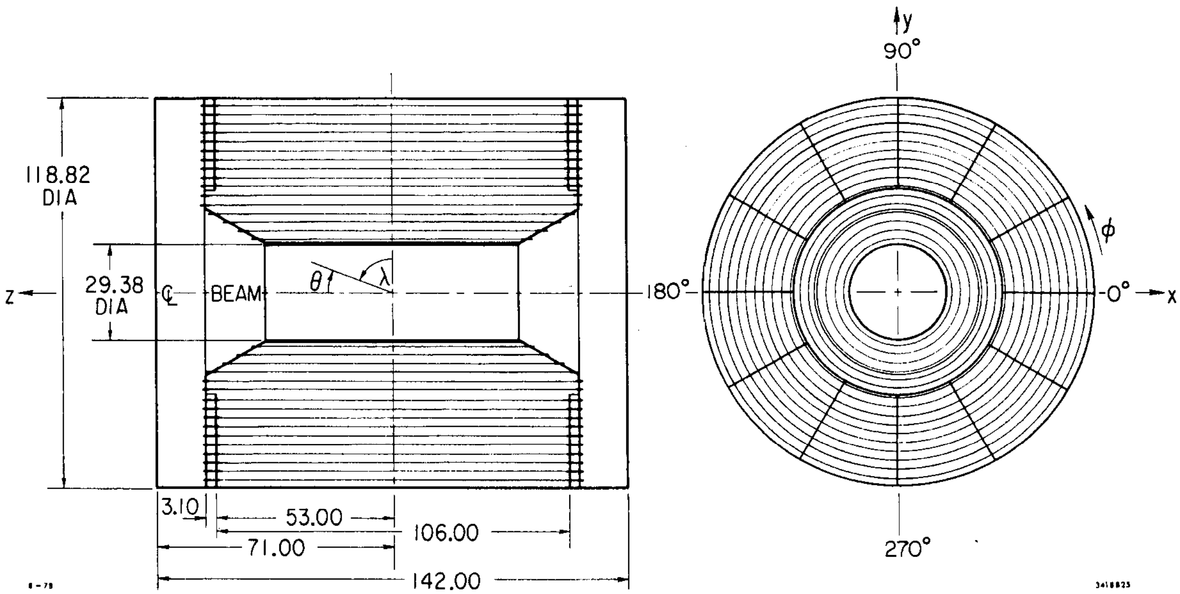

Fig. 10. Schematic of drift chamber showing coordinate systems.

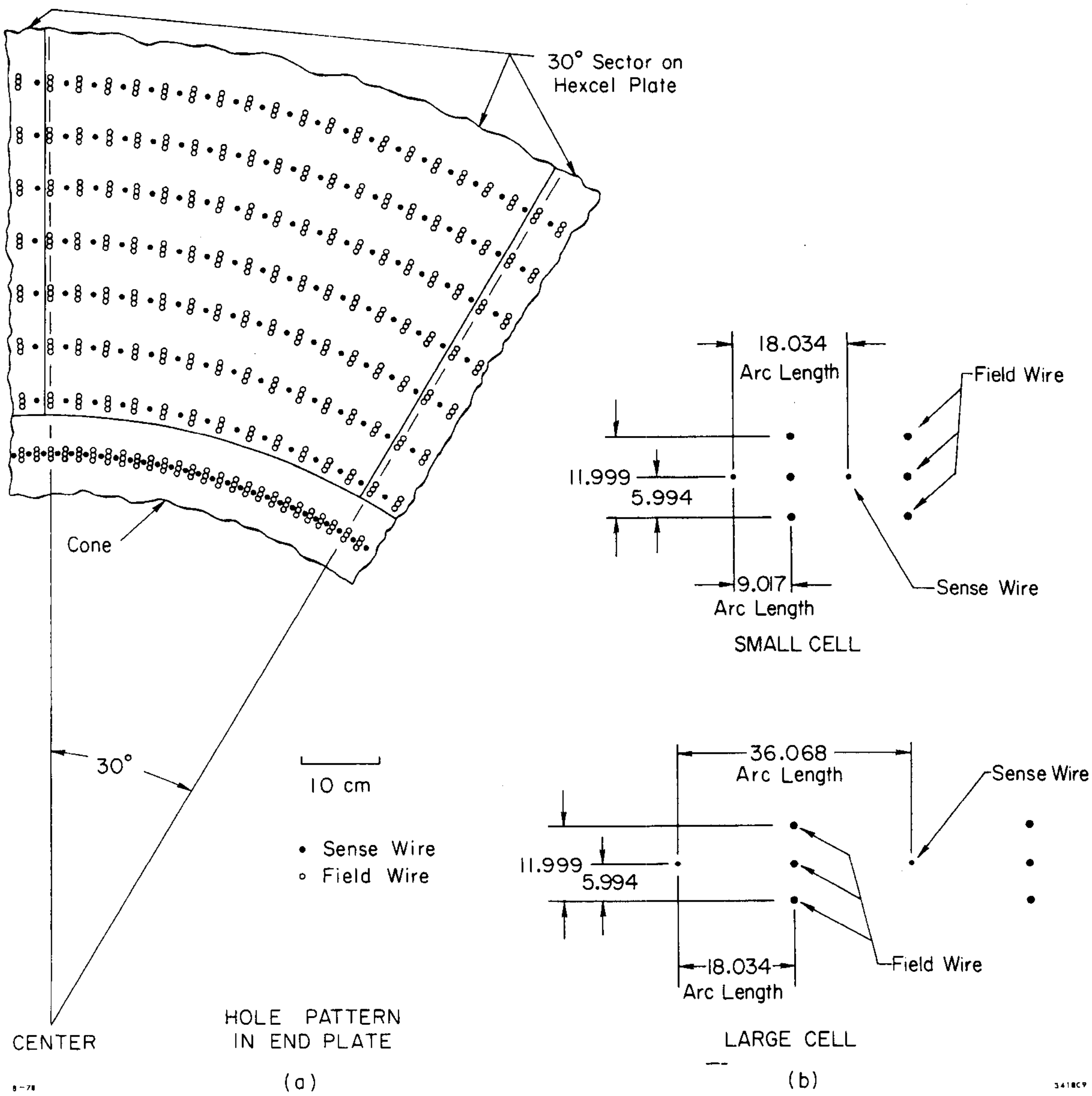

Fig. 11. Schematic of hole pattern and cell sizes in the drift chamber

The wire pattern (which repeats every 30° azimuthally) is given by layer in Table V. There are two cell sizes, small and large (9.02 and 18.03 mm drift space, respectively) which are formed by 4 wires as shown in Fig. 11. The small cells are in the cone, and the large cells are in the hexcel section. Three of the wires are for field-shaping and are 152 μm diameter. The wire composition is Cu - Be alloy #25, Temper A. The sense wires are 38.1 μm diameter, made of the same alloy. All the wires have a silver plating which helps maintain a uniformly smooth surface, reduces oxidation and aids in the manufacture.

The use of Cu-Be alloy provided many advantages in chamber construction. The alloy allows up to $\sim 40\%$ elongation of the 38 μm wire under a tension of half its tensile strength (3.05×10^{6} g/cm^{2}). The chamber was strung almost entirely from the inner to the outer layer, applying only marginal tension to all the wires, to avoid any tangling. Wires were positioned in the precision holes of the endplates by Delrin-Nylon feedthroughs (see Fig. 12). The wires are positioned in the larger (.375 mm diameter) holes of the brass insert, by consistently drawing them to larger azimuths; they are epoxied and pinned in place. After completing the first six layers, the endplates were separated ~ 1.3 cm (stretching the wires to their elastic limit). The remaining 10 layers were strung and the endplates separated another ~ 2.5 cm putting both outer and inner layers well beyond their elastic limit, and placing all sense wires at the same tension (~ 40 grams). The simultaneous stretching of all the wires deforms the endplate dynamically and insures equal tension on the wires. The sagitta of the sense wires is $\sim 350 \pm 50$ μm, as a result of gravity.

TABLE V

Layer Index (# of HV cables)	Radius (mm)	Active Length (mm)	Stereo Angle (degrees)	Number of Cells
6	413.6	1984.1	0	144
7	482.6	2222.9	+3.12	168
8	551.5	2461.7	-2.90	192
9	620.4	2700.5	0	216
10	689.4	2786.4	+2.90	240
11	758.3	2786.4	-2.90	264
12	827.2	2641.6	0	144
13	896.2	2641.6	+3.07	156
14	965.1	2641.6	-3.07	168
15	1034.0	2641.6	0	180
16	1103.0	2641.6	+3.07	192
17	1171.9	2641.6	-3.07	204
18	1240.8	2641.6	0	216
19	1309.8	2641.6	+3.07	228
20	1378.7	2641.6	-3.07	240
21	1447.7	2641.6	0	252

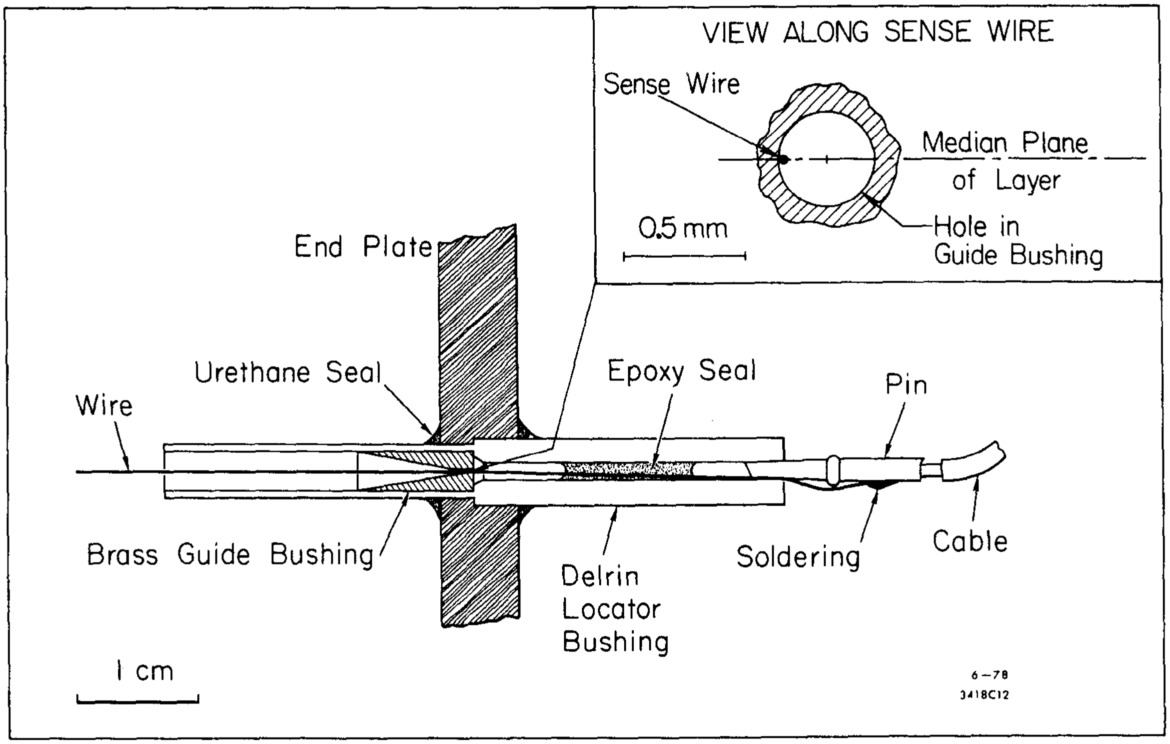

Fig. 12. Detail of the feedthrough used in the drift chamber.

(ii) Electrostatic structure

The cell design has the major advantages of simplifying construction and reducing material in the chamber to a minimum ($\sim .1\%$ r.l.). It does not however provide the optimum electric field. Fig. 13 shows a contour plot of the small and large cell electric field magnitude. The sense wires (center) are held at virtual ground, while the field wires are at -2.85 kV and -3.40 kV respectively. A projection of the magnitude in the median plane is shown in Fig. 14. These plots use a thin-wire, large distance approximation to calculate the field from an array of ~ 100 wires. In the absence of any extra field shaping, we see from Fig. 13 that the field is only radial for $\sim 1/2$ the cell and deviates substantially from radiality beyond that. This effect is especially true in the large cells. As a result of the field shape which alters electron drift paths, a complicated relationship is expected between the time measured and a track's position in the cell. In particular, strong angle dependence is expected for large distances. The details are discussed in Chapter III.

Another problem of the cell structure is an electrostatic instability in the small cells. High voltage is supplied to the chamber through distribution boxes which segment each large (small) layer into 12 (24) cell groups (see Ref. 4 for details). In the small cells, the electric field is sufficiently large that a short circuit in one segment will frequently cause the adjacent segment's edge wire to pull over and break. This problem is removed by coupling the high voltage segments with 600 kΩ, so that a short will pull the whole layer down simultaneously.

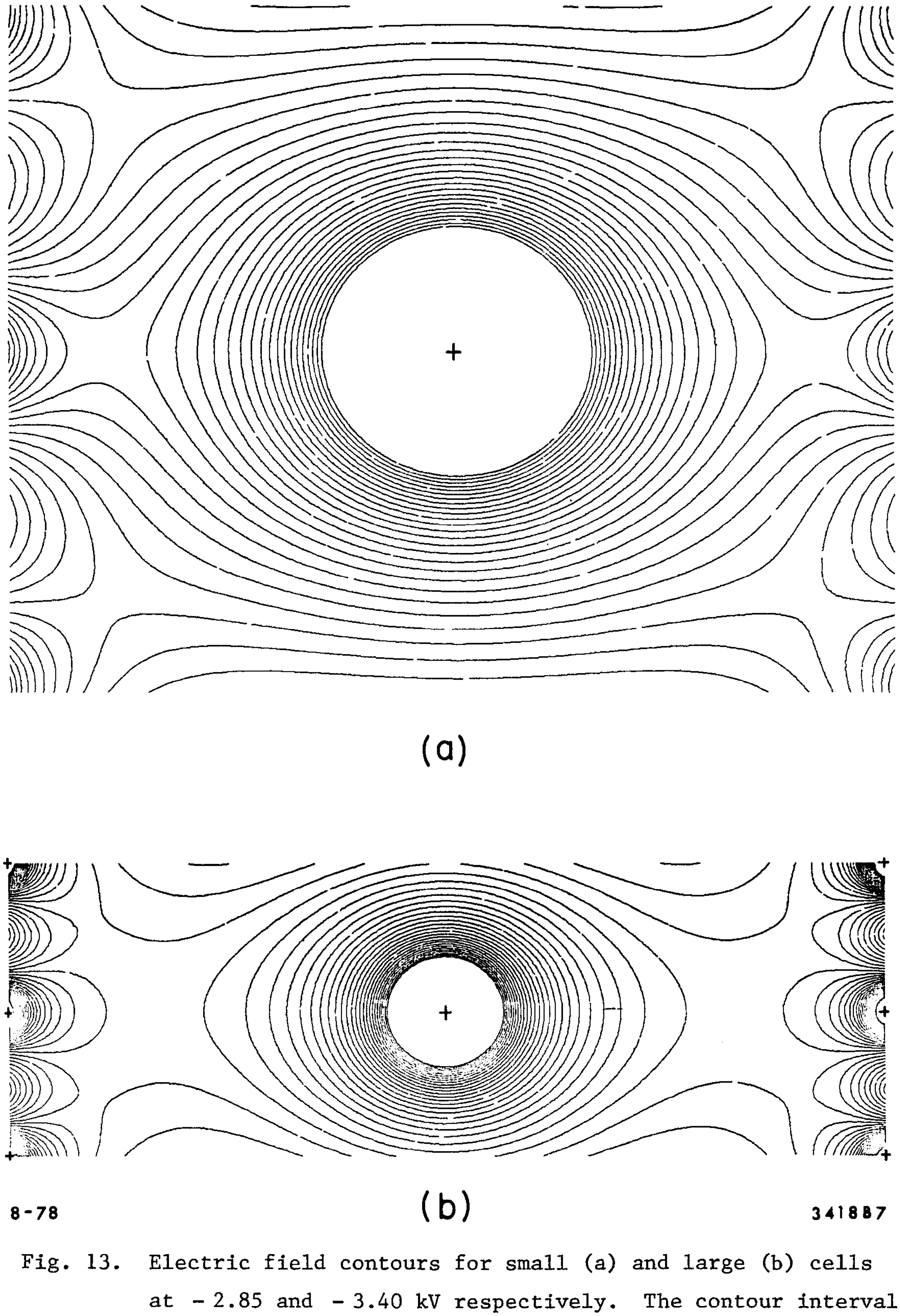

Fig. 13. Electric field contours for small (a) and large (b) cells at -2.85 and -3.40 kV respectively. The contour interval is 50 V/cm. Wire positions are marked by crosses. The effect of the boundary wall on the field of layer 21 is shown in (c).

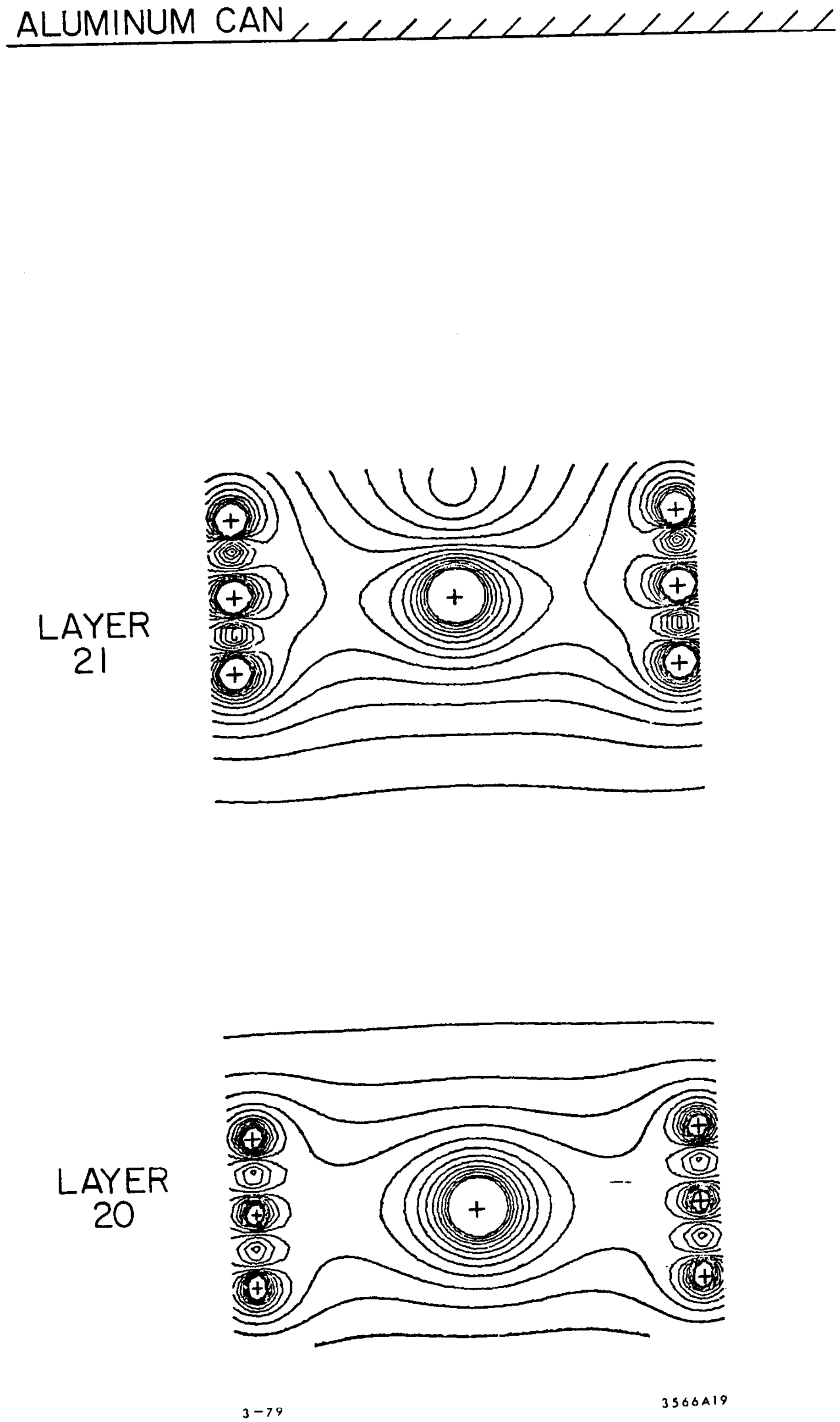

(c)

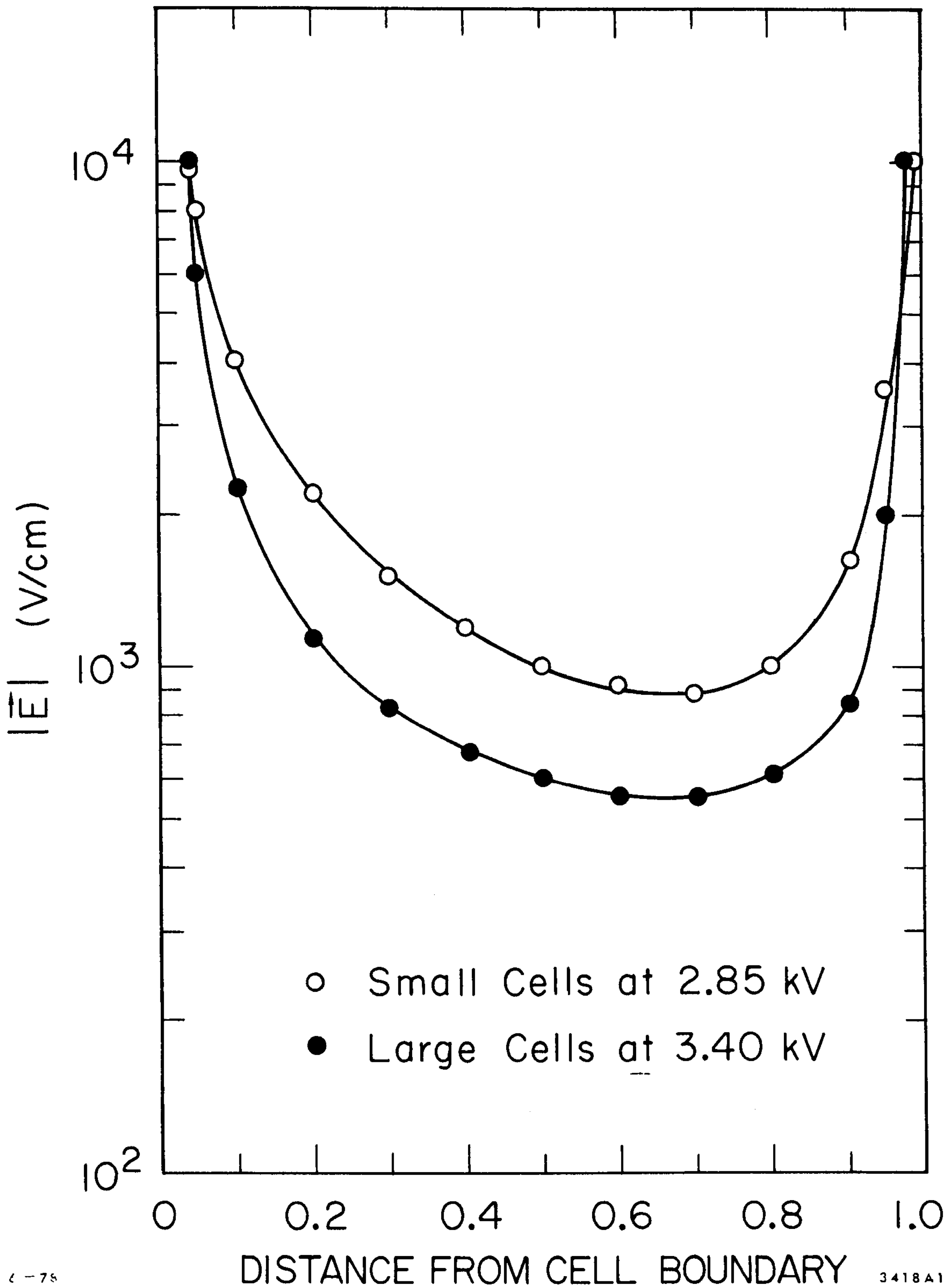

Fig. 14. Electric field in the median plane of a drift cell.

(iii) Gas mixtures

A number of different gas mixtures were tested in a prototype chamber. Argon and ethane or ethylene both were seriously considered. It was important for the chosen gas to have a large average drift velocity over the cell (~ 5 cm/ sec) and to be sufficiently linear in the range of electric fields encountered in the cell. Immunity to polymerization in the SPEAR synchrotron radiation background was also desired. Measurements of drift velocity were made using a device described in Ref. 4. Curves are shown in Fig. 15. The large cells have a substantial fraction of their area in an electric field of ~ 700 - 800 V/cm. This is just on the knee of the curves of ArC_2H_6 and ArC_2H_4 drift velocity. The variation of drift velocity in the cell further complicates the distance to time relationship. The use of 38 μm wire helped raise the average field in the cell and also improved efficiency at large distances from the sense wire. An ArC_2H_6 (1:1) mixture was chosen over ArC_2H_4 because of a somewhat more linear behavior and a more stable (against polymerization) single bond structure. No evidence for polymerization was ever found on wires removed from the chamber.

The gas in the system (~ 18 m^3) is recirculated at ~ 1.3 m^3/hr, and fresh gas added at a rate of ~ .17 m^3/hr. The gas has O_2 removed as water vapor by use of a palladium catalyst, the addition of 2.5 cm^3/min H_2 into the gas, and a molecular sieve. To avoid diffusion and outgassing, which proved to be problems in prototype chambers, all plumbing in the system is copper.

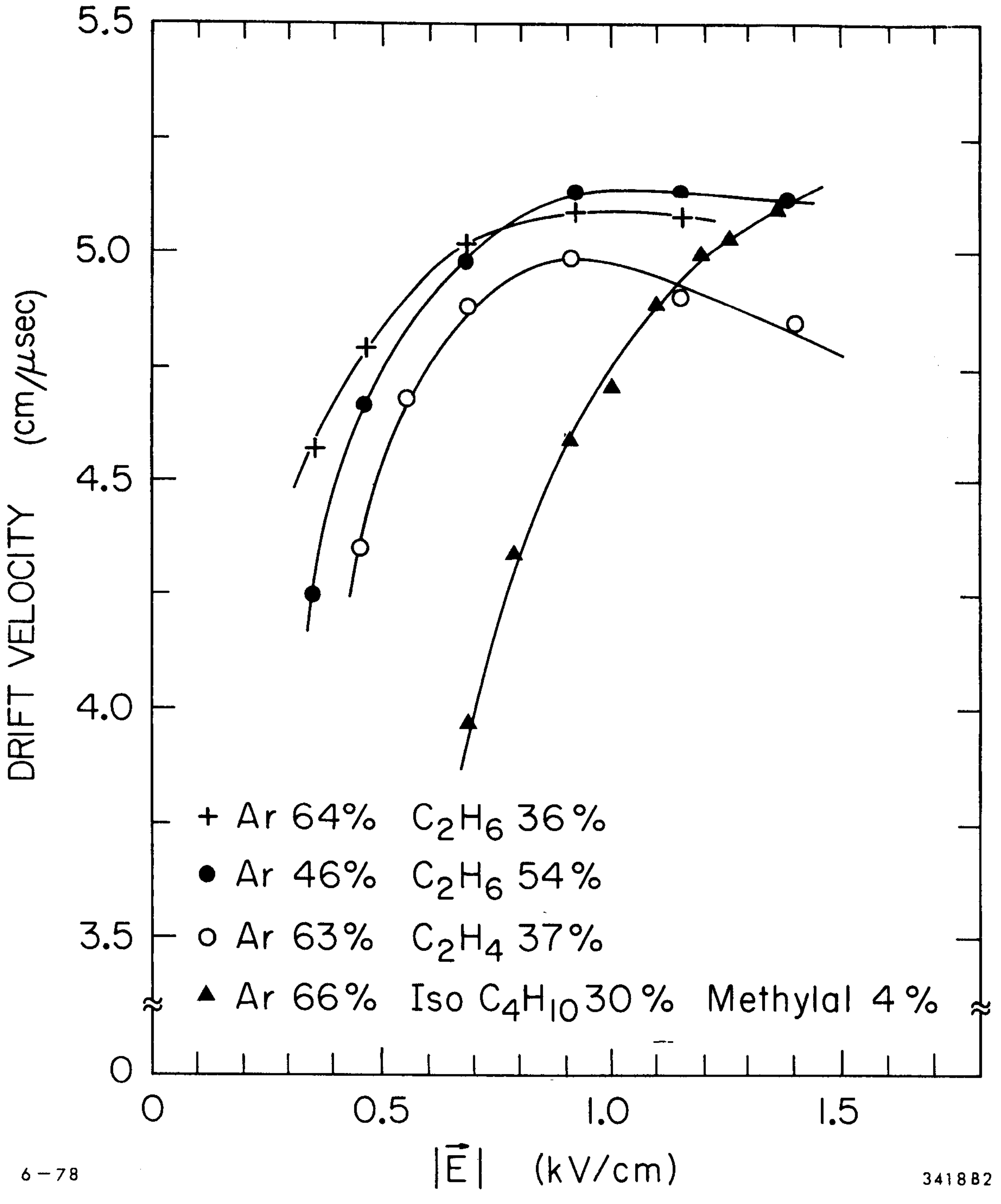

Fig. 15. Drift velocity measurements on several gas mixtures.

(iv) Electronics

The sense wires are connected to a pin which holds them in place in the feedthrough and provides contact to a 50 Ω coaxial cable which carries the signals to the preamplifier-discriminator-line driver circuit shown in Fig. 16. Each coaxial cable is grounded at the chamber face. The signals are then sent differentially to a TAC module (see Ref. 3) which performs time-to-amplitude conversion, for 32 channels. The TAC additionally provides a 32 bit shift register of "hit" wires for the secondary trigger logic, and an OR of this register for the primary trigger (see Fig. 17). The TACs operate in a "common stop" mode. They begin charging only when a wire is hit, and all are stopped simultaneously by a signal ~ 460 ns after BEAMX. The digitization of each channel is performed by a microprocessor (BADC) within the crate.[4] The BADC reads each TAC channel, performs an offset and gain correction for the channel, and stores a time and channel label for all cells that are above pedestal. Each BADC services ~ 600 channels, storing constants for each channel and the results of the digitizations in a $4K \times 16$ bit memory. The BADC's are read out by the host computer which records the raw event data on magnetic tape.

The drift chamber calibration is done by applying a pulse to all the field wires, through the high voltage network, which then couples capacitively to the sense wires. This acts as an isochronous start to each channel, with a stop being supplied at a variable delay time t_i later. By repeating this procedure for five delays up to 200 ns, a line can be fit giving the gain and offset of each channel. The pedestal is measured by a "read" without pulsing. The time distribution

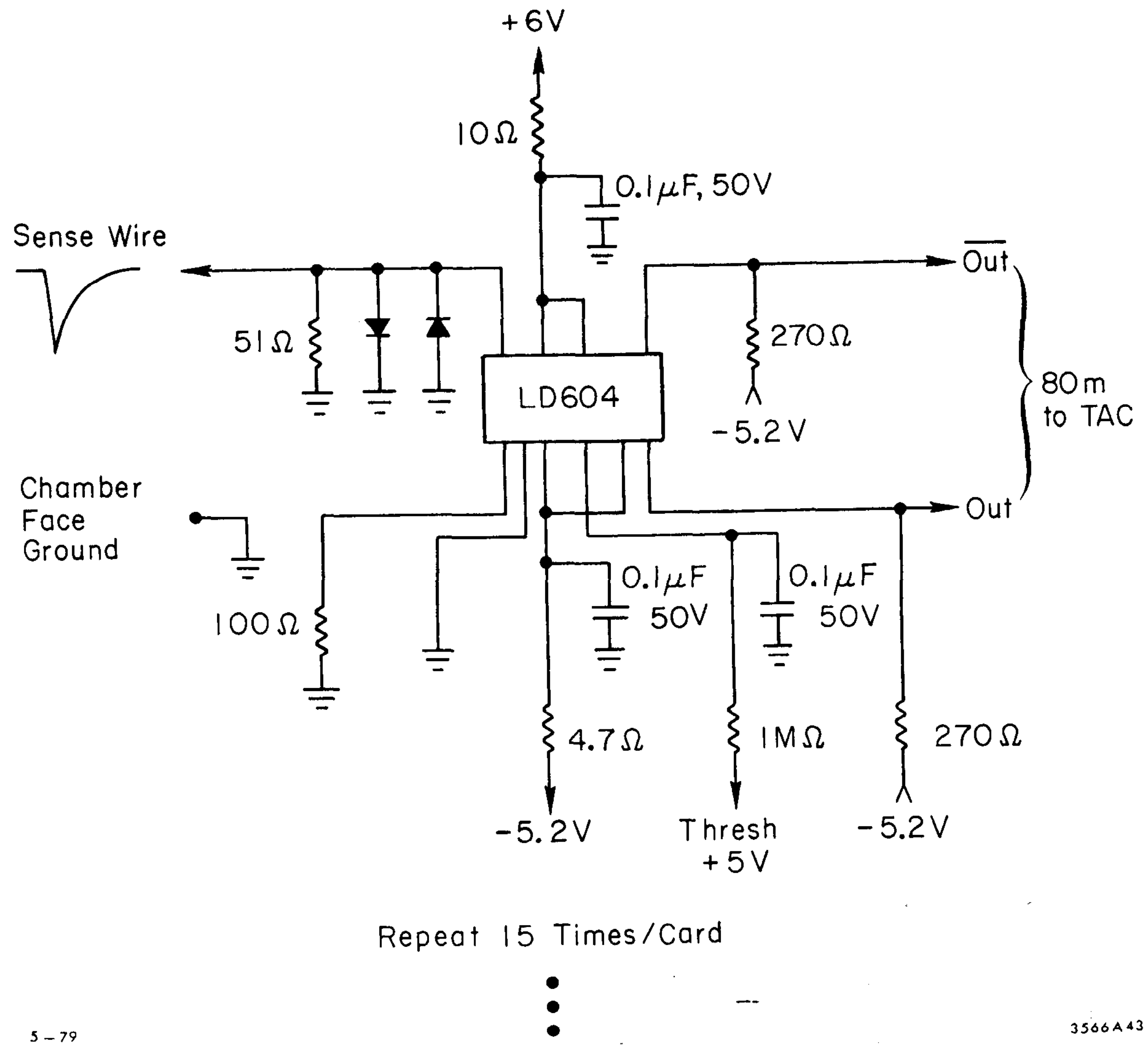

Fig. 16. Schematic of the preamplifier-discriminator card.

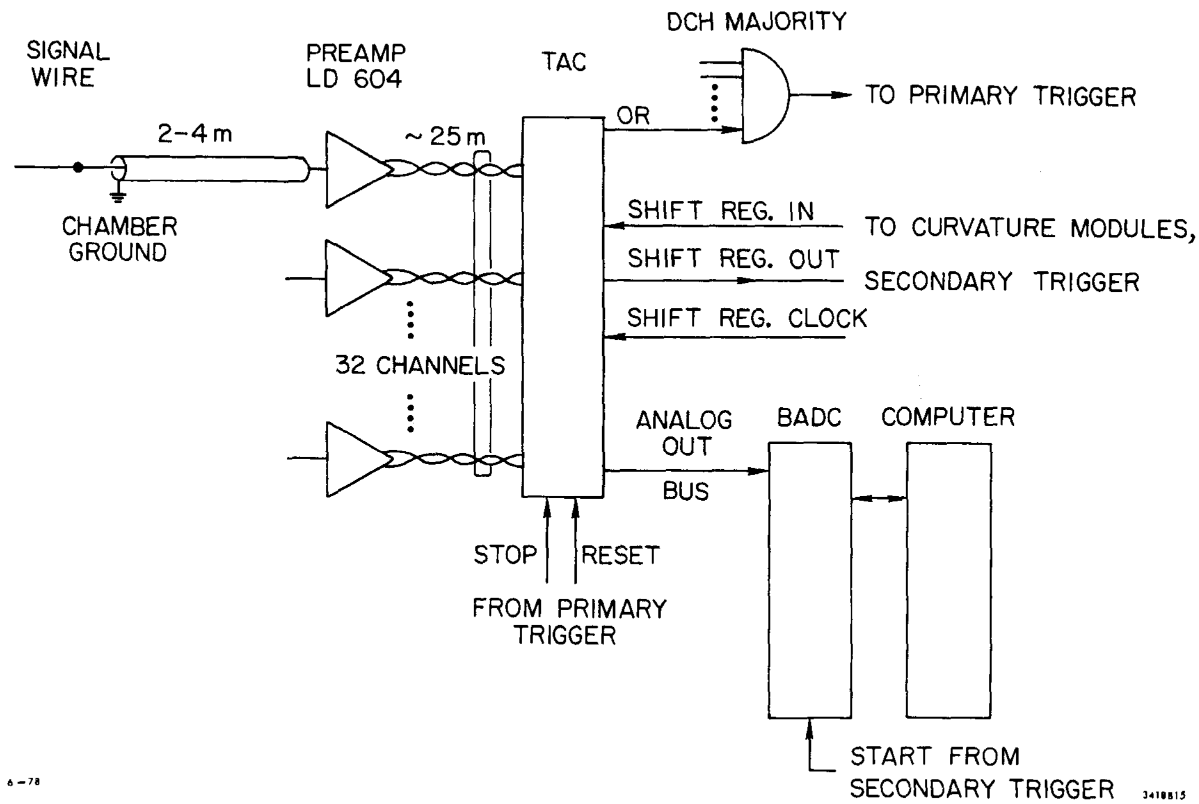

Fig. 17. Scheme for the readout electronics. Portions of the primary and secondary trigger which involve the Drift Chamber are shown.

obtained for a fixed t_i indicates that the average resolution is ~900 ps (HWHM) through the system. The TAC and BADC alone have a time resolution of ~350 ps. As indicated earlier, the liquid argon electronics are similar. The TAC-BADC is replaced by a SHAM-BADC combination; electronic calibration is performed by injecting charges onto the lead strips of each module and measuring the response of the SHAM.

(v) Drift chamber performance

The chamber is plateaued by fixing all layers but one at their operating voltage. Tracks from cosmic events are extrapolated through the odd layer. Efficiency at each voltage is measured by the frequency that the struck cell in the odd layer fires. This "cell" efficiency is monitored online. Figure 18 shows plateaus for two typical layers. These curves extend to ~3.1 and ~3.9 kV respectively before pulse shape deteriorates, geigering begins and electrostatic forces (in the small cells) become a problem. Tests with 20 μm wire in the same cell geometry indicated a wider plateau (~100 V more). The operating points of the chamber are - 2.95 kV and - 3.5 kV for small and large cells. The outermost layer faces a ground plane (the aluminum can) and must operate at - 3.9 kV to have the same efficiency. Its plateau shows a much more gradual rise.

Figure 19 shows the drift time distributions for a set of large and small cells. The width of these distributions and the drift distance determine a mean drift velocity. The shape is gradually sloping, reflecting the nonlinear relation between time and distance. If the cell were uniformally populated, the properly normalized integral of the drift time distribution would provide an estimate of

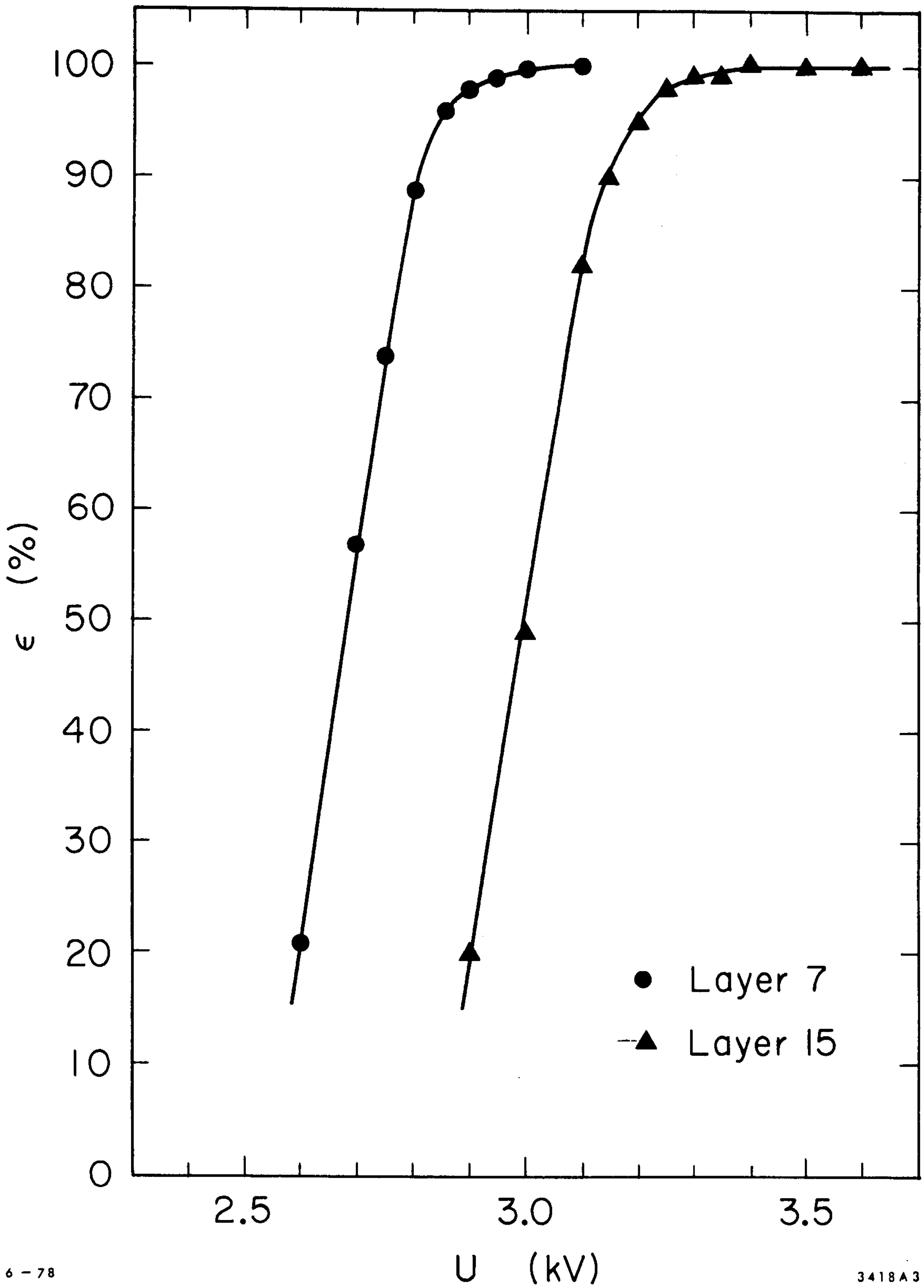

Fig. 18. Layer efficiency from cosmic ray tracks. Dead wires have been removed.

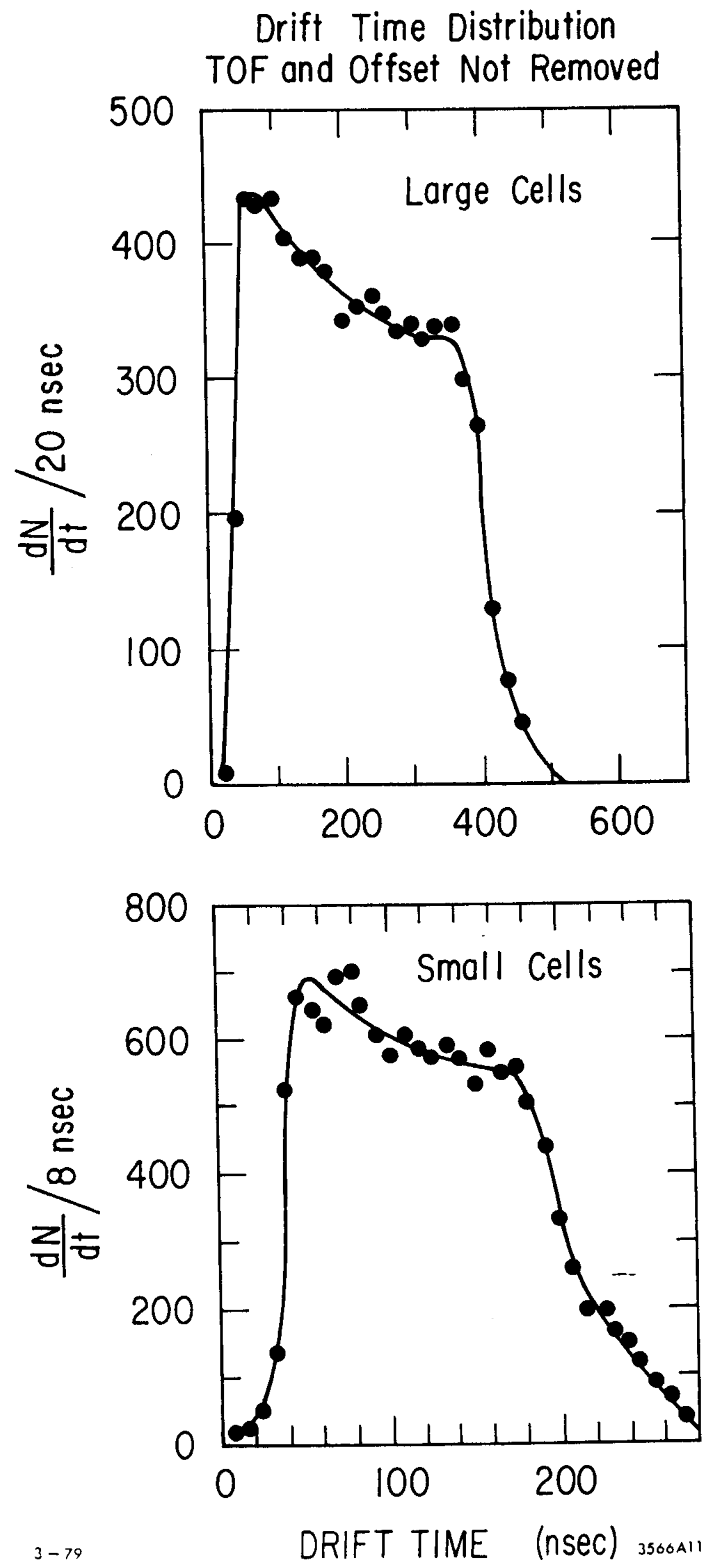

Fig. 19. Typical raw drift time distributions for large and small cells.

this relationship. The average drift velocities for the small (large) cells is 5.0 (4.8) cm/μsec. These values are used in the fast tracking algorithm described in Chapter III.

(vi) Major problems

Four weeks after beginning continuous operation of the chamber at SPEAR a serious problem of electrical discharge in the gas occurred. The effect was manifested as a large (>100 μa/cell) sustained current in certain high voltage distribution segments of the small cell layers. The cause was determined to be field wires which had been contaminated with the high dielectric epoxy used in the fastening of the wires. The effect was enhanced when the ionization in the gas was increased either by the introduction of an artificial radioactive source, or by the operation of SPEAR with large beam currents at high energies ($E_{cm} > 5$ GeV). The latter leads to synchrotron leakage into the chamber and subsequent photoionization of the gas and photoelectric effect on the wire surfaces. A model proposed for the discharge is that the dielectric on the field wires builds up a large positive charge on its surface creating a large electric field gradient near its edges. This field eventually injects electrons from the surface into the gas and initiates a sustained discharge. The buildup characteristics of the current and the discharge itself were reproduced in a test chamber before we actually had evidence of epoxy on the field wires. We eventually replaced more than 200 cells in the affected region to cure the problem.

REFERENCES

1. Sands, M., Stanford Linear Accelerator preprint SLAC-REPORT-121 (1970).

2. Berndt, M., *et al.*, Stanford Linear Accelerator preprint SLAC-PUB-2289 (1979); Helm, R. H., Stanford Linear Accelerator preprint PEP-NOTE-273 (SPEAR-214) (1978).

3. Cisneros, E., *et al.*, Stanford Linear Accelerator preprint SLAC-PUB-1844 (1976).

4. Breidenbach, M., *et al.*, Stanford Linear Accelerator preprint SLAC-PUB-2032 (1977).

5. Brafman, H., *et al.*, Stanford Linear Accelerator preprint SLAC-PUB-2033 (1977).

6. Davies-White, W., *et al.*, Nuclear Instrum. Methods **160**, 227 (1979).

7. See, for example: Charpak, G. and Sauli, F., Nucl. Instrum. Methods **108**, 413 (1973); Schultz, Guy, CERN Internal Report EP76-19 (1976), "Etude D'un Detecteur De Particules A Trés Haute Precision Spatiale (Chambre á Drift)."

III. CHARGED TRACK RECONSTRUCTION

INTRODUCTION

In this chapter, I will discuss the charged track pattern recognition and fitting. In addition I detail the determination of the time-to-distance relation within the drift cells.

FAST TRACK ASSOCIATION (TLTRKR)

The input data stream from the BADC consists of a list ordered by layer and azimuth, of hit wires and their drift times (in units of .1 ns). These are referred to as dazms (drift chamber azimuths). The hardware track counters (described in Chapter II) provide a list of roads found by the curvature modules of the secondary trigger. These consist of an azimuth and curvature, for each hardware track. The width of the mask at each of the 6 axial layers is also known.

Before the input data is used, the list is searched for groups of ≥12 adjacent cells. These are flagged, and avoided in track reconstruction. Their origin is usually in hardware problems, showers, or low momentum grazing tracks. Individual cells with drift times outside the expected limits are also removed. Both these techniques greatly reduce the extra combinations sought by the pattern recognition algorithms.

Hardware tracks do not have cell numbers "attached" to them. Thus the algorithm (TLTRKR) first tries reconstructing the trigger logic roads, and attaching hit wires to them. This is performed in the 6 axial layers. The measured drift time (t_m) is converted to a distance (s) using a constant drift velocity. The angle of incidence α in the layer measured from the radial direction is estimated from the curvature and layer radius, and the distance of closest approach (DCA) position is determined. Since we cannot measure on which side of the sense wire the track passed, we are left with an ambiguity in the position. Simple circle fits trying all combinations on several cells in the road, usually resolves these "side-of-the-wire" ambiguities and determines the remaining cells that should lie on the track. Problems occur for small t_m (< 10 ns), and these dazms are left on the track, with ambiguities unresolved. A search is then made to attach nearby non-axial dazms to the track, thus resolving their ambiguities.

The TLTRKR algorithm is ~85% efficient for finding tracks. It suffers however from its primary requirements of high axial layer efficiency (which is not always available) and well separated tracks. In using a constant drift velocity, the space resolution is only ~500 μm. This makes it inefficient for sorting tracks passing close together, and tracks having low momentum. It also has problems with steeply dipped tracks that exit the chamber before layer 15. TLTRKR is the basic online program, allowing fast enough reliable track reconstruction to sample ~20% (on Σ5) and ~95% (on VAX780) of the tracks.

FINAL TRACK FINDING AND FITTING (TRAKR, ARCS)

In order to fully exploit the drift chamber efficiency and precision, two other algorithms (TRAKR and ARCS) are employed offline after one pass through TLTRKR. This package performs three functions:

1. Fit TLTRKR track candidates, either passing or rejecting them based on χ^2 (if rejection occurs, a redetermination of ambiguities is attempted).

2. From the pool of unused dazms associate tracks and attempt ambiguity resolution.

3. Fit collections of dazms with mostly resolved ambiguities (resolving the remaining ambiguous ones).

The fitting procedure (ARCS) used in cases 1 and 3 is described in complete detail in Ref. 1. Its basic features are outlined here since it is specific to the drift chamber design and function. Appendix A contains a summary of the basic equations.

The algorithm ARCS performs a 3-space linear least-squares fit to an orbit in the drift chamber. The orbit parameters are ϕ, K ($= 1/p \cos \lambda$), S ($= \tan \lambda$), x, y, z (see Fig. 10, Chapter II). Since a helix is being fit, only five of these are independent; the orthogonal parameters η, and ξ are substituted for x, y, z. The first, η, is a displacement from the starting point (x_o, y_o, z_o) along the local magnetic field direction $\hat{h}$, while ξ is along the local direction $\hat{t} \otimes \hat{h}$ (where $\hat{t}$ lies tangent to the local orbit).

The fit is performed to a set of linked helices, formed by stepping successively from layer to layer (~7 cm radially). Each step uses the average magnetic field between the layers. Denoting the 5 orbit parameters α_μ, the set of starting values α_u^o and the measured drift times t_i^M, and DCA's d_i^M ($i = 1,N$; $N = 16$ maximally), the fitting procedure follows.

At each layer i:

1. Construct analytically the distance of closest approach d_i based on the α_u^o. Wire sag is accounted

for in the vertical displacement, based on an estimate of position along the wire.

2. Determine an estimate for d_i^M based on t_i^M, the wire propagation time, the time of flight (assume $\beta = 1$), the layer, the local angle of incidence, and ambiguity (see details in the following section).

3. Determine an estimate for σ_i^M, the measurement error based on the incidence angle, layer, t_i^M, and ambiguity.

4. Calculate analytically the 5 derivatives $\partial d_i / \partial \alpha_\mu$.

Using 1-4 ARCS minimizes the function:

$$\chi^2 = \sum_{i=1}^{N} \left[\left(d_i^M - d_i(\alpha_u) \right) / \sigma_i^M \right]^2$$

with respect to α_μ. The procedure is to linearize the set of 5 equations $\partial \chi^2 / \partial \alpha_\mu$, substituting $\alpha_\mu = \Delta\alpha_\mu + \alpha_\mu^o$ and solving for $\Delta\alpha_\mu$. Iterating 1-4 once or twice, using the new α_μ^o on each step, the procedure converges to the orbit parameters minimizing χ^2. This iterative procedure has several advantages. Convergence is rapid because the α_u vary nearly linearly with the d_i. In the limit of a uniform field, the procedure becomes exact, and does not suffer from the cumulative truncation error of a fully numerically integrated orbit. The stereo layers are treated just as the axial layers are. Finally (and most importantly), the iteration provides an estimate of the χ^2 and d_i for the next step without a recalculation of the orbit. This is particularly important for final ambiguity resolution, for it allows a testing of many ambiguity choices before recalculating the new orbit.

On the last iteration, an error matrix Σ given by:

$$\Sigma^{-1}_{\mu\nu} = \frac{1}{2} \partial^2\chi^2 / \partial\alpha_\mu \partial\alpha_\nu$$

is calculated. Additive contributions for multiple scattering in the drift chamber gas and wires are applied to Σ. Contributions for other materials are left out, until the final vertex fitting is done (this allows for vees not originating at the origin).

The final pass at track finding is also done in TRAKR. The track finding algorithms use the simple approximation (see Appendix A) relating azimuth to curvature and dip angle in both axial and stereo layers (i = layer index):

$$\theta_i = \theta_0 + r_i/2\kappa \pm \alpha_i \tan\lambda$$

By forming combinations of pairs of axial layers ($\alpha = 0$), curvature (κ) histograms can be searched for peaks, and those dazms collected to form track candidates. Adjacent stereo layers can be paired, removing the $\alpha \tan\lambda$ term, and treated as single layers of mean radius and θ, allowing κ to be determined, and their attachment to a track of similar κ and θ_0 found from axial layers only. The procedure can then be reversed and the $\alpha \tan\lambda$ term computed individually and required to coincide (as a cross check) with other points on the track. These procedures tend to be slow because of the large numbers of combinations. Their success lies in the fact that the pool of unused dazms is small. This in turn depends on the efficiency of TLTRKR, and the noise free quality of the data.

The final step before the ARCS fit is fast ambiguity resolution. This is applied to TLTRKR tracks failing an ARCS χ^2 cut, and TRAKR found tracks. An orbit is constructed using crude values of α_μ. Seven dazms are used (≤ 4 axial) to construct the 2^7 ($= 128$) possible orbits, coinciding to both ambiguities in each dazm. As can be seen in Appendix A, a single calculation of $\partial d_i / \partial \alpha_\mu$, and only a single matrix inversion is necessary to get the χ^2 for all 2^7 orbits. A loose χ^2 cut is applied, retaining up to 15 candidates. Next, an approximate residual is computed for both ambiguities of every other dazm in the road. This also is a fast calculation. These dazms are attached if the residual is sufficiently small. Of the 2^7 initial trials, the one attaching the maximum number of dazms is chosen. Ties are broken by the minimum χ^2 of the track, plus the χ^2 from residuals of attached dazms.

The original selection of 7 dazms is a tradeoff of time and reliability. It is found that while 7 dazms determine a helix with two degrees of over-constraint, the ambiguity resolution within it alone is minimal, and more hits are usually needed. It is clear that all combinations (up to 2^{16}) could be attempted, but at a very large computing cost. The ambiguity resolution as outlined uses only somewhat more time than 2^7 calculations, and still retains reliability. The importance of pre-tracking with TLTRKR can be seen in Table I, where the timing of algorithms is compared. These numbers have not been corrected for small (~15%) differences in efficiency. In our offline analysis, TLTRKR is combined with a knowledge of the total number of drift chamber hits and TOF, to filter cosmic rays and 1 prong beam gas events from reaching ARCS and TRAKR. These background events often constitute more than half the triggers.

TABLE I

Average Time/Track in ms on IBM-168

Algorithm	Function	Multiprong	2 Prong
TLTRKR	Find & crude fit	17	15
TRAKR & ARCS	Find & good fit	145	95
TLTRKR & TRAKR & ARCS	Full finding and fitting	86	42

DETERMINATION OF THE TIME-TO-SPACE RELATIONSHIP

In this section I describe the method by which measured drift times are related to space distances for use in the tracking. In determining the proper time-to-space relationship several effects were considered:

1. Electric field shape in the cell (and thus the drift velocity variation).
2. Magnetic field and the symmetries it introduces (recall $F_{magnetic} \sim 3 \times 10^{-3} F_{electric}$).
3. Signal propagation on the sense wires (z-dependence) (≤ 5 ns $\approx .25$ mm).
4. Time of flight (≤ 10 ns $\approx .5$ mm).
5. Boundary layers and the shape of their fields.

The drift chamber by construction, inherently couples tracking information into the relationship between measured time (t_{ADC}) and physical distance from sense wires. Effects 3 and 4 above can only be removed after an estimate of the orbit is known. In the following, I refer to t as the measured time, meaning 3 and 4 have been removed.

A track passing through a cell can be parametrized by its distance of closest approach to the sense wire (DCA), the side of the sense wire ($\pm$ DCA), and the incidence angle (α) from the normal to the cell. In the absence of a magnetic field, the sign of α would be irrelevant, however the 4.16 kg magnetic field introduces an asymmetry (see Fig. 1). In one direction electrons drift against the magnet force, in the other, with it. This dependence is only on the sign of α, and not on DCA or its sign, except for the outermost layer whose field is distorted in the inner and outer radial halves as a result of the outer aluminum ground plane.

In general, tracks passing close to the sense wire ($\lesssim$ 2 mm) see a strong, nearly radial electric field. The average drift velocity should be nearly-angle-independent for $t < t_c$. Beyond this region, the actual drift path and integrated drift time become a complicated function of the primary ionization location (parametrized on average by DCA and α). At any α, there should exist a time t_f for which the function of t (with $t < t_f$), representing the effective (or average) drift velocity, is smooth and slowly varying. t_f represents the cut-off, when primary ionization has taken place in the region of rapidly changing electric field, near the field wires. Beyond t_f, some corrections are expected to be necessary. Here again, a knowledge of the approximate orbit is necessary to determine α and t_f.

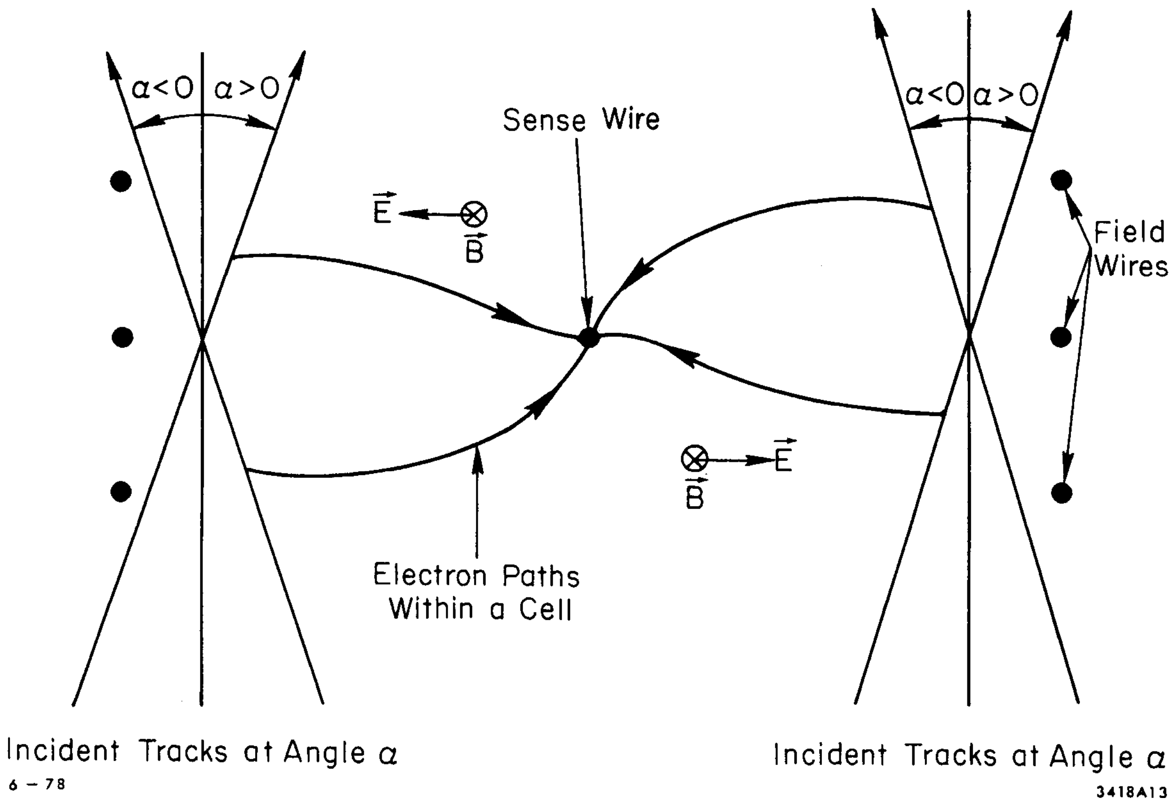

Fig. 1. Symmetry of drift paths within a cell.

The function chosen for time-to-space conversion follows the guidelines of the physics above. By parametrizing in effective velocity $\bar{\nu}$ (so that DCA = $\bar{\nu}t$), we are using a variable which is close to the physics of the cell. It is relatively smooth because it is an integral of local velocities, which can vary rapidly over a drift path. The function is a polynomial in t constructed to be continuous and differentiable. Interpolation to the measured angle α is used, to guarantee speed in computation. The form used is:

$\underline{t \le t_c}$

$$\bar{\nu} = \bar{\nu}_1(L) + \bar{\nu}_2(L)(t - t_c)^2 + \bar{\nu}_3(L)\ \beta_1(\alpha = 0)(t - t_c) \qquad (1)$$

$\underline{t_f \ge t > t_c}$

$$\bar{\nu} = \bar{\nu}_1(L) + \bar{\nu}_3(L)\left[\beta_1(\alpha)(t - t_c) + \beta_2(\alpha)(t - t_c)^2\right] \qquad (2)$$

$\underline{t > t_f}$

$$\bar{\nu} = \bar{\nu}_1(L) + \bar{\nu}_3(L)\Big[\beta_1(\alpha)(t - t_c) + \beta_2(\alpha)(t - t_c)^2 + C_{FW}(\alpha)(t - t_f)^2\Big] \qquad (3)$$

The variables $\bar{\nu}_1$, $\bar{\nu}_2$, $\bar{\nu}_3$ are determined for each layer averaged over α. The variables β_1, β_2, and C_{FW} are α-dependent, and are averaged for layers 6-11, 12-20, and 21 separately. t_c is typically 20 to 40 ns (~1 to 2 mm), while the t_f depend on angle and cell size, and are chosen to be ~50 ns less than the maximum drift time at a given angle. $\bar{\nu}_1$, $\bar{\nu}_2$, and $\bar{\nu}_3$ may depend weakly on the sign of DCA, in order to account for small geometric uncertainties in the wire positions. The variations with the sign of DCA are less than 100 μm (2 ns) on average. Larger variations can take place when one or more layers are shut off, and a natural dependence on the sign of DCA (at fixed α), is introduced on the adjacent layers. We therefore retain the ability to make these corrections. The angular variation of β_1, β_2, and C_{FW} is handled by an interpolation of $\bar{\nu}$ from 10^o bins of α. Figures 2a,b show the form of $\bar{\nu}$ for large and small cells, at several angles. Figures 3a,b shows the form of $\bar{\nu}t$ over the same range.

Layer 21 is treated somewhat differently because of its distorted electric field shape, as discussed in Chapter II. In addition to the parametrizations above β_1, β_2 have explicit dependence on the sign of DCA, as well as α.

To find the parameters ν_1, ν_2, ν_3, β_1, β_2, C_{FW} we chose to use an iterative, self-consistent approach, employing actual data. A track sample is selected from muon pair and hadronic events which have been found by TLTRKR using nominal drift velocities. The data sample includes ~2500 muon pairs and ~2500 hadron events (~10,000 single tracks), which at SPEAR energies requires several days of running time. The muon events provide a set of fairly straight tracks which are important for ν_1, ν_2, and ν_3. The hadrons provide the lower momentum tracks necessary for the determination of the β_1, β_2, and C_{FW} terms.

Each track in the sample is fit through ARCS using an initial estimate for the constants. At each layer, α and DCA_{fit} are determined from the fit. Using t (where the estimated orbit has removed z and TOF dependence), a $DCA_{predicted}$ is calculated. It is thus possible to form a residual at each layer from $(DCA_f - DCA_p)$. The Eqs. (1) through (3) are linearized in the parameters ν_1, ν_2, ν_3, β_1,

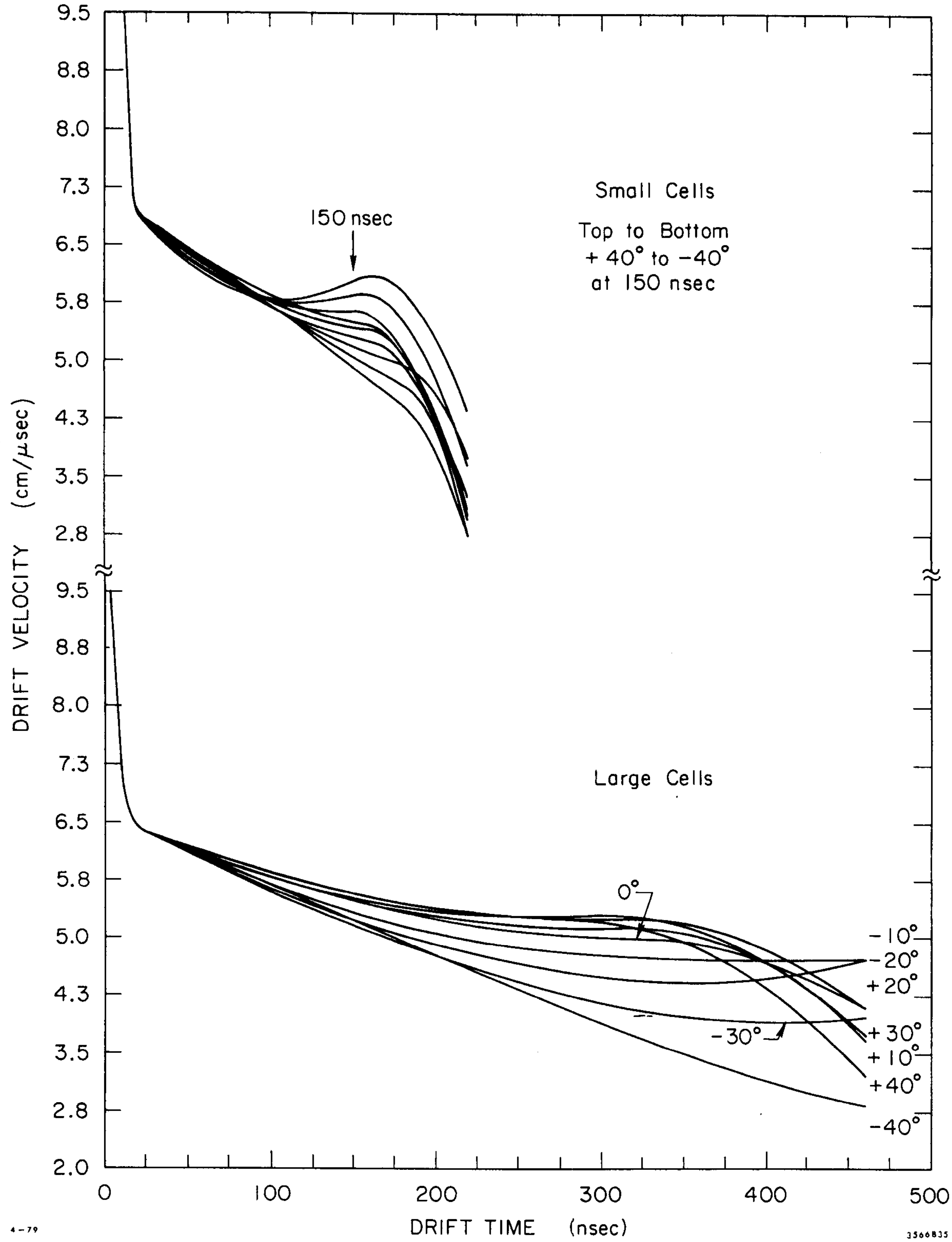

Fig. 2. Effective drift velocity vs. measured drift time at various incidence angles, for small (a) and large (b) cells.

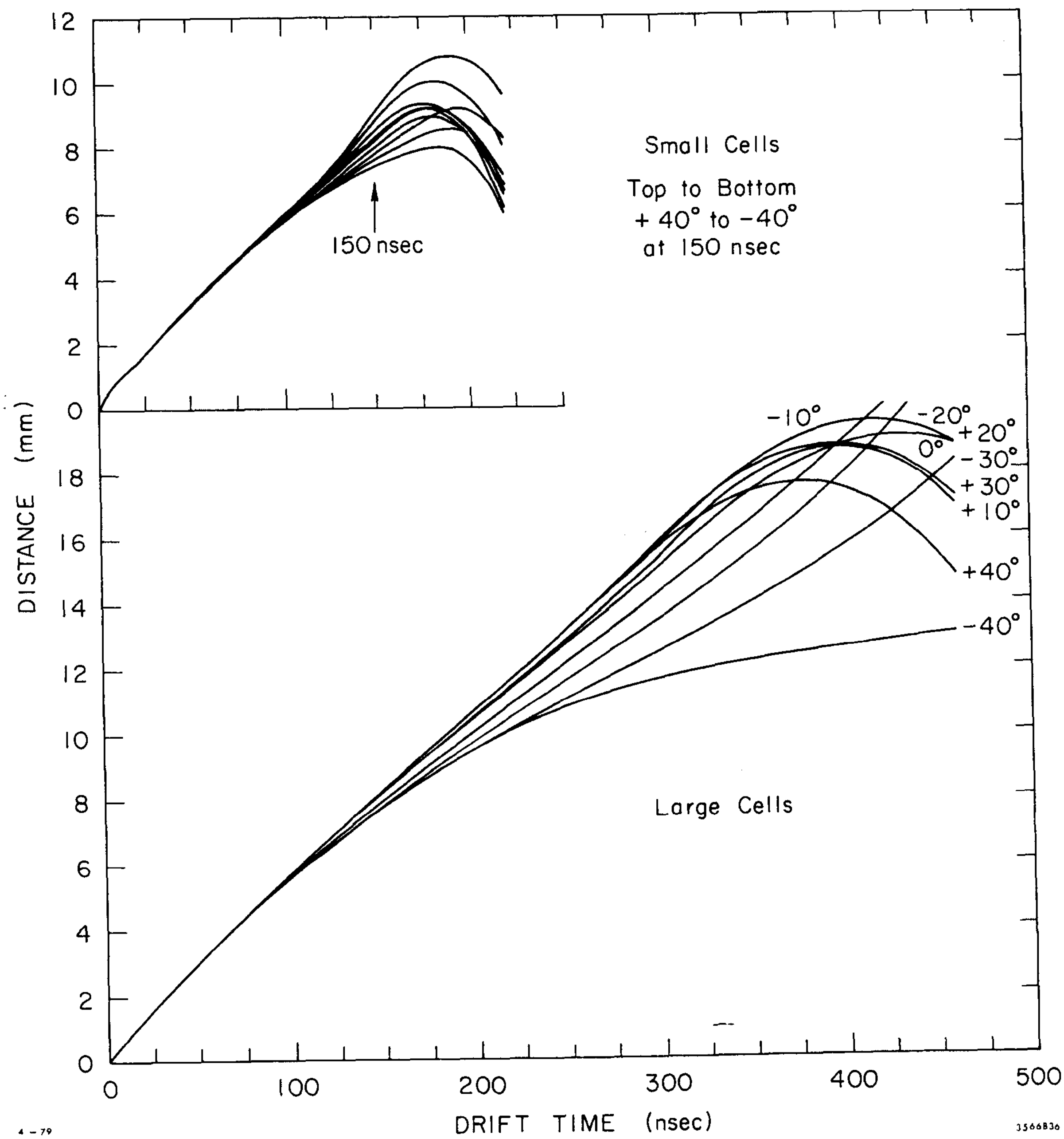

Fig. 3. Effective drift distance vs. measured drift time at various incidence angles, for small (a) and large (b) cells. The functional form is plotted beyond the physical region of the cell, thus appearing double valued.

β_2, C_{FW} (e.g., $\beta_1 \rightarrow \beta_1 + \delta\beta_1$). Many χ^2 are formed for the pairs involving ν_1 and ν_3 (by layer), β_1 and β_2 (at each of 9 angles, over layers 6-11, 12-20, 21), and ν_2 (by layer) and C_{FW} (by angle) individually. These are accumulated over the data sample, and the linear equations solved at the end for the change in parameters (e.g., $\delta\beta_1(30^o)$). Appendix C contains the mathematical details. The usual procedure changes <u>only</u> one pair at any one iteration (e.g., only ν_1 and ν_3) and then retracks and repeats the iteration, changing the other in the next iteration. To speed convergence we usually over-correct by ~50% on the first few iterations. Convergence usually occurs after ~4 iterations. The χ^2 and <residual> versus t provide monitors of the progress.

At the end of the iteration, we have a measurement of the chamber resolution (σ) at different angles α and on each layer. σ is determined from the FWHM of the distribution of residuals. The residual distributions tend to have non-Gaussian tails which fall on the early drift time side, corresponding (we believe) to δ-rays. Approximately 1% of the dazms may be δ-rays. These values are fit to parabolas in t and are used in the ARCS fitting procedure (see Fig. 4a,b). Figure 5 shows a typical set of residual plots integrated over all angles and times. The tails have been removed from these plots. As is seen, the entire technique is self-consistent, in that the determination of the constants seeks to minimize the same quantity as ARCS, over a data sample which reflects the <u>current</u> chamber conditions.

The drift chamber constants are sensitive primarily to changes in high voltage, gas composition, and atmospheric pressure. A voltage

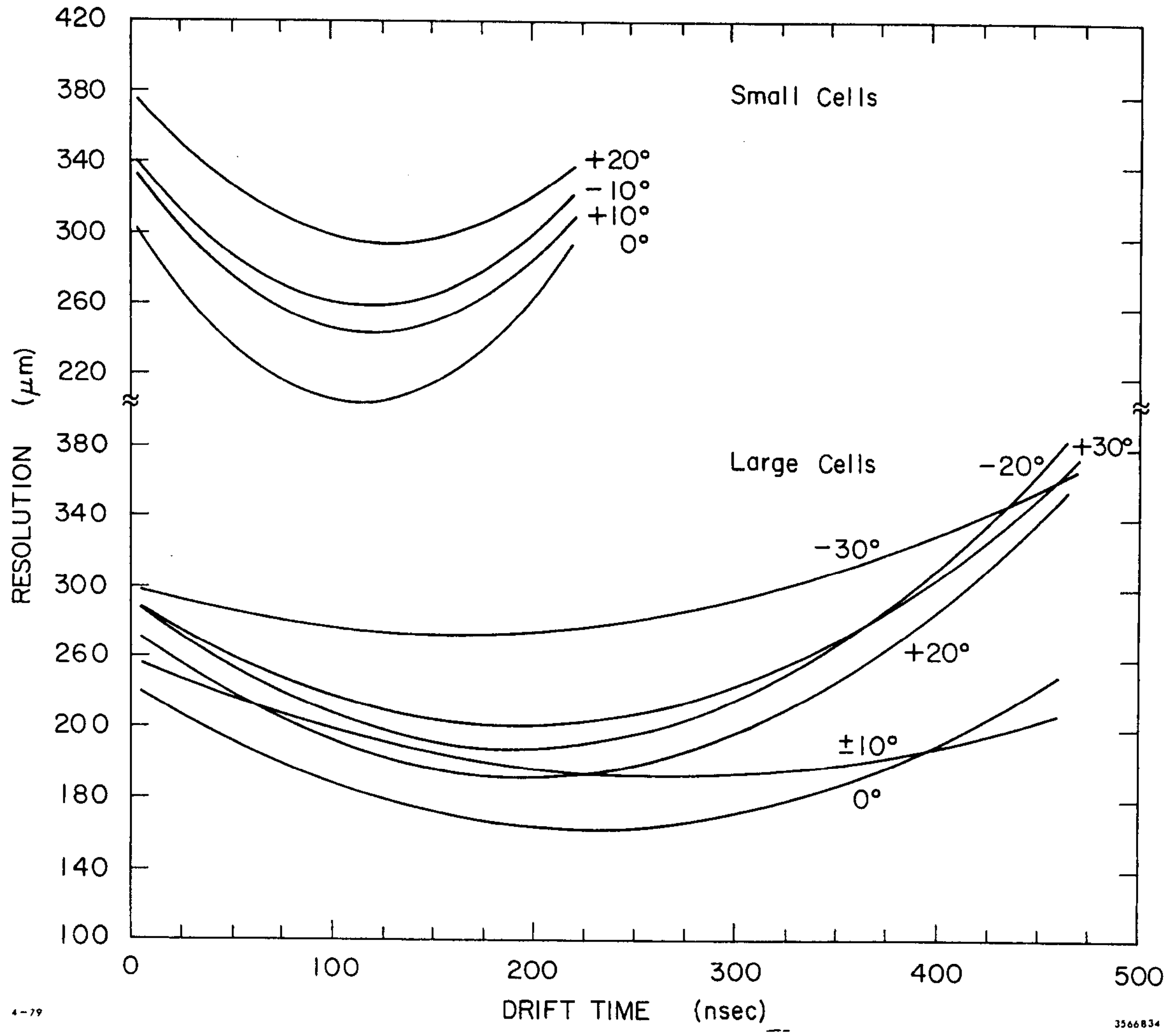

Fig. 4. Typical fitted resolution versus measured drift time and incidence angle for small (a) and large (b) cells.

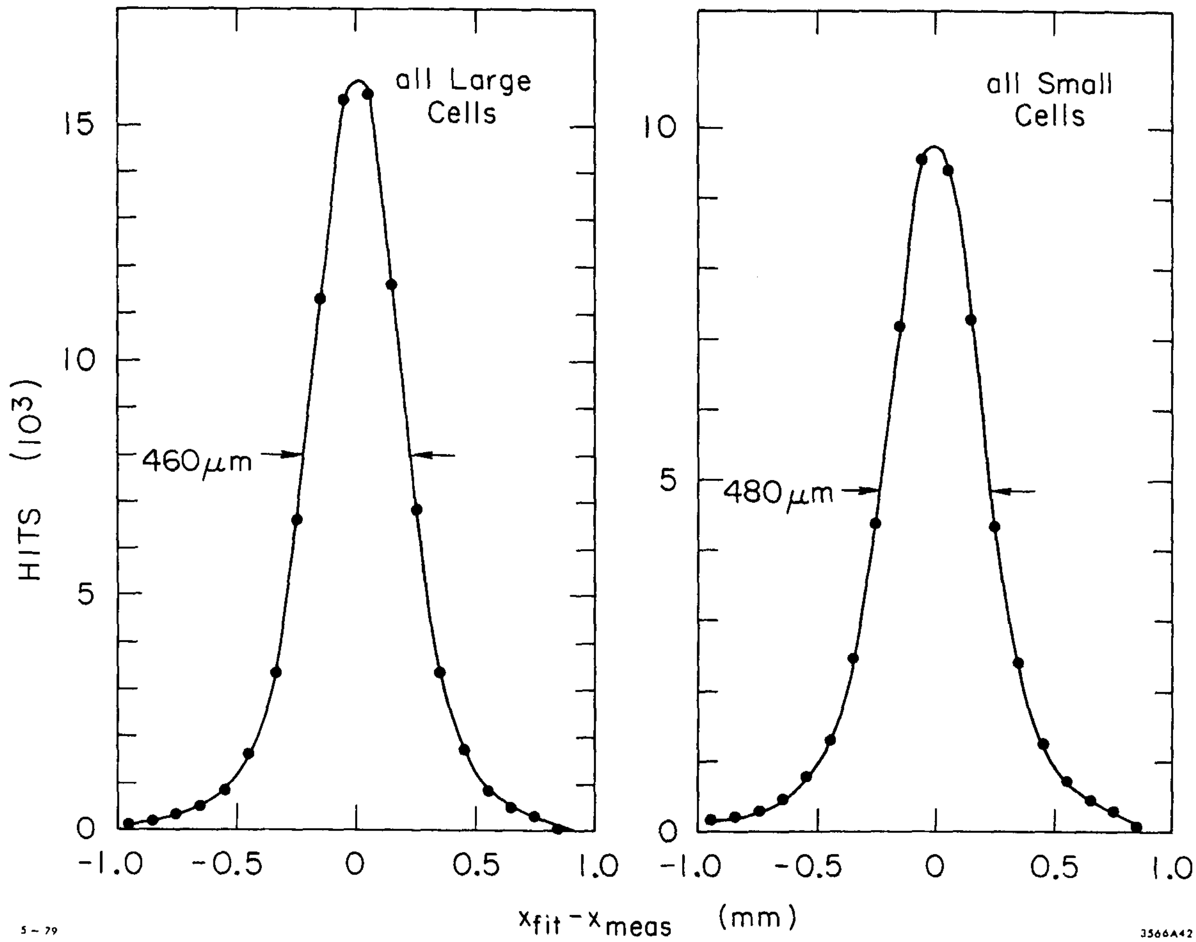

Fig. 5. The space resolution for large and small cells averaged over drift times and incidence angles in a typical sample of hadron events.

reduction of 50v typically introduces changes in drift times of ~1 ns. The chamber is normally run within ±10v of a nominal setting, however we are often required to lower voltages 100 to 200 volts on individual layers. This forces us to re-calculate constants or a degradation of resolution will be suffered. Variations in gas composition should occur at a slow rate since the replacement time of the chamber gas is several weeks. After shut down periods (where no gas has been flowing), we usually observe large changes in the drift velocities over the first several weeks, even when the chamber is purged several times. We attribute this to residual oxygen trapped in the hexcel and back-diffusing into the new gas.

Variations in atmospheric pressure (p) can change the drift velocity (ν is expected to be a function of E/p), however our sensitivity is not great. We are limited by statistics to a determination of constants every 3 to 4 days at most. This usually averages out any strong variations. Temperature variation is expected at a level of .1%/^{o}C. This is negligible since the magnet maintains gas temperature within ±2^{o}C. In several months of data where no known problems existed, we found variations over time in the fitted drift velocity to amount to the equivalent of ~50 μm. These variations appeared uniformly over the cells. Given these considerations, our technique is to examine residuals of tracks over periods of ~1 week running time, or when any of the known problems (described above) have taken place. If no significant changes have occured, these blocks are combined into 2-3 week blocks and used as a starting point for the next set of data.

The major factors contributing to the constant part of the total chamber resolution are the time resolution ($\sigma_t \lesssim 45$ μm) and the wire position ($\sigma_m \lesssim 100$ μm). This latter number is derived from mechanical construction and endplate deformation uncertainties. It is not well known and in fact varies somewhat over the chamber. The non-constant part of the resolution function is determined by two factors: diffusion ($\sigma \propto \sqrt{t}$) for long drift paths, and ionization statistics for short paths near the sense wire.

MOMENTUM RESOLUTION

The drift chamber provides between 7 and 16 points from which an orbit is reconstructed and the 5 track parameters ϕ, k, $s = \cot\theta$, ξ η are determined. In the following section I will discuss effects contributing to the observed momentum resolution. I will then discuss the idea of the vertex-constrained fit and remaining problems in both geometry and track reconstruction.

The projection of a particle's helical orbit into the xy plane normal to the magnetic field, is a circle. While five points clearly specify the problem, a minimum of 7 are required from the track finding algorithms. A measurement of curvature provides a measurement of transverse momentum. It is well known that curvature error varies linearly as the sagitta error, and inversely as the square of the track length in projection.[2] A more precise statement can be made when more than 3 points are used to determine the sagitta.[3] The expressions for N+1 points measured along the trajectory are given in Appendix B. Using typical values for L, H, N, ε of 1.04 meter, 4.15 kg, 13, 220 μm respectively, we obtain the following errors:

$$\left(\frac{\delta p_\perp}{p_\perp}\right)_m \approx 1.02\%\ p_\perp \tag{1}$$

$$(\delta\phi)_m \approx .65\ \text{mr} \quad . \tag{2}$$

L_R/L is approximately 9×10^{-3} r.l. for the ArC_2H_6 and wires. This gives us multiple-scattering errors of:

$$\left(\frac{\delta p_\perp}{p_\perp}\right)_{ms} \approx 1.45\% \tag{3}$$

$$(\delta\phi)_{ms} \approx .7\ \text{mr}/p\beta c \tag{4}$$

The error in polar angle determination is

$$(\delta\theta)_m \approx 3.6\ \text{mr} \tag{5}$$

$$(\delta\theta)_{ms} \approx .82\ \text{mr}/p\beta c \tag{6}$$

In each case, the expression assumes a track that is fairly stiff (≥ 95 MeV/c), and whose polar angle, θ, is great enough to carry it through a large number of layers ($|\cos\theta| \lesssim .70$). When moving beyond these bounds, the value of N drops and L decreases, rapidly increasing the measurement error. Furthermore, for large dip angles an increase in scattering material is also expected.

The full momentum resolution has two dominant terms, whose relative sizes are shown in Figs. 6a,b. The L-dependence is explicitly left in below:

$$\left(\frac{\delta p_\perp}{p_\perp}\right)^2 = \frac{(1.45\%)^2}{L} + \left(\frac{1.02\%\ p_\perp}{L^2}\right)^2 \tag{7}$$

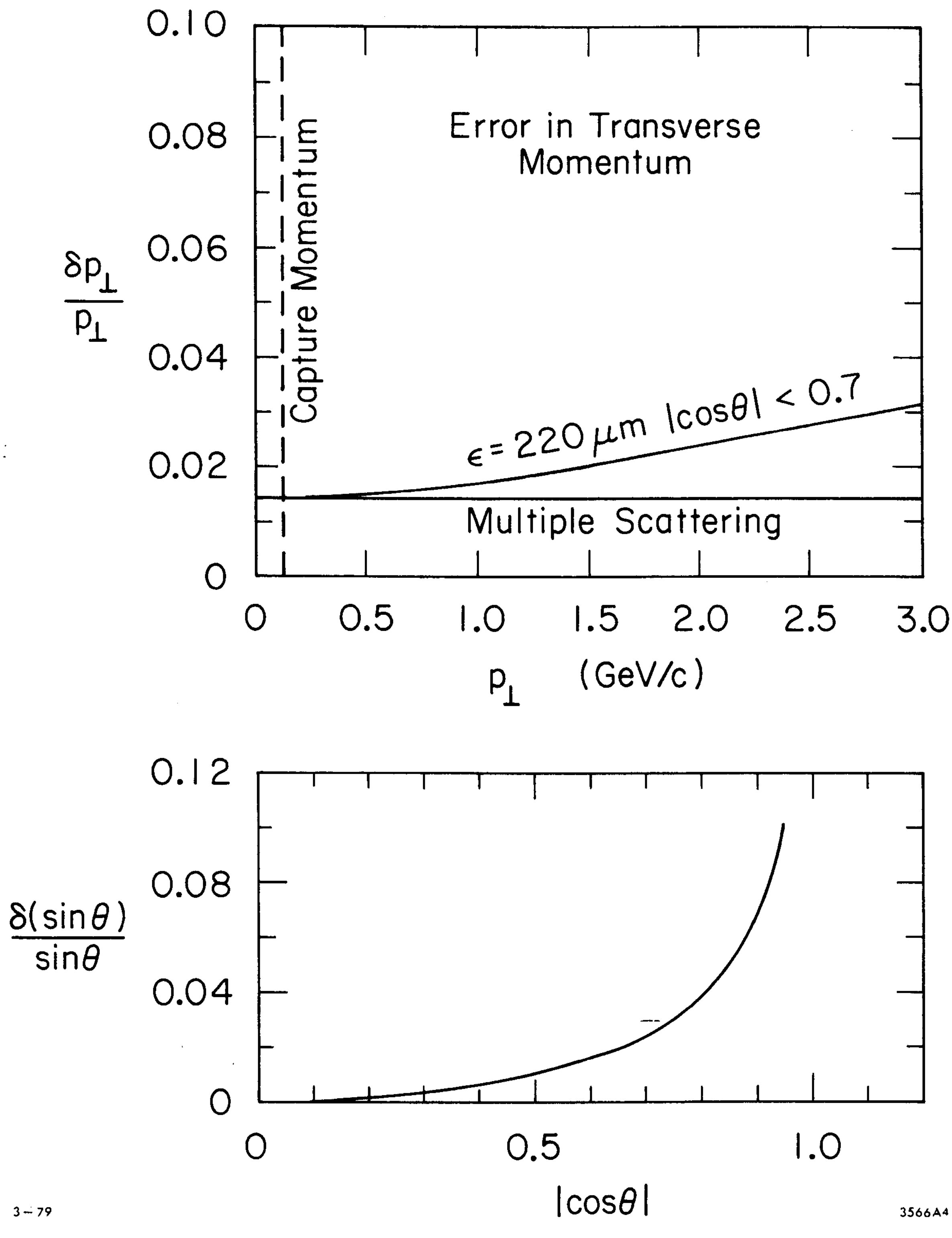

Fig. 6. Model for the momentum resolution in the central part of the detector.

$$\left(\frac{\delta(\sin\theta)}{\sin\theta}\right)^2 \cong \frac{1}{(1-\cos^2\theta)} \quad (\cos^2\theta)\left(\frac{3.6\ \mathrm{mr}}{L}\right)^2 \tag{8}$$

It is clear that except near the edges of acceptance the angular error from (8) is small.

We can compare this model with the observed resolution for muon pairs from the $\psi(3096)$. The advantage of this decay is that the detector properties alone are measured, since the beam energy resolution is ±2 MeV and the ψ width is considerably smaller. Since the ψ is produced essentially at rest, the muon-pair mass resolution measures the momentum resolution directly:

$$M_{\mu_1+\mu_2} = \left|p_{\mu_1}\right| + \left|p_{\mu_2}\right| \quad ; \quad \delta p = \delta M/\sqrt{2} \tag{9}$$

Figure 7 shows $M_{\mu_1\mu_2}$ with a superimposed fit to a gaussian plus a flat background. To avoid broadening on the low-mass side resulting from final state radiation, the fit is constrained to $M_{\mu_1\mu_2} > 3$ GeV. The fit shows in fact a small degree of such broadening below the peak. The width σ_M is 54 ± 1 MeV, while our prediction from (7) is 45 MeV. The difference may arise from an average resolution which is somewhat poorer than 220 μm because of non-gaussian tails (arising from δ-rays, incorrect ambiguities, errors in dazm attachment and geometrical errors in chamber alignment). In addition the effect of material before the drift chamber has not been accounted for entirely.

VERTEX CONSTRAINT

Thus far I have only discussed the one-track fit, which makes to use of the vertex information inherent in the beam interaction point (IP). From the IP, a particle traverses the beam pipe, pipe counters,

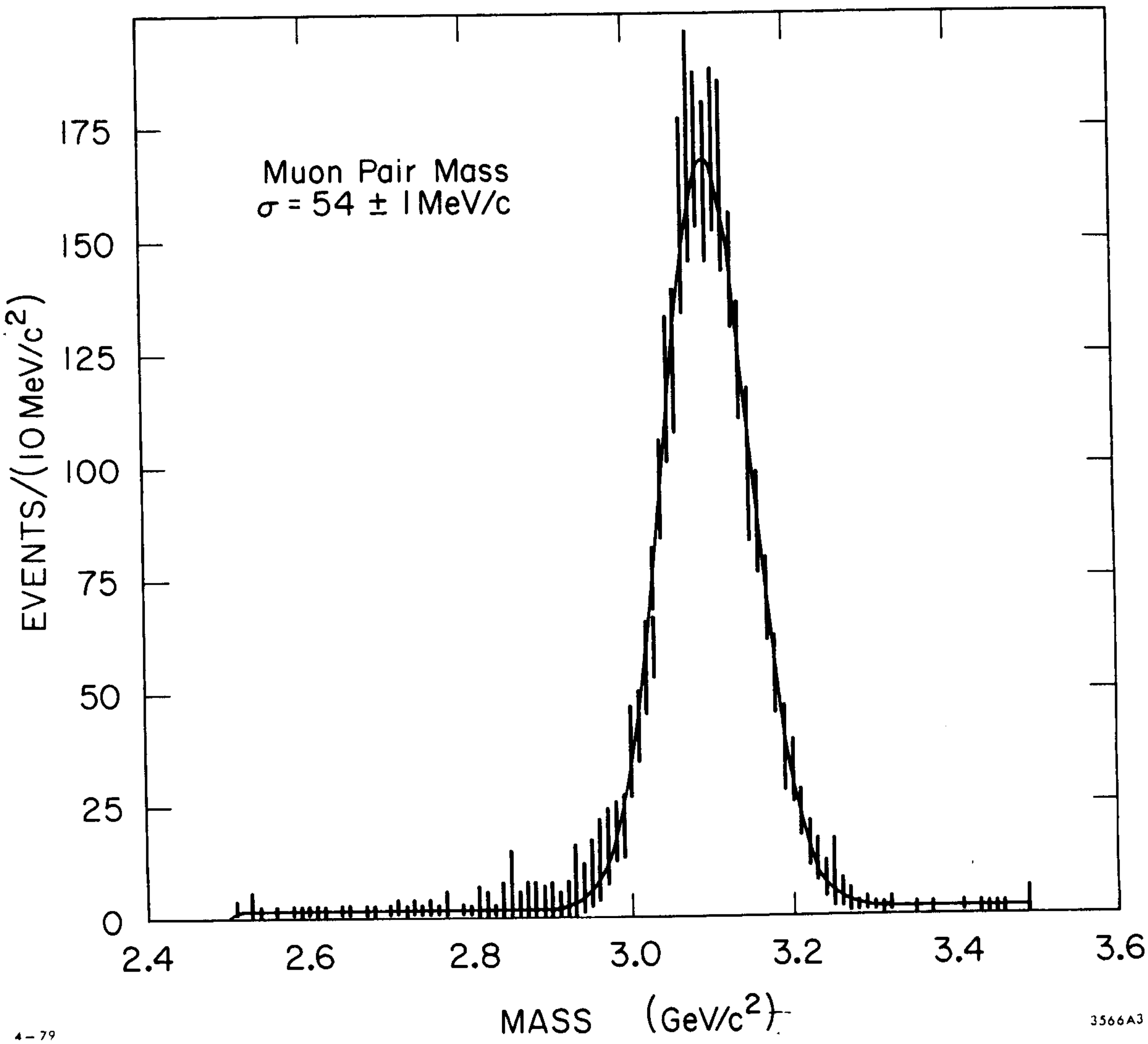

Fig. 7. Mass from muon pairs at the $\psi(3095)$; tracks unconstrained to a vertex.

and Lexan gas seal (see Table I, Chapter II), which is 37.3 cm in projection. If the IP were well known, the inclusion of it in a fit would greatly reduce the measurement error; as can be seen from (7), the dependence is $\sim 1/L^2$. In using the IP, we must additionally traverse $\sim 6 \times 10^{-2}$ r.l. of material, however most ($\sim 5 \times 10^{-2}$ r.l.) is within 12 cm, providing a short level arm for multiple scattering. The measured beam size from the monitors, at $E_b = 1.885$, is:

$$\sigma_x^b \approx .3 \text{ mm} \qquad \sigma_y^b \approx .02 \text{ mm} \qquad \sigma_z^b \approx 25 \text{ mm} \tag{10}$$

Using one-track fits to Bhabha and muon-pairs in vertical and horizontal ϕ wedges of $\pm 25^\circ$, the measured distributions of x, y, z at minimum distance of approach to the origin give the beam position. The error in the beam-constrained fit is taken as the error in the determination of the beam position ($\sigma_i/\sqrt{N}$) in quadrature with the beam size σ_i^b. This beam position measurement is performed either in groups of ~10 runs or at energy changes, to account for variations in the beam orbits. The width of these distributions (Bhabhas and muon-pairs), at the $\psi(3770)$ are:

$$\sigma_x^M = 1.1 \text{ mm} \qquad \sigma_y^M = 1.3 \text{ mm} \qquad \sigma_z^M = 28 \text{ mm} \tag{11}$$

Using (2)-(6), the projected error in r and z at the origin is

$$\sigma_r^T \approx .3 \text{ mm} \qquad \text{and} \qquad \sigma_z^T \approx 2\text{-}4 \text{ mm}$$

Including three scattering centers at 8, 12, and 37 cm respectively, for beam pipe, pipe counter and Lexan increases these errors to:

$$\sigma_r^T \approx .4 \text{ mm} \quad \text{and} \quad \sigma_z^T \approx 2\text{-}4 \text{ mm} \qquad (12)$$

We see that in x,y the measurement and multiple scattering are somewhat larger than the average beam size $\sqrt{\left(\sigma_x^b\right)^2 + \left(\sigma_y^b\right)^2}$, thus a beam constraint is useful. In z, the beam size dominates the measurement error. From (11), it is clear that other processes are broadening the measured σ_x^M, σ_y^M. Since electrons are used in measuring (11), this can be radiative broadening in the final state, combined with shifts in the orbit within the sample used for determination.

Using the beam position as another measurement changes $\delta p_\perp / p_\perp$ from 1.02% $p_\perp$ to .54% $p_\perp$ or $\delta M_{\mu_1\mu_2} \approx 35$ MeV (fixing the multiple-scattering contribution). Figure 8 shows the beam constrained data and Gaussian fit. The measured value is $43 \pm .8$ MeV. The result shows most of the improvement in resolution expected. As in the nonconstrained fit, we still do not obtain the expected value. The same problems discussed earlier apply here as well.

THE VERTEX RECONSTRUCTION

In order to classify events for filtering and for valid use of the beam position information, a sequence of vertex reconstruction steps are taken after one-track fits are done:

(1) Large Region Association. An attempt is made to fit tracks with $r \leq 15$ cm and any z (from the origin), to a single point in space, minimizing a χ^2 of transverse and longitudinal differences from this point. A weight is used to properly handle low momentum (poorly measured) tracks. Tracks are successively removed if they contribute more than 100 to the χ^2, and the fit repeated.

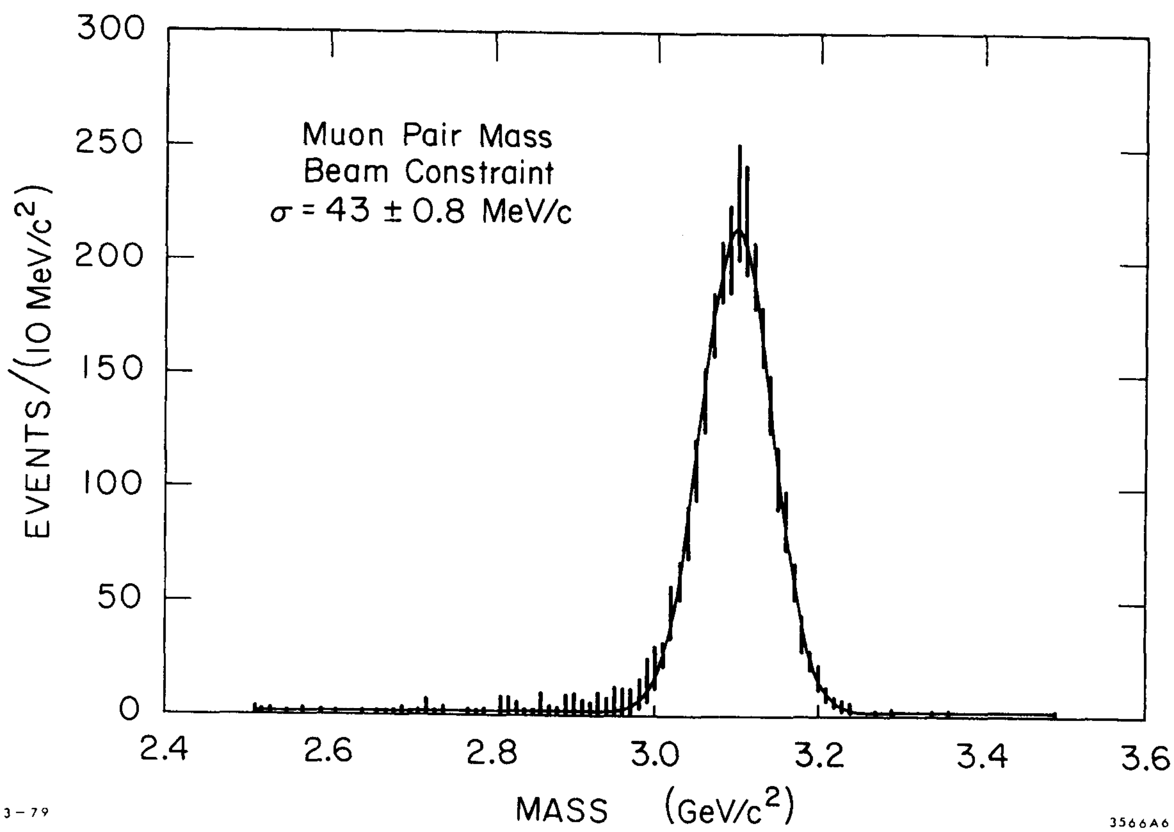

Fig. 8. Mass from muon pairs at the $\psi(3095)$; tracks are constrained to the beam position.

(2) Pipe Counter Cut. If the radius of the vertex in (1) is ≥ 4 cm, the event is classed as a pipe event.

(3) Vee Finding. A search over all one track fits for γ conversions, K_s^o and Λ^o are made. The K_s^o, Λ^o tracks are fit to a secondary vertex, and a virtual track added to the track list. For a description of vee-finding, see Chapter V.

(4) Small Region. A small region $r \leq 1.5$ cm, $|z| < 15$ cm from the predetermined beam crossing point, is defined. All tracks lying within this region and not forming a vee are beam-constrained. The size of this region is chosen to remove erroneous tracks, radiating tracks, and tracks which decay from a false constraint to the beam position point.

(5) Neutral Pions. π^o are found as discussed in Chapter V. Each π^o is treated as a secondary vertex.

The virtual tracks associated with vees are added to the primary vertex but are not included in the beam-constrained fit. The event classification is based on either the large region or the beam constrained fit (when available the latter is used). Extra tracks may often exist in hadron events with a good primary vertex. If $r < 4$ cm and $z < 10$ cm, these events are classed as hadrons, with extra tracks indicated.

REFERENCES

1. Trilling, G. H. and Johnson, A.D., LBL Internal Memo TG-301 (1978).
2. Prog. Nucl. Tech. and Instrum. (edited by Farley), p. 265, Vol. II (1967).
3. Gluckenstein, R. L., Nucl. Instrum. and Methods 24, 381 (1963).

IV. MEASUREMENT OF THE $\psi(3770)$ RESONANCE

INTRODUCTION

With the discovery of the two narrow resonances $\psi(3095)$ and $\psi(3695)$,[1,2] the popularity of the charm hypothesis[3] increased. These two resonances were associated with the production and decay of a bound system of a charmed quark (c) and antiquark later designated "charmonium".[4] The discovery of charmed D mesons[5] (associated with $c\bar{u}$ and $c\bar{d}$ quark combinations) provided further evidence for the charm hypothesis. Between these two discoveries, the development of potential models to describe the charmonium system took place.

The general features of most models are a nonrelativistic Hamiltonian consisting of a free particle term, a term involving short-range forces between quarks, and a quark confinement term to account for large distance behavior.[6] The short range forces are electromagnetic and strong (arising from single gluon exchange). The latter is assumed to have the same radial and spin dependent form as the usual Coulomb force, modified in strength only by an appropriate coupling constant. The form usually includes an $1/r$ term (r being the quark separation) as well as spin-spin, spin-orbit and tensor couplings. Models with more general radial dependence have been constructed.[7] The coupling constants and overall scale are generally left as free parameters, to be fixed by observed level splittings, energies and widths. The confinement term is typically either a linear, logarithmic or quadratic in r. As is shown in Ref. 6, the gross features of the level ordering are determined by this term, whereas the fine and hyperfine structure and properties such as level width are sensitive to the short-range terms.

Figure 1 shows an example of the level ordering in such a model. The large leptonic widths of the ψ and ψ' (4.8 and 2.1 KeV, respectively) suggest that they be assigned to 1^3S_1 and 2^3S_1 states. The confinement term of the potential pushes the 2P level below the 2S level.[6] In a pure Coulomb potential these would be degenerate. Spin-spin forces are expected to split the triplet and singlet S, P and D multiplets. The triplets are further split by spin-orbit forces in the short-range potential. The ^3D has one component $\left(^3D_1\right)$ with $J^{PC} = 1^{--}$ (i.e., the photon quantum numbers). The pure D wave has no amplitude at the origin, and hence no leptonic width in the simplest models. A non-vanishing second derivative of the radial wave function can, however, lead to a finite leptonic width. This occurs through mixing of the $^3D_1$ and the nearby $^3S_1$ level by the tensor force.[6] The leptonic width generated is estimated to be ~ 20 eV. Stronger mixing arises through the addition to the model of a decay sector which can connect bound levels such as the $^3D_1$ and $^3S_1$.[8,9] A broad resonance ~ 80 MeV above the ψ', and having a narrow leptonic width (~ 250 eV) was discovered just two years after that prediction.[10]

The resonance $\psi(3770)$ or ψ'' provides a unique place for studying D mesons in e^+e^- interactions. The ψ'' lies between $D\bar{D}$ and $D\bar{D}^*$ threshold (3.726 and 3.870 GeV, respectively). Because it is only ~ 80 MeV above the ψ' and ~ 40 MeV above $D\bar{D}$ threshold and has a total width (~ 25 MeV) which is two orders of magnitude greater than the ψ', we are lead to attribute this width solely to the strong decay of the ψ'' to $D\bar{D}$; (E1 γ transitions to the $^3P_{0,1,2}$ states are expected to contribute less than ~ 500 KeV in total width). Under this assumption, the ψ'' appears as an enhancement in the charm

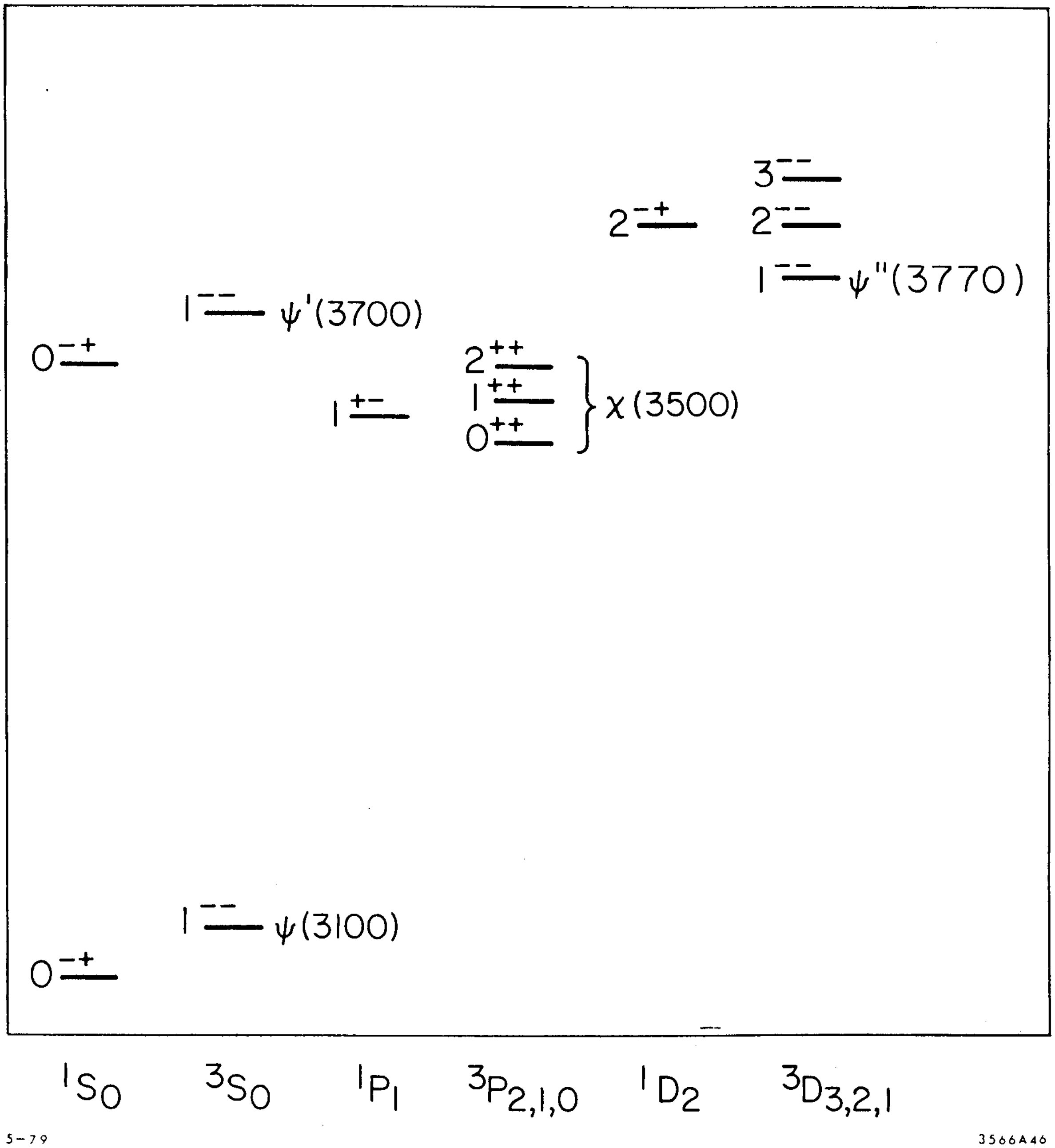

Fig. 1. Typical energy level diagram for the charmonium system. Here a linear and coulomb potential is employed. The well established states are indicated.

production cross section of ~ 10 nb.[11] Making the further assumption that the ψ'' has unique isospin (0 or 1) implies that it decays equally to D^+D^- and $D^o\bar{D}^o$ (before phase-space corrections). Thus, a measurement of the ψ'' resonance allows a determination of the branching fractions of D's (rather than only the cross section for D production times the branching ratio to any particular mode). These branching ratios could previously only be measured crudely by using one detected D as a "tag" and searching for specific final states in the recoiling $\bar{D}$. The remainder of this chapter is devoted to a remeasurement of the ψ'' resonance parameters with the Mark II. The cross sections derived will be used in subsequent chapters.

DATA REDUCTION

To determine resonance parameters, data were collected at twenty-two energies, starting below the ψ' and going up to the $D\bar{D}^*$ threshold. These data were combined with two fixed energy blocks taken at other times. The statistical error on each scan point averaged about 7%, corresponding to about six hours of data collection time. The beam energy over the ψ' tail was kept within ± 200 KeV of the central energy and ± 400 KeV for the remainder of the scan points.

For this data, R(the ratio of hadronic to μ-pair cross sections) was computed by the techniques of Ref. 12. Some corrections described below were necessary to account for problems with the hardware during some of the data collection. Table I summarizes the data points taken. R values contain only a correction for the $\tau^\pm$ and a radiative correction for the continuum ($\sim 9\%$). No radiative corrections for the ψ, ψ' or ψ'' are made. The errors shown are purely statistical. The absolute

TABLE I

Data Points and Fit Corrections

E_{beam} (GeV)	$\sigma_{\mu\mu}$ (nb)	$R_{measured}$	$R_{radiatively\ corrected}$	$\sigma_{\psi''}$ (nb)
1.8350	6.44	2.41 ± 0.15	2.18 ± 0.15	-0.26 ± 0.97
1.8460	6.37	7.10 ± 0.43	2.06 ± 0.43	-1.08 ± 2.87
1.8520	6.33	4.56 ± 0.33	2.28 ± 0.33	+0.33 ± 2.09
1.8580	6.29	3.62 ± 0.29	2.08 ± 0.29	-0.90 ± 1.82
1.8640	6.25	3.69 ± 0.29	2.67 ± 0.29	1.71 ± 1.81
1.8700	6.21	3.51 ± 0.20	2.66 ± 0.20	1.88 ± 1.24
1.8730	6.19	3.39 ± 0.20	2.60 ± 0.20	1.62 ± 1.24
1.8760	6.17	3.97 ± 0.23	3.49 ± 0.23	5.56 ± 1.42
1.8790	6.15	4.13 ± 0.23	3.76 ± 0.23	6.84 ± 1.41
1.8820	6.13	4.35 ± 0.32	4.04 ± 0.32	8.46 ± 1.96
1.8850	6.11	4.39 ± 0.32	4.13 ± 0.32	9.55 ± 1.95
1.8855	6.10	3.96 ± 0.29	3.47 ± 0.29	6.33 ± 1.77
1.8860	6.10	4.26 ± 0.31	3.81 ± 0.31	8.19 ± 1.89
1.8880	6.09	3.88 ± 0.30	3.32 ± 0.30	5.97 ± 1.83
1.8910	6.07	3.26 ± 0.25	2.64 ± 0.25	2.43 ± 1.52
1.8940	6.05	3.08 ± 0.24	2.46 ± 0.24	1.45 ± 1.45
1.8970	6.03	2.99 ± 0.25	2.39 ± 0.25	1.08 ± 1.51
1.9000	6.01	3.26 ± 0.26	2.64 ± 0.26	2.85 ± 1.56
1.9060	5.97	2.63 ± 0.22	2.13 ± 0.22	-0.72 ± 1.31
1.9120	5.94	3.07 ± 0.25	2.49 ± 0.25	2.10 ± 1.48
1.9180	5.90	2.65 ± 0.23	2.20 ± 0.23	-0.22 ± 1.36
1.9240	5.86	2.79 ± 0.23	2.31 ± 0.23	0.76 ± 1.35
1.9300	5.83	2.78 ± 0.24	2.32 ± 0.24	0.81 ± 1.40
1.9360	5.79	2.93 ± 0.24	2.42 ± 0.24	1.80 ± 1.39

value of R between the two fixed energy points was found to vary by approximately 7%, whereas statistical errors were less than 2%. These have been combined into the fit by introducing this systematic error, assumed to have resulted from changes in the hardware.

During the scan, we did not have any liquid argon calorimeter (LA) information. This causes all normalizing Bhabhas to fall into the normalizing μ-pair category. These QED events selected by geometry, momentum and pulse height cuts are normally used to monitor luminosity. The luminosity from the small angle monitor tracked the sum of these normalizing pairs within statistical errors. Corrections to R for the filtering down of multiprong QED events into hadron classes amounted to approximately 1%. These corrections were estimated by comparing data at the ψ'', where LA information was available with the same data, removing the LA information.

The overall systematic error is estimated to be 10%, with contributions coming from event selection and background subtraction (5%), estimation of detection efficiency (5%) and luminosity monitoring (7%).[12] Point-to-point fluxuations are expected to be less than 4%, and are small compared to our average statistical error of 7%. It will be seen that the systematic error is comparable to the statistical error on the leptonic width, and thus contributes a large part of the error on the charm cross section measurement.

THE FITTING FUNCTION

To determine the ψ'' parameters (e.g., Γ_{ee}, Γ_{tot}, $M_{\psi''}$) a least-squares fit of the observed energy dependence of R to a 10 parameter function was performed.

The parameters used were:

1. Mass ψ
2. $\Gamma_{ee}\ \psi$ — ψ leptonic width
3. Mass ψ'
4. $\Gamma_{ee}\ \psi$ — ψ' leptonic width
5. R_{flat} — flat background
6. R_{charm} — coefficient of threshold term for $D\bar{D}$
7. Mass ψ''
8. $\Gamma_{ee}\ \psi''$ — ψ'' leptonic width
9. $\Gamma_{tot}\ \psi''$ — ψ'' total width
10. r — interaction radius for Γ_{tot} (W) .

The fitting function is a sum of components:

i. ψ and ψ' radiative tails in the standard form:[13]

$$\tilde{\sigma}(W) = \frac{6\pi^2}{M^2}\, t\, \Gamma_{ee} \left[\left(\frac{W-M}{E}\right)^t \frac{1}{W-M} - \frac{1}{E} + \frac{W-M}{2E^2}\right]$$

where W is the center-of-mass energy, $E = W/2$, M is the ψ or ψ' mass and t is given:

$$t = \frac{2\alpha}{\pi}\left[\ln\left(W^2 / M_e^2\right) - 1\right]$$

For all the fitting, M and Γ_{ee} for the ψ are fixed to 3.095 GeV and 4.8 KeV. Except for the study of systematics, the mass of the ψ' is fixed to 3.684 GeV.

ii. Nonresonant backgrounds are included in the form of a constant plus a threshold term:

$$R(W) = R_{flat} + R_{charm} \left(\frac{P_D}{E_D}\right)^3 \theta\left(E - M_D\right)$$

iii. The ψ'' resonance is parametrized as a simple nonrelativistic p-wave Breit-Wigner. To account for the proximity to $D\bar{D}$ threshold, an energy dependent total width $\Gamma_{tot}(W)$ was introduced. The energy dependence includes a phase space factor, a barrier penetration factor and a relativistic correction:[14,15]

$$\sigma_{\psi''}(W) = \frac{3\pi(\hbar c)^2}{M^2} \cdot \frac{\Gamma_{ee}\,\Gamma_{tot}(W)}{(W-M)^2 + \frac{\Gamma^2_{tot}(W)}{4}}$$

$$\Gamma_{tot}(W) = \Gamma_{tot}\left(\frac{T^+ + T^o}{T^+_{peak} + T^o_{peak}}\right)\left(\frac{2M}{M+W}\right)$$

where T^+ or $T^o = p^3/1 + (rp/\hbar c)^2$, where p is the D^+ or D^0 momentum, and r is the classical interaction radius.

The width, Γ_{tot}, which is the fit parameter, is the value at the peak $\left(\text{i.e., } \Gamma_{tot}(W=M)\right)$. Here we have introduced the assumption of an equal contribution from D^+D^- and $D^o\bar{D}^o$ up to phase space factors.

In the fit, the physical Breit-Wigner is radiatively corrected by numerically performing the integrals:[13]

$$\tilde{\sigma}(W) = (1+\varepsilon)\,\sigma(W) - \frac{t}{E}\int\left(1 - \frac{k}{W}\right)\sigma(W-k)\,dk$$

$$+ t\int\left[\sigma(W-k) - \sigma(W)\right]\left(\frac{k}{E}\right)^t \frac{dk}{k}$$

where

$$\varepsilon = \frac{2\alpha}{\pi}\left(\frac{\pi^2}{6} - \frac{17}{16}\right) + \frac{13}{12}\,t$$

Since the observed width of the ψ'' is significantly greater than the SPEAR energy resolution $\left(\Gamma_{tot} / \Gamma_{beam} > 10\right)$ the resolution function was not folded into the integral. At the peak of the Breit-Wigner, the radiative correction amounts to a 25% difference in produced and observed cross section.

RESULTS OF THE FITS

As discussed above, the remaining parameters are Γ_{ee}, ψ', ψ'' mass, Γ_{ee}, Γ_{tot}, R_{flat}, R_{charm} and r. Successful fits were obtained for values of r from 1 to 10,000 fermi and all results were basically insensitive to the exact value. For all subsequent fits, r was fixed to 2.5 fermi.

The standard fit results were:

$$\psi'\ \Gamma_{ee} = 1.45 \pm .12 \text{ KeV}$$

$$\psi''\ \text{Mass} = 3.7639\ {}^{+\,.00162}_{-\,.00165}\ \text{GeV}/c^2$$

$$\psi''\ \Gamma_{ee} = 276\ {}^{+\,40.3}_{-\,38.0}\ \text{eV}$$

$$\psi''\ \Gamma_{tot} = 23.5\ {}^{+\,5.54}_{-\,4.84}\ \text{MeV}$$

$$R_{flat} = 2.22 \pm .060$$

$$R_{charm} \approx 0.0$$

The errors here were derived from the least-squares fit and correspond to a change of 1 in χ^2. Figure 2a shows the observed

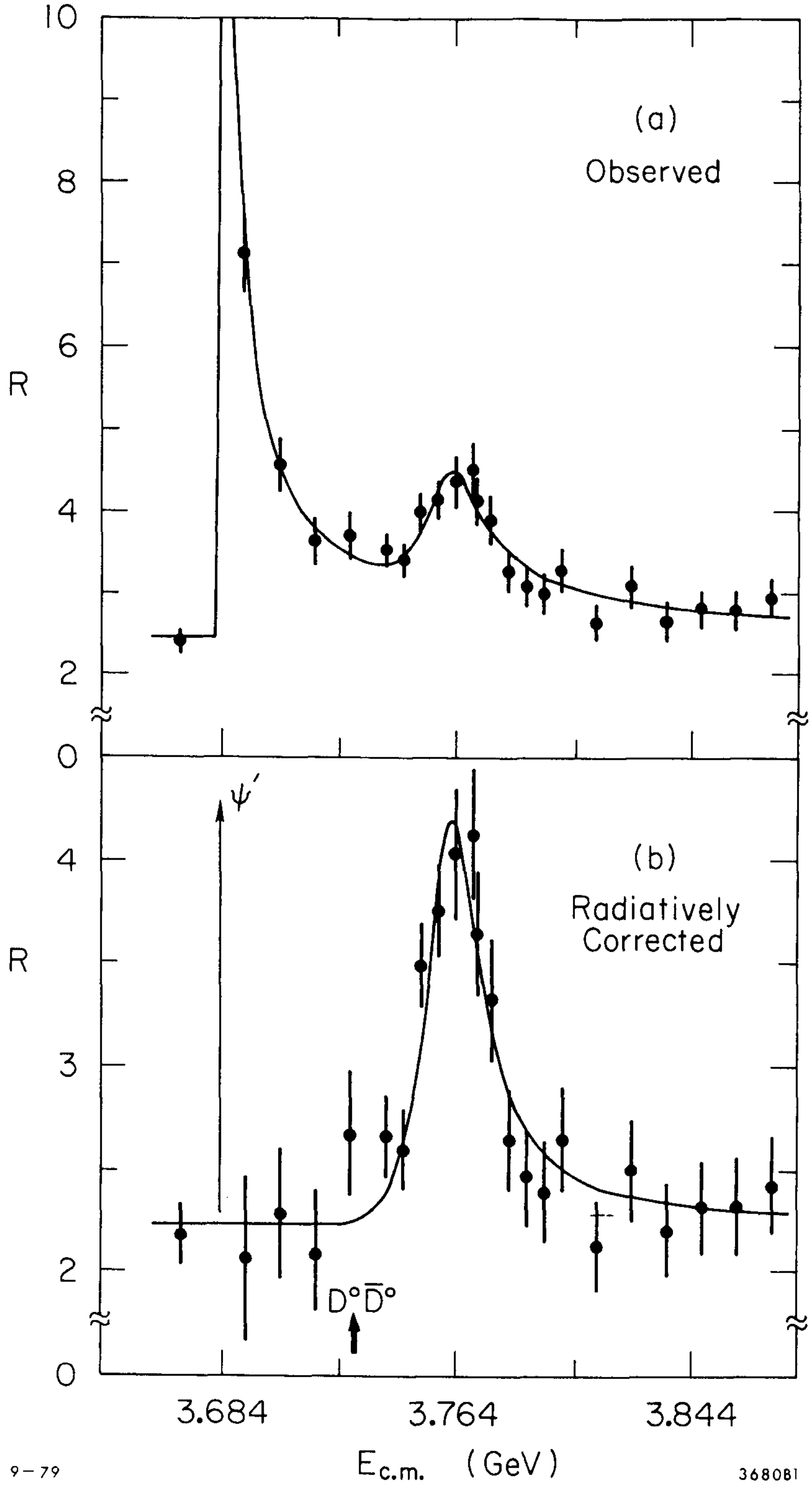

Fig. 2. (a) The data as observed is plotted in units of R. A radiative correction for the continuum (~ 9 %) has been applied. Full radiative corrections are applied in (b). The curve is the fit to the data.

spectrum with this fit, Fig. 2b shows the radiatively corrected spectrum and Fig. 3 shows the raw data after removal of backgrounds and tails. The χ^2/df for this fit is 12.4/17 df.

SYSTEMATIC ERRORS

Systematic errors arise from several sources, and are examined next.

Overall Scale of R

The systematic error in R is expected to be $\lesssim 10\%$. This error contains estimates of our uncertainty in event selection ($\pm 5\%$), efficiency ($\pm 5\%$), and luminosity monitoring ($\pm 7\%$). This error should be in the form of a scale change rather than a shape change in R. A shift of the data by $\pm 10\%$ leaves the ψ'' mass invariant, changes Γ_{ee} less than 10% and Γ_{tot} less than 2%.

Tail of ψ'

The ψ' tail depends on both its mass and leptonic width. The mass is taken as the measured value 3.684 ± 0.005 GeV. The error here is principally an absolute error ($\sim 0.13\%$) based on our knowledge of the energy calibration storage ring. It is known however that the setting error is better than ~ 200 keV since SPEAR was able to locate the ψ' peak both before and after this scan at the previously determined energy. The fits are not sensitive to any small changes in the ψ' mass, but are somewhat sensitive to the less well determined width. To demonstrate these effects the ψ' mass and width were allowed to vary. The mass of the ψ' moved $\lesssim 200$ keV, the ψ'' mass was unaffected ($\Delta M \approx 0.2$ MeV), the leptonic width and total width changed $< .5\%$. Fixing the ψ' width and mass at the published values resulted in a

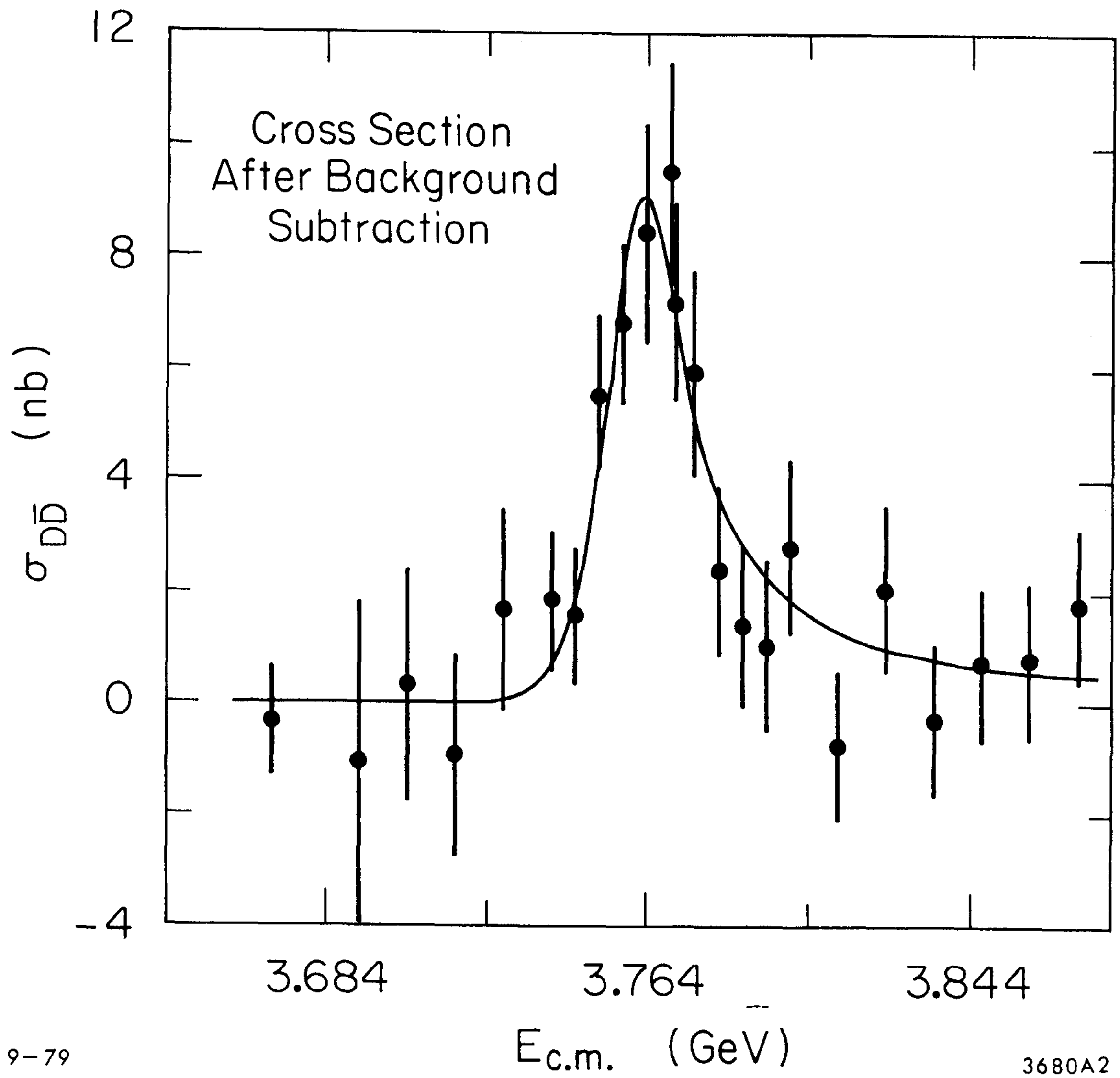

Fig. 3. The observed total cross section where all backgrounds have been subtracted off.

poor fit $\left(\chi^2/\mathrm{df} = 2.2\right)$ with Γ_{ee} and Γ_{tot} of the ψ'' changing by $\sim 4\%$ and 6%, respectively, and the mass increasing about 0.9 MeV. The fit was unable to accommodate the points below the ψ'' peak. It thus appears that the largest errors that can be introduced by the tail subtraction are small compared to the relevant statistical errors.

Background Terms

The form chosen for the background shape can introduce a systematic error. The magnitude of the flat background in the fit is well determined (fit error $\lesssim 3.0\%$). By making 1σ variations in the background, the mass of the ψ'' was seen to move less than 0.1 MeV, but the total and leptonic widths changed by as much as 8%.

As expected, these fits had poorer χ^2 because there was no way to compensate for the points below the ψ' and above the ψ'' structure. Any other reasonable smooth background which accommodated these parts of the spectrum would introduce considerably smaller changes to the ψ'' parameters.

The β^3 threshold term is consistent with zero in most of the fits which we have explored. The errors indicate the insensitivity to this term because of the small values of β near threshold.

Interaction Radius

When r was varied from .1 fermi to 10,000 fermi, slow changes in Γ_{ee} and Γ_{tot} were observed. In the poorest fit (r = .1 fermi), Γ_{ee} changed by $\pm$ 31 eV, and the total width by $\pm$ 3.1 MeV.
While the radius does not significantly affect the ψ'' parameters, its value (together with a knowledge of the D^+ and D mass) does determine the $D^o\bar{D}^o$ and D^+D^- decay fraction and error. At the center-of-mass energy 3.771 GeV, the $D^o\bar{D}^o$ fraction varies from 0.599 to 0.533 as r

changes from 0 to ∞. An average value of 0.57 ± 0.03 is suitable for the neutral fraction at this energy. This 5% error is small compared to the approximately 15% errors on Γ_{tot} and Γ_{ee} that are expected.

Fits which assumed no energy dependence in the width have somewhat better χ^2, since the high mass side of the ψ'' tends to fall between the data points more symmetrically. The parameters of these fits change negligibly, so the energy dependent width was retained.

RESULTS

Based on these fits and estimates of the systematics, the following ψ'' parameters are found:

$$\begin{aligned} \text{Mass} &= 3.7639 \pm (.0016)_{\text{statistical}} \\ &\quad \pm (.0010)_{\text{systematic}} \\ &\quad \pm (.0049)_{\text{calibration}} \qquad (\text{GeV}) \end{aligned}$$

$$\Gamma_{ee} = 276 \pm (39)_{\text{statistical}} \pm (31)_{\text{systematic}} \qquad (\text{eV})$$

$$\Gamma_{tot} = 23.5 \pm (4.8)_{\text{statistical}} \pm (1.7)_{\text{systematic}} \qquad (\text{MeV})$$

The systematic and statistical errors are combined in Table II for comparison with LGW[16] and DELCO[17] results. While the widths appear in reasonable agreement, the mass obtained appears to be 6 and 8 MeV lower than both previous measurements.

The discrepancy in mass has not been resolved. Since all data were taken at SPEAR, the 4.9 MeV calibration error should not be used in a comparison. Table II contains the mass measured relative to the ψ' indicating in reality an ~3 standard deviation difference.[18,19] Two checks performed with the current data were to reconstruct the D^0 mass, and to compare the measured SPEAR energy (flip-coil) with another independent measurement (a transductor on the bend magnets). The reconstructed D^0 mass (based on nine events $D^0 \rightarrow K^{\pm}\pi^{\mp}$) yielded $M_{D^0} = 1863.2 \pm 1.1$ MeV, and would have changed in direct (1:1) proportion with a change in beam energy. The latter check showed agreement within 1 MeV over the bulk of the running time, between transductor and flip-coil energy readings. The conclusion is that no shift in SPEAR energy occurred during the scan. It should be noted that the LGW and DELCO results are not entirely independent in that the same energy measurements were recorded in both experiments.

TABLE II

Comparison of Resonance Parameters

	M(MeV)	Γ_{ee}(eV)	Γ_{tot}(MeV)	$M-M_{\psi'}$(MeV)
LGW	3772 ± 6.	345. ± 85.	28. ± 5.	88. ± 3.
DELCO	3770 ± 6.	180. ± 60.	24. ± 5.	86. ± 2.
This experiment	3764 ± 5.	276. ± 50.	24. ± 5.	80. ± 2.

CROSS SECTIONS

The luminosity-averaged energy of our fixed block data is 3.771 ± 0.001 GeV and corresponds to an enhancement in the charm cross section of:

$$\sigma_{total} = 6.99 \pm (.84)_{statistical} \begin{pmatrix} + .71 \\ - .69 \end{pmatrix}_{systematic} \quad \text{(nb)}$$

The statistical error (~12%) accounts for the correlation between Γ_{ee} and Γ_{tot} in the fit. The systematic error is an estimate based on maximum variations in R, and the resulting changes in the fit parameters. No error is included for the ± .001 GeV window. The slope is estimated to be about 0.4 nb/MeV at 3.771 GeV.

Using the assumptions discussed earlier, the single D cross sections at 3.771 GeV are given:

$$\sigma_{D^o} = 8.0 \pm .95 \; (\pm 1.21)(\text{nb})$$

$$\sigma_{D^+} = 6.0 \pm .72 \; (\pm 1.02)(\text{nb})$$

At the peak, the total charm cross section from our data is:

$$\sigma_{tot}(3.764) = 9.3 \pm (1.1) \begin{pmatrix} + .90 \\ - .93 \end{pmatrix} \; (\text{nb})$$

This is about 10% lower than the LGW ($\sim$ 10.3 nb) result at 3.772 GeV. Radiatively corrected, our data show a peak enhancement in R of ~ 2.0 units, whereas LGW ~ 2.2, and DELCO ~ 1.5,[18,19] with the differences resulting from $\Gamma_{ee} / \Gamma_{tot}$ for each experiment.

MIXING AND THE CHARMONIUM MODEL

The large leptonic width that is observed is strong evidence for the coupled-channel approach to the charmonium model.[20] A purely bound state model predicts leptonic widths from the tensor forces of about 20 eV. The mixing angle ε of the ψ' and ψ'' is then only $\sim 6^o$. Using the observed leptonic widths for these levels (2.1 ± .4 and .276 ± .050 keV, respectively), the mixing angle is estimated to be

$$\varepsilon = \tan^{-1}\left(\frac{M_{\psi''}}{M_{\psi'}} \sqrt{\frac{\Gamma_{ee}(\psi'')}{\Gamma_{ee}(\psi')}} \right) \approx 20.3 \pm 2.8^o$$

The coupled-channel model predicts a width of $\sim$ 150 eV, considerably closer to the observed value. Thus, the mixing of bound states near threshold through the decay sector appears to play an important role in determining the properties of the charmonium spectrum. It should be noted that further support for these models comes from the behavior of the D and D^* production cross sections in the 4 GeV region.[20]

The charmonium model interpretation of the ψ'' as a $^3D_1$ level is not without contenders. Another class of models exist which incorporate it as a p-wave resonance of a 4-quark ($c\bar{c}q\bar{q}$) state.[21] These can be thought of either as "molecules" formed of bound "atoms" of $\bar{D}$ and D ($c\bar{q}$) separated by a centrifugal barrier, or simply as states of four bound quarks. In a similar fashion, the peak at 4.028 in the e^+e^- total hadronic cross section is treated as a p-wave $D^*\bar{D}^*$ molecule. These arguments lead to the prediction of another resonance near $D\bar{D}^*$ threshold. No evidence for such a state has been reported. In addition to these p-wave states, as many as forty-eight s-wave states (accessible by single pion decays of p-wave states such as $\psi(4.028)$ and $\psi(4.42)$) are predicted. These would have the signature of the slow pion, but as yet have not been observed.

The present state of our knowledge has not ruled out the molecular interpretation. Similarly, the molecular interpretation would not rule out the conclusions we derive from the charmonium picture on D production cross sections, unless new decay channels of the ψ'' were opened up. This may be ruled out theoretically because the lowest mass of the theoretical states are not energetically accessible by pion decay.

REFERENCES

1. Aubert, J. J., *et al.*, Phys. Rev. Lett. 33, 1404 (1974); Augustin, J. E., *et al.*, Phys. Rev. Lett. 33, 1406 (1974); Bacci, C., *et al.*, Phys. Rev. Lett. 33, 1408 (1974).

2. Abrams, G. S., *et al.*, Phys. Rev. Lett. 33, 1453 (1974).

3. Bjorken, J. D., and Glashow, S. L., Phys. Lett. 11, 255 (1964).

4. See for example, Applequist, T., and Politzer, D. H., Phys. Rev. Lett. 34, 43 (1975); De Rujula, A., and Glashow, S. L., Phys. Rev. Lett. 34, 46 (1975).

5. Goldhaber, G., *et al.*, Phys. Rev. Lett. 37, 255 (1976).

6. See for example, as a good summary: Eichten, E., *et al.*, Phys. Rev. D17, 3090 (1978) and Jackson, J. D., *European Conference on Particle Physics*, Budapest (1977).

7. Schnitzer, H. J., Phys. Rev. Lett. 35, 1540 (1975).

8. Eichten, E., *et al.*, Phys. Rev. Lett. 36, 369 (1975) (also see Reference 6).

9. Eichten, E., *et al.*, Phys. Rev. Lett. 36, 500 (1976) (also see Reference 8); for more recent calculations including mixing from intermediate states, see Misra, S. P., *et al.*, Preprint IP/BBSR/79-14.

10. Bacino, W., *et al.*, Phys. Rev. Lett. 40, 671 (1978); Rapidis, P. A., *et al.*, Phys. Rev. Lett. 39, 526 (1977).

11. Peruzi, I, *et al.*, Phys. Rev. Lett. 39, 1301 (1977).

12. Siegrist, J. L., October 1979, Thesis (Stanford University).

13. Jackson, J.D., and Scharre, D. L., Nucl. Instrum. Methods 128, 13 (1975).

14. Cool, R. L., and Marshak, R. E., Advances in Particle Physics, Vol. 2; Interscience, New York, N. Y., 1968; p. 193.

15. The interpretatin of r comes from the calculation of a barrier penetration factor. r is the classical square well radius beyond which no binding occurs.

16. Rapidis, P. A., *et al.*, Phys. Rev. Lett. 39, 526 (1977).

17. Bacino, W., *et al.*, Phys. Rev. Lett. 40, 671 (1978).

18. Private Communication — Bacino, W., University of California at Los Angeles.

19. Private Communication — Feldman, G., Stanford Linear Accelerator.

20. Appelquist, T., Barnett, M., and Lane, K., Annu. Rev. Nucl. Sci., Vol. 28 (1978).

21. See for example, DeRujula, A. and Jaffe, R. L., MIT-CTP-658 (1977), DeRujula, A., *et al.*, Phys. Rev. Lett. 38, 317 (1977); Cox, P., Park, S. Y. and Yildiz, A., HUTP-76/A177 (1976); and Nussinov, S. and Jidhu, D., Fermilab-PUB-76/70-THY (1976).

V. DECAY MODES OF CHARMED MESONS

INTRODUCTION

This chapter is devoted to detailing the methods used in identifying various decay modes of the D mesons and to measuring their branching ratios. As discussed in the previous chapter, these latter measurements are possible only at the $\psi(3770)$, where the cross section for charm production is determined directly by measuring the ψ'' resonance parameters along with the background. In addition, a unique kinematic constraint is obtained because the data are taken below DD^* threshold (~3.868 GeV) and D mesons can only be produced in pairs with unique momentum. It will be shown that for most decay modes this information can be used to substantially improve the mass resolution and reduce backgrounds.

The weak-hadronic decays of the D mesons can be characterized from the standard form of the charged weak current in the SU(2) ⊗ U(1) model[1] expanded to include six quarks:[2]

$$J_u = (\bar{u}, \bar{c}, \bar{t})\, \gamma_u (1-\gamma_5)\, U \begin{pmatrix} d \\ s \\ b \end{pmatrix}$$

$$U = \begin{pmatrix} c_1 & s_1c_3 & s_1s_3 \\ -s_1c_2 & c_1c_2c_3 + s_2s_3e^{i\delta} & c_1c_2\bar{c}_3 - s_2c_3e^{i\delta} \\ -s_1s_2 & c_1s_2c_3 - c_2c_3e^{i\delta} & c_1s_2s_3 + c_2c_3e^{i\delta} \end{pmatrix}$$

where $c_i = \cos\theta_i$, $s_i = \sin\theta_i$.

Here U is the unitary matrix which mixes the mass eigenstates (d,s,b) through the weak interaction. The three angles θ_i and phase δ represent the four allowed degrees of freedom in U. In the limit of four quarks, U reduces to the simpler matrix involving only the upper left quadrant, and containing only one mixing angle θ_c (= θ_1) usually called the Cabibbo angle. In this simpler picture $c \to s$ is favored over $c \to d$ (just as $u \leftrightarrow d$ is favored over $u \leftrightarrow s$ in the decay of light non-charmed hadrons). Returning to the six quark picture, Fig. 1 shows the four possible combinations of the decay of a free charmed quark, and the factors introduced at the two vertices by the mixing angles. Current limits on the mixing angles come from measurements of neutron beta decay ($c_1 = 0.974 \pm 0.002$), and kaon and hyperon decay ($c_3 s_1 = 0.225 \pm 0.005$, implying $\theta_3 \lesssim 20^\circ$).[3] The values of s_2 and δ are small but less certain, being estimated by the $K_S^o - K_L^o$ mass difference, and by CP violation in kaon decays, coupled with theoretical calculations. The smallness of s_1 and s_3 suggest immediately that 1-a will represent the dominant decay of the c quark followed by 1-b and c (down by $\sim(s_1/c_1)^2 \approx 0.05$) and finally 1-d (down by $\sim(s_1/c_1)^4 \approx 3 \times 10^{-3}$).

Diagrams in the form of 1-a represent $\Delta S = \Delta C$ transitions leading to hadronic final states like:

$$D^o \to K^-(n\pi)^+ \;,\; \bar{K}^o(n\pi)^o$$
$$D^+ \to K^-(n\pi)^{++} \;,\; \bar{K}^o(n\pi)^+ \quad .$$

The Cabibbo suppressed diagrams 1-b and 1-c either change the final kaon to a pion ($\Delta S = 0$, $\Delta C = 1$) or add an extra kaon to the final state, respectively. These decays are expected at a rate of ~5% of the first diagram. The doubly suppressed diagrams like 1-d are $\Delta S = -\Delta C$ and cannot in principle be observed unless the full final state ($D\bar{D}$) is reconstructed.

The decay modes most readily searched for are those with either all charged particles or no more than a single neutral pion. This is

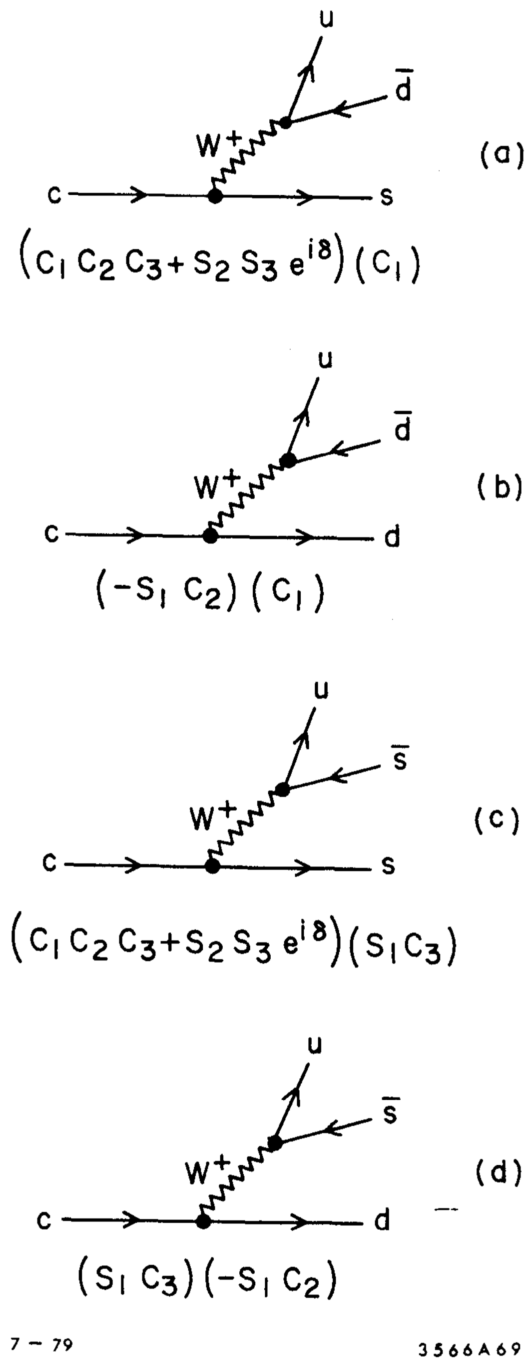

Fig. 1. (a) Cabibbo allowed weak transition, (b) Cabibbo suppressed transition of the charm quark, (c) Cabibbo suppressed transition of the light quark, (d) both light and heavy quarks decay weakly through suppressed currents.

basically a limitation imposed by the poor neutral particle detection efficiency discussed in Chapter II. Table I shows the decay modes to which we expect to be sensitive. Charge conjugate modes are not explicitly shown.

CHARGED PARTICLE SELECTION

The construction of the primary vertex was discussed in Chapter III. Tracks which do not fall in the primary vertex but are still used are required to satisfy a cut of ±15 cm in Z and 4 cm in R (from the primary vertex). These tracks will have poorer momentum resolution. All tracks must satisfy a loose criteria on fit quality: $\sqrt{\chi^2/\text{deg. freedom}} \leq 7$. This eliminates the long tail of the χ^2 distribution. A final cut requires that, given the reconstructed momenta and angles, the track must attach ≥ 55% of the expected dazms. This cut removes most tracks which are erroneously constructed from small numbers of random hits with a negligible removal of real tracks.

CHARGED PARTICLE IDENTIFICATION

The TOF system described in Chapter II provides the means to distinguish charged π-K-p and π-e over specific momentum ranges. The flight time resolution (σ) is known a priori, and therefore a convenient separation of particles can be achieved by using the measured momentum (p), flight time (t_m) and path length (L) to calculate a probability for a given mass hypothesis (M):

$$P(M) = \frac{1}{N} e^{-(t_m - t_p(M))^2/2\sigma^2}$$

where

$$t_p = L\sqrt{p^2 + M^2} \,/\, pc$$

TABLE I

2 Body	3 Body	4 Body	5 Body
$\pi^+\pi^o$	$^*K^-\pi^+\pi^+$	$^*K^-\pi^+\pi^+\pi^-$	$K^-\pi^+\pi^+\pi^-\pi^+$
$\pi^+\pi^-$	$^*K^-\pi^+\pi^o$	$^{**}K^o_s\pi^+\pi^+\pi^-$	$^{**}K^o_s\pi^+\pi^+\pi^-\pi^-$
$^*K^+\pi^-$	$^*K^o_s\pi^+\pi^-$	$K^-\pi^+\pi^+\pi^o$	
K^+K^-	$K^-K^+\pi^+$	$K^+\pi^-\pi^+\pi^-$	
$K^o_s\pi^o$	$K^o_sK^+\pi^-$	$\pi^+\pi^-\pi^+\pi^-$	
$^*K^o_s\pi^+$	$K^o_s\pi^+\pi^o$		
$K^o_sK^+$	$\pi^+\pi^+\pi^-$		

* Branching fraction reported[4,5,6]

** Decay mode seen[6]

and

$$N = \sum_i P(M_i) \qquad i = \pi, K, p \quad \text{or} \quad \pi, e$$

Figure 2 shows the separation for $K\pi$, Kp, and πe as a function of momentum for an average flight path of 1.75 m. The left scale is in units of σ assuming a 300 ps resolution for t_m. The average resolution for our full sample was $\sim$315 ps, and the average flight path was somewhat longer. The π-K separation below 1 GeV/c is expected to be about 3σ, with tracking errors, reduced flight paths, counter edges, etc., reducing this somewhat. Since D mesons produced at the $\psi(3770)$ are very slow (288 and 255 MeV/c for D^0, D^+, respectively), the most energetic (2-body) decays produce particles with laboratory momenta less than 1.1 GeV/c, suggesting separation at the 1σ level for π and K. While these figures are valid in events of charmed origin, background events, events with erroneous momenta or flight paths, multiple hits in TOF counters, and edge hits all tend to broaden these distributions. For all the following work π, K and p will be separated by selecting the highest normalized weight $P(M_i)$, requiring $P(M_i) \geq 0.40$, and finally requiring t_m be within 4σ of the predicted time. The last requirement prevents the use of totally erroneous times which have been normalized to give reasonable weights. Particles which fail these criteria are assigned pion identification as are particles missing the TOF system. This should introduce less than a 2% overall π-K misidentification since the tracking solid angle is only ~10% greater than the coverage and the K:π ratio is typically 1:5.

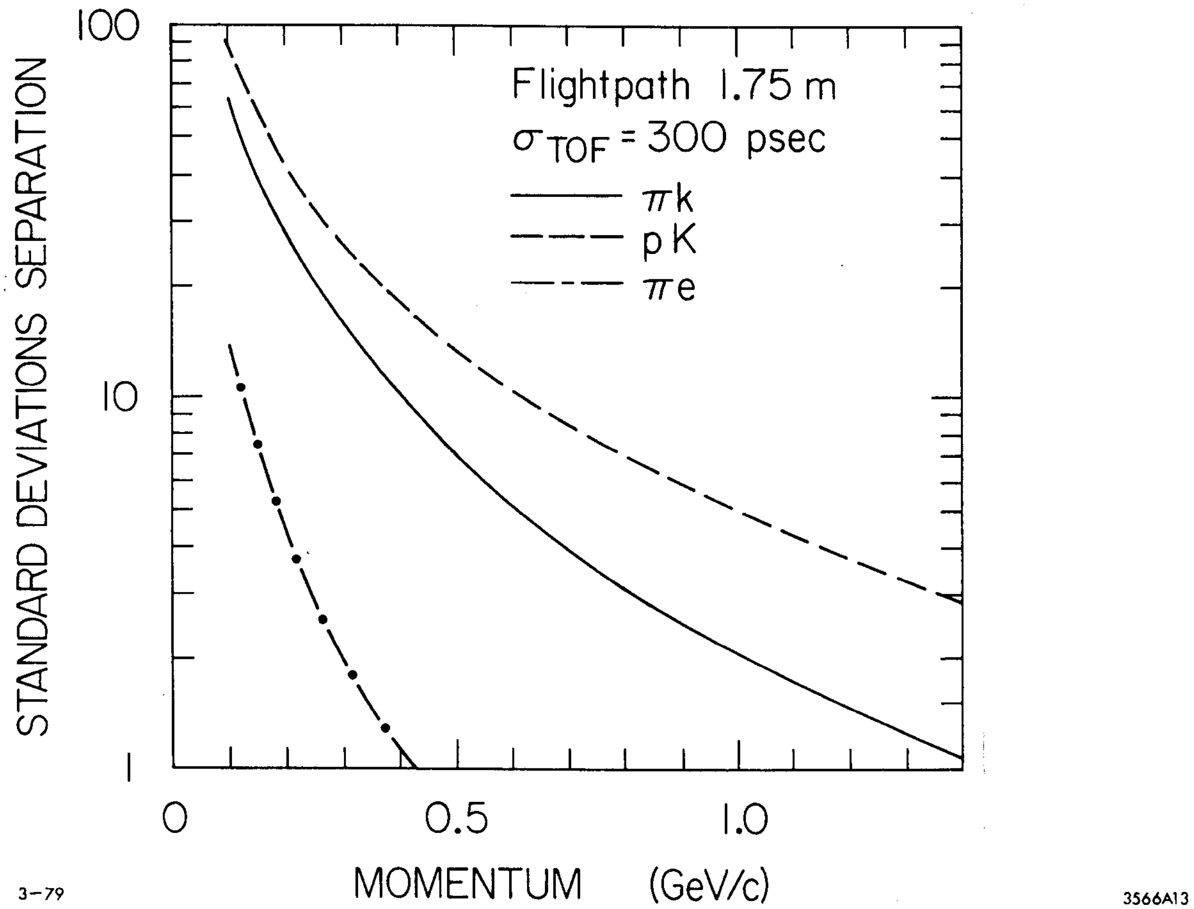

Fig. 2. TOF separation for particles versus momentum.

For tracks below 300 MeV/c, the π-e hypothesis can be tested by TOF. By requiring an $e^{\mp}$ weight of 90% and a measured time within 4σ of the expected time, clean separation is obtained below about 275 MeV/c with negligible loss. From 275 to 300 MeV/c the tight cut is necessary because of the large overlap of the π and e TOF distributions and the large π:e ratio in the data. For the purpose of identifying D mesons, the liquid argon information on charged tracks is ignored. This is necessary because the probability of a π being called an e ranges from 5-8% (this is detailed in the next chapter). For a 3 or 4 body decay the subsequent reduction in π efficiency reduces the overall D detection efficiency by 20-30%.

Muons are identified above 1 GeV. The number actually found is negligible (since D decays populate lower momenta), and, as seen in Chapter II, the efficiency is high ($\gtrsim 99\%$) and misidentification rate low ($\lesssim 1\%$).

Energy Loss Corrections

All tracks are corrected for energy losses in the material traversed along their flight paths. Given a mass hypothesis and momentum, β is calculated and the momentum change (δp) is computed:

$$\delta p = \left(\frac{3.69}{\beta^{2.65}}\right)\left(\frac{1}{\cos\lambda}\right) \text{ MeV/c} \quad \text{for } \beta < .93$$

$$\delta p = \left(\frac{4.46}{\cos\lambda}\right) \text{ MeV/c} \quad \text{for } \beta > .93$$

where λ is the dip angle. This correction is based on a fit to dP/dx [7] in carbon for $\pi^{\mp}$, $K^{\mp}$, $p^{\mp}$, with a cutoff at $\beta = 0.93$. The materials traversed are described in Chapter II. The expression used fits the data within a few percent, with deviations in the correction amounting to $\gtrsim 15\%$ only below 200 MeV/c for kaons and 300 MeV/c for protons.

RECONSTRUCTION OF K^o

The $\pi^+\pi^-$ decay (68.61%) of the K^o_s provides a clean method of reconstructing and utilizing K^o. While the $\pi^o\pi^o$ mode is usable in principle, the low π^o detection efficiency and poorer π^o momentum resolution (the vertex position is not known) forces the use of the former decay mode.

The technique for reconstruction is entails searching for all opposite sign $\pi^{\mp}$ (as separated by the TOF technique of the last section) which cross in xy projection. Only a loose cut of ±15 cm in Z and ±30 cm in R as well as the χ^2 and dazm attachment cuts previously discussed are applied. The radial position (in xy projection) of the crossing point is required to be ≥2 mm and ≤30 cm. The lower cut is a compromise to reduce background from other tracks (whose measurement error fakes crossing). The upper cut eliminates second crossings; it is far out on the expected tail for K^o_s coming from D decays. At the radius of crossing both tracks must lie within 9 cm in Z of each other. At this point momenta are recalculated at the position of crossing. The pions are corrected for dE/dx losses based on the radius. The final criterion that is applied is on the actual direction of the K^o_s. The variable ξ is defined as the difference in projected angle from the beam intersection point to the vee and the reconstructed vee direction. The $|\xi|$ distributions are shown in Figs. 3a-e for various radial intervals. A cut at $4\sigma_\xi$ is made, and the resulting invariant mass plotted in Fig. 4. The FWHM is ~12 MeV. At this point, a broad

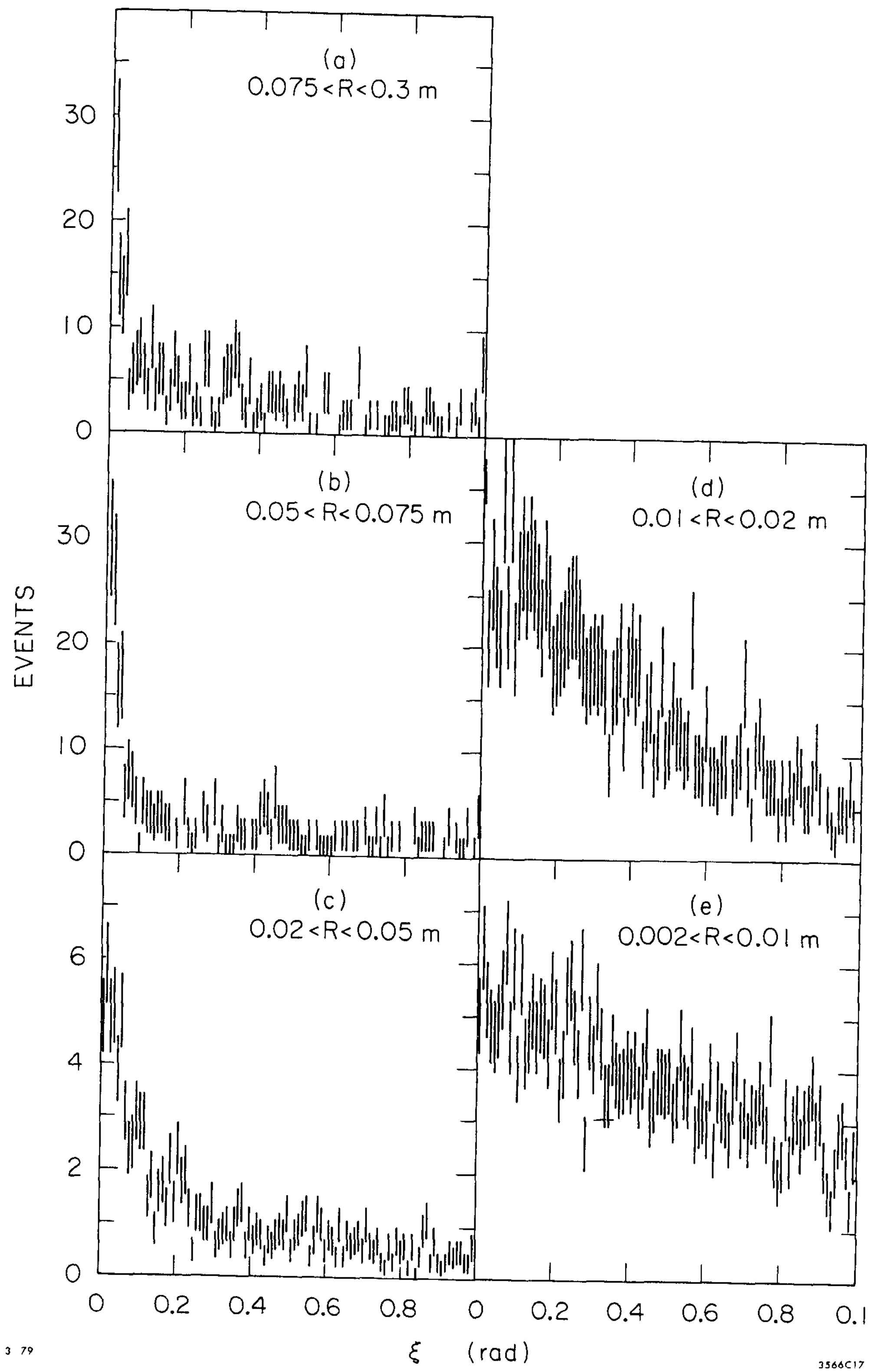

Fig. 3. Distribution of the angle ξ by transverse intersection (R).

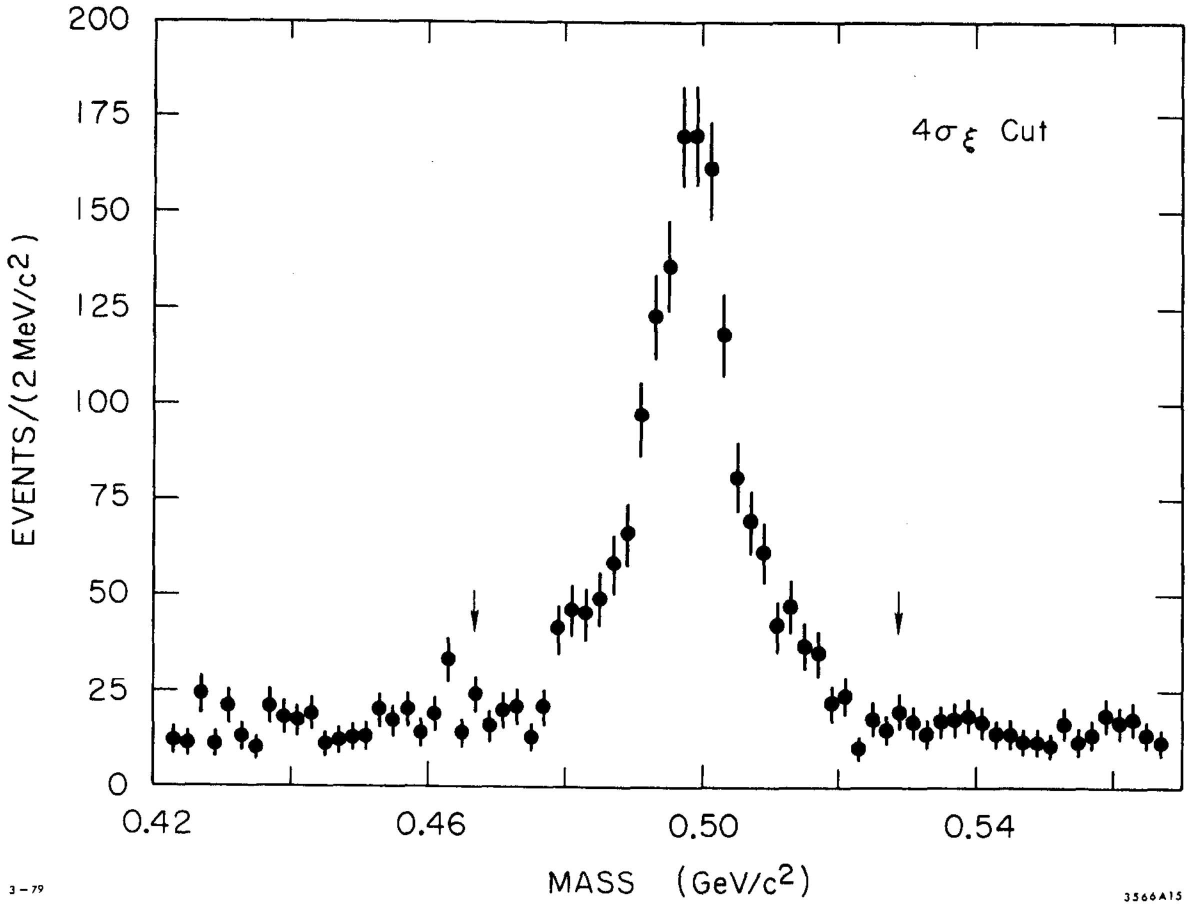

Fig. 4. The $\pi^+\pi^-$ invariant mass after a $4\sigma_\xi$ cut is applied. The arrows show the region where a 1C fit is attempted.

±30 MeV cut in the mass is made and a 1C fit to the K_s^o mass is performed. The χ^2 distribution is shown in Fig. 5. A χ^2 cut of 7 introduces essentially no loss in signal in a region of approximately ±20 MeV/c as expected. Figure 6 shows the resulting detection efficiency for isotropically produced K_s^o vs. momentum, as determined by Monte Carlo. For later analysis I have opened up the χ^2 cut to $\chi^2 \leq 12$ (99.9% level) and reduced the mass interval to ±18 MeV.

RECONSTRUCTION OF π^o

Neutral pions are found through their 2 photon decay mode. Photons are detected in the liquid argon with efficiencies discussed in Chapter II. The π^o are reconstructured by first forming the invariant mass of all pairs of photons. The photons are assumed to come from the primary vertex in the event and are required to have energies greater than 100 MeV to reduce the background from fake photons. These fake photons arise from noise in the electronics and contribute about 0.1 photon/evt. To reduce combinations, modules which have more than 6 photons are removed. Photons are also required to be more than a half strip-width apart. These arise from "split photons" (photons mistakenly separated by software), charge track interactions, or noisy channels in one or more strips of a module. Figure 7 shows a typical $\gamma\gamma$ mass spectrum after these simple cuts. We see the FWHM is ~60 MeV/c^2, and the signal is comparable to the background. To use the π^o for studying decays, we make a mass cut $60 < M_{\pi^o} < 220$ and perform a 1C fit of the $\gamma\gamma$ pair to the π^o mass allowing both energy and position to be varied. The χ^2 distribution is shown in Fig. 8. The π^o are required to have a $\chi^2 < 8$ and the

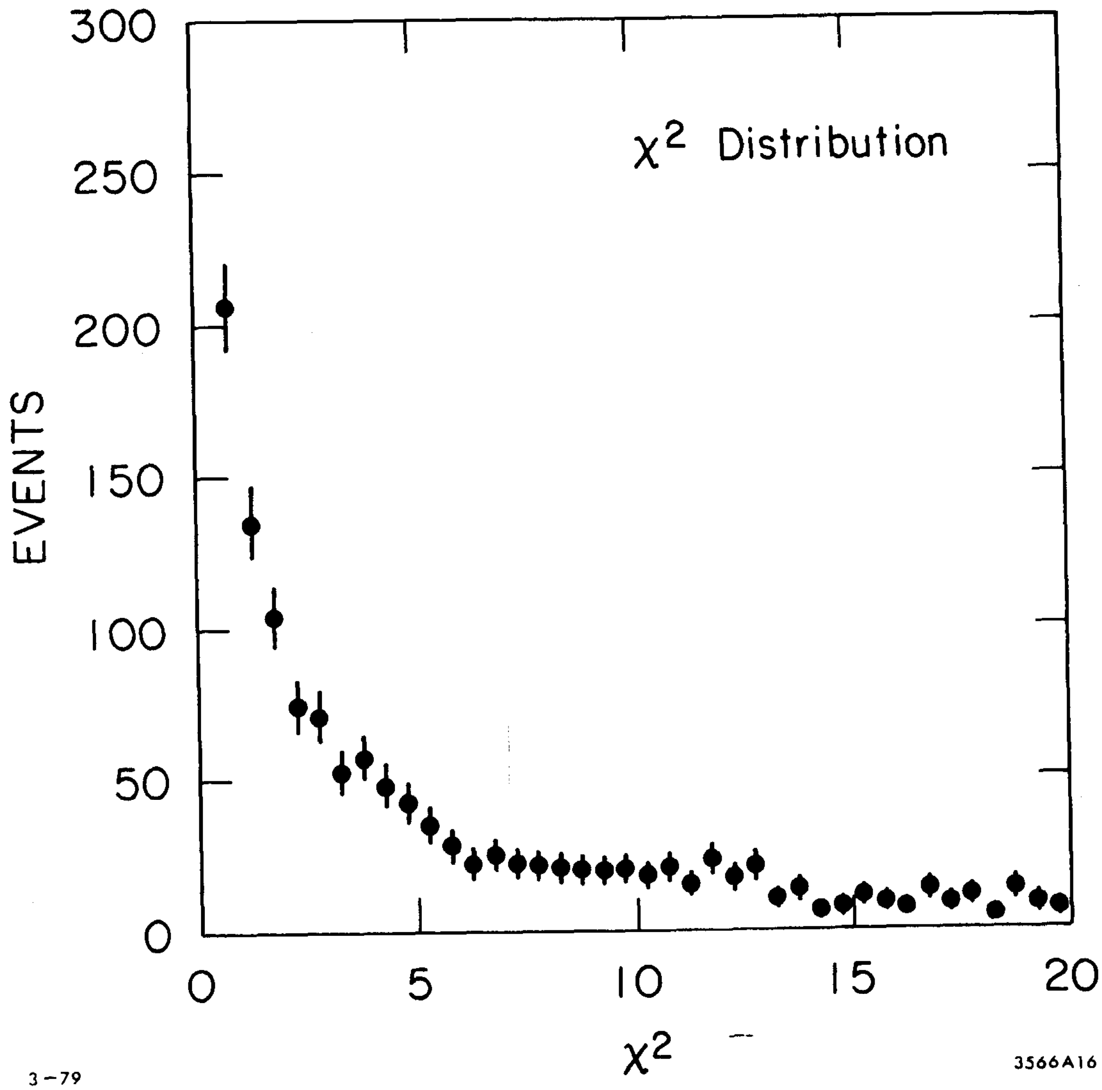

Fig. 5. χ^2 distribution for 1C fit to K_s^o mass.

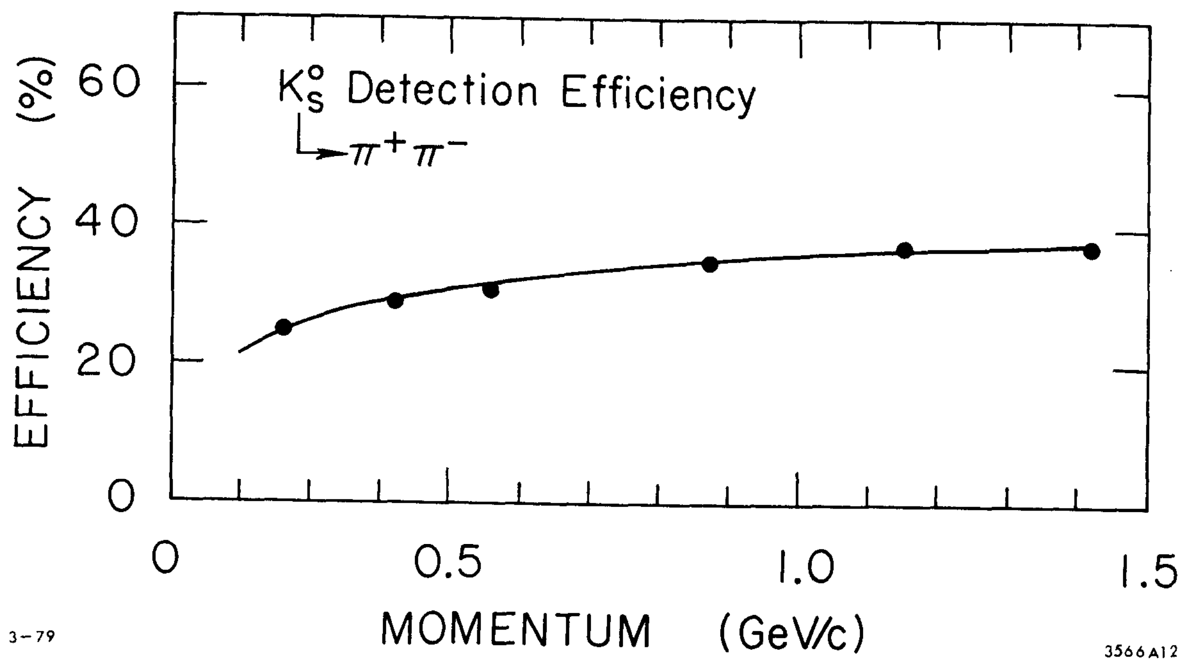

Fig. 6. K^0_s efficiency versus momentum for isotropic production.

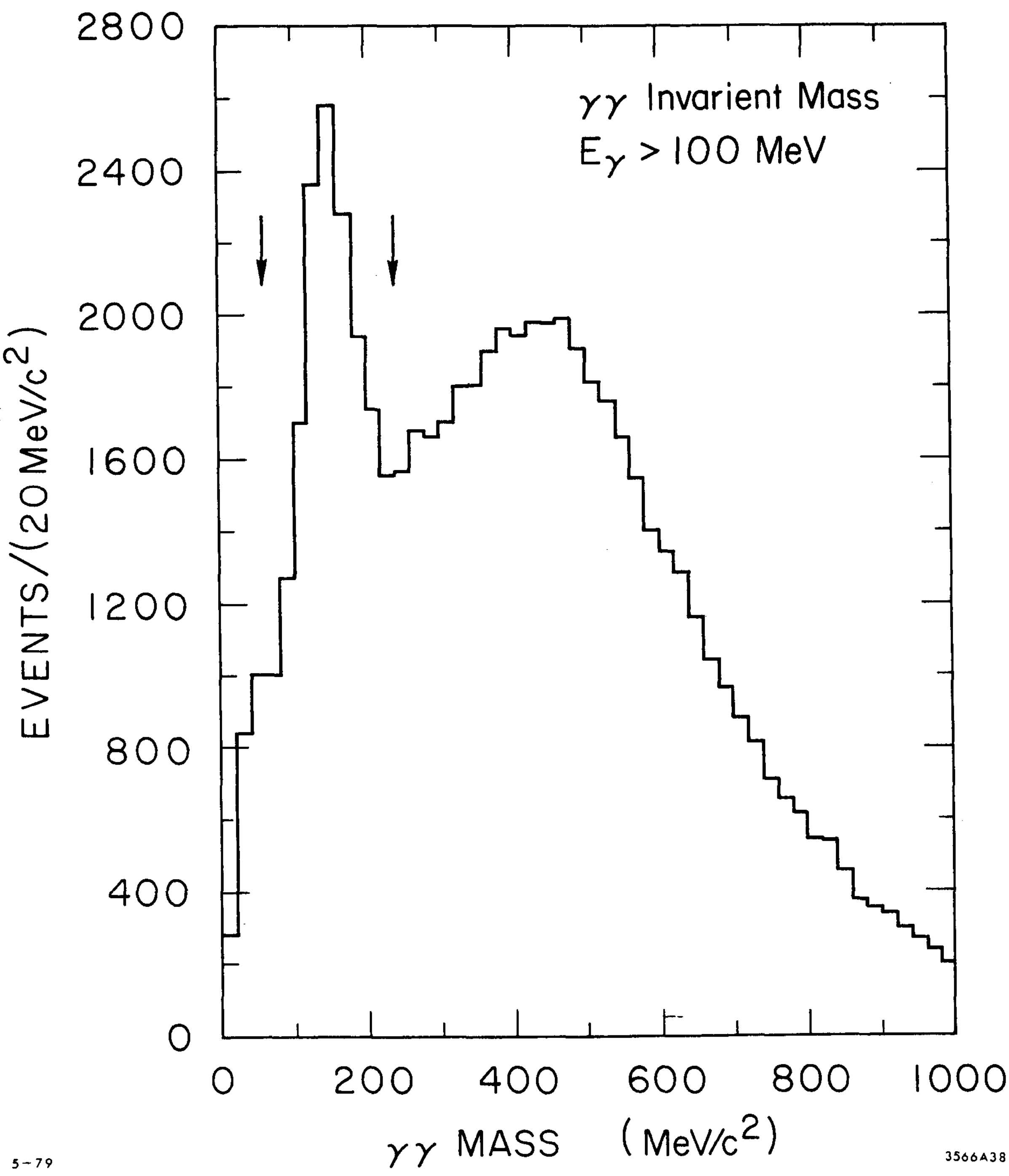

Fig. 7. $\gamma\gamma$ invariant mass requiring E_γ > 100 MeV.

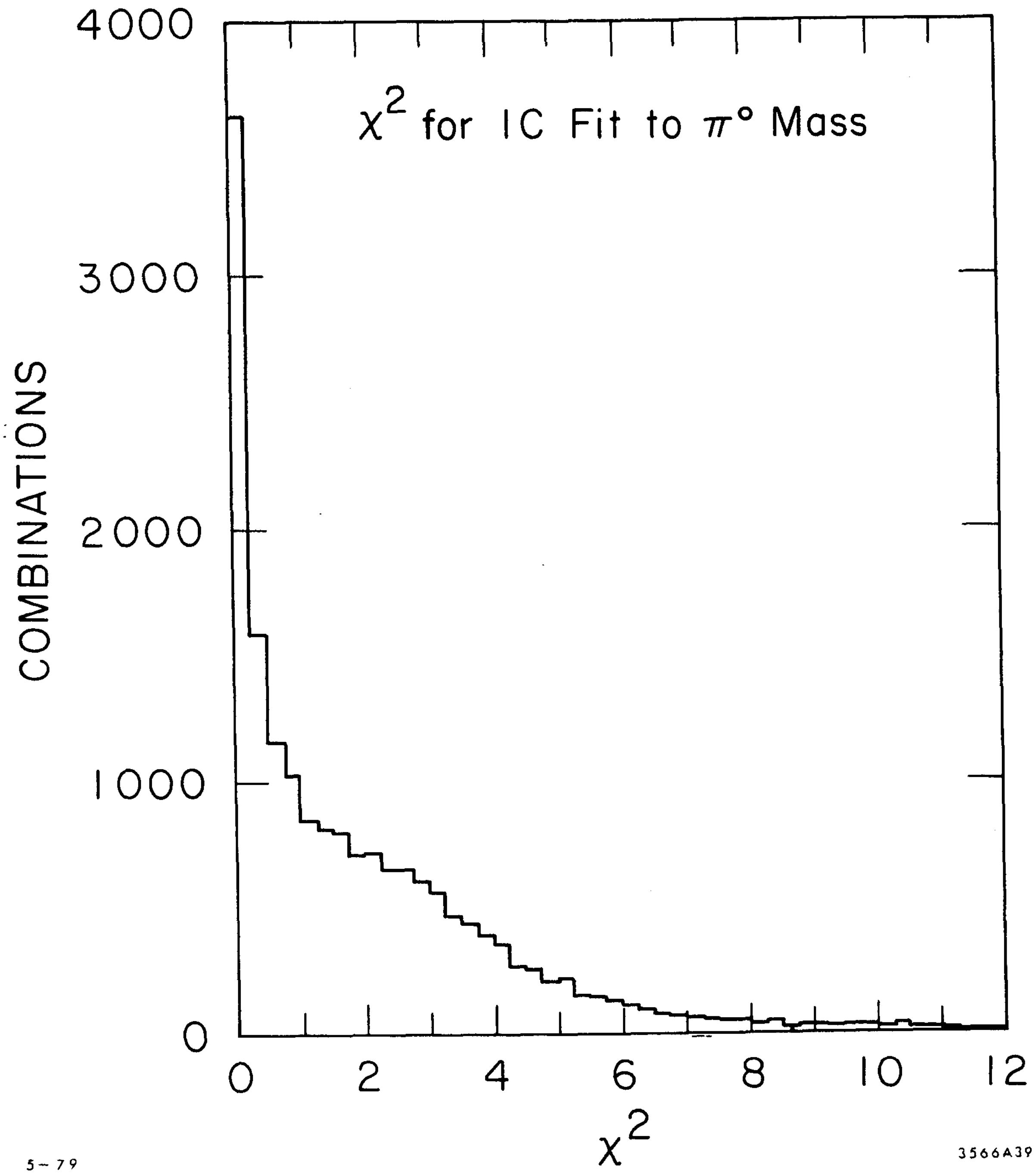

Fig. 8. χ^2 distribution for 1C fit to π^0 mass.

fitted π^o direction must lie within 30 mr of the original direction.

THE BEAM CONSTRAINT

The conventional technique used to search for decay modes of a particle is to form the invariant mass of the possible decay constituents. In the case of the 2-body D decays, momentum resolution is influenced strongly by the drift chamber resolution because momenta reach 1 GeV/c. If we naively ignore π and K masses, and assume a back-to-back decay of a D^o at rest, we might expect a $K^{\mp}\pi^{\pm}$ mass resolution of:

$$\delta m \approx \sqrt{2}\,\delta p_{\pi,K} \approx 25\ \mathrm{MeV}/c^2 \qquad .$$

This is close to the observed value of 22 MeV/c^2. In higher multiplicity decays we do somewhat better, because the momentum error introduced by the softer tracks is smaller.

We can however improve the mass resolution significantly, since we know that D mesons are produced in pairs at the ψ''. Under this assumption we can constrain the D decay products to the beam energy (E_b) which is a well measured quantity ($\sigma_E \approx$ 1.3 MeV, see Chapter II). The error in mass which was previously dominated by the term containing the error in energy (because $P_D \lesssim$ 290 MeV/c) is now reduced more than an order of magnitude:

$$\begin{aligned} M^2 &= E_b^2 - P_D^2 \\ \delta M^2 &= 2\left(E_b^2\,\delta^2 E_b + P_D^2\,\delta^2 P_D\right)^{1/2} \qquad . \end{aligned} \tag{1}$$

Here I have used the fact that E_b is uncorrelated with P_D. Using values for a typical 2-body decay $D^o \to K^-\pi^+$, $\delta M \approx 2.2$ MeV/c^2.

In the case of decays with single π^o's the beam energy constraint and the $\gamma\gamma$ mass constraint (to the π^o) can be used to fix the photon energies:

$$E_b = E_c + E_{\gamma 1} + E_{\gamma 2} \tag{2}$$

$$M^2_{\pi^o} = 2E_{\gamma 1}\, E_{\gamma 2}\left(1 - \cos\theta_{12}\right) \quad . \tag{3}$$

Here E_c is the energy of the charged tracks, and θ_{12} the angle between the photons in the π^o. If θ_{12} is assumed to be well measured (typically $\sigma_{\theta_{12}} \lesssim 8$ mr), then Eqs. (2) and (3) can be solved simultaneously for $E_{\gamma 1}$ and $E_{\gamma 2}$ thus allowing a recalculation of the π^o momenta. The system will have either one, two or no solutions (see Fig. 9). When two solutions occur, the one corresponding to the minimum χ^2 formed of the γ-ray energies and resolution is chosen. When no solution occurs, the solution $E_{\gamma 1} = E_{\gamma 2}$ is taken. Equation (1) can then be used to calculate a mass.

In either of the cases mentioned above, a criteria must be established before applying the beam constraint. The correct criteria holds that the calculated energy must be close to the expected energy, assuming the $D\bar{D}$ hypothesis. In the case of charged modes, this is typically $\pm$(35-60) MeV. For neutral modes, it is ~200 MeV, owing to the poorer resolution of the two photons. It is observed that opening up this cut will tend to increase background as well as introduce double counting in the multibody modes where soft pions are present. An alternative cut to the energy difference is a cut on the difference

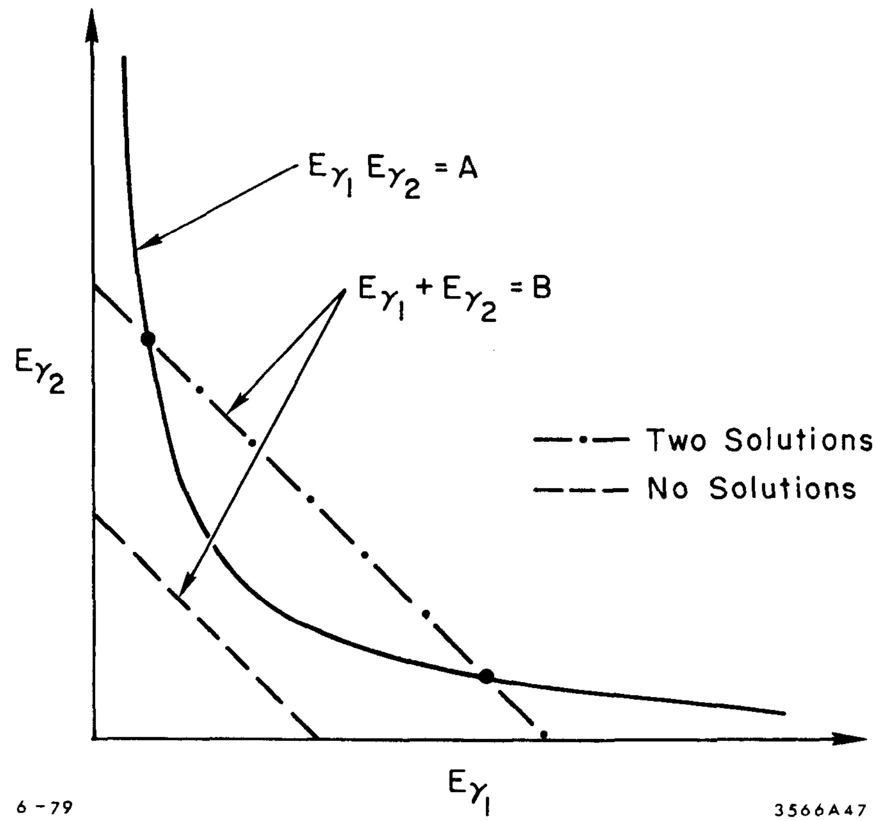

Fig. 9. Graphical solution for photon energies.

of the recoil mass from the observed mass. The resolution in this variable is proportional to approximately twice the energy resolution.

The beam-constraint (BC) technique has a major drawback in searching for decay modes which can be confused with more prominent modes by the TOF misidentification $K^{\mp} \rightleftarrows \pi^{\mp}$. In the search for Cabbibo suppressed modes such as $D^o \rightarrow K^+K^-$ or $D^o \rightarrow \pi^+\pi^-$, a single interchange of K or π will yield the prominent $K^{\mp}\pi^{\pm}$ decay mode. If under this interchange the resulting diparticle combination is constrained to the beam energy, it will appear in the $D^o \rightarrow K\pi$ mass peak because its total momentum is independent of the particle mass assignments and its energy has been constrained. Experimentally the problem is the reverse of my example where dominent $K^{\mp}\pi^{\pm}$ gets turned into suppressed $K^{\mp}K^{\pm}$ or $\pi^{\mp}\pi^{\pm}$. In the final section the technique for finding such modes is discussed.

MONTE CARLO SIMULATION

To determine the detection efficiency and mass resolution for each decay mode of Table I, a Monte Carlo simulation of the Mark II is used. The simulation generates events based on a specific D decay hypothesis. The decay products are tracked through the detector generating raw data which eventually is passed through the standard tracking, vertex finding, and event identifying algorithms to generate a simulated data-summary tape. The tape is then analyzed with the same programs used to examine real data thereby determining efficiencies, resolutions and background shapes.

The detector simulation incorporates most of the features of the actual detector. The vertex position for the primary decay is given the measured beam crossing dimensions (see Chapter II). Charged particle tracking incorporates multiple scattering, energy loss (both radiation and dE/dx), muclear absorption and scattering, and decay possibilities. Drift chamber hits are thrown using an inverted form (i.e., distance-to-time) of the measured nonlinear time-to-distance relation (see Chapter II). The resolution function is also inverted and employed, as well as a single cell efficiency (96%). Additional hits in cells adjacent to a given track are added based on the position and angle of the track. The times in these adjacent cells are either correlated or random based on the particle's incidence angle and proximity to a cell boundary. The distributions were obtained from real data. This drift chamber contains the direct effect of δ-rays added at a 1% level to the Monte Carlo data.

The TOF measurement is modeled using a gaussian TOF distribution with the observed resolution for the data sample. Neutral tracks (photons) are given detection efficiencies, position resolutions and energy resolutions typical of the data sample. Photons can pair-produce in the ~.06 X_0 of material just beyond the interaction point, up to the drift chamber inner cylinder. The effect of photon conversions beyond the drift chamber is incorporated into the resolution and efficiency functions.

To find the properties of specific decay modes, the Monte Carlo was run to generate events of the type:

$$e^+e^- \to D\bar{D}$$

→ mode under study (one D)

→ general decay model, or alternate mode (other D)

The $D\bar{D}$ were produced with 1.885 GeV per particle and an angular distribution:[6]

$$\frac{dN}{d(\cos\theta)} \propto \sin^2\theta \qquad .$$

This corresponds to the production of a pair of pseudoscalars from the virtual photon in the e^+e^- annihilation. The general decay model used is a variation of a statistical isospin model.[8] The modification includes the reduction of the overall mean charged multiplicity to ~2.4, based on a previous measurement.[9] The isospin breakdown of each multiplicity is kept intact except for two body modes where $K^o\pi^{\mp}$ and $K^{\mp}\pi^{\pm}$ have been reduced by half to approximate the kaon momentum distribution observed. All the hadronic decays are thrown according to phase space. The semileptonic decays have been added as 20% of the total.[10] A matrix element for the lepton in the decays:

$$D \to K\ell\nu_\ell$$

$$D \to K^*\ell\nu_\ell$$

is included,[11] with V-A currents and the vector and axial vector form factors constant and in a ratio 1:10 for the $K^*\ell\nu$ mode. Additional non-resonant $K\pi\ell\nu$ has also been added. The breakdown of the model is shown in Figs. 10a,b. Later changes involved reduction of the high multiplicities and variation of the semileptonic branching ratios (see Chapt. VI).

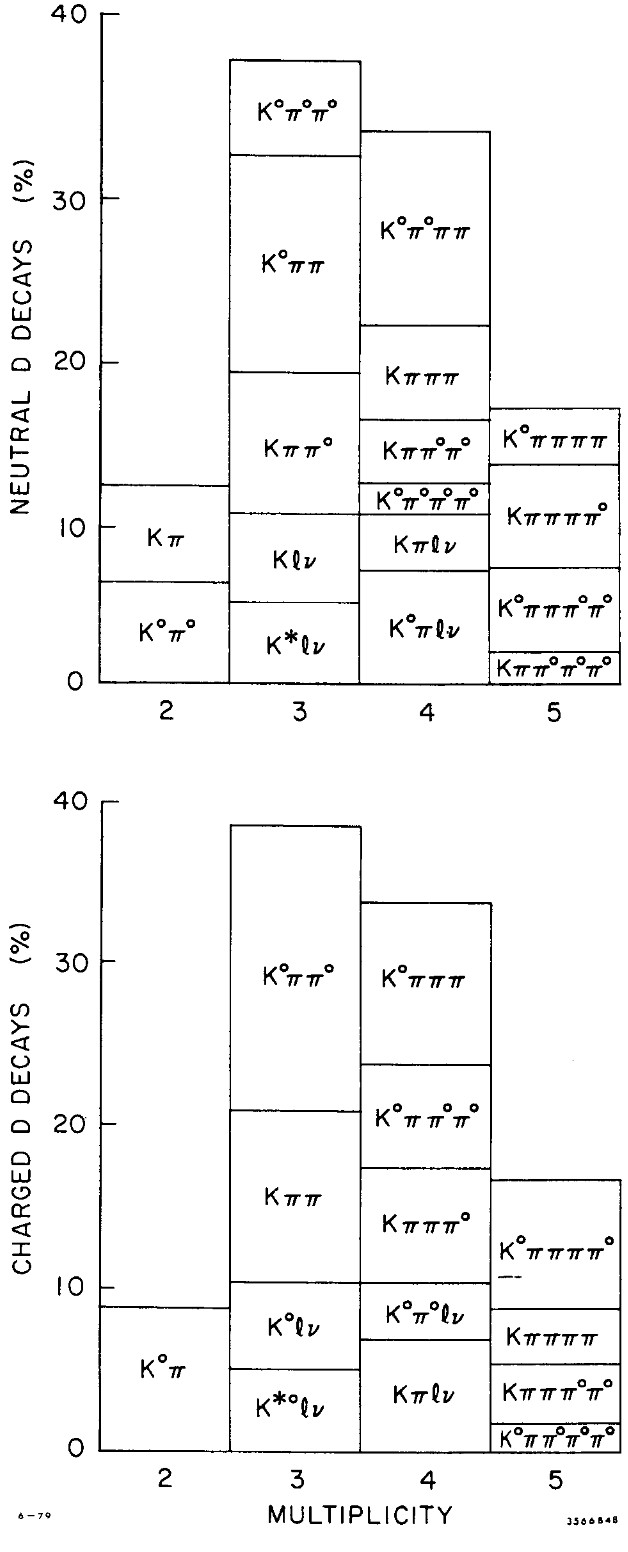

Fig. 10. Variation of statistical isospin model used to simulate neutral (a) and charged (b) D decays.

RESULTS FOR NON-SUPPRESSED DECAY MODES

Table II presents a summary of all the decay modes investigated. Corresponding mass plots (beam-constrained) for each of these modes are given in Figs. 11, 12 and 13 with the loosest cuts, to see signals. These contain D^o, D^+ charged modes, and modes involving π^o, respectively. The number of events in most plots was determined after making tighter fiducial cuts, from a maximum-likelihood fit to the data in 1 MeV/c^2 bins. A flat or sloped background extending from $\sim$1.825 to 1.878 GeV/c^2 was assumed in addition to a gaussian of expected resolution for the signal. The branching ratios contain systematic error in the cross section measurement ($\sim$20%) and Monte Carlo determined tracking efficiency ($\sim$6-10% for charged, 15% for π^o modes) as well as 25% uncertainty in the correction for nuclear interaction effects. Additional error for Monte Carlo statistics is included (typically $\lesssim$25% of the statistical error). The luminosity was taken to be 2850 nb^{-1}. The uncertainty in luminosity is already incorporated into the error on the D production cross section, while for $\sigma\cdot B$, ±5% is used. An uncertainty for background shape has been included in the errors, as well as an estimate of model dependence of the 3, 4 and 5 body efficiencies (≤5%) for vector meson contributions.

Figure 14 shows two additional modes of the $D^{\mp}$ ($K^{\pm}\pi^{\mp}\pi^{\mp}\pi^{\mp}\pi^{\pm}$ and $K^{\pm}\pi^{\mp}\pi^{\mp}\pi^{o}$) which appear at a significance of $< 2\sigma$. These have been included in Table II as well. The number of events is again determined by a fit with the added constraint of the $D^{\mp}$ mass (1868.3 Me V/c^2).

TABLE II

Cross Section x Branching Ratio and Absolute

Branching Ratios for Non-Suppressed Modes

Mode*	Signal**	ϵ	δE (MeV)	$\sigma \cdot B$ (nb)	B(%)
$K^- \pi^+$	263.0 ± 17.0	.386	50	.24 ± .02	3.00 ± 0.62
$\bar{K}^o \pi^o$	8.5 ± 3.7	.017	200	.18 ± .08	2.19 ± 1.13
$\bar{K}^o \pi^+ \pi^-$	32.0 ± 7.7	.040	50	.28 ± .08	3.51 ± 1.14
$K^- \pi^+ \pi^o$	37.2 ±10.0	.024	300	.54 ± .18	6.76 ± 2.57
$K^- \pi^+ \pi^+ \pi^-$	185.0 ± 18.0	.095	40	.68 ± .11	8.54 ± 2.09
$\bar{K}^o \pi^+$	35.7 ± 6.7	.090	60	.14 ± .03	2.32 ± 0.67
$K^- \pi^+ \pi^+$	239.0 ± 17.0	.221	40	.38 ± .05	6.32 ± 1.52
$\bar{K}^o \pi^+ \pi^o$	9.5 ± 5.5	.004	300	.93 ± .55	15.40 ± 9.80
$\bar{K}^o \pi^+ \pi^+ \pi^-$	21.0 ± 7.0	.015	30	.51 ± .18	8.40 ± 3.48
$K^- \pi^+ \pi^+ \pi^- \pi^+$	< 11.5	.021	20	≤ 0.23	≤ 4.1% (@ 90% C.L.)
$K^- \pi^+ \pi^+ \pi^o$	6.4 ± 3.9	.002	200	1.18 ± .88	20.00 ± 15.00

* Charge conjugate modes included.

** Includes uncertainty in background shape.

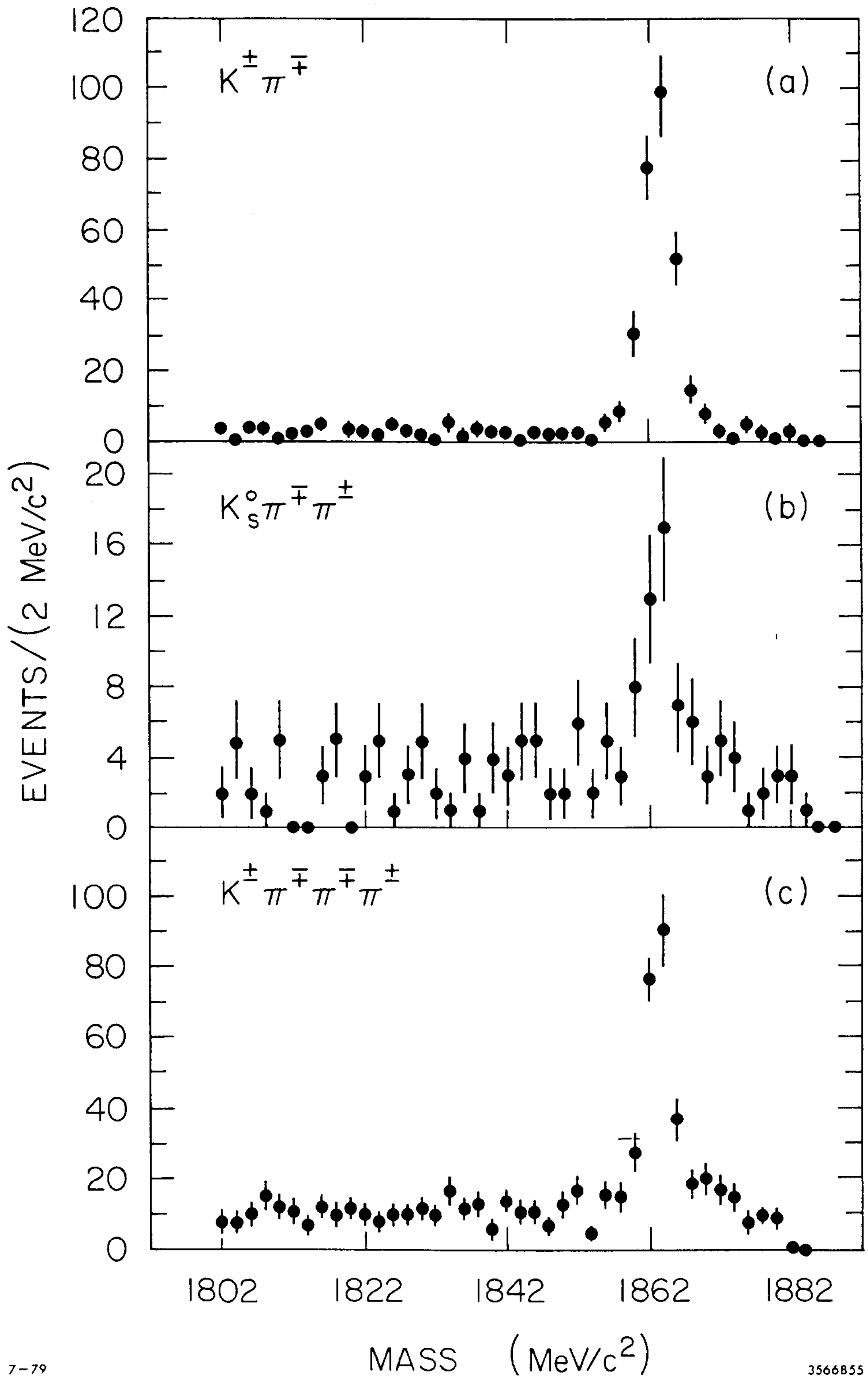

Fig. 11. Neutral D meson decays detected through all charged particles (beam-constrained).

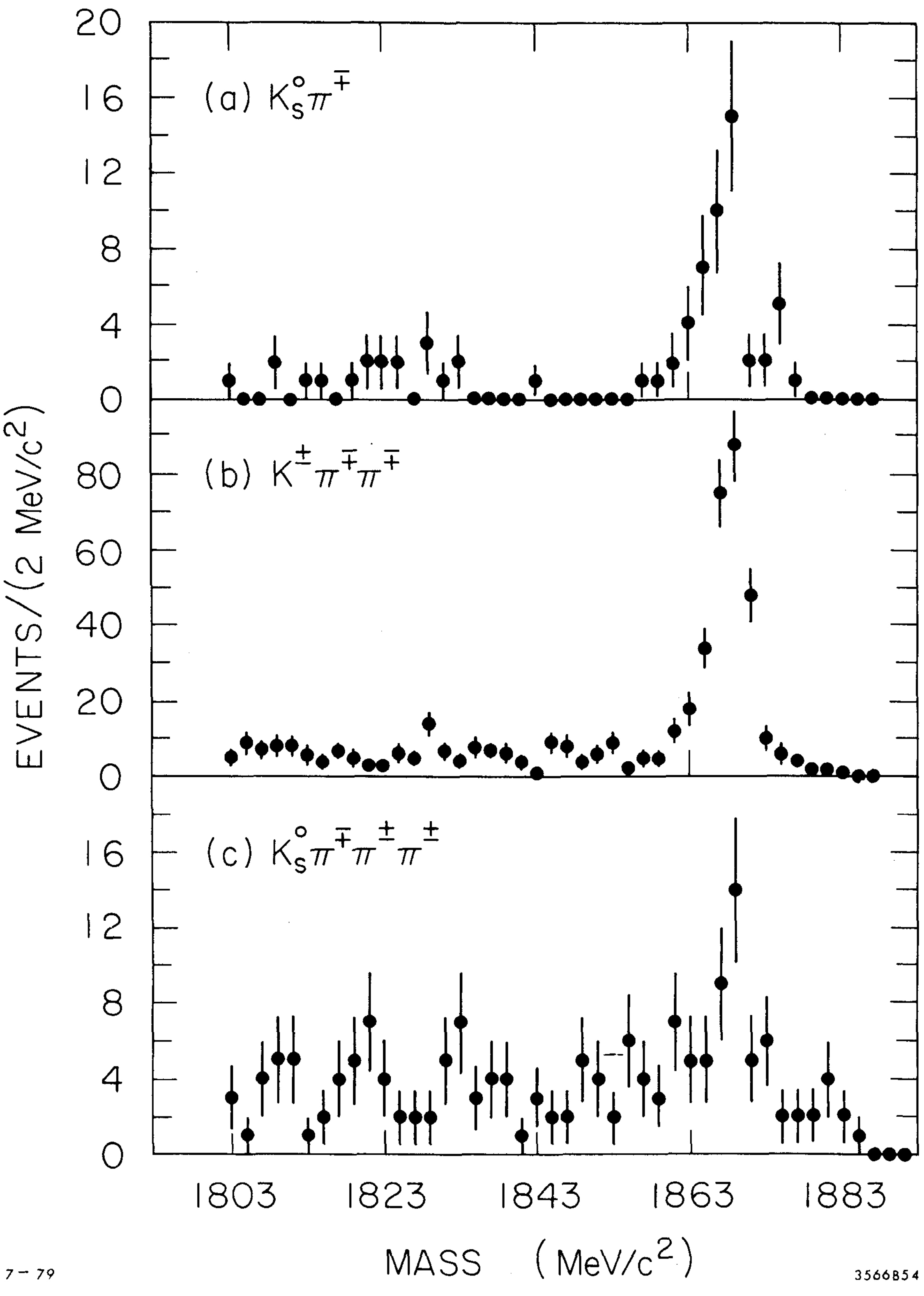

Fig. 12. Charged D meson decays detected through all charged particles (beam-constrained).

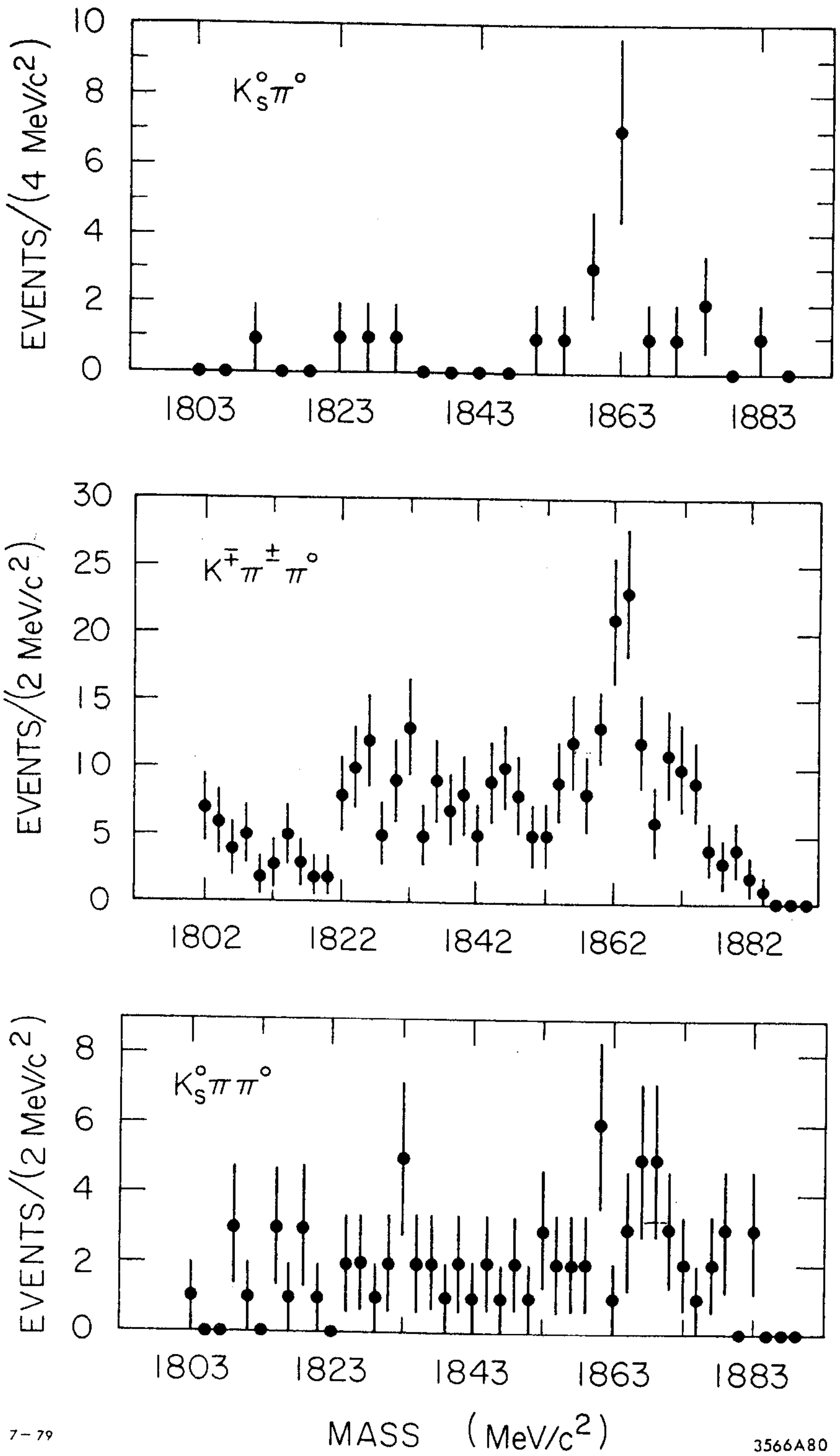

Fig. 13. D decays involving π^0 and charged particles (beam-constrained).

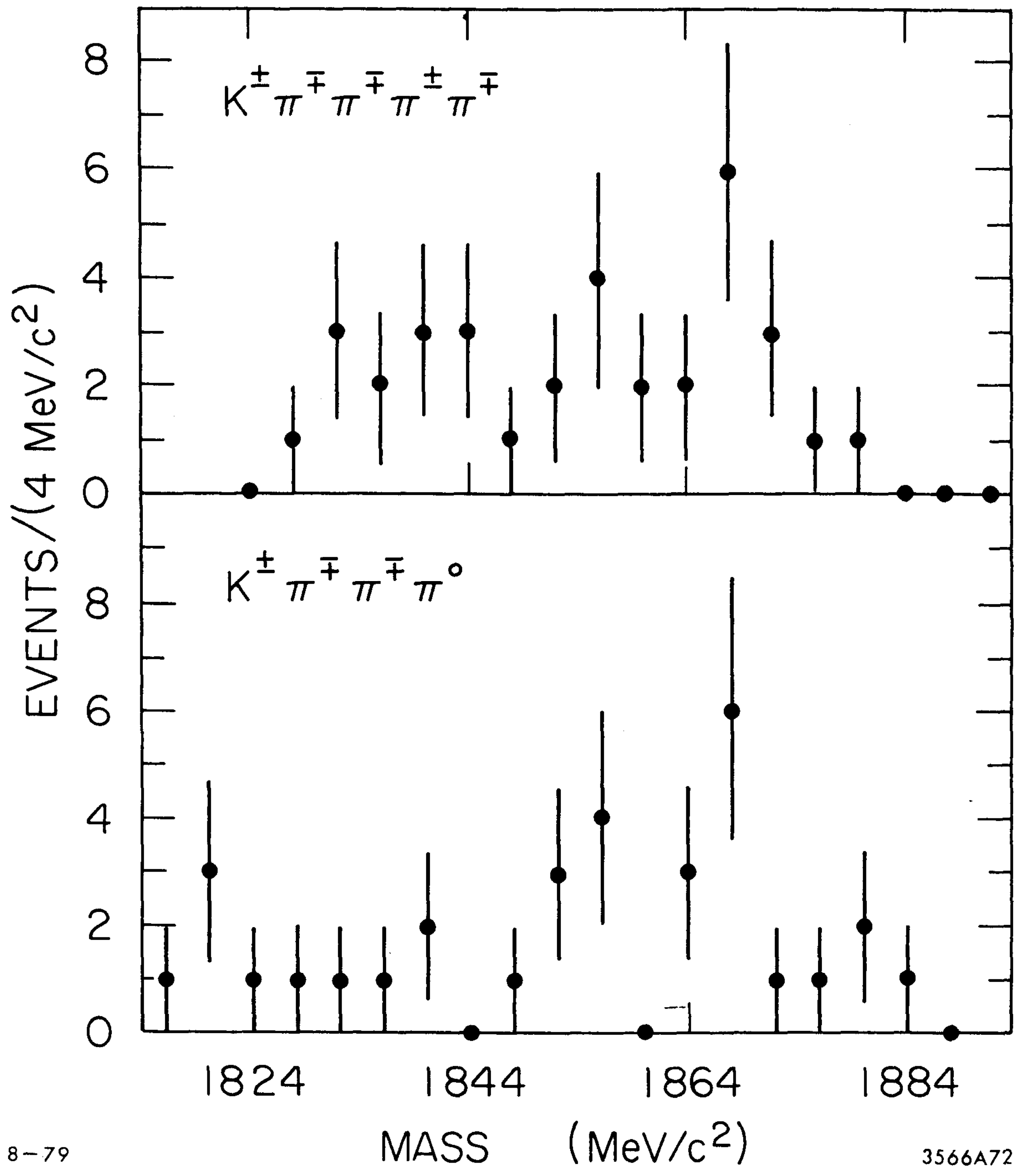

Fig. 14. Charged D decays to $K^{\pm}\pi^{\mp}\pi^{\mp}\pi^{\mp}\pi^{\pm}$ and $K^{\pm}\pi^{\mp}\pi^{\mp}\pi^{0}$ (beam-constrained).

CABIBBO SUPPRESSED DECAYS

The previous discussion of the BC technique pointed out the limitation of its use where $K \rightleftarrows \pi$ misidentification from a prominent mode is possible. The problem can be avoided by making conventional invariant mass plots, however, no gain in signal to background is achieved. This gain is essential when searching for decay modes suppressed by factors of 20, and particularly in all pion modes, where combinatorics along creates a substantial background. To recover some background rejection, the knowledge that D pair-production is taking place can be employed. Particle combinations can be required to have the correct D momentum (P_D) before being entered in a mass plot. To further reduce background, TOF information for all particles can be required. This will principally remove K's entered as π's where no TOF is available, and reduce efficiency by $\sim$15% for two-body decays with 1 or 2 pions.

The two-body combinations $\pi^{\mp}\pi^{\pm}$ and $K^{\mp}K^{\pm}$ are most readily obtained since their geometrical acceptance is large ($\sim$0.6). Figures 15a,b,c show a plot of the $K^{\mp}\pi^{\pm}\pi$, $\pi^{\mp}\pi^{\pm}$, and $K^{\mp}K^{\pm}$ mass vs. the TOF weight product (for each particle hypothesis). This weight is essentially the joint probability of identifying the $K^{\mp}\pi^{\pm}$ or $K^{\pm}K^{\mp}$ combination correctly. Prominent bands at 1743 and 1983 MeV/c^2 are $K^{\mp}\pi^{\pm}$ which, by misidentification (to $\pi^{\mp}\pi^{\pm}$ or $K^{\mp}K^{\pm}$ respectively), appear at the wrong mass. The KK events are clustered at high weights while the $\pi\pi$ events appear to be spread more uniformly. The reason is that the particles in the KK combination are distributed in momentum about 150 MeV lower than those in the $\pi\pi$ combination, and are therefore

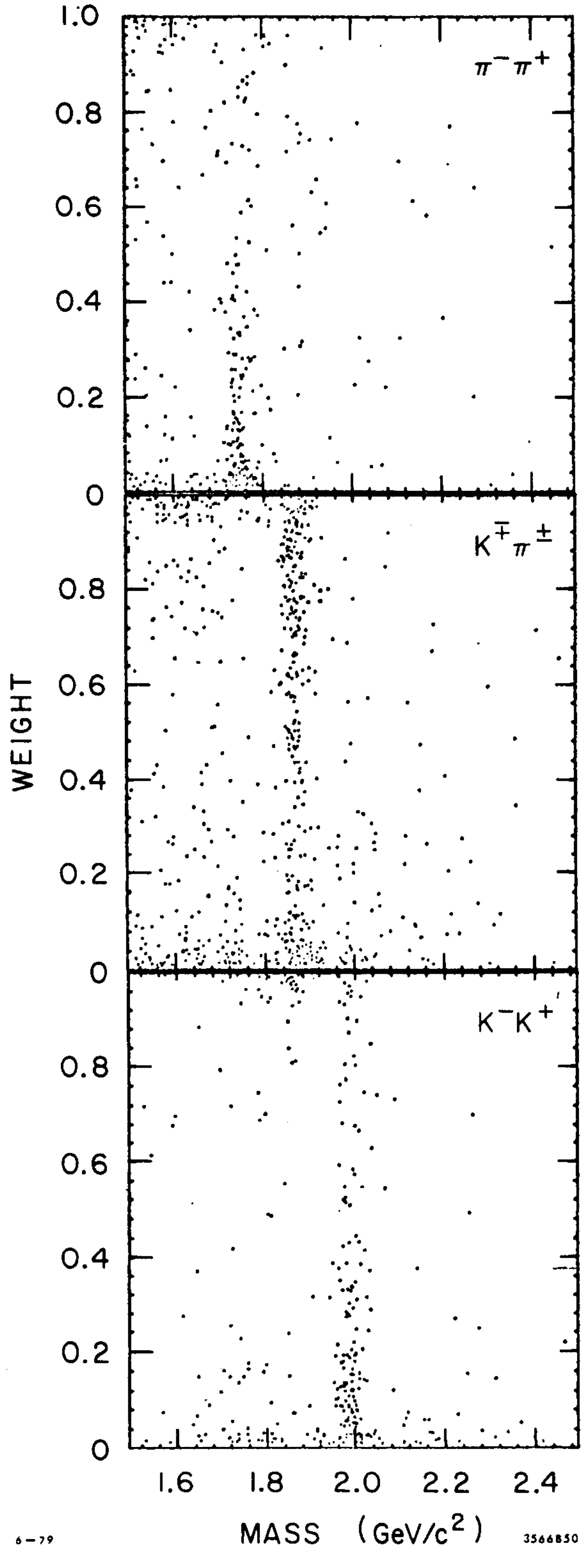

Fig. 15. Invariant mass versus TOF probability for $\pi^+\pi^-$, $K^\mp\pi^\pm$ and K^+K^- combinations.

better separated from π of the same momenta. Higher pulseheight for the slower kaons may also provide somewhat better resolution. A cut of 0.3 in joint probability (or individual P_π and $P_K < 54\%$) is chosen, leading to loss of at most 1 $\pi\pi$ event and 4 KK events between 0.05 and 0.3. The results are not sensitive to this cut.

After applying this cut on TOF, the momentum cut on P_D of the diparticle combination can be made. A D^0 with energy 1885 MeV (beam energy) should have a momentum of 288 MeV/c. The two-body decays are predominantly back-to-back, which implies a momentum error of $\sim$25 MeV/c if the D moves along the π or K direction or $\sim$5 McV/c in the same case where the D moves orthogonally to the π or K. The latter is clearly favored and an RMS error of $\sim$10 MeV/c is observed as the width of the Kπ momentum distribution (where $\sim$230 decays are seen). In Figs. 16a,b,c plots of Kπ, KK, and $\pi\pi$ invariant mass vs. Δp are shown, where $\Delta p = \left(P_D^{observed} - P_D^{expected}\right)$ McV/c. The bands are $\Delta p = \pm 30$, ± 50 and ± 110 MeV/c, yielding a signal region and two control regions, respectively. Figures 17a,b,c show mass projections of the signal regions of these plots. These projected plots distinctly show the misidentification peaks of the $K^{\mp}\pi^{\pm}$ at 1863 ± 120 McV/c^2 in the $\pi\pi$ and KK channels.

The number of events is determined by performing a maximum-likelihood fit with Poisson statistics to each of these plots. The control regions are smoothed in each plot as a function of mass (in 20 MeV/c^2 bins) to determine the background shape. That these control regions adequately describe the background in the signal region can only be tested by looking in the mass region of the signal band where

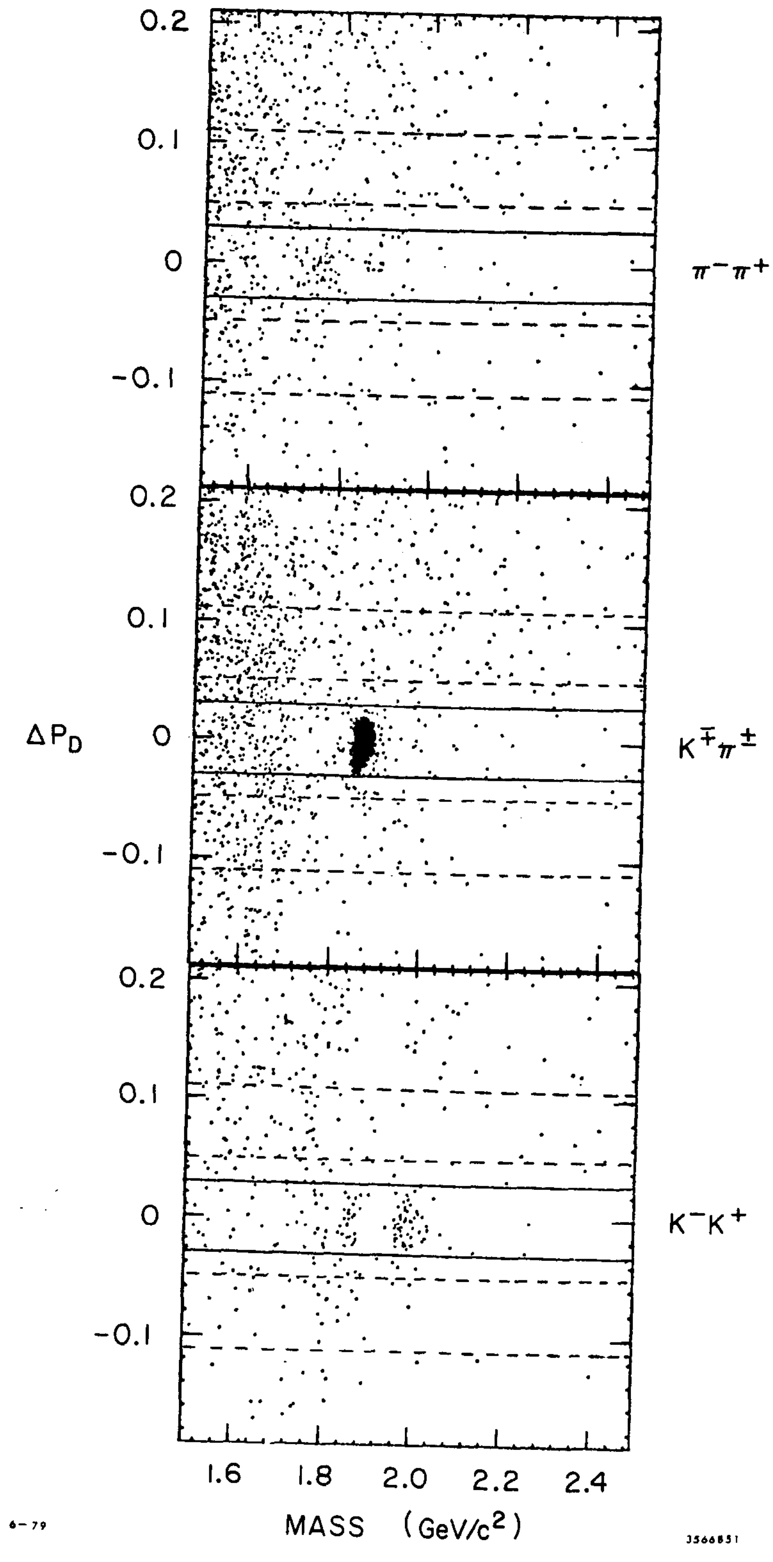

Fig. 16. Invariant mass versus (expected-observed) momentum for $\pi^+\pi^-$, $K^\pm\pi^\mp$ and K^+K^- combinations.

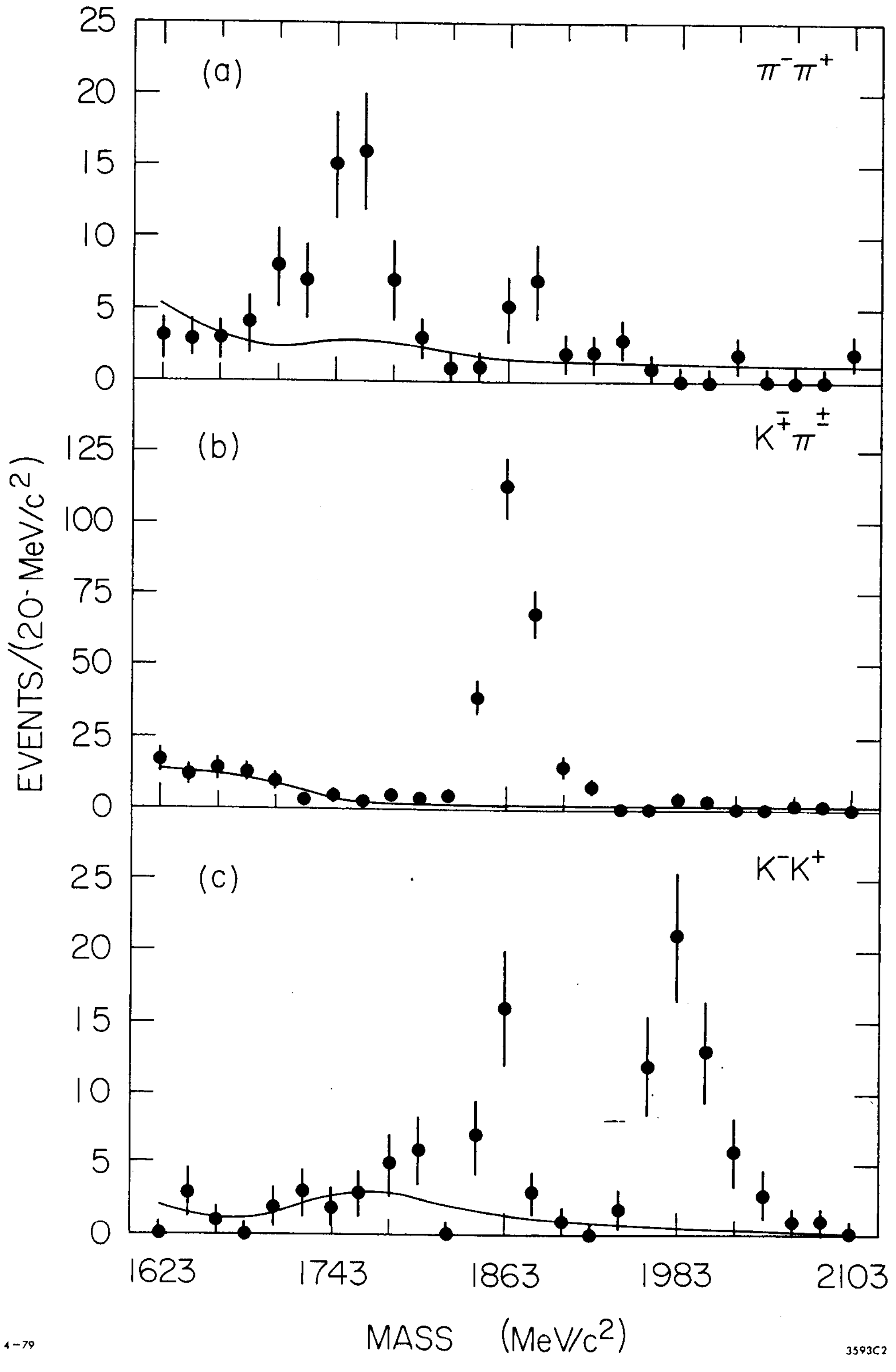

Fig. 17. Projections onto the invariant mass axes for $\Delta P_D = \pm$ 30 MeV/c. Curves are fitted background from sidebands in ΔP_D.

there is neither signal nor misidentification. In both KK and $K\pi$ plots the number of background events expected is within 1σ of the number found. In the $\pi\pi$ case, the number expected is $\sim 2\sigma$ lower. The background was entered into the fit as a single bin giving an expected number of events, with the sidebands determining the observed number. The signal and misidentification peaks were parametrized using the shape derived from seven 20 MeV/c^2 bins around 1863 MeV/c^2 in the $K^{\pm}\pi^{\mp}$ plot, after background subtraction. These were normalized to unity and entered with a single multiplier at the signal and misidentification positions of each plot. Thus, three independent parameters characterized each fit: the magnitude of the background, the signal, and the misidentification peaks. The results of the fit are given in Table III with statistical errors.

TABLE III

D^o Cabibbo Suppressed Modes

Mode	# Events	Relative Detection Efficiency	Corrected # Events
$K^{\pm}\pi^{\mp}$	234.5 ± 15.8	1.00	234.5 ± 15.8
$\pi^{\mp}\pi^{\pm}$	9.3 ± 3.9	1.19	7.8 ± 3.3
$K^{\pm}K^{\mp}$	22.1 ± 5.2	0.84	26.3 ± 6.2

These errors are determined by observing the nearly gaussian shape of the likelihood function (in the single variable N_s = number of signal events), and taking:

$$\sigma_{N_S} = \left\{ \frac{\partial^2 \omega}{\partial N_S^2} \right\}^{-\frac{1}{2}}$$

Here ω is the negative log-likelihood function.[12] The error associated with the assumption of signal shape is equal to about 4%. The background assumption where it could be checked, was accurate to 15%, which corresponds to an error of 9% in the $\pi\pi$ and 3% in the KK determinations. Finally, while the fit reflects the overall error in the magnitude of the backgrounds, local fluctuations could amount to as much as 25% (of the background) in the signal region. For $\pi\pi$ and KK this contributes an uncertainty of 14% and 5%, respectively.

The Monte Carlo described in the previous section is used to calculate the detection efficiencies given in Table III. The different efficiencies arise principally from in-flight kaon decays which result in either a momentum or TOF error. The statistical error in the efficiency is ±6%. The estimated systematic error from the Monte Carlo is 25% of the correction or ±4% of the signal.

The combined systematic errors are 19% and 10% for $\pi\pi$ and KK respectively. When added in quadrature with the statistical errors the ratio of partial widths obtained is:

$$\Gamma(\pi^+\pi^-)/\Gamma(K^+\pi^-) = 0.033 \pm 0.015$$

$$\Gamma(K^+K^-)/\Gamma(K^+\pi^-) = 0.113 \pm 0.030$$

The momentum of the particles in $\pi\pi$, $K\pi$, KK are 921, 864 and 789 MeV/c, respectively. This implies a phase-space reduction of KK by 8.7% and a $\pi\pi$ enhancement of 6.6% relative to $K\pi$.

Two other two-body channels $D^+ \to \pi^+\pi^0$ and $\bar{K}^0_S K^+$ can also be examined. In the case of $K^0_S K^\mp$, the BC technique cannot be used because of the presence of the $K^0_S\pi^\mp$ decay. The $\pi^\mp\pi^0$ mode is unique however because the only channel which it can be confused with is

$K^{\mp}\pi^{0}$. This latter is a $\Delta C = -\Delta S$, twice Cabibbo suppressed decay. Therefore, for $\pi^{\mp}\pi^{0}$ the BC technique can be used. Figures 18 and 19 show the $\pi^{\mp}\pi^{0}$ mass plot, and the $K^{0}K^{\mp}$ and $K^{0}\pi^{\mp}$ plots. For $\pi\pi^{0}$, a maximum likelihood fit is performed in 1 MeV/c^2 bins assuming a flat or sloped background plus a gaussian of fixed width ($\sigma \approx 2.2$ MeV/c^2) and mass (1868.3 MeV/c^2). The $K^{0}K^{\mp}$, $K^{0}\pi^{\mp}$ system is analyzed by the same technique as the $\pi^{+}\pi^{-}$, $K^{+}K^{-}$ system. A 0.20 weight is required for the $K^{\mp}$ and $\pi^{\mp}$. Raising this cut to 0.40 changes the net signal by no more than 1 event. Table IV summarizes the results. The values in the last column contain estimates of relative and statistical errors. The statistics are low because of detection efficiency, however, the same trend of larger $K\bar{K}$ rates is apparent in the D system as in the D^{0} system.

TABLE IV

$D^{\mp}$ Cabibbo Suppressed Modes

Mode	# Events	Relative Detection Efficiency	Corrected # Events	Branching Ratio Relative to $K^{0}\pi$
$\pi^{\mp}\pi^{0}$	< 7.5 @ 90% C.L.	1.03	< 80	< 0.30
$K^{0}K^{\mp}$	5.62 ± 3.03	0.71	87	0.25 ± 0.15
$K^{0}\pi^{\mp}$	31.50 ± 5.83	1.00	346	1.00

The search for three and four-body Cabibbo suppressed decay modes is considerably more difficult because of the large combinatorial background. The problem of feed-down from non-suppressed modes also exists. Three modes have been examined; $\pi^{+}\pi^{-}\pi^{+}$, $\pi^{+}\pi^{+}\pi^{-}\pi^{-}$, $K^{\mp}K^{\pm}\pi^{\mp}$.

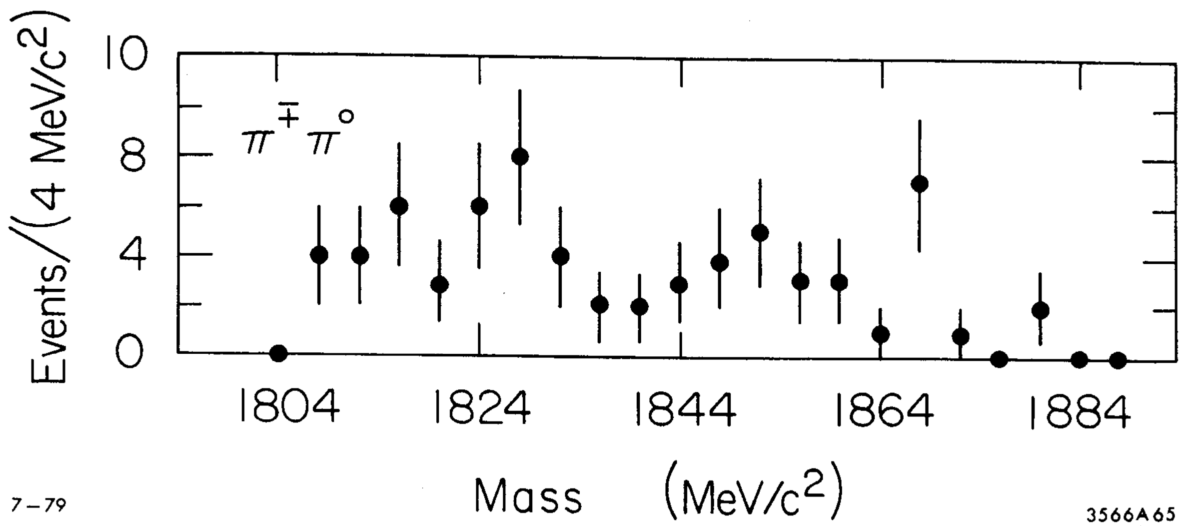

Fig. 18. $\pi^{\mp}\pi^{0}$ beam-constrained mass.

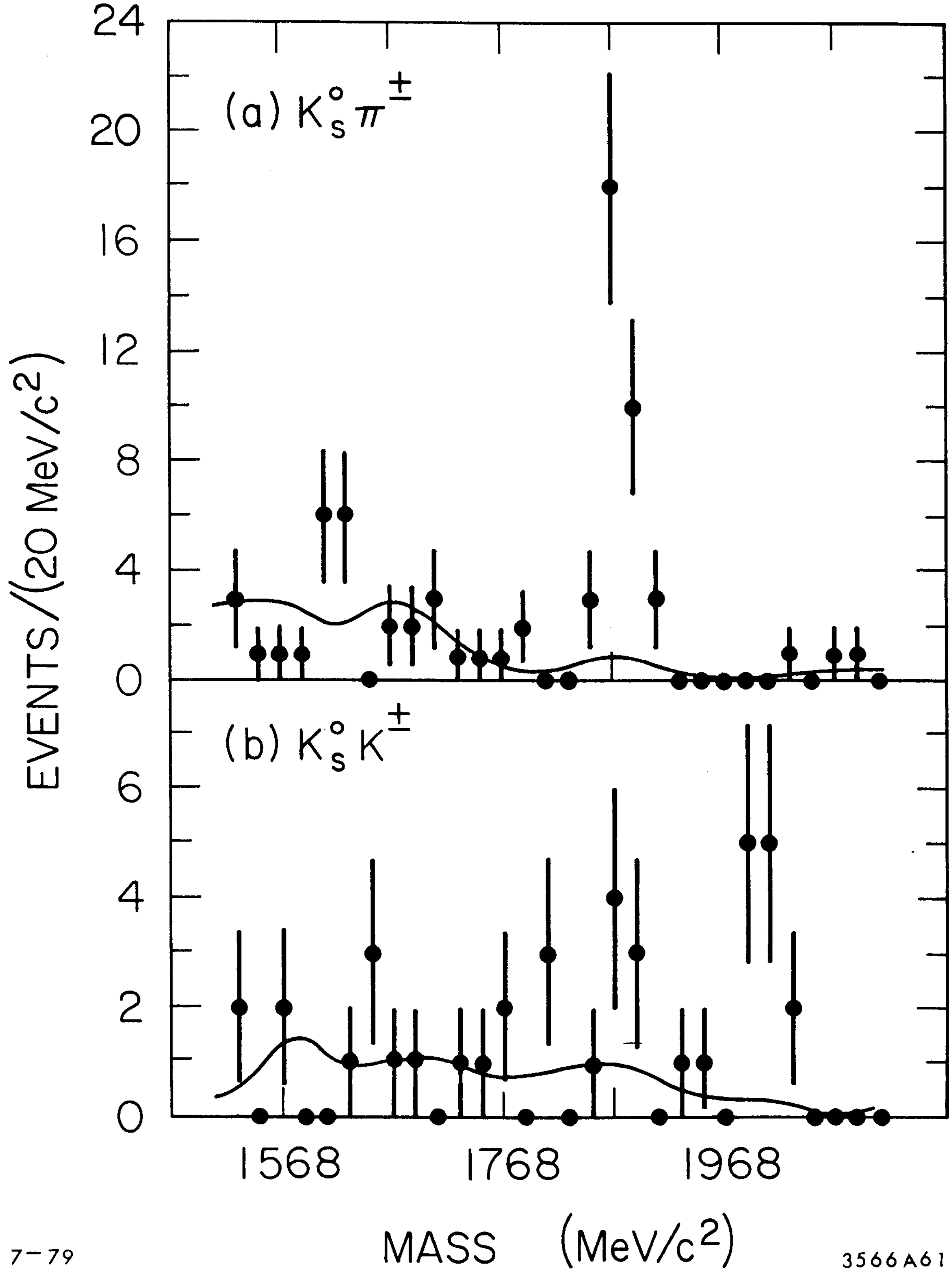

Fig. 19. $K_S^o\pi^\mp$ and $K_S^oK^\pm$ mass projections, for $\Delta P_D = \pm$ 30 MeV/c.

Figures 20, 21, and 22 show BC plots as well as plots requiring $|\delta P_D| \leq 30$ MeV/c. All particles are assigned a single hypothesis by the usual technique, rather than weighting them. The all-pion modes are always plotted requiring no $\pi^+\pi^-$ combination to lie within ±40 MeV/c^2 of the K^o_s mass. This eliminates the $K^o_s\pi^\mp$ and $K^o_s\pi^\pm\pi^\mp$ non-suppressed background. We are then left with the problem of $K^\mp \leftrightarrows \pi^\pm$. In the three and four pion modes, time-of-flight is additionally required on all tracks. In $K^\mp K^\pm\pi^\pm$, the $K^\mp$ had to hit time-of-flight counters, but the $\pi^\mp$ did not. This is sufficient since we are only concerned with $\pi^\mp \to K^\mp$ misidentification. The feed-down from the non-suppressed modes is estimated by Monte Carlo and summarized in Table V. Column 3 is the fraction of observed events of the non-suppressed type, which can end up in the suppressed mode plot.

TABLE V

Estimates for Feed-Down from Non-Suppressed Modes

Non-Suppressed Mode Produced	Suppressed Mode Detected	Feed-down Fraction
$K^-\pi^+\pi^+$	$\pi^+\pi^-\pi^+$	.024
$K^-\pi^+\pi^+\pi^-$	$\pi^-\pi^-\pi^+\pi^+$	< .003
$K^-\pi^+\pi^+$	$K^-K^+\pi^+$	< .002

Table VI summarizes the results for these decay modes with limits set on each branching ratio relative to $K^\pm\pi^\mp\pi^\mp$ and $K^\pm\pi^\mp\pi^\mp\pi^\pm$, respectively, including statistical and systematic errors.

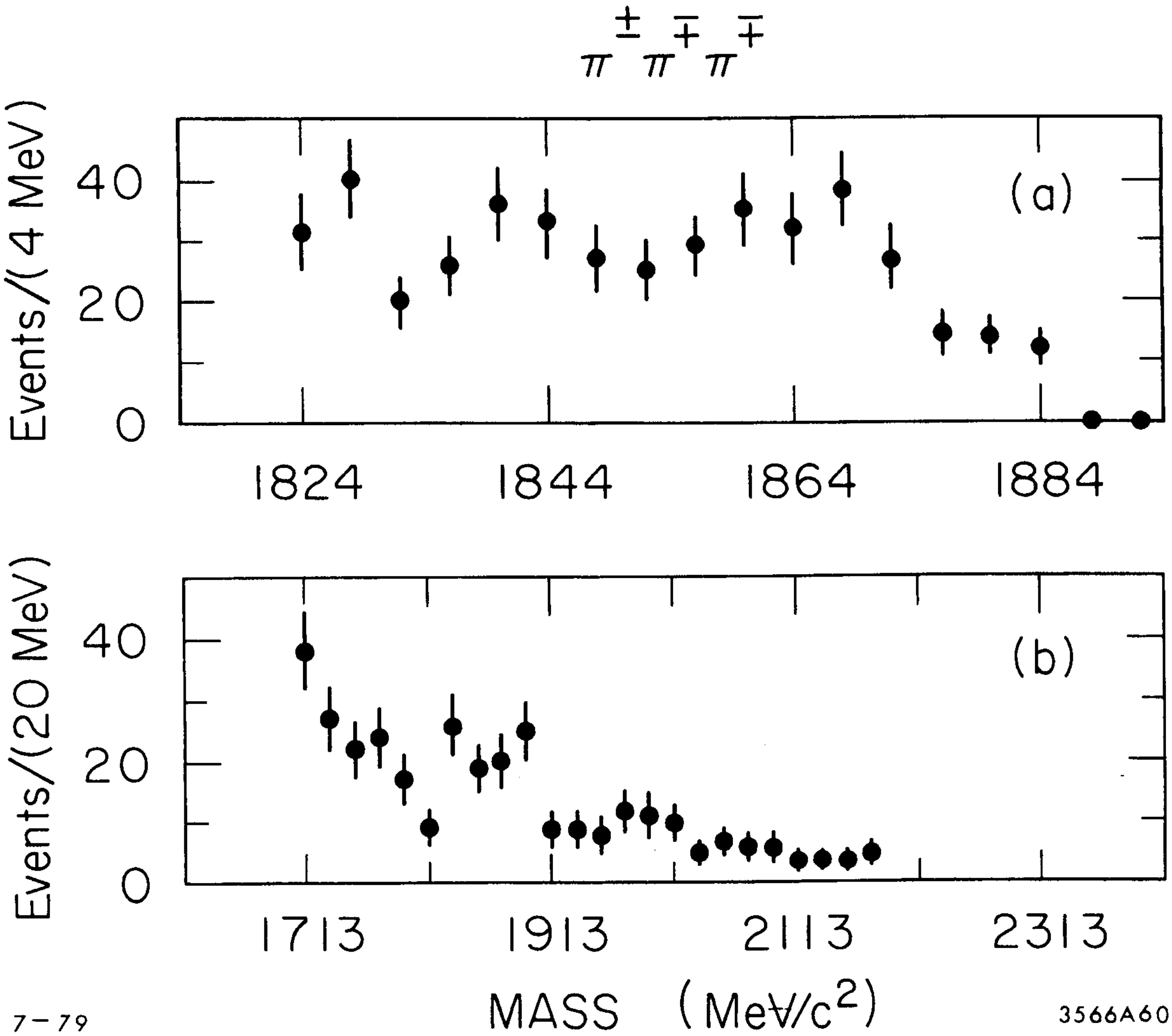

Fig. 20. $\pi^{\mp}\pi^{\pm}\pi^{\pm}$ (a) beam-constrained mass, (b) invariant mass with $\Delta P_D = \pm$ 30 MeV/c.

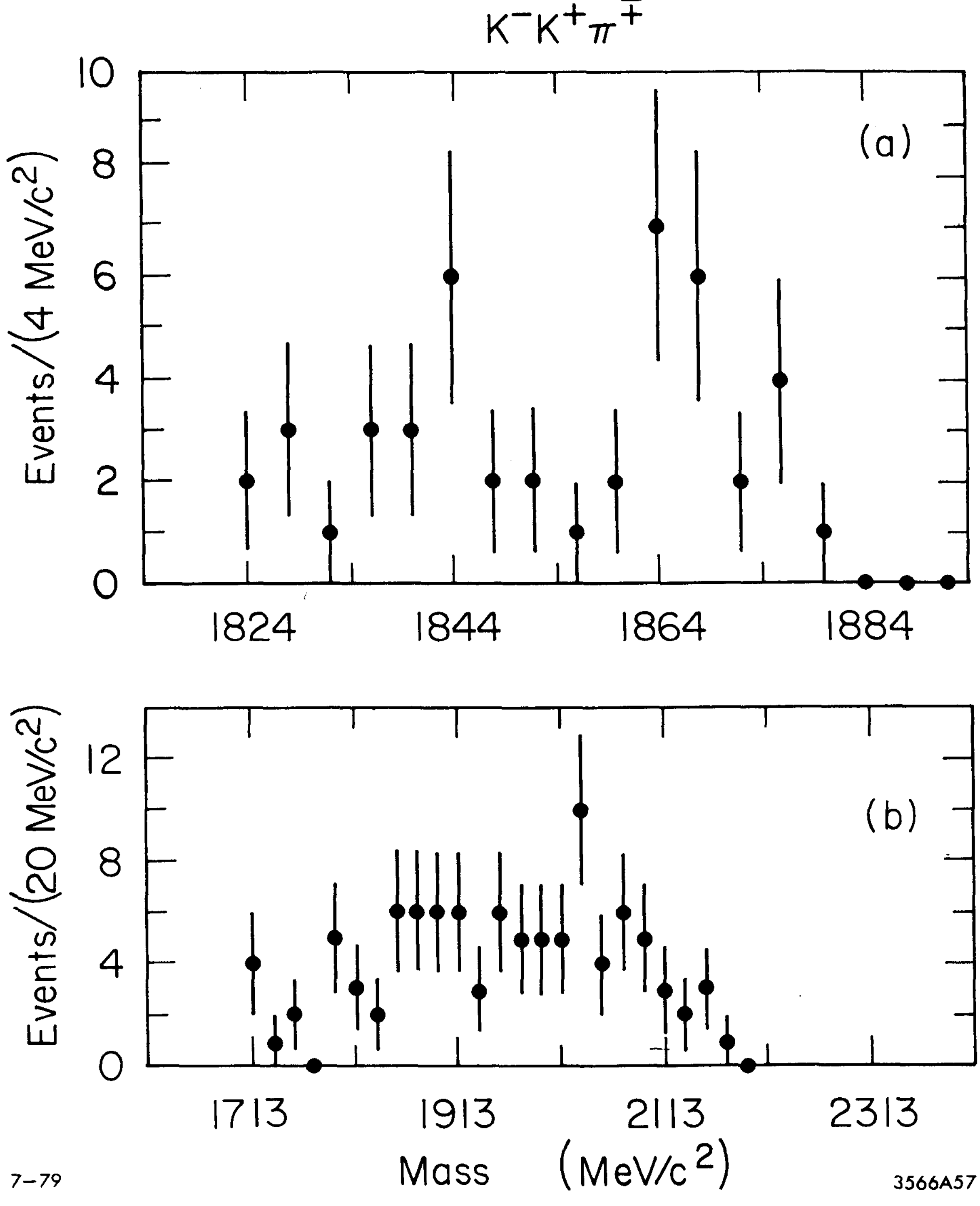

Fig. 21. $K^\pm K^\mp \pi^\mp$ (a) beam-constrained mass, (b) invariant mass with $\Delta P_D = \pm$ 30 MeV/c.

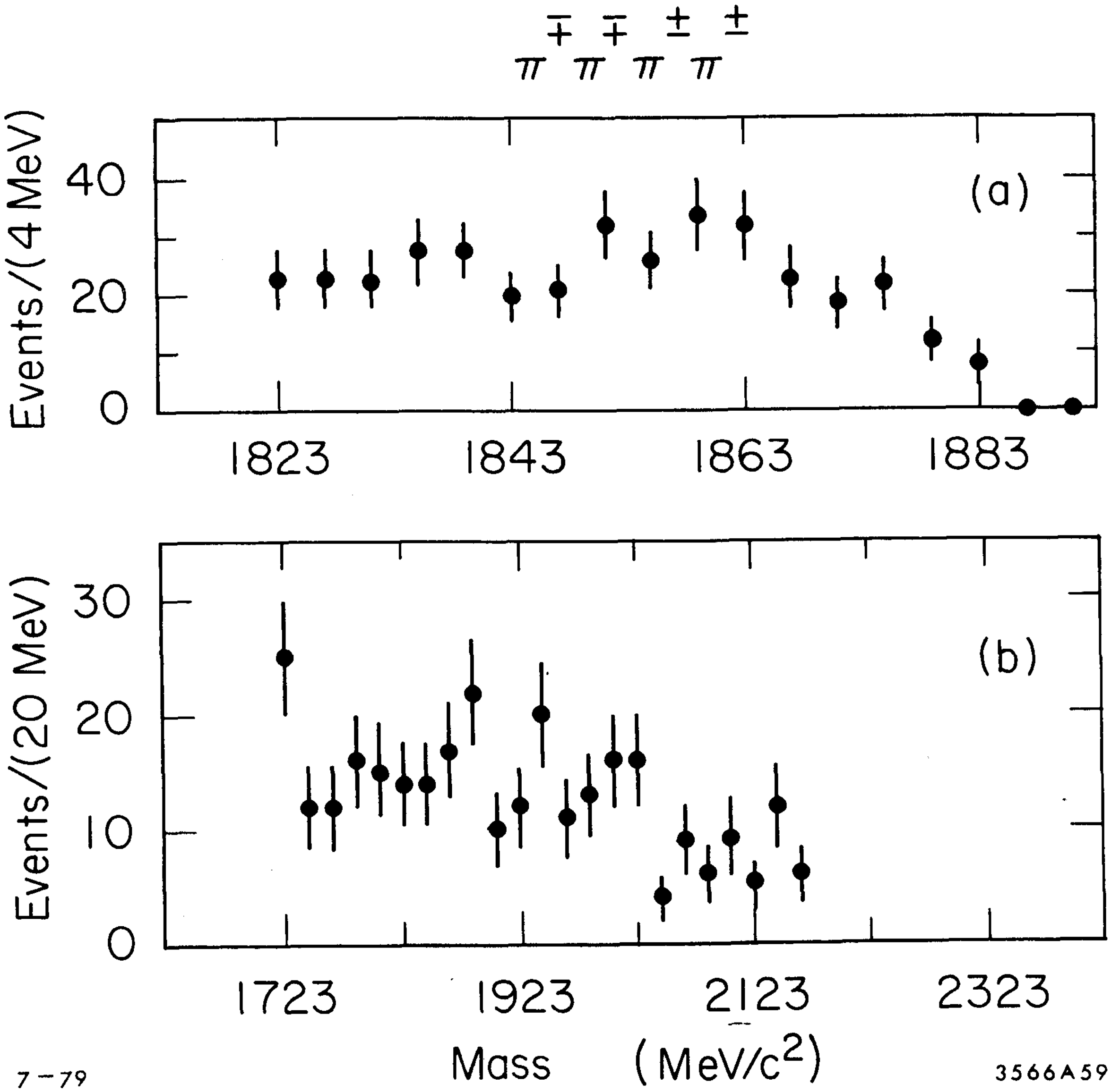

Fig. 22. $\pi^{\pm}\pi^{\pm}\pi^{\mp}\pi^{\mp}$ (a) beam-constrained mass, (b) invariant mass with $\Delta P_D = \pm$ 30 MeV/c.

TABLE VI

3- and 4-Body Suppressed Modes

Mode	Observed	Feed-down	Relative ε	Relative Br (%) (@ 90% C.L.)
$\pi^{\mp}\pi^{\pm}\pi^{\mp}$	14.4 ± 9.1	6.1 ± 1.5	1.12	< 0.084
$K^{\mp}K^{\pm}\pi^{\mp}$	8.7 ± 4.0	< 0.5	0.56	< 0.140
$\pi^{+}\pi^{-}\pi^{+}\pi^{-}$	14.1 ± 8.3	< 0.6	1.28	< 0.210

SUMMARY

The measured branching ratios for non-suppressed decays were summarized in Table II. These are compared with previous results[4,5,6] in Table VII. Reasonable agreement with most of the earlier results is observed. Large differences appear to occur only in the $K3\pi$ and $K\pi\pi^{o}$ modes, however the previous measurements had considerably large errors. In addition to these results, several new decay modes have been measured. In particular, the large solid angle for photon detection has permitted measurements of the $K^{o}\pi^{o}$ and $K^{o}\pi\pi^{o}$ modes, and provided evidence for the $K2\pi\pi^{o}$. The all charged particle decays $K^{o}3\pi$ and $K4\pi$ have also been measured.

The Cabibbo suppressed D decays into the two body channels $K\bar{K}$ and $\pi\pi$ were both previously reported[13] to have branching ratios relative to $K\pi$ of < 7% (@ 90% C.L.). These measurements were performed at higher center-of-mass energies. The $\pi\pi$ rate is consistent with the 3.3 ± 1.5% measured in this experiment. The KK upper limit however is ~1σ lower than the value of 11.3 ± 3.0% reported here. Upper limits for $Br(D^+ \to \pi^+\pi^+\pi^-)$ and $Br(D^+ \to K^+K^-\pi^+)$ were given[13] as .3% and .6% respectively. These are consistent with the values of 8.4% and 14% reported in Table VI relative to the non-suppressed decays. In Table IV, values for the two body $D^{\mp}$ Cabibbo suppressed decays were reported. The upper limit for $\pi\pi^0$ of 30% relative to $K^0\pi$ is not very stringent. The K^0K rate of 25 ± 15% is large, and may be following the trend of the $D^0 \to K\bar{K}$ rate. It is not however directly related to $K^0\pi^{\pm}$ by SU(3) as is $\pi\pi^0$ (see Chapter VII).

TABLE VII

Comparison of Branching Ratios

Mode	Br(This Experiment)%	Br(LGW)%[4,5,6]
$K^-\pi^+$	3.0 ± 0.6	2.2 ± 0.6
$\bar{K}^0\pi^0$	2.2 ± 1.1	< 6
$\bar{K}^0\pi^+$	2.3 ± 0.7	1.5 ± 0.6
$K^-\pi^+\pi^+$	6.3 ± 1.5	3.9 ± 1.0
$K^-\pi^+\pi^0$	6.8 ± 2.6	12.0 ± 6.0
$\bar{K}^0\pi^+\pi^-$	3.5 ± 1.1	4.0 ± 1.3
$K^-\pi^+\pi^+\pi^-$	8.5 ± 2.1	3.2 ± 1.1

REFERENCES

1. Glashow, S. L., Iliopoulos, J. and Maiani, L., Phys. Rev. D2, 1285 (1970).
2. Kobayashi, M. and Maskawa, K., Prog. of Theor. Phys. 49, 652 (1973).
3. See for example: Harari, H., SLAC-PUB-2234 (1978); Shrock, R. E., Breiman, S. B. and Wang, L. L., BNL Report BNL-25936 (1979); Barger, V., Long, W. F. and Pakvasa, S., University of Hawaii, Report UH-511-335-79 (1979).
4. Peruzzi, I. *et al*., Phys. Rev. Lett. 39, 1301 (1977).
5. Scharre, D. L. *et al*., Phys. Rev. Lett. 40, 74 (1978).
6. Feldman, G., SLAC Summer Institute on Particle Physics (Ed. by M. Zipf), p. 241 (1977).
7. Trower, UCRL-2426, "Range-Momentum", Vol. IV (1966).
8. Peshkin, M. and Rosner, J. L., Nucl. Phys. B122, 144 (1977); Rosner, J. L., Orbis Scientiae (1977), Coral Gables; Quigg, C. and Rosner, J. L., Phys. Rev. D17, 239 (1978).
9. Vuillemin, V. *et al*., Phys. Rev. Lett. 41, 1149 (1977).
10. Braunschweig, W. *et al*., Phys. Lett. 63B, 47 (1976); Brandelik, R. *et al*., Phys. Lett. 70B, 125 (1977); Feller, J. M. *et al*., Phys. Rev. Lett. 40, 274 (1978); Kirkby, J., DELCO, Hamburg Conference (1977), p. 3.
11. See for example: Ali, A. and Yang, T. C., Phys. Lett. 65B, 275 (1976); Jackson, J. D., Brandeis Summer Institute, 353 (1962).
12. Orear, J., UCRL-8417, 9 (1958).
13. Piccolo, M. *et al*., Phys. Lett. 70B, 260 (1977).

VI. INCLUSIVE PROPERTIES OF D MESON DECAYS

INTRODUCTION

In the previous chapter we dealt with measurements of D meson decays where all final products are observed. Detection efficiency readily consumes the channels directly observable. In this chapter the decays of D's into $K\pi$, $K2\pi$, $K3\pi$, $K^0_S\pi$ are used as tags to study the inclusive properties of decaying D's known to be recoiling off the tag. The tag allows us to distinguish D^+ and D^0 properties unlike ordinary inclusive measurements. Three quantitative measurements can be made:

$\langle n_c \rangle$ (average charge multiplicity)

$Br(D \to K^{\pm}X)$, $Br(D \to K^0X)$

$Br(D \to e\nu X)$

The first measurement provides clues to the multiplicity breakdown of D decays and allows comparison with various models predicting the distribution of charged and neutral particles and decay modes. The measurement of strangeness in the final state provides a test of the standard model of the weak interaction (see Introduction, Chapter V) where at least one strange particle (K^0 or $K^{\pm}$) per D decay is expected. Since the expected strangeness is known, a measure of the Cabibbo-suppressed decay rate is possible. The last quantity of interest is the semileptonic branching ratio for D mesons. In particular, we measure the individual $D^{\pm}$ or D^0 branching ratios, and thus obtain an estimate of the $D^{\pm}/D^0$ lifetime.[1] Here the assumption of equal leptonic partial widths $\left(\Gamma(D^{\pm} \to e\nu X) = \Gamma(D^0 \to e\nu X)\right)$ or equivalently a $\Delta I = 0$

transition, in the Hamiltonian, implies:

$$\frac{\tau^{\pm}}{\tau^{o}} \doteq \frac{\Gamma(D^{o} \to \text{all})}{\Gamma(D^{\pm} \to \text{all})} = \frac{Br(D^{\pm} \to e\nu X)}{Br(D^{o} \to e\nu X)}$$

It is only at the $\psi(3770)$ that the individual strangeness and leptonic branching ratios can be measured directly because only there is the recoil of the tagged $D^{o}(D^{\pm})$ uniquely a $\bar{D}^{o}(D^{\mp})$.[2]

Tagged events can also be used to look for new D decay modes by performing 6C and 3C fits (0 and 1 missing hadron) to each event. Additionally, a check of absolute branching ratios can be made by counting 3C and 6C fits into various directly measured decay modes. With typical branching ratios less than 10%, detection efficiencies a few percent and several hundred tags, we expect to see only a few events in any mode. Thus, statistics will be a limiting factor.

TAG SAMPLE SELECTION

The tag samples vary slightly for each analysis presented below. For multiplicity studies, D mesons decays are identified by a TOF weight cut (≥ 0.4/track) whereas other studies simply use the joint probability (P) formed of TOF weights ($P \geq 0.25$/decay). For $K\pi$, $K2\pi$ the cut in energy before the beam-constraint is applied was ± 50 MeV/c^2 whereas for $K3\pi$ and $K^{o}\pi$ it was ± 30 MeV/c^2 and ± 60 MeV/c^2, respectively. The signal region was chosen $\pm$ 6 MeV/c^2 around the D mass except in the $K3\pi$ where ± 4 MeV/c^2 was used. The tighter cuts on the $K3\pi$ tag reduce the large background and almost eliminate double counting of decays ($\lesssim 5\%$). We are left with a sample of almost 500 D^{o} and 300 $D^{\pm}$ tags.

MULTIPLICITY

The simplest measurement to perform is that of mean charge multiplicity. Tracks opposite a D tag satisfying the criteria of Chapter V are counted without attempt to identify them ($K_s^o \to \pi^+\pi^-$ are counted as two tracks when produced). An additional cut of $|\cos\theta| \leq 0.74$ is applied to insure agreement between Monte Carlo and data tracking efficiency. The observed multiplicity distribution is shown in Figure 1. The cross-hatched background distribution was obtained from tags in the mass band below the D mass (1.800 - 1.855 GeV/c^2). To obtain the produced distribution, the procedure called "unfolding" is employed. The mathematical details are given in Appendix D. The basic procedure is to numerically solve the overconstrained linear system for the vector P_j of produced events of multiplicity j:

$$\sum_{\substack{j=0 \\ \text{or } 1}}^{m} \varepsilon_{ij} P_j + b_i = D_i \quad . \qquad i = 1,n \text{ detected particles}$$

Here ε_{ij} is the probability of detecting i particles when j are produced. B_i is the observed background vector and D_i the observed multiplicity vector. The matrix ε_{ij} is determined by Monte-Carlo and differs from a pure binomial efficiency matrix (i.e., a triangular matrix determined purely from geometric acceptance), because it allows for processes which leave more charged particles in the final state than the initial state. These can arise from both physics (e.g., gamma conversions, π^o Dalitz decays, etc.), as well as tracking problems (e.g., generation of fake tracks). For the purpose of this study, the D decay model described in Chapter V is used.

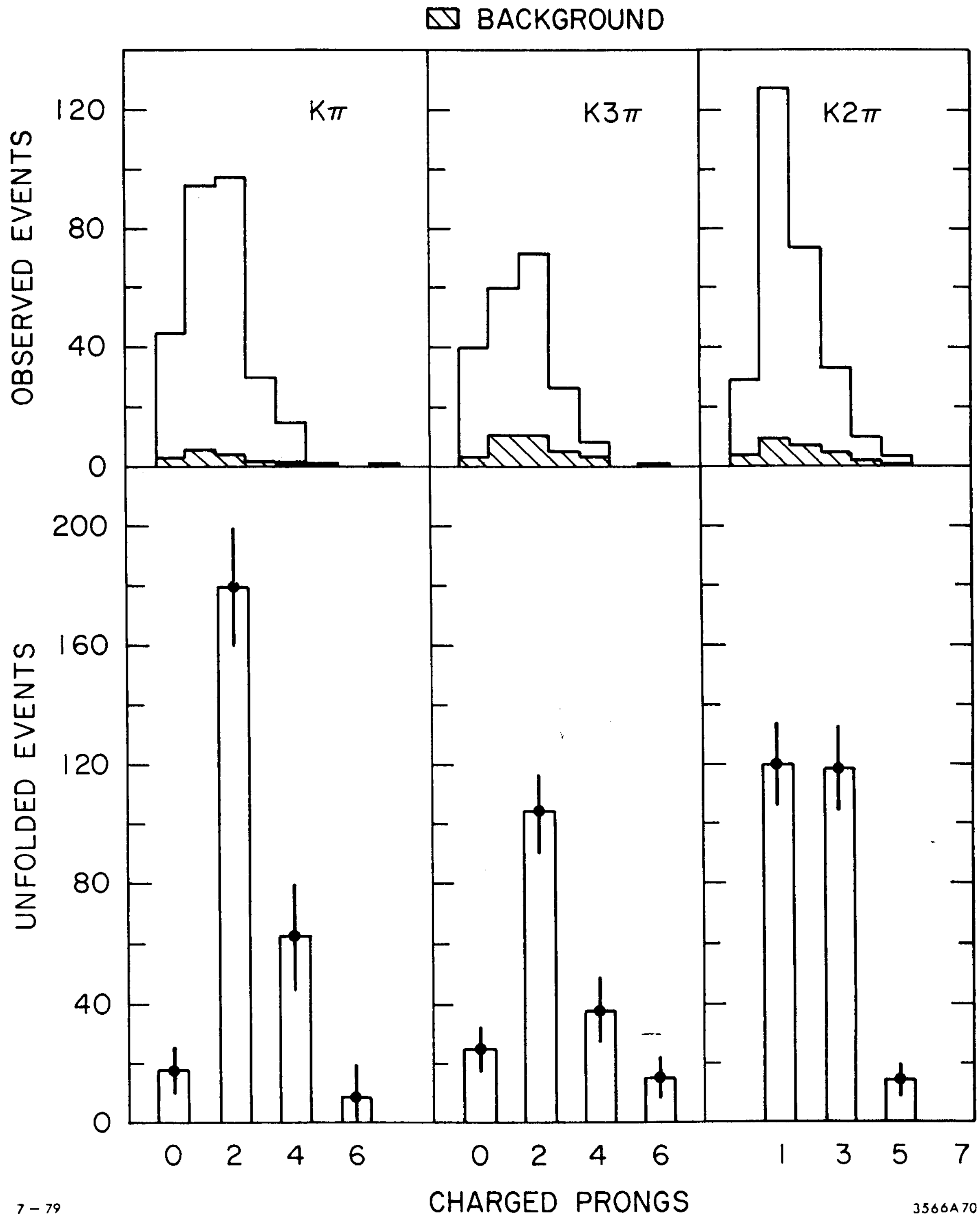

Fig. 1. Observed and unfolded multiplicity for $D^{o} \rightarrow K\pi$, $K3\pi$ and $D^{\pm} \rightarrow K2\pi$.

To estimate errors associated with model dependence, the extreme case of a binomial model is used. The effect of the background subtraction is tested by adjusting its value by its overall statistical error and repeating the unfold. The actual sensitivity to shape is hard to measure – there is no way to know how to properly redistribute the background multiplicity. Given its relatively small total contribution, the error introduced by the statistics of the background within the fit is assumed to suffice.

Table I shows the results of the unfold procedure for $K\pi$, $K2\pi$, $K3\pi$ tags. The value of $\langle n_c \rangle$ agrees remarkably well for the two D^o modes. The error associated with the $K3\pi$ measurement is larger than the other two modes principally because of overall statistics and the magnitude of the background relative to the signal. The results compare well with the previous measurement of the LGW experiment[3] yielding 2.3 ± 0.3 for $\langle n_c \rangle$ for both D^o and $D^{\pm}$.

TABLE I

Results of Multiplicity Unfolds

Tag	Number of Events	Background Events	$\langle n_c \rangle$	Statistical Error	Model Error	Background Error	Total Error
$K^{\mp}\pi^{\pm}$	283	16.7	2.46	0.12	0.08	0.05	0.15
$K^{\pm}\pi^{\mp}\pi^{\mp}\pi^{\pm}$	211	31.3	2.48	0.19	0.10	0.18	0.29
$K^{\pm}\pi^{\mp}\pi^{\mp}$	282	25.0	2.16	0.11	0.07	0.10	0.16

Table II shows the fractional breakdown of D^o and D^+ distributions ($K\pi$ and $K3\pi$ are combined). The errors here reflect only statistical

TABLE II

Unfolded Fraction by Multiplicity (%)

Multiplicity:	0	2	4	6
D^o(Mark II)	9.6 ± 2.5	63.0 ± 5.4	22.2 ± 4.7	5.2 ± 3.1
D^o(LGW) [3]	8.5 ± 3.	73 ± 10	16 ± 4.0	2.5 ± 1.5

Multiplicity:	1	3	5
$D^{\pm}$(Mark II)	47.6 ± 05.6	46.8 ± 5.6	5.6 ± 2.4
$D^{\pm}$(LGW) [3]	37 ± 10.	60 ± 12.	3.0 ± 3.0

error from the unfold procedure. Systematic errors are comparable. The agreement within multiplicities is reasonably good in both cases given previous statistics. It is interesting to note that in both $D^{\pm}$, and D^o the relatively low multiplicities appear to dominate, with $D^{\pm}$ going almost exclusively to one and three charged particle states.

Several simple models for estimating the multiplicity distributions and branching fractions for massive hadron decays are given in Ref. 4. These provide a guide to the general properties of D decays with a minimum of dynamical assumptions. To derive nonleptonic branching ratios these models must generate both a multiplicity distribution and a means of determining the breakdown of each multiplicity into specific charge states.

Multiplicity distributions are determined either through thermodynamic agruments (the statistical model), or through the assumption that matrix elements for successive pion emission are simply related by a single constant. The latter is called the Constant Matrix Element (CME) model, which in general produces a narrower multiplicity distribution ($\langle n \rangle \approx 3.4$) than the statistical model ($\langle n \rangle \approx 4.3$).

Within each multiplicity, the breakdown into specific charge states is performed using only the constraint of isospin. The D^+ decays to a unique 3/2 isospin state, while the D^o can decay to either a 1/2 or 3/2 state. If the weak-hadronic decays obey the $\Delta I = 1$ $|\Delta I_3| = 1$ relation, then specific predictions can be made concerning bounds in the breakdown of charge states within each multiplicity. Since the number of invariant isospin amplitudes increases rapidly with multiplicity, the charge state fractions are calculated with the statistical postulate wherein each isospin amplitude is treated equally and added incoherently in each decay. For the D^o, a statistical average of $I = 3/2$ and $I = 1/2$ amplitudes is taken (i.e., the resulting fraction is the value calculated for $I = 3/2$ and $I = 1/2$ separately, weighted by the number for individual amplitudes). In each case, the statistical value should lie between any bounds derived otherwise. In general, good agreement with experiment is only expected for large multiplicity decays.[4] For the statistical-isospin model, the mean charged particle multiplicity ($\langle n_c \rangle$) is found to be 3.0 for D^o decays and 3.1 for $D^{\pm}$ decays. The CME (Constant Matrix Element) model for multiplicities, in conjunction with the statistical hypothesis yields $\langle n_c \rangle$ for D^o and $D^{\pm}$ of 2.4 and 2.5 respectively, considerably closer to the measured values. It must be pointed out that the semileptonic decays are present in our measurement and could significantly reduce $\langle n_c \rangle$. It is likely that this could be a very large effect if the multiplicities were found to be low, (i.e., $K\ell\nu$ the dominant decay) and the branching ratios themselves found to be large in the $D^{\pm}$. This point will be discussed further in the sections on semileptonic decays.

STRANGENESS

In this section a measurement of the strange particle content of D^{0} and $D^{\pm}$ decays is presented. In each case the strangeness of the tag predicts the strangeness of the recoil system under the usual weak interaction ($c \rightarrow s$) current. The observation of particles of incorrect strangeness provides evidence for Cabibbo suppressed decays, or in the D^{0} case, mixing of D^{0} and $\bar{D}^{0}$.[5]

Charged particles recoiling off the tagged D are identified by TOF using the procedure described in Chapter V. Pions from 0.6-1.1 GeV/c momentum are misidentified as kaons in D decays at a 1-14% rate dependent on momentum. Since most pions are indeed well below 1 GeV/c, the correction is small and can be made by folding the observed pion spectrum opposite a tag, with the misidentification probability determined by Monte Carlo. The correction is made separately by charge relative to the strangeness of the tag.

The $K\pi$ tag has a unique problem in that it is possible to interchange π and K identification while still detecting the D. This is found to occur at a rate of $\sim 3.3 \pm 1.3\%$ by Monte Carlo calculation. A correction is applied on the final counting.

The tag sample contains a small fraction of background events. The effect of the background is estimated by the use of the lower mass range from 1.800-1.855 GeV/c^2. As will be seen, the background events tend to conserve strangeness very well.

Kaon detection efficiency is determined by Monte Carlo using the D decay models similar to those described in the previous chapter. Charged kaons are lost predominantly through their in-flight decay and the resulting error in momentum and TOF. It is only in the case of the D^0 that we have sufficient statistics to examine the production model. Figure 2 shows a typical D^0 model which reproduces the observed distribution of $K^{\pm}$ well. Various models were examined, varying multiplicity to give a reasonable match to $\langle n_c \rangle$, the K^0:$K^{\pm}$ fractions, and the $\pi^{\pm}$ spectra opposite the tags. The variation of $K^{\pm}$ efficiency was found not to be strongly sensitive to multiplicity, with overall variations in efficiency of less than $\sim$10% of the correction.

The results for charged kaon content are presented in Table III. The corrections in each case are explicitly shown. The final numbers contain systematic error for model dependence of the efficiency.

Natural kaons are searched for in tagged events as well. The detection efficiency is also determined by Monte Carlo calculation. Two backgrounds for K_s appear. The first is the non-resonant production under the D tag (i.e., fake tags). The second background is from erroneous K_s reconstruction. Here the estimate is made by Monte Carlo since the proper charge correlations and multiplicities are important. In addition to the statistical error, this correction introduces a large uncertainty.

The results are summarized in Table IV for neutral kaons divided among the tags. No breakdown by suppressed and non-suppressed decays is possible, for the neutral kaons.

In Table V, I have summarized the results of this analysis and those of Reference 3, combining the two tag channels each for the D^0 and $D^{\pm}$. The results presented in Table V are in reasonable agreement with the previous measurements shown. The improvement in statistics (and, in part systematic error) allows for several interesting observations.

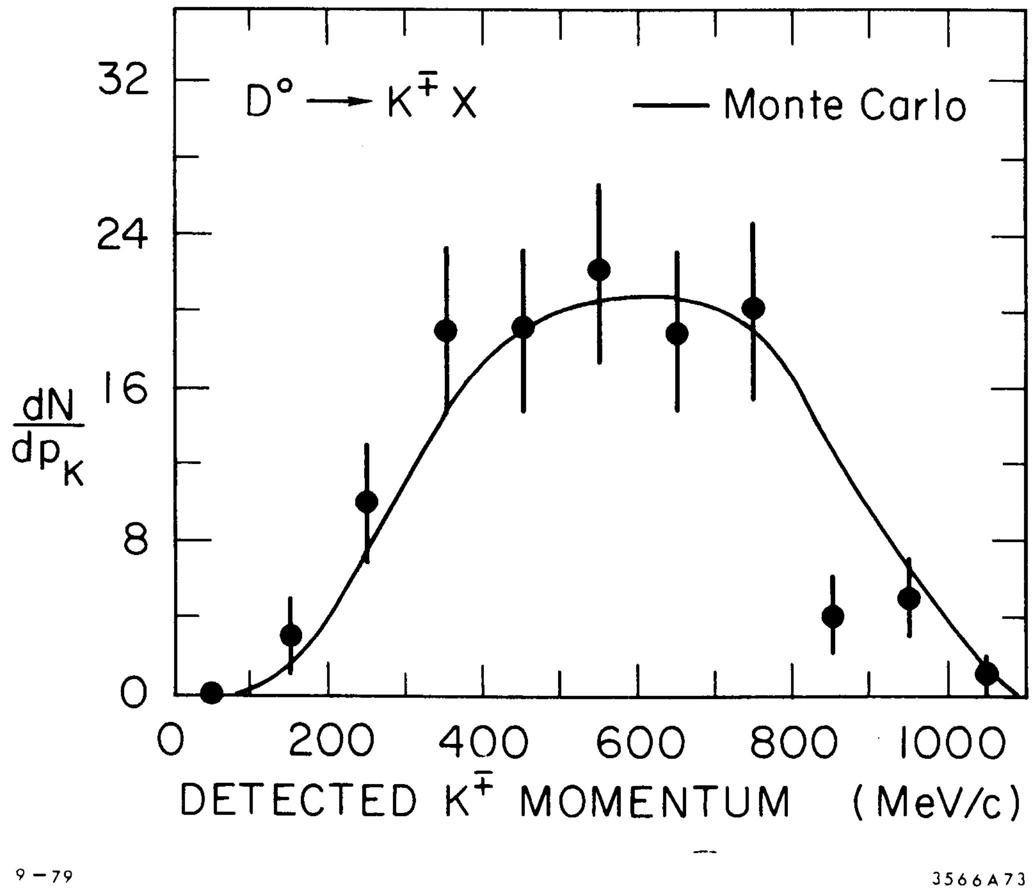

Fig. 2. Observed $K^{\pm}$ momentum distribution from D^0 decays. The curve is a Monte-Carlo D production model.

TABLE III

Charged Kaon Content

Tag Mode	Nonsuppressed		Suppressed	
	$K\pi$	$K3\pi$	$K\pi$	$K3\pi$
Tags	324.0	217.0	324.0	217.0
Background	22.0	37.6	22.0	37.6
Net Tags	302. ± 18.0	179.0 ± 14.7	302. ± 18.0	179.4 ± 14.7
Observed $K^{\pm}$	72.	49.	16.	9.
Hadron Mis. Id.	−0.70 ± 0.35	−0.15 ± 0.15	−2.30 ± 1.15	−1.66 ± 0.83
$\pi K \rightleftarrows \pi K$	+2.9 ± 1.14	----	−2.90 ± 1.14	----
Background Events	−1.82 ± 0.60	−4.66 ± 0.85	−0.81 ± 0.40	−0.80 ± 0.36
Net Kaons	72.4 ± 8.6	44.2 ± 7.1	10.0 ± 4.3	6.5 ± 3.1
Efficiency*	.440 ± .023	.440 ± .023	.440 ± .023	.440 ± .023
Produced $K^{\pm}$	166. ± 22.	101. ± 17.	22.9 ± 10.	15.0 ± 7.2
Branching Ratio (%)	55. ± 7.8	57. ± 11.	7.6 ± 3.3	8.4 ± 4.1

Tag Mode	Nonsuppressed		Suppressed	
	$K2\pi$	$K^{o}\pi$	$K2\pi$	$K^{o}\pi$
Tags	297.0	40.0	297.0	40.0
Background	31.8	3.0	31.8	3.0
Net Tags	265 ± 17.2	37.0 ± 6.30	265 ± 17.2	37.0 ± 6.30
Observed $K^{\pm}$	23.	3.	11.	1.
Hadron Mis. Id.	−0.26 ± 0.13	−0.02 ± 0.17	−2.35 ± 1.15	−0.51 ± 0.25
$\pi K \rightleftarrows \pi K$	----	----	----	----
Background Events	−2.32 ± 0.55	−0.79 ± 0.36	−1.93 ± 0.50	0. ± .16
Net Kaons	20.4 ± 4.8	2.2 ± 1.8	6.7 ± 3.6	0.49 ± 1.04
Efficiency*	.395 ± .022	.395 ± .022	.395 ± .022	.395 ± .022
Produced $K^{\pm}$	51.7 ± 12.	5.6 ± 4.6	17.0 ± 9.2	1.2 ± 2.4
Branching Ratio (%)	19.5 ± 4.7	15.1 ±12.7	6.4 ± 3.5	3.4 ± 6.8

*Includes 5% systematic error for tracking simulation.

TABLE IV

Neutral Kaon Content

Tag	Events	Background	Net	Observed K^0_S	Background
$K\pi$	324	22.0	302 ± 18.0	12 ± 3.5	0.4 ± .3
$K3\pi$	217	37.6	179 ± 14.7	5 ± 2.2	1.1 ± .4
$K2\pi$	297	31.8	265 ± 17.2	13 ± 3.6	1.0 ± .4
$K^0\pi$	40	3.0	37 ± 6.3	5 ± 2.2	0.2 ± .2

Tag	Random Background	Efficiency*	Produced Kaons	Branching Ratio (%)
$K\pi$	1.8 ± .9	.090 ± .016	108 ± 44	36 ± 15
$K3\pi$	1.1 ± .5	.090 ± .016	31 ± 26	17 ± 14
$K2\pi$	1.6 ± .8	.095 ± .017	109 ± 43	41 ± 17
$K^0\pi$	0.2 ± .1	.095 ± .017	48 ± 25	130 ± 71

*Includes all systematic errors (15% model, 7% vertexing, tracking).

TABLE V

Summary of Inclusive Branching Ratios

		D^0 (%)	$D^{\pm}$ (%)
$Br(D \to K^- x)$	This experiment*	56 ± 11	19 ± 5
	LGW (Inc. K^+X)	35 ± 10	10 ± 7
$Br(D \to K^+ x)$	This experiment*	7.9 ± 2.9	6.0 ± 4.0
	LGW	----	6.0 ± 6.0
$Br(D \to K^0 x)$	This experiment*	29 ± 11	52 ± 18
	LGW	57 ± 26	39 ± 29

*Includes systematic error for model dependence.

First, the Cabibbo suppressed modes appear at a level of $\sim 3\sigma$ and 2σ above zero in the neutral and charged D's, respectively. In the neutral case, this interpretation requires negligible $D^0\bar{D}^0$ mixing. This is probably valid because of the short lifetimes currently given to the D's (see following sections), as well as the smallness of the off-diagonal terms in the mass mixing matrix.[16]

Care must be exercised in interpreting the remaining numbers. In principle, the $B(D \to K^- X)$ and $B(D \to K^0 X)$ fractions can have contributions from the Cabibbo suppressed decays as well.

If we assume that $(c \to d)$ and $(u \to d)$ transitions are equal and are individually equal to $\sim \tan^2 \theta_c$ (5%) inclusively, then suppressed modes might occur about equally in two forms:

$$\text{(i)} \quad \pi\pi + (n\pi) \ ,$$

$$\text{(ii)} \quad K\bar{K} + (n\pi) \ .$$

Ignoring any leading corrections, the $K\bar{K}$ modes will have an excess wrong strangeness $K^{\pm}$ about half the time, and a K^0 the other half. This implies that non-suppressed modes of the D^0 decay $\sim 52 \pm 10\%$ to charged K, and only $25 \pm 11\%$ to neutral K. The $D^{\pm}$ similarly decays $16 \pm 5\%$ to charged K and $49 \pm 18\%$ to neutral K.

Both these numbers fall short of the estimated 90% expected for nonsuppressed decays. The statistical and CME models[4] described in the previous section predict that hadronic decays produce a charged to neutral K ratio:

$D^{\pm}$	$K^{\mp}:\bar{K}^0$	32:68
D^0	$K^{\mp}:\bar{K}^0$	40:60

These numbers would be modified substantially (toward the measured rates) if there are large semileptonic branching ratios into dominant channels like $\bar{K}^0 \ell\nu$ or $K^- \ell\nu$. This will be discussed again in the following sections.

INDEPENDENT BRANCHING RATIO MEASUREMENTS

The sample of tagged events can be used to estimate in an independent way the absolute branching fractions for several decay modes. Each tagged event is kinematically fit[6] to the hypothesis:

$$e^+e^- \rightarrow D^0\bar{D}^0$$
$$\bar{D}^0 \rightarrow \text{tag } (K\pi,\ K3\pi)$$
$$D^0 \rightarrow K\pi,\ K3\pi$$

$$e^+e^- \rightarrow D^-D^+$$
$$D^+ \rightarrow \text{tag } (K2\pi)$$
$$D^- \rightarrow K2\pi$$

In the case where all charged particles are observed, we have six constraints (four constraints from total energy and momentum, and two constraints from the D masses). Alternately, one missing charged particle can be allowed, reducing the fit to three constraints (3C).

Events with a probability greater than 10^{-4} were scanned. The 3C fits were required to have drift chamber hits in the predicted azimuthal region for the missing track. The events accepted were required to have a χ^2 probability $\geq 1\%$. The backgrounds were estimated by the excess events at higher χ^2 which appeared substantial (14 events less 4 background) only in the K2π 3C fits where the semileptonic decays $K_S^o \ell\nu$ and $(K\pi)^{\pm}\ell\nu$ (with $e \to \pi$, and any charged track missed) are expected to introduce a larger background. Table VI summarizes the results. The efficiencies are determined essentially by geometry and decay probability. The expected events are calculated from the size of the tag sample, and the branching ratios of Chapter V. Double tags (e.g., 6C fits of $K\pi$:$K\pi$, etc.) are counted twice. It is clear that the observed numbers of events are in agreement with the expected numbers, although the observed rates tend to be higher. It is possible that the observed events have a background which peaks at low χ^2, (i.e., $K^o\pi^+\pi^-$ is detected as $K3\pi$), and contributes additional events. The overall trend suggests that this may be the case.

TABLE VI

Summary of 3C and 6C Tagged Event Fits

Tag	Recoil	Constraints	$\bar{\varepsilon}$ (± 20%)	Observed Events	Expected Events
$K\pi$	$K\pi$	6	.52	4 ± 2	4.3
	$K\pi$	3	.22	5 ± 3	1.8
	$K3\pi$	6	.17	6 ± 3	3.3
	$K3\pi$	3	.28	4 ± 3	5.5
$K2\pi$	$K2\pi$	6	.25	6 ± 3	3.5
	$K2\pi$	3	.44	10 ± 4	6.1
$K3\pi$	$K3\pi$	6	.17	6 ± 3	2.7
	$K3\pi$	3	.28	7 ± 3	1.2
	$K\pi$	6	.52	6 ± 3	2.2
	$K\pi$	3	.22	4 ± 3	3.7

SEMILEPTONIC DECAYS

As indicated in the introduction, tagged events can be used to measure the relative semileptonic branching fractions of neutral and charged D mesons. This provides a direct measure of the relative lifetimes of the charmed mesons,[1] as well as an estimate of their absolute lifetimes.

All tracks opposite a tag and satisfying the geometric criteria (in r, z, χ^2) of Chapter V are considered as candidates. TOF criteria for K-π-p defined in Chapter V is applied, removing K and p tracks. An additional requirement of probability under the kaon hypothesis of less than 5% is imposed. This cut removes less than 3% of the candidate tracks which were previously labeled as pions. The number of remaining $K^{\pm}$ identified as $\pi^{\pm}$ will then be negligible ($\lesssim 1\%$).

For $P < 300$ MeV/c these candidate tracks are classified as π or e by TOF. An electron candidate is required to have a TOF within 4σ of that predicted by its momentum. Under the π-e hypothesis, it must have a weight > 0.9. The election efficiency (ε) and hadron misidentification rate $\left(P_{h \to e}\right)$ are estimated by Monte-Carlo using the known TOF resolution.

For $P > 300$ MeV/c, TOF and liquid argon calorimeter information is combined to classify $e^{\pm}$ and $\pi^{\pm}$. The technique employed is called Recursive Partitioning.[7] Briefly, a binary decision tree is constructed using 23 measured variables such as momentum, TOF, and properties of the electromagnetic shower development. The variables are selected and the exact cuts found by examining the regions of the multidimensional space populated by pure samples of $\pi^{\pm}$ and $e^{\pm}$. The pure samples or "training vectors" are selected from radiative Bhabha events,

γ conversions and $\psi(3095)$ pionic decays. The efficiency and hadron misidentification rate $\left(P_{h\to e}\right)$ are measured self-consistently by using a random selection of 80% of the training sample to generate the decision tree, and testing with the remaining 20%.

Figure 3 shows the expected value of $P_{h\to e}$ versus track momentum As a test of the separator, the pions from ~ 2000 K_s^0 decay in the $\psi(3770)$ sample were classified. The K_s^0 had tighter than usual cuts in mass to reduce background. In Figure 3, the rate at which these pion "trial vectors" were classified incorrectly as electrons is shown. The results are in excellent agreement with the expected rate for $P_{h\to e}$. Table VII summarizes these misidentification rates as well as electron detection efficiencies as a function of momentum.

As in previous sections, the tags are $K\pi$, $K2\pi$, $K3\pi$ and $K^0\pi$. In each case, the charge of the lepton in the recoil system can be predicted by the strangeness of the tag. This provides a powerful tool with which to estimate the background from the large hadron misidentification rate.

There are three types of background which must be addressed:

(i) Backgrounds which are charge-asymmetric. These arise from hadron misidentification, and the observation that the charge distribution opposite tagged D mesons is not in general symmetric, but depends on the charge of the tag.

(ii) Charge-symmetric backgrounds independent of the tag strangeness. These are $e^{\pm}$ from electromagnetic processes (e.g., γ conversion, π^0 Dalitz decays).

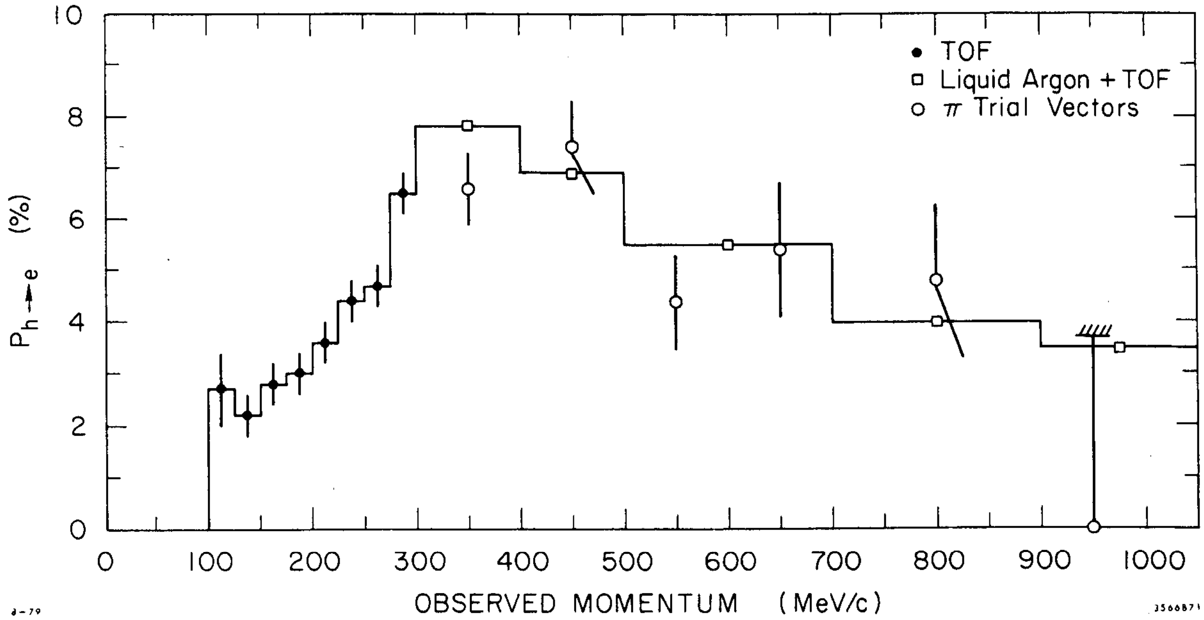

Fig. 3. Probability of hadrons being misidentified as electrons versus momentum. Open circles show the results of a test of the separation using pions from $K_S^o \to \pi^+\pi^-$.

TABLE VII

Electron Efficiency and Hadron

Misidentification Rates

Momentum (MeV/c)	ε_e *	$P_{h \to e}$
100-150	.96	.025
150-200	.95	.029
200-250	.84	.040
250-300	.62	.056
300-400	.67	.078
400-500	.64	.069
500-700	.75	.055
700-900	.82	.040
900-1000	.85	.035

* For candidate tracks averaged over the data sample.

(iii) Falsely tagged events. These are events lying within the D mass region, which are not D's, or events resulting from $K^{\pm} \rightleftarrows \pi^{\pm}$ interchange (which occurs in the decay $D^{0} \to K\pi$ only).

The contributions from (i) are directly calculated knowing $P_{h \to e}$, and the momentum and charge distribution of tracks opposite the tag. All candidate ($e^{\pm}$ and $\pi^{\pm}$) tracks are divided by charge into "right sign" and "wrong sign" groups. The former have the sign of the strangeness of the tag, and the latter have the opposite charge. The net number of right or wrong sign electrons $\left(N_e^r, N_e^w\right)$ is calculated as:

$$N_e^r = \sum_P \left\{ N_e^r(P) - N_c^r(P)\left(1 - f_e\right) P_{h \to e}(P) \right\}$$

$$N_e^w = \sum_P \left\{ N_e^w(P) - N_e^r(P)\left(1 - f_e\right) P_{h \to e}(P) \right\} \quad .$$

Here N_c^r, N_c^w are the initial number of candidate tracks $\left(e^{\pm}, \pi^{\pm}\right)$, and f_e is an estimate of the fraction of candidates which are electrons. The value 0.084 was used throughout. Any error in f_e is reduced by the factor $P_{h \to e}$ which is typically 0.05.

The contribution from source (ii) can be reduced by scanning all events with electron candidates for γ-conversion pairs. Events with a tagged electron and either another track or set of drift chamber hits with an opening angle $\lesssim 10^{\circ}$ were eliminated. This amounted to five D^{0} and eight $D^{\pm}$ events. In seven of these events, both tracks were found, with at least one track being tagged as an $e^{\pm}$. The remaining electrons from symmetric sources were estimated by assuming that in the absence of other backgrounds N_e^w should vanish. This assumption is valid because any source of symmetric $e^{\pm}$ will contribute equally to the right and wrong sign categories. Thus, the net electron yield is given by:

$$N_e = N_e^r - N_e^w \tag{1}$$

The effect of $K^{\pm}$ decays on this estimate has been considered. The only significant source of electrons come from $K^{\pm} \to e^{\pm}\pi^{o}\nu$ (the branching ratio is 4.82%). Using the measured branching ratios for D's decaying to charged kaons (see the previous section) and our acceptance, we expect to observe $.48 \pm .24$ electrons in the total D^{o} sample, and $.10 \pm .05$ electrons in the $D^{\pm}$ sample. The error is taken as 50% of the correction. These will all be wrong sign electrons, leading to a small underestimate of the net electron yield. The decays $K^{\pm} \to \mu^{\pm}X$ are 67% of the K decay rate. Muons from K decays have a slightly different $e^{\pm}$ misidentification rate ($\sim .75\ P_{h \to e}$) and thus cause an overestimate of the number of wrong sign particles misidentified as $e^{\pm}$. The result is therefore an overestimate of the net electron yield. For the D^{o} tags this implies an excess $.2 \pm .1$ electrons, and for $D^{\pm}$ only $.05 \pm .03$. Because these two K decay contributions are small, and tend to cancel, the net correction will only be included as a systematic error on the final electron yields.

The contaminations introduced from the two sources in (iii) are also small. Sidebands from 1.800 - 1.855 GeV/c^2 are used to estimate the background from falsely tagged D's. The $D^{o} \to K\pi$ has the problem of $K \leftrightarrows \pi$ interchange ($\sim$ 3.3% of the events) and is corrected by adjusting this fraction of right and wrong sign electrons before subtraction.

Table VIII contains a summary of the electron yield calculation for each type of tag, with corrections for all backgrounds described above. The final column indicates a distinct difference in the electron yield of the $D^{\pm}$ and D^{o} decays.

The electron energy spectra for $D^{\pm}$ and D^{o} derived from the above technique are shown in Figure 4. The data are uncorrected for the acceptance, and are shown with statistical errors only. The small ($\lesssim$ 1 event) non-resonant and interchange backgrounds have not been removed. They are distributed approximately uniformly over the plot. The curves in Figure 4 are theoretical shapes[9] for detected electrons produced from $D \rightarrow Ke\nu$ and $D \rightarrow K^{*}e\nu$. They have been normalized to the observed number of events (uncorrected) with $E_e \geq$ MeV. The general shape and cutoff of the observed spectra indicate reasonable agreement with the theoretical expectation. The small statistics make a fit to $Ke\nu$ versus $K^{*}e\nu$ insignificant however the need for a $(K\pi)e\nu$ component appears evident, as was found by earlier experiments.[8,10,11]

Because electron spectra from D^{o} and $D^{\pm}$ decays should be identical (the masses differ by only $\sim$ 5 Mev/c^2), a direct comparison can be made without an acceptance correction. From the data in Table VIII we find the central value of $\tau^{\pm}/\tau^{o} \approx 3.08$. Using the statistics of the calculation, and performing a maximum likelihood fit to the observed quantities (with Poisson statistics), we find the ratio to be:

$$\tau^{\pm}/\tau^{o} = 3.08^{+4.1}_{-1.3} \qquad (2)$$

The errors here are statistical. The likelihood function is shown in Figure 5. Since the ratio of the two quantities is measured, contributions

TABLE VIII

Semileptonic Rate Calculation

Tag Mode	Tags	Background Events	N_e^r	Right-Sign Background	Net Right-Sign $e^\pm$
$K\pi$	298 ± 18	22 ± 5	25	9.91 ± 0.77	15.1 ± 5.06
$K3\pi$	179 ± 15	37 ± 6	11	7.50 ± 0.69	2.50 ± 3.39
$K2\pi$	260 ± 17	31 ± 6	35	14.5 ± 0.96	20.5 ± 5.99
$K^o\pi$	35 ± 7	4 ± 2	4	1.78 ± 0.32	2.22 ± 2.03

Tag Mode	N_e^w	Wrong-Sign Background	Net Wrong-Sign $e^\pm$	N_e
$K\pi$	13	7.61 ± 0.69	5.39 ± 3.68	9.70 ± 6.25
$K3\pi$	5	4.15 ± 0.51	0.85 ± 2.29	2.64 ± 4.09
$K2\pi$	4	3.74 ± 0.48	0.26 ± 2.06	20.2 ± 6.34
$K^o\pi$	0	0.45 ± 0.17	-0.45 ± 1.01	2.67 ± 2.27

Tag Mode	$K^\pm \rightleftarrows \pi^\pm$ Correction	Background Correction	Net $e^\pm$	$D^o / D^\pm$ Tags Summed*
$K\pi$	-0.63 ± 0.25	+1.13 ± 0.63	10.2 ± 6.3	12.3 ± 7.6
$K3\pi$	--	-0.59 ± 0.68	2.1 ± 4.2	
$K2\pi$	--	-0.22 ± 0.74	19.9 ± 6.4	23.3 ± 6.7
$K^o\pi$	--	+0.75 ± 0.37	3.4 ± 2.3	

* Includes systematic errors for K decay contribution.

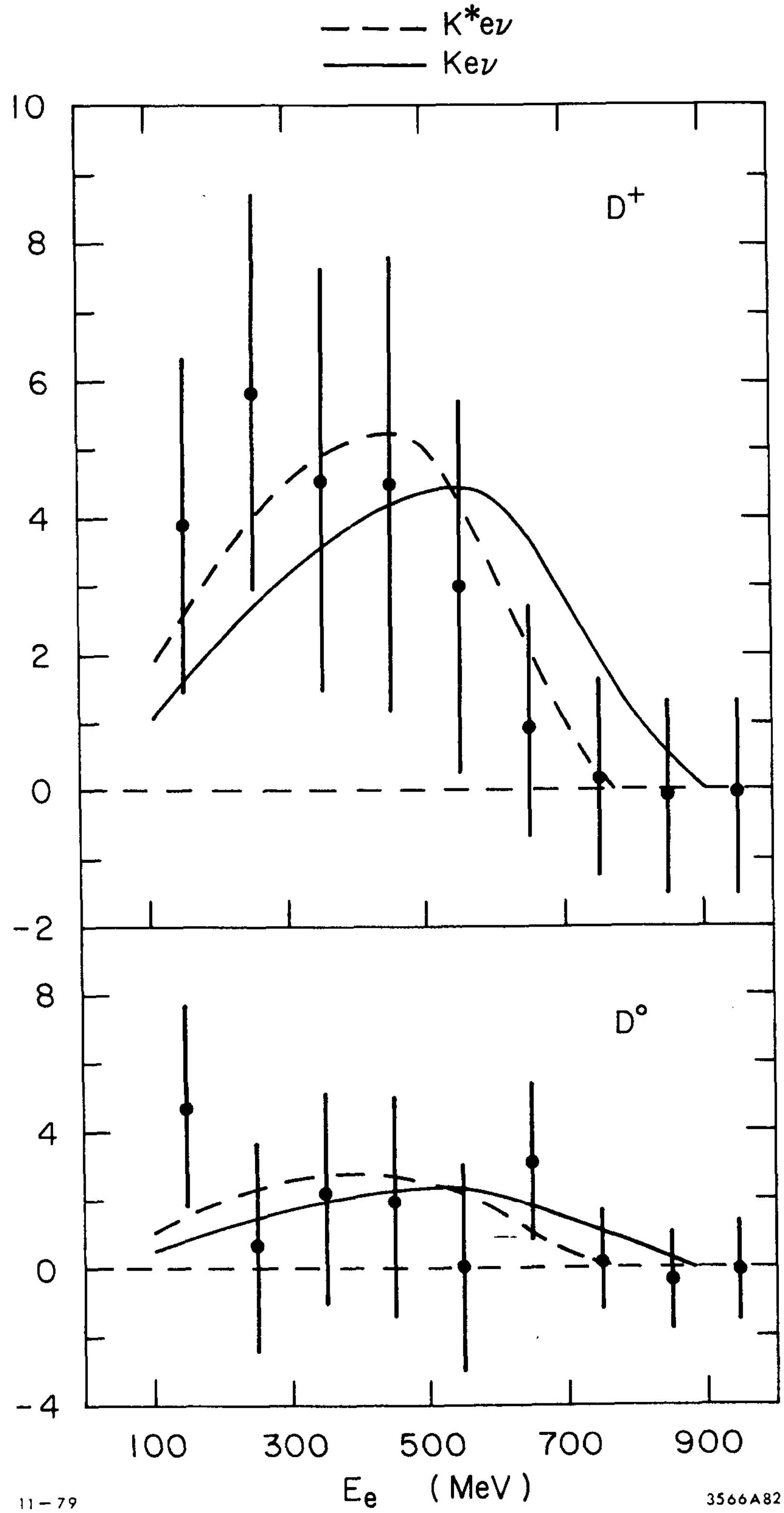

Fig. 4. Momentum spectrum of electrons from tagged $D^{\pm}$ (a) and D^{o} (b) events. The theoretical curves are normalized to the total number of events above 100 MeV/c.

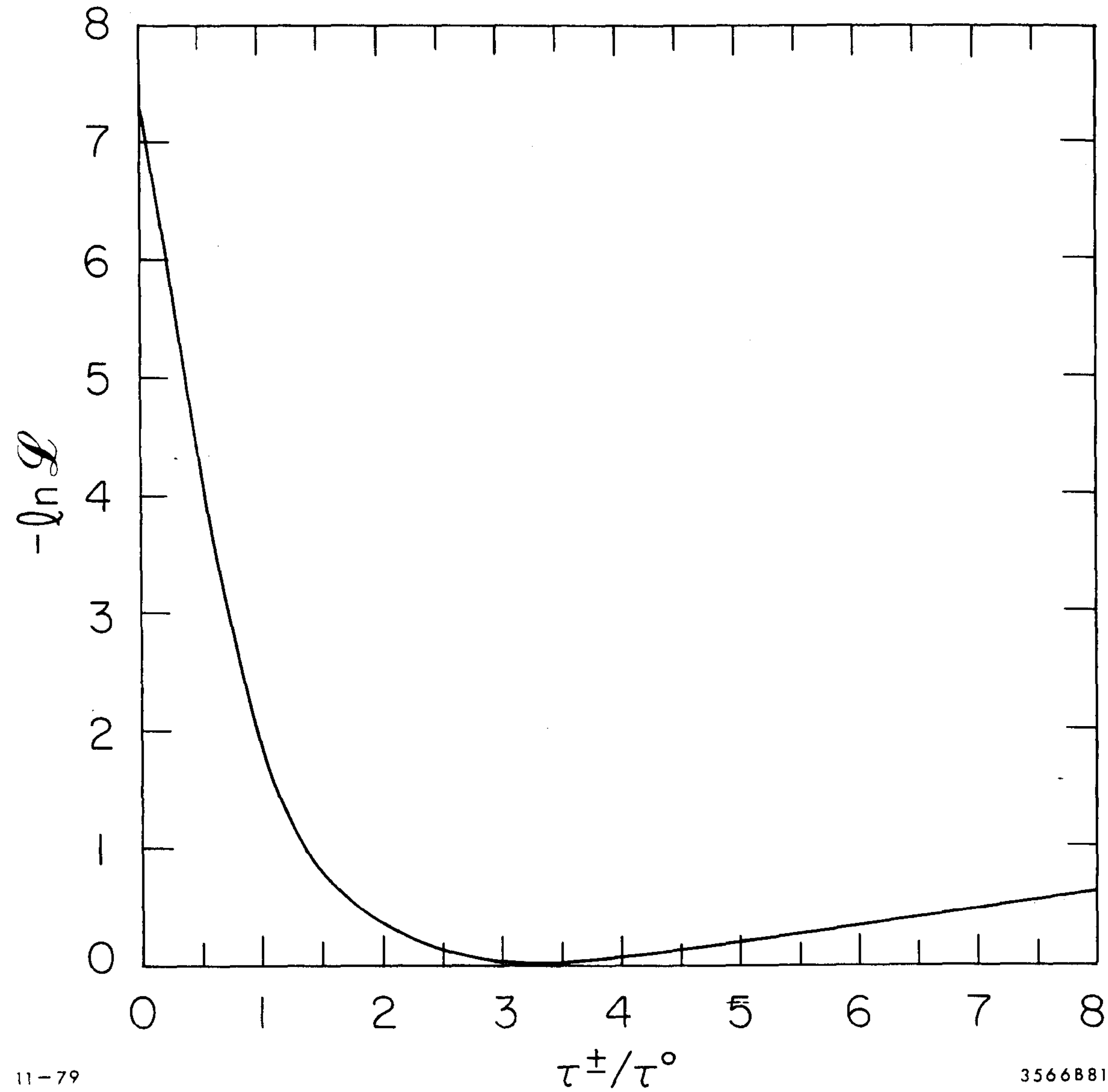

Fig. 5. The $-\ln$ of the likelihood function for $\tau^{\pm}/\tau^{0}$.

of many systematic errors are reduced. In particular, we estimate the total systematic error to be about 16% of the ratio, with ∿5% from the uncertainty in $P_{h\to e}$ (assuming 25% absolute uncertainty), 7% from the γ conversion scan, and 13% from assumptions about the background representation. Statistically, (2) represents a 2σ deviation from unity of $\tau^{\pm}/\tau^{o}$. Adding systematic errors we find $\tau^{\pm}/\tau^{o} = 3.1^{+4.2}_{-1.4}$, thus weakening the statement somewhat.

The deviation from unity of $\tau^{\pm}/\tau^{o}$ reflects the difference in total widths of neutral and charged D mesons. This difference is not unexpected, in part because of the greater range of final state isospins (1/2,3/2) available to the D^{o} in its nonleptonic final states. Assuming a $\Delta I = 1$ form for the weak decay Hamiltonian and the range of isospins of the final state mesons in the decay of a D, the ratio of hadronic widths is given:[1]

$$0 \leq \frac{\Gamma_h(D^+)}{\Gamma_h(D^o)} \leq 3$$

Here the lower (upper) bound comes from pure $I = 1/2$ (3/2) final states. A looser bound on the total widths was derived[12] using the triangle relation[13] among (specific) two body decay amplitudes (again assuming $\Delta I = 1$ in the weak Hamiltonian):

$$A(D^+ \to \bar{K}^o\pi^+) - A(D^o \to K^-\pi^+) + \sqrt{2}\, A(D^o \to \bar{K}^o\pi^o) = 0$$

The bounds are then set by measured branching ratios:

$$\max\,(0,\rho_-^2) < \tau^o/\tau^{\pm} < \rho_+^2$$

where

$$\rho_{\pm} = \sqrt{\frac{B_-}{B_+}} \pm \sqrt{\frac{2b_0}{B_+}}$$

Here B_+, B_-, b_0 are the measured branching fractions for D's decaying to $\bar{K}^0\pi^+$, $K^-\pi^+$ and the $\bar{K}^0\pi^0$ upper limit, respectively. Using the values of B_+, B_- and b_0 from Chapter V (2.1%, 2.8% and 3.6% at 90% C.L.) the limits become $0 < \tau^0/\tau^\pm < 9$. Our measurement of $B(D^0 \rightarrow \bar{K}^0\pi^0) \approx 2\%$, reduces the upper limit to ~ 7. In each case our measured value $3.1 \begin{smallmatrix} +4.2 \\ -1.4 \end{smallmatrix}$ from (2) appears consistent with these theoretical expectations. It is interesting to note that a difference in lifetimes is consistent with the limits imposed by measurements of the average semileptonic branching ratio of D mesons and individual $D^\pm$, and D^0 production cross sections at higher center of mass energies in e^+e^-.[14] Finally, preliminary measurements of two-electron events at the $\psi(3770)$ from data taken with the DELCO detector at SPEAR also indicate evidence for a difference in semileptonic branching ratios.[15] The preliminary value of $\tau^\pm/\tau^0 > 5.8 \pm 1.5$ was reported by that experiment, and is consistent with (2).

MULTIPLICITY IN SEMILEPTONIC EVENTS

Figure 6 shows the observed multiplicity distribution opposite the tag for the electron events of Figure 4. The observed multiplicity in the $D^\pm$ events indicates strong one and three prong components, with negligible events at higher multiplicities. In the D^0 case it is not as clear because of large statistical errors, however the events significantly populate only the multiplicities as far out as four prongs. These distributions are not unlike those of the full event sample analyzed in the previous sections. They suggest that $Ke\nu$ and $K^*e\nu$ or $(K\pi)e\nu$ decays saturate the semileptonic modes. A similar conclusion

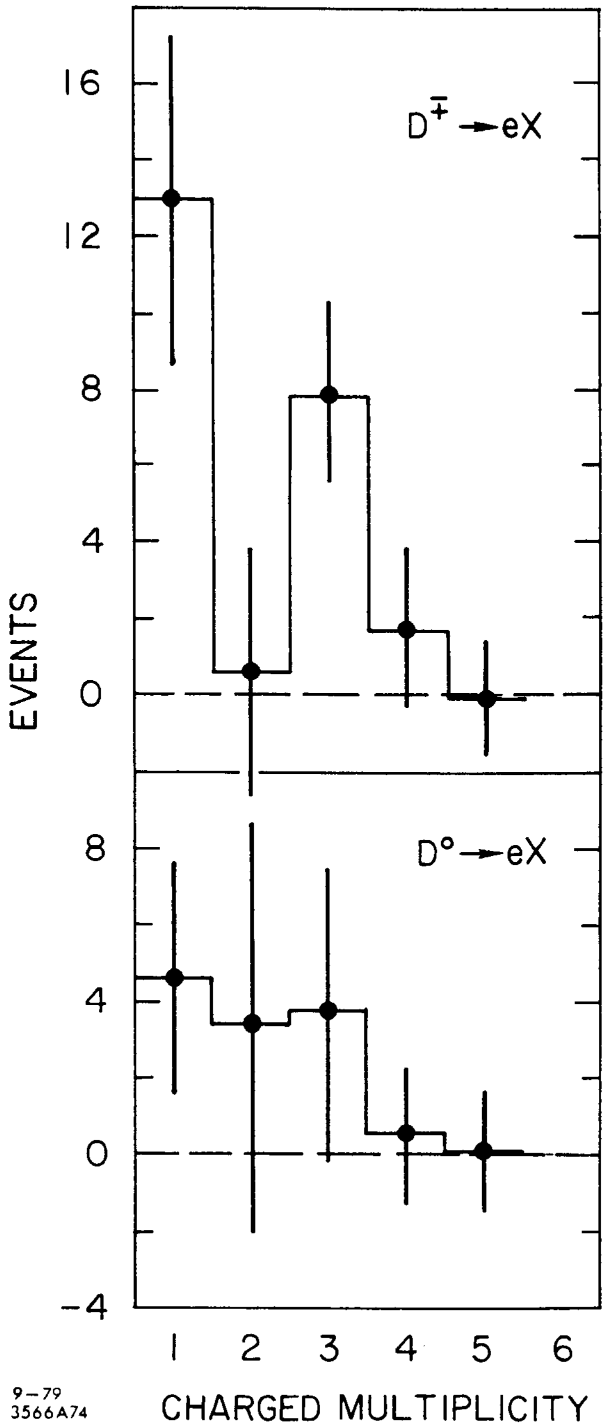

Fig. 6. Observed charged particle multiplicity opposite the tagged D for the events in Figure 4.

can be drawn regarding this saturation in multiplicity (for semileptonic D decays) from measurements of the shape of the electron spectrum at the $\psi(3770)$.[8,10,11] The data in these previous measurements appear consistent with contributions from $Ke\nu$, $\pi e\nu$, $K\pi e\nu$ or $K^*e\nu$. No higher multiplicities were required to account for the shape of the electron spectrum. This is also the theoretical predjudice, as soft-pion theorems[16] and simple phase space arguments[14] indicate that the decays into higher multiplicities from higher mass resonances should be small. It was suggested in Reference 17 that gluon radiative corrections may be sufficiently large that they dampen the form factors for producing high momentum electrons in the semileptonic D decays. This softening of the spectrum could replace the K^* or $(K\pi)$ component.

The data in Figure 6 can be "unfolded" under the $Ke\nu$ or $K^*e\nu$ hypotheses, to determine the ratio of these two components. Since we are dealing with a $\Delta I = 0$ transition, replacing K^* with $(K\pi)$ should only change the momentum of the hadrons (not their proportions), hence K^* approximates $(K\pi)$ for this calculation. The unfold determined successfully the relative proportions for the D^+, yielding $68 \pm 28\%$ of the events coming from $K^oe\nu$. The D^o errors were too large to be meaningful. The errors here are statistical only. The indication is that the $D^\pm$ favors the K^o component, while little is learned from the D^o. Considering the errors, the D^o spectrum would not be inconsistent with the $D^\pm$ fit. If this is the case, and the $D^\pm$ dominates the semileptonic decays as indicated in the previous section, then the average spectrum should favor the non-resonant $Ke\nu$ mode. In Reference 8, the value $61 \pm 16\%$ $Ke\nu$ is found for single electron decays of D's, in reasonably good agreement. The statistics of our measurement indicate some need for the K^* component ($\sim 1\sigma$ from 0) but not sufficiently strong to rule out the conjecture[17] that radiative gluon corrections soften the spectrum, rather than K^* or $K\pi$ modes.

INDIVIDUAL BRANCHING RATIOS

Individual branching ratios may be obtained by estimating the inclusive electron efficiency (ε_e), when a tagged D is present. For events generated as pure $Ke\nu$ and pure $K^*e\nu$, the values obtained by Monte Carlo are 0.47 for both $K^*e\nu$ and $Ke\nu$. The errors from statistics are dominant (30% D^+, 62% D^o). Additional systematic error from the γ conversion scan, background assumptions, correction procedure, and simulation contribute another 24% and 26% to $D^\pm$ and D^o respectively. If we assume that $K^oe\nu$ and $K^*e\nu$ are the dominant sources (consistent with the observed multiplicities) then 0.47 may be used for the average efficiency.

Using this efficiency and the values of Table VIII, the separate charged and neutral branching fractions are calculated:

$$\begin{aligned} B(D^\pm \to e\nu X) &= 16.8 \pm 6.4\% \\ B(D^o \to e\nu X) &= 5.5 \pm 3.7 \end{aligned} \qquad (3)$$

A value for the average D branching ratio to electrons is obtained for experiments measuring one electron per event at the $\psi(3770)$ by weighting the values in (3) by the D production ratio (phase space factors):

$$(.43 \pm .03)\big(B(D^\pm \to e\nu X)\big) + (.57 \pm .03)\big(B(D^o \to e\nu X)\big) = 10. \pm 3.2\%$$

This value is in good agreement with the two previous measurements of average semileptonic D branching ratios at the $\psi(3770)$: $8.0 \pm 1.5\%$ [8] and $7.2 \pm 1.8\%$. [11]

D MESON LIFETIMES

The measurements of the previous sections provide the separate semileptonic branching ratios of $D^{\pm}$, and D^{o}, as well as an estimate of their composition ($Ke\nu$ or $K^{*}e\nu$). To measure the D lifetime, a theoretical estimate of the total leptonic plus semileptonic width $\Gamma(D \to e\nu) + \Gamma(D \to e\nu X)$ or a partial width $\Gamma(D \to Ke\nu)$, $\Gamma(D \to K^{*}e\nu)$ would be needed. The pure leptonic decays of the D are Cabibbo suppressed and should be negligible compared to semileptonic decays.[16] They can be estimated:

$$\Gamma(D^{+} \to \mu^{+}\nu) \approx \frac{M_D}{M_K}\,\Gamma(K^{+} \to \mu\nu) \approx 1.9 \times 10^{8}\ \mathrm{sec}^{-1} \qquad (4)$$

The weak beta-decay of a free charmed quark has been estimated using the form of the μ decay width including the mass of the decay lepton, replacing ordinary leptons with quarks:[14,16]

$$\Gamma^{o}(c \to se\nu) = \cos^{2}\theta_c \left(\frac{M_c}{M_\mu}\right)^{5} \Gamma(\mu \to \mathrm{all})\, f\left(\frac{M_s^{2}}{M_c^{2}}\right) \qquad (5)$$

where

$$f(x) = 1 - 8x + 8x^{3} - x^{4} - 12x^{2}\,\ell n\, x \quad .$$

Using constituent quark masses ($M_s = .48$ GeV, and $M_c = 1.66$ GeV) one obtains $\Gamma(c \to se\nu) = 2.4 \times 10^{11}\ \mathrm{sec}^{-1}$. The function $f(x)$ accounts for the s quark mass, and has a value of $\sim .54$ here. Finally, using the same approach, but calculating lowest order gluon vertex and bremstraulung renormalizations (in direct analogy to QED μ decay)[17,18] the expression in (5) is corrected to:

$$\Gamma(c \to se\nu) = \Gamma^{o}(c \to se\nu)\left(1 - \frac{2}{3\pi} \alpha_s(M_c^2)\, g\left(\frac{M_s}{M_c}\right)\right)$$

$$= \Gamma^{o}(c \to se\nu)(.63)$$

$$= 1.5 \times 10^{11}\, \mathrm{sec}^{-1}$$

Using $M_s = .48$, $M_c = 1.66$, $\alpha_s(M_c) \approx .7$, $g(.30) \approx 2.5$. It is interesting to note the size (35%) of these gluon corrections unlike the comparable radiative corrections to μ decay which are ~.4%.[19]

An alternate approach has been to extrapolate the partial width for $D_{\ell 3}$ from $K_{\ell 3}$ decays. As in the K decays, the f_- form factor term is ignored because of the small lepton mass, and only the f_+ term is retained.[20] Then assuming constant and equal form factors for K and D, the $D_{\ell 3}$ width is given:[14]

$$\Gamma(D^{o} \to K^{-}e\nu) = 2 \cot^2 \theta_c \left(\frac{M_D}{M_K}\right)^5 \frac{f\left(\left(\frac{M_K}{M_D}\right)^2\right)}{f\left(\left(\frac{M_\pi}{M_K}\right)^2\right)} \Gamma(K^{+} \to \pi^{o}e\nu)$$

$$\approx 1.1 \times 10^{11}\, \mathrm{sec}^{-1}$$

Here problems arise from the uncertainty in the assumption of constant and equal form factors for the D and the K. In particular, the possibility of q^2 dependence of the form factors may change this width considerably. In one calculation[21] additional q^2 dependence in the form of a single pole increases the width by 30% to $\sim 1.4 \times 10^{11}$ sec^{-1}.

If the $K:K^*$ fraction measured above is used, we obtain then a total width of 1.62 to $2.1 \times 10^{11}\ \mathrm{sec}^{-1}$ which again might be reduced by $\sim .6$ if QCD corrections are applied. Given these estimates, we see that the theoretical $\Gamma(D \to e\nu X)$ ranges from 1. to $2. \times 10^{11}\ \mathrm{sec}^{-1}$.

Using the branching ratios from (4) for $D^{\pm}$ and D^{o} semileptonic decays, and $\Gamma(D \to e\nu X) = 1.5 \pm 0.5 \times 10^{11}\ \mathrm{sec}^{-1}$, the lifetimes are estimated to be:

$$\tau^{\pm} = \frac{16.8 \pm 6.4\%}{1.5 \pm 0.5 \times 10^{11}\ \mathrm{sec}^{-1}} = 11.2 \pm 5.1 \times 10^{-13}\ \mathrm{sec}$$

$$\tau^{o} = \frac{5.5 \pm 3.7}{1.5 \pm 0.5 \times 10^{11}\ \mathrm{sec}^{-1}} = 3.7 \pm 2.8 \times 10^{-13}\ \mathrm{sec}$$

SUMMARY

Numerous inclusive measurements have been presented in this chapter and wherever possible compared with previous results. All such comparisons appear consistent. The results of these measurements are summarized below:

(i) Absolute branching fractions for $K\pi$, $K2\pi$, $K3\pi$ measured with tags appear in agreement with those values presented in Chapter V.

(ii) Charged particle multiplicity measured for D^{o} and $D^{\pm}$ indicate some differences. The D^{o} has a mean of 2.46 ± 0.15 while the $D^{\pm}$ mean is 2.16 ± 0.16. The CME and statistical models discussed generally predict larger hadronic multiplicities (~ 2.4 and 3.1, respectively). The indication of a large asymmetry in the semileptonic decay rates suggests that the multiplicity for the $D^{\pm}$ should be substantially lowered, more consistent with the data. The D^o already agrees reasonably well with these models.

(iii) The strangeness observed in D decays remains puzzling as in previous measurements. In particular, the $D^{\pm}$ rate of $19 \pm 5\%$ is considerably smaller than the ~32% expected from the statistical model of purely hadronic decays. Here again, the addition of the seemingly large semileptonic rate into $K^o \ell\nu$ and $(K^o\pi^o)\ell\nu$ suppresses the charged K rate even more. In D^o and $D^{\pm}$ decays, the rate which charged kaons from Cabibbo suppressed decays are observed is $7.9 \pm 2.9\%$ and $6.0 \pm 4.0\%$, respectively.

(iv) The semileptonic branching ratios for D^o and $D^{\pm}$ appear to be different with values obtained $16.8 \pm 6.4\%$ and $5.5 \pm 3.7\%$, respectively. The average rate is consistent with previous measurements at the $\psi(3770)$. The difference in rates implies a difference in lifetimes of the $D^{\pm}$ and D^o. Using the estimate $\Gamma(D \to e\nu X) = 1.5 \pm 0.5 \times 10^{11}$ sec^{-1}, the lifetimes are $11.2 \pm 5.1 \times 10^{-13}$ and $3.7 \pm 2.8 \times 10^{-13}$ sec, respectively.

(v) Finally, a measurement of the multiplicity suggests that the fraction of D^+ decaying semileptonically to $K^o \ell\nu$ is $\approx 68 \pm 28\%$.

REFERENCES AND FOOTNOTES

1. Peshkin, M., Rosner, J. L., Nucl. Phys. B122, 144 (1977); Pais, A., Trieman, S. B., Phys. Rev. D15, 2529 (1977); also see Rosner, J. L., Reference 14, for a general discussion.
2. Feldman, G. J., *et al*., Phys. Rev. Lett. 38, 1313 (1977).
3. Vuillemin, V., *et al*., Phys. Rev. Lett. 41, 1149 (1978).
4. Rosner, J. L., Orbis Scientiae (1977), Coral Gables, and Phys. Rev. D17, 239 (1978); Fermi, E., Phys. Rev. 92, 452 (1953); ibid., Peshkin, M.
5. Kingsley, R. L., Phys. Lett. 63B, 329 (1976).
6. The kinematic fitting program SQUAW is used, adapted to the Mark II data formats.
7. Friedman, J. H., IEEE Trans. on Computing, April 1977 (Stanford Linear Accelerator Center, SLAC-PUB-1573).
8. Bacino, W., *et al*., Phys. Rev. Lett. 43, 1073 (1979).
9. See for example Ali, A., and Yang, T. C., Phys. Lett. 65B, 275 (1976); Jackson, J. D., Brandeis Summer Institute, 353 (1962).
10. Brandelik, R., *et al*., Phys. Lett. 70B, 397 (1977).
11. Feller, J. M., *et al*., Phys. Rev. Lett. 40, 274 (1978).
12. Takaiwa, Y., Inst. of Phys., University of Tsukuba, preprint UTHEP-28 (1978).
13. Kingsley, R. L., Treiman, S. B., Wilczek, F., Zee, A., Phys. Rev. D11, 1919 (1975); *ibid*., Peshkin, M., and Rosner, J. L.; Altarelli, G., *et al*., Nucl. Phys. B88. 295 (1975) and Phys. Lett. 57B, 277 (1975).

14. Rosner, J. L., University of Minnesota preprint 78-1181; Katuya, M., Iowa State University preprint 79-0652 (1979).

15. Kirkby, J., Proceedings of the 1979 Lepton Photon Conference, Fermi National Accelerator Laboratory (to be published).

16. Gaillard, M. K., Lee, B. W., Rosner, J. L., Rev. Mod. Phys. 47. 2771 (1975).

17. Suzuki, M., Nucl. Phys. B145, 420 (1978).

18. Cabibbo, N., Maiani, L., Phys. Lett. 79B, 109 (1978).

19. See for example, Commons, E. D., Weak Interactions, (McGraw Hill, 1973) P. 44.

20. *Op. cit.*, Commons, p. 225.

21. Fakirov, D., and Stech, B., Nucl. Phys. B133, 315 (1978).

VII. CONCLUSIONS

In the previous chapters, measurements have been presented on the production properties of D mesons in e^+e^- annihilation, as well as on the decay properties in the form of branching fractions and inclusive particle measurements. The measurements of the $\psi(3770)$ have been interpreted in detail in light of previous measurements and theoretical models within the body of Chapter IV. Therefore, the results will be summarized only briefly here. The remainder of the chapter will be devoted to a detailed comparison of the inclusive measurements and branching fractions with currently viable theoretical predictions. Comparisons with previous experiments have already been given in the appropriate sections. As will be shown, the measurement presented of the relative total widths for D^o and $D^{\pm}$ is important for comparison with many models. An attempt will also be made to compare the inclusive measurements with the direct estimates of branching fractions, providing a further test of the self-consistency of these measurements and models.

THE $\psi(3770)$ RESONANCE

The measurement of the $\psi(3770)$ provides a third independent set of resonance parameters, as well as an estimate of the charm production cross section needed for the measurement of absolute D meson branching fractions. The evaluation of the leptonic width which is of particular importance for charmonium models, was measured as 276 ± 50 eV, lying directly between the two previously reported values[1] of 180 and 345 eV. This helps resolve the large discrepancy in the early measurements.

As pointed out in Chapter IV, this large leptonic width cannot be accommodated into simple charmonium potential models because the mixing of the S and D wave states by tensor forces is an order of magnitude too small. The mechanism introduced by Eichten et al.,[2] of mixing through continuum states predicted the $\psi(3770)$ mass and leptonic width remarkably well. The same model also treats $D\bar{D}$, $D\bar{D}^*$ and $D^*\bar{D}^*$ production (above threshold) reasonably well, suggesting that the approach is a sound one.

BRANCHING RATIOS FOR NONSUPPRESSED DECAYS

I will begin by going over several models of charm particle decay properties, comparing them in turn with the measurements of inclusive properties as well as the absolute measurements of branching ratios presented in Chapter V.

Statistical Models

As pointed out in Chapter VI, these models provide us with an idea of the scope of D meson decays, but in their lack of dynamics they are not expected to work in detail. In particular, uncertainties in size and composition of the semileptonic decays, neutral particle (η,η') decays, and hadronic decays (with ρ, K^* ...) all cast doubt upon their predictive power for absolute branching ratios.

In Chapter VI it was shown that in the hadronic decays, these models (statistical and CME, respectively) predicted $\langle n_c \rangle_{D^0} = 3.0$ and 2.4 and $\langle n_c \rangle_{D^\pm} = 3.1$ and 2.5. The charged:neutral kaon content for hadronic decays was found to be approximately 40:60 and 32:68 for D^0 and $D^\pm$ in both models. The measurements of D^0 and $D^\pm$ semileptonic branching fractions from Chapter VI indicate that these decays may account for $\sim 32\%$ of all D decays. For the D^o, only about 10% of the branching fraction is semileptonic. Furthermore, since the decays appear dominated by $Ke\nu$ rather than $(K\pi)e\nu$, we expect a substantial suppression of $\langle n_c \rangle$ in the $D^{\pm}$ (the contribution to charged multiplicity for $D^{\pm}$ is ~ 2.0 charged particles/semileptonic decay) and a smaller effect for the D^o. The measured values of $\langle n_c \rangle_{D^o} = 2.46 \pm 0.15$ and $\langle n_c \rangle_{D^+} = 2.16 \pm 0.16$ are closer to the narrow CME model, and prefer the suppression associated with the semileptonic decays.

In a similar fashion, the kaon content of D decays is affected by the large variation in semileptonic rates. The charged K fraction of the $D^{\pm}$ is diminished in the model (the rate is about 0.22 $K^{\pm}$/semileptonic decay) reducing the prediction of 32% toward the measured $17 \pm 5\%$, without altering the D^o rate significantly. Thus, we can conclude that these gross features of the model modified by the addition of the semileptonic decays begin to resemble the data.

As pointed out, the prediction of relative branching ratios is probably more reliable than absolute rates. These are made using only the assumption that weak hadronic decays go via $\Delta I = 1$, into D^o and $D^{\pm}$ final states having I = (3/2 and 1/2) or (3/2), respectively. Because of the additional range of isospin channels in the D^o case, most derivable limits are very loose. Table I gives the predictions of the statistical model, wherein the statistical postulate is applied, for D^o and $D^{\pm}$ decays. These are compared in Table II with the data of Chapter V, Table II, using the measured values of $\sigma \cdot B$ and removing systematic errors wherever possible. The agreement with experiment is not overwhelming; however, one must consider that the errors are still large and other dynamic effects (e.g., resonant substructure) may be occurring.

TABLE I

Predictions of the Statistical Model [3]

D^0 Statistical Model			
Modes	I = 1/2	I = 3/2	Statistical Average
$K^-\pi^+$	2/3	1/3	0.50
$\bar{K}^0\pi^0$	1/3	2/3	0.50
$\bar{K}^0\pi^+\pi^-$	1/2	6/15	0.45
$K^-\pi^+\pi^0$	1/3	7/15	0.40
$K^0\pi^0\pi^0$	1/6	2/15	0.15
$K^-\pi^+\pi^+\pi^-$	3/10	6/25	0.27
$\bar{K}^0\pi^+\pi^-\pi^0$	9/20	12/15	0.47
$K^-\pi^+\pi^0\pi^0$	1/5	1/5	0.20
$\bar{K}^0\pi^0\pi^0\pi^0$	1/20	2/25	0.06
$\bar{K}^0\pi^+\pi^-\pi^+\pi^-$	2/9	4/21	0.20
$K^-\pi^+\pi^+\pi^-\pi^0$	16/45	38/105	0.36
$\bar{K}^0\pi^+\pi^-\pi^0\pi^0$	14/45	34/105	0.32
$K^-\pi^+\pi^0\pi^0\pi^0$	4/45	11/105	0.10
$\bar{K}^0\pi^0\pi^0\pi^0\pi^0$	1/45	2/105	0.02

$D^{\pm}$ Statistical Model	
Modes	Statistical Average
$\bar{K}^0\pi^+$	1.00
$K^-\pi^+\pi^+$	0.40
$\bar{K}^0\pi^+\pi^0$	0.60
$\bar{K}^0\pi^+\pi^+\pi^-$	0.40
$K^-\pi^+\pi^+\pi^0$	0.32
$K^0\pi^+\pi^0\pi^0$	0.28
$K^-\pi^+\pi^+\pi^-\pi^+$	0.19
$\bar{K}^0\pi^+\pi^-\pi^+\pi^0$	0.48
$K^-\pi^+\pi^+\pi^0\pi^0$	0.21
$\bar{K}^0\pi^+\pi^0\pi^0\pi^0$	0.12

TABLE II

Comparison of Statistical Model with Data

Ratio of Partial Widths	Data	Pure		Statistical Average
		$I = 1/2$	$I = 2/3$	
$K^-\pi^+ / \bar{K}^o\pi^o$	1.37 ± 0.67	2.00	0.50	1.00
$\bar{K}^o\pi^+\pi^- / K^-\pi^+\pi^o$	0.52 ± 0.22	1.50	0.86	1.13
$K^-\pi^+\pi^+ / \bar{K}^o\pi^+\pi^o$	0.41 ± 0.25	--	0.67	0.67
$\bar{K}^o\pi^+\pi^+\pi^- / K^-\pi^+\pi^+\pi^o$	0.43 ± 0.34	--	1.25	1.25

The statistical model can be used in conjunction with the measured branching ratios and observed multiplicity distribution to provide a rough check of the $19 \pm 5\%$ measured $K^\pm$ branching ratio of $D^\pm$. The observed charged particle multiplicity distribution has only $\sim 5.6 \pm 2.4\%$ in the five prong category. These can arise from $K^o 3\pi$ decays ($2.9 \pm 1.2\%$), $K4\pi$ ($< 4.1\%$), $K^o 3\pi\pi^o$ ($< 3.5\%$ using statistical model and the $K4\pi$ rate), as well as the unknown ≥ 6 body decays such as $K4\pi\pi^o$, $K^o 3\pi\pi^o\pi^o$, et cetera. Since the charged multiplicity is nearly saturated by ≤ 5 body decays, we can ignore higher multiplicity sources of $K^\pm$. The sources are then $K^\pm\pi^\mp\pi^\mp$ ($6.3 \pm 1.5\%$), $K^- 2\pi\pi^o$ ($20 \pm 15\%$), $K4\pi$ ($< 4.1\%$) and $(K^\mp\pi^\pm)e\nu$ ($5.4 \pm 2.7\%$). Assuming equal $(K^\mp\pi^\pm)\mu\nu$ ($5.4 \pm 2.7\%$) and using the statistical model to estimate $K2\pi\pi^o\pi^o$ ($< 4.1\%$) we obtain $Br(D^+ \to K^- X) < 45 \pm 16\%$. The discrepancy with the measured $19 \pm 5\%$ comes predominantly from the measurement of $K2\pi\pi^o$. A 1σ reduction would make the 90% limit quite consistent with the inclusive rate. Note the use of the statistical model was minimal here. To repeat a similar argument for the D^o unfortunately requires more use of the model, and therefore less reliability.

SU(3) Predictions

Beyond the statistical model, attempts have been made to embody more dynamical assumptions into charmed meson decays. In strange particle decays (kaons, hyperons) it has been found empirically that the nonleptonic decays are greatly enhanced over the semileptonic decays and in the former the $\Delta I = 1/2$ transitions dominate the $\Delta I = 3/2$ ones by about a factor of 20 in amplitude. This enhancement has been termed the "$\Delta I = 1/2$ rule." Short range QCD effects can only account for about 25% of the enhancement.[4] Current investigations center around the belief that this enhancement results from the so-called "penguin" operators,[5] which involve only the $\Delta I = 1/2$ current. While these diagrams appear in kaon decays, they don't appear in allowed D decays, thus suggesting[6] that if this were the source of the enhancement, it would be smaller in charmed meson Cabibbo allowed decays. This in turn would imply that the semileptonic decays would take a larger fraction of the total width. A rough upper bound of $\sim$ 40% comes from a naive free quark decay model (see Ellis et al., Ref. 6), where the charmed quark is decayed weakly, and the light quark treated as a spectator. Our measurement of branching ratios to semileptonic final states of $\sim$ 11% and $\sim$ 34% for D^0 and $D^{\pm}$ respectively seems to indicate that a nonleptonic enhancement factor could be present. However, in neither case does it appear as large as in strange particle decays.

In the absence of the "penguin" diagram explanation for the $\Delta I = 1/2$ rule, several authors[7] have attempted to extend the enhancement into the nonleptonic charmed meson decays. In the SU(3) limit of three quarks, the current-current form of the nonleptonic weak interactions

Hamiltonian $\left(H_W \sim \frac{1}{2}(J^\dagger J + JJ^\dagger)\right)$ has the group representation: [7]

$$H_W \sim \{8\} \otimes \{8\} = \{27\} \oplus \{8_S\} \oplus \{8_A\} \oplus \{10\} \oplus \{10^*\} \oplus \{1\} .$$

Requiring H_W to be symmetric and strangeness changing reduces it to:

$$H_W \sim \{27\} \oplus \{8_S\} .$$

The $\Delta I = 3/2$ transitions are confined to the {27} while the {8} has $\Delta I = \frac{1}{2}$ only, [7] leading to the association of the {8} with nonleptonic enhancement and the $\Delta I = \frac{1}{2}$ rule. This is often denoted "octet enhancement". In SU(4), the analogous expansion for the form of H_W is given:

$$H_W \sim [15] \otimes [15] = [84_S] \oplus [45_A] \oplus [45_A] \oplus [20_S] \oplus [15_S] \oplus [15_A] \oplus [1] .$$

Requiring only symmetric and charm changing pieces removes $[45_A]$, $[15_A]$ and [1]. Einhorn et al., [7] show that $[15_S]$ is also absent for $\Delta S = \Delta C$ transitions. The remaining SU(4) multiplets are $[84_S] \oplus [20_S]$. Further decomposition into SU(3) subgroups gives $\{6\} \oplus \{8\} \oplus \{6^*\}$ for the [20] where {6} and $\{6^*\}$ are $\Delta C = \pm 1$. The [84] is complicated, but again Einhorn et al., [7] show that only the $[\{3\} \oplus \{15_M\}]$ and $[\{3^*\} \oplus \{15_M\}]$ are $\Delta C = \pm 1$, and in fact the {3} and $\{3^*\}$ do not appear in the Hamiltonian. In Ref. 8, Wang et al., show that the {3} and $\{3^*\}$ re-emerge in the more general six quark model. Making no further assumptions, the four quark model has only three independent reduced matrix elements relating all D^+ and D^0 two-body pseudoscalar-pseuloscalar decays. Extending "octet enhancement" to an SU(4) invariant interaction implies dominance of the [20] over the [84] because it contains the SU(3) enhanced {8} while [84] contains the suppressed {27}.

Carrying this further suggests that the {6} piece of [20] dominates the {15} for charm decays. This line of reasoning is carried out by Einhorn et al.,[7] where only the sextet piece is allowed. This leaves only one matrix element in the two-body decays and predicts the absence of <u>all</u> leading $D^{\pm}$ decays proportional to $\cos^4 \theta_c$ (e.g., $\bar{K}^o \pi^+$, $K^{*o}\rho$, ...) while retaining the leading decays of the D^o. Again, it is unclear what the actual size of the enhancement factor in SU(4) would be, beyond the small calculable QCD effect.[6,7] If it were as large as in strange particle decays, then semileptonic decays ($\sim \cos^2 \theta_c$) of the D^o would be small (< 1%), while those of the $D^{\pm}$ might compete favorably with the nonleptonic decays.[7] Furthermore, the suppression of the leading $D^{\mp}$ decays might tend to reduce the total kaon content of the nonleptonic decays, as the Cabibbo suppressed decays begin to compete favorably with the nonsuppressed ones.[13] These <u>extreme</u> effects are not strongly in evidence in the data. The evidence that these effects are occurring at some level is the difference in D^o and $D^{\pm}$ semileptonic branching ratios (implying a difference in hadronic widths), and the apparent reduction of $K^{\mp}$ in $D^{\pm}$ final states. That we see $\bar{K}^o \pi^+$ (2.3 ± 0.7%), a forbidden decay in this scheme, either implies {6} dominance is wrong, or that the decay <u>is</u> suppressed, but $\Gamma(D^+) \ll \Gamma(D\ )$. This latter requirement on the widths is reflected in the data presented in Chapter VI, where $\tau^{\pm}/\tau^{o} = 3.1 {+4.2 \atop -1.4}$.

In the two-body nonsuppressed decays, {6} dominance predicts only one relation among amplitudes that can be tested, namely $2\,\mathrm{Br}(D^o \rightarrow \bar{K}^o \pi^o) = \mathrm{Br}(D^o \rightarrow K^- \pi^+)$. This is the same result obtained by requiring D^o final states of pure $I = \frac{1}{2}$ (see Table II). The measured ratio of 0.73 ± 0.35 is close to the expected value of 0.5.

The conclusions regarding {6} dominance are interesting. The data tend to go in the predicted direction, implying consistency with some enhancement of {6} beyond the expected short range QCD effects.[4] Quantitative calculations of these effects are discussed in the following sections, within the Heavy Quark Decay Model.

An interesting independent test of {6} dominance has been proposed by Rosen[8] using $D^{\pm}$, D^{0} and $F^{\pm}$ lifetimes. The $u \leftrightarrow s$ symmetry (V-spin invariance) in the {6} implies that the D^{0} and $F^{\pm}$ (both V-spinors) must have approximately equal nonleptonic widths if {6} dominance is valid.[8] Since the semileptonic widths for D^{0} and $F^{\pm}$ are approximately equal (assuming $c \rightarrow s\ell\nu$ predominates), the total $F^{\pm}$ and D^{0} widths are approximately equal, and hence their lifetimes as well. Rosen[8] presents an alternative to {6} dominance which shortens the D^{0} lifetime relative to the $D^{\pm}$ and $F^{\pm}$. The diagrams contributing to leading charm meson decay are shown in Fig. 1. Rosen suggests that the D^{0} decays via (b) may be significant, if the D^{0} mass is not large enough for asymptotic freedom assumptions to be valid (which make (a) dominate). $F^{\pm}$ and $D^{\pm}$ do not proceed by (b).

The lifetime of the D^{0} would therefore be shortened relative to the $D^{\pm}$. $F^{\pm}$ decays proceed by (a) and (c); however, Rosen argues that the leptonic plus nonleptonic contributions from (c) are at most 15% of the $F^{\pm}$ total width. Thus, as in the $D^{\pm}$ case, $F^{\pm}$ decays proceed mostly by (a), and would have about the same total decay width if the diagrams were calculated assuming $\bar{q}$ simply a spectator in (a). The validity of the last assumption is suggested only by the closeness of the measured $17 \pm 6\%$ $B(D^{\pm} \rightarrow e\nu X)$ to the expected 15 - 20% rate in such a free quark model. In conclusion, the measurement of the $F^{\pm}$ lifetime is a possible

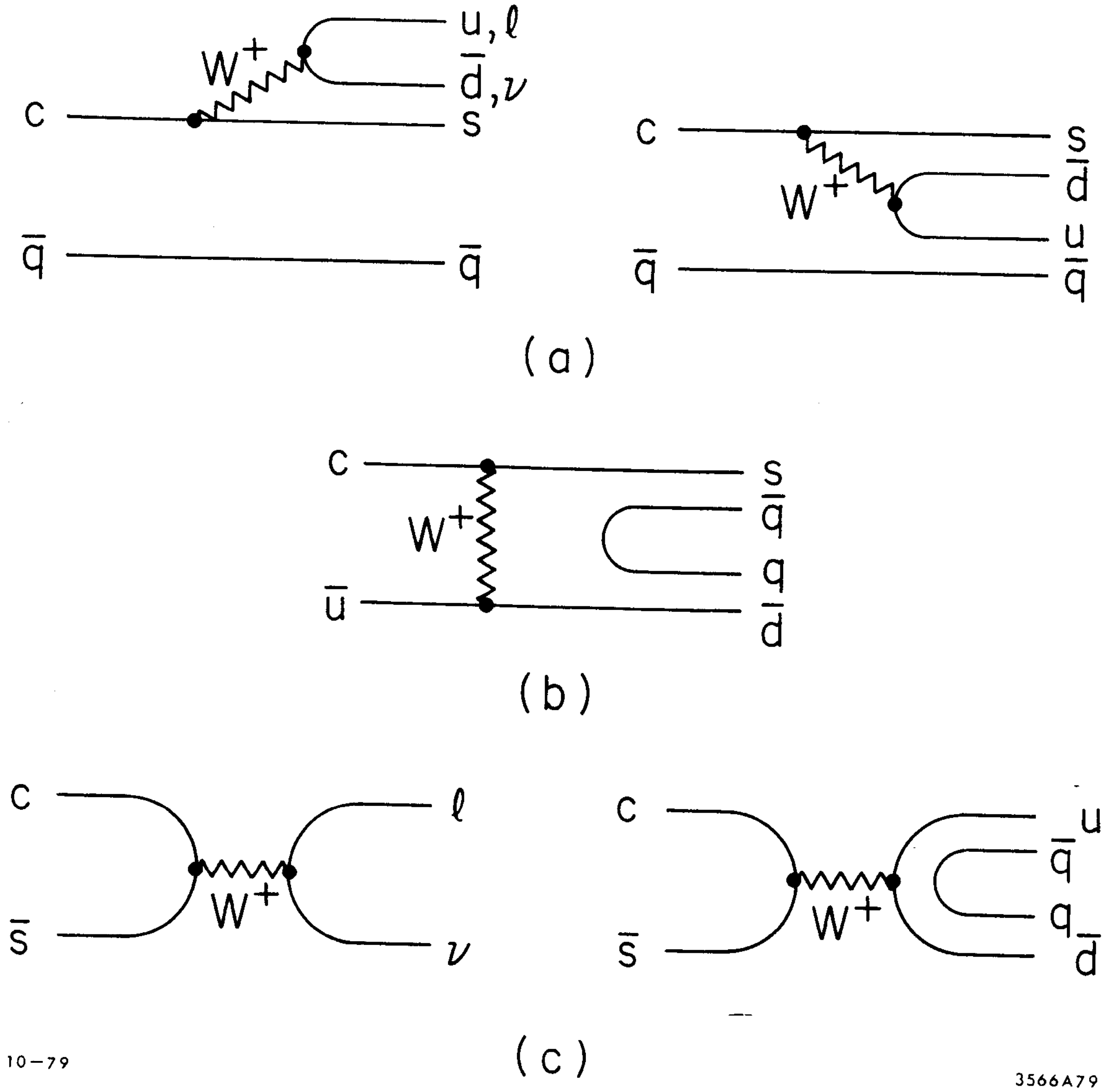

Fig. 1. Diagrams for charmed meson decays.

means for resolving the question of {6} dominance. Very preliminary measurements [10] from emulsions in a neutrino-induced charm production experiment have reported fourteen events of charmed origin: two Λ_c^+, four D^o, one $F^{\pm}$ and three ambiguous $F^{\pm}/D^{\pm}$ events. The D^o events have $\langle \tau^o \rangle \approx .7 \pm 10^{-13}$ sec while the one $F^{\pm}$ yields $\tau^+ \approx 3.6 \pm 10^{-3}$ sec. The ambiguous events appear to have $\langle \tau^+ \rangle \approx 9. \pm 10^{-13}$ sec. The single unambiguous event favors the $F^{\pm}$ life close to the D^o as {6} dominance implies.

Heavy Quark Decay Models

Numerous authors [11] have attempted to exploit the high mass of charmed particles to simplify calculations of both the partial widths to two-body and semileptonic final states, as well as full widths. In particular, it is argued that the decays of charmed mesons can be calculated accurately using a weak current-current form for the Lagrangian (see for example, Fakirov and Stech, Ref. 11) ignoring the complications of the strong interactions. The justifications lie in asymptotic freedom arguments, the absence of "penguin diagrams" and the assumption for two-body decays that final state interactions are negligible. Decays are assumed to occur via diagrams where the light quark is a spectator (as in Fig. 1a) while the hard gluon production of quark pairs (as in Fig. 1b) is ignored. [11]

The effects of color and the small (~ 3.2x) QCD enhancement fac-factors of the [20] to [84] coupling constants [4] are entered into the calculation. In some versions of the model [12] a further attempt is made to calculate the final recombination rates by factorization of the currents and insertion of form factors, or by drawing on calculations from semileptonic $\tau^{\pm}$ decays. Otherwise, one or more unknown amplitudes remain. The problem with these calculations is the resulting prediction of equal nonleptonic widths for D^0 and $D^{\pm}$ which thus results in equal lifetimes. The $Br(D^{\pm} \to e\nu X) = Br(D^0 \to e\nu X) \approx 13 - 15\%$ in these models, being reduced by QCD enhancement from the 20% expected in a free quark model[11] (with color, but no enhancement). Koide[13] has suggested that in these models, the calculation of the total width should be modified. He suggests that the $D^{\pm}$ and D^0 diagrams in the heavy quark decay model which yield color "connected" or "disconnected" (see Fig. 1a) final states[14] must be added coherently in the $D^{\pm}$ case, and incoherently for the D^0, because only for the D decay does one obtain distinct final states from these two classes of graphs. In addition, moderate {6} enhancement beyond QCD is invoked. The resulting calculation yields $\tau^{\pm}/\tau^0 \approx 5$, which is considerably closer to the data. A similar calculation by Guberina et al., obtains essentially the same result.[13]

Thus while these models may correctly calculate the partial widths (e.g., interference is handled correctly), the relative charged and neutral branching ratios obtained must be scaled by the correct ratio of total widths. Additional uncertainty in the correct enhancement factor still remains, though. In Table III, the measured two-body rates are compared with several of these models.[11]

The lack of agreement is fairly large in both examples. In particular, the $\bar{K}^0\pi^0 : K^-\pi^+$ for which we expect to have the uncertainty in total widths taken out, deviates dramatically. The smallness of the $\bar{K}^0\pi^0$ is expected in all such models as a result of cancellation of amplitudes arising from the [20] and [84] if only QCD enhancement is assumed.[15] The effect is often termed "color" suppression".

TABLE III

Comparison of Two-Body Data with Heavy Quark Decay Models [11]

	Data	Faikrov and Stech	Cabibbo and Maiani	Barger and Pakvasa	Jagannathan and Mathur
$\frac{Br(D^0 \to \bar{K}^0 \pi^0)}{Br(D^0 \to K^- \pi^+)}$	0.73 ± 0.35	0.024	0.025	0.028	0.024
$\frac{Br(D^0 \to K^- \pi^+)}{Br(D^+ \to \bar{K}^0 \pi^+)} \frac{\tau^{\pm}}{\tau^0}$	$(1.29 \pm 0.30) \frac{\tau^{\pm}}{\tau^0}$	1.67	1.67	1.85	1.71

Koide [13] and Guberina et al., [13] have shown that the assumption of additional {6} enhancement beyond QCD can both bring the total widths and these two-body branching ratios within the experimental values. The [20] and [84] cancellation is reduced in the $\bar{K}^0 \pi^0 / K^- \pi^+$, and the difference in total widths of D^0 and $D^{\pm}$ accounts for the $K^- \pi^+ / \bar{K}^0 \pi^+$ discrepancy.

Donoghue and Holstein [15] suggest that the violations of these estimates may arise, however, from final state interactions involving the S wave $K\pi$ resonance $\kappa(1400)$. This resonance could effectively convert the more dominant $K^- \pi^+$ to $\bar{K}^0 \pi^0$, thus violating the model's predictions at a significant enough level to account for the discrepancy. Deshpande et al., [17] suggest that final state soft gluon exchange may effectively reduce the $\bar{K}^0 \pi^0$ suppression and show that modifications introduced leave the model otherwise unchanged. Given these considerations, it is not clear that these oversimplified models are generally reliable.

BRANCHING RATIOS FOR CABIBBO SUPPRESSED DECAYS

The last section contained a discussion of several theoretical approaches to the calculation of decay rates for D mesons. In this section they will be reapplied to the case of the Cabibbo suppressed two- and three-body decays which have been measured.

SU(3) Predictions

The simplest predictions come from relations among the decays assuming SU(3) invariance, with Cabibbo factors coming from the simple four-quark model (see Introduction, Chapter V). For $\pi^+\pi^-$, K^+K^-, $K^\pm\pi$, $\bar{K}^o\pi^+$ and $\pi^o\pi^+$ we have :[16]

$$\frac{\Gamma(K^-K^+)}{\Gamma(K^-\pi^+)} = \frac{\Gamma(\pi^-\pi^+)}{\Gamma(K^-\pi^+)} = 2\,\frac{\Gamma(\pi^o\pi^+)}{\Gamma(\bar{K}^o\pi^+)} = \tan^2\theta_c \qquad (1)$$

(within relative momentum factors).

Here θ_c is the same mixing angle as in strange particle decays, and $\tan^2\theta_c \approx 0.05$. These relations result essentially from the U-spin ($s \leftrightarrow d$) transformation property of Cabibbo-suppressed current and require no dominance assumptions. No simple prediction for $\bar{K}^oK^+$ relative to $\bar{K}^o\pi^+$ can be made, since their amplitudes involve more than one reduced matrix element. Under the assumption of complete sextet dominance, $\Gamma(\bar{K}^o\pi^+) = 0$, $\Gamma(\pi^+\pi^o) = 0$, while $\Gamma(\bar{K}^oK^+) \propto \cos^2\theta_c \sin^2\theta_c$ and is related to the $K^-\pi^+$, $\pi^-\pi^+$, K^-K^+ amplitudes.

The measurements of Chapter V show that:

$$\frac{\Gamma(\pi^-\pi^+)}{\Gamma(K^-\pi^+)} = 0.033 \pm 0.015\ , \qquad \frac{\Gamma(K^-K^+)}{\Gamma(K^-\pi^+)} = 0.113 \pm 0.030\ ,$$

$$\frac{\Gamma(\pi^o\pi^+)}{\Gamma(\bar{K}^o\pi^+)} = < 0.30\ (90\%\ \text{C.L.})\ , \qquad \frac{\Gamma(\bar{K}^oK^+)}{\Gamma(\bar{K}^o\pi^+)} = 0.25 \pm 0.15\ . \qquad (2)$$

To remove relative momentum factors implies raising the $K\bar{K}$ rates $\sim 8\%$ and lowering the $\pi\pi$ rates about 7% relative to $K\pi$. The most disturbing quantity is the K^+K^- rate, because it is well measured and also deviates significantly ($\sim 2\sigma$) from the expected $\sim 5\%$. The $\pi^+\pi^-$ rate is lower by about 1σ. The $\pi\pi^0$ rate and $\bar{K}^0K$ rates are poorly measured and do not pose a problem.

In order to maintain SU(3) symmetry and account for the observed rates in (2), several authors[8,18,19] have extended the SU(3) predictions to the six-quark model (see Introduction, Chapter V for definitions), thus allowing for additional mixing between different quark flavors under the weak interaction. The addition of the $\{3\}$[8] complicates matters and leads to five invariant matrix elements where only three existed previously in the four-quark model. Of all three relations given in (1), only a simple one between $\pi^+\pi^0$ and $\bar{K}^0\pi^+$ widths remains with $\tan\theta_c$ (= 0.231 ± 0.005 from Ref. 20) replaced by $\tan\theta_c'$ which is the ratio of mixing angles for $c \leftrightarrow d$ and $c \leftrightarrow s$ in the Kobayashi-Maskawa (KM) matrix:

$$\begin{aligned} \tan^2\theta_c &= |s_1\, c_3/c_1|^2 \\ \tan^2\theta_c' &= |s_1\, c_2/(c_1c_2c_3 + s_2s_3\, e^{i\delta})|^2 . \end{aligned} \tag{3}$$

The loose limit from (2) on $\Gamma(\pi^+\pi^0)/\Gamma(\bar{K}^0\pi^+)$ is easily satisfied within the four-quark model, and within the six-quark model as well since current limits[21] place $\tan^2\theta_c' < 0.02 - 0.13$. No simple prediction for $\bar{K}^0K$ is obtained, without invoking the value of $\tau^\pm/\tau^0$ and sextet dominance.

The simple U-spin relation (1) between the $K^-\pi^+$, $\pi^+\pi^-$ and K^+K^- no longer exists and is replaced by several triangle inequalities[8,18,19] which contain tan θ_c, tan θ_c' and the ratio of two reduced matrix elements. It is pointed out by all these authors [8,18,19] that these inequalities are accomodated within the six-quark model given the current limits on the mixing parameters. These values are determined independently from neutron beta decay, kaon decays, the $K_S^o - K_L^o$ mass difference, and CP violation.[20] Wolfenstein [19] has explored the possibility that the $\pi^+\pi^-$ rate can be used to determine the quadrant of δ (the CP violating parameter), under the exact SU(3) assumption. The $K\bar{K}$ basically measures the $u \leftrightarrow s$ current which is better done in ordinary strange particle decays. By using a triangle inequality and assuming the U-spin matrix elements are real, Wolfenstein relates (2) directly to tan θ_c and tan θ_c'. Then using the limits[20] on the three mixing angles, cos δ is constrained to be less than zero.

The question of SU(3) breaking effects have been discussed extensively.[8,15,18,19,21,22,23] The proposed sources of such breaking are final state interactions, helicity suppression, the penguin operators, and the ratio of f_K/f_π (the pion and kaon beta decay constants). To point out some of the problems these introduce, consider the last where Barger et al.,[21] extends the heavy quark decay model to encompass the new mixing angles, calculating all matrix elements for the two-body suppressed decays. The K^+K^- rate is enhanced by the SU(3) breaking value of $(f_K/f_\pi)^2$, but is still proportional to the old $u \leftrightarrow s$ current. The $\pi^+\pi^-$ rate is suppressed by $(\tan\theta_c')^2$ using the new mixing angles. By using the data in (2), they obtain the opposite result that $\cos\delta > 0$, than in the unbroken SU(3) limit.[19]

Final state interactions were discussed with respect to the $\bar{K}^o\pi^o$ rate in the previous sections. While some authors feel they may be be significant [15] in the $\pi\pi$, $K\bar{K}$ case, the lack of any S wave phase shifts in $\pi\pi$ or $K\bar{K}$ scattering near the D mass region [24] leads others [18] to believe that this effect is not important in the suppressed decays.

Helicity suppression is a dynamical effect proposed [15] as a source of some of the difference in the $K\bar{K}$ and $\pi\pi$ rates. Basically, in the two-body $\pi\pi$ case one is dealing with all light quarks moving away from each other rapidly, while in the $K\bar{K}$ case, two of the quarks are heavy. In analogy with the decay $\pi^+ \to \mu^+\nu$ versus $\pi^+ \to e^+\nu$, a suppression results in the latter from angular momentum conservation and the greater alignment of the electron spin against its direction of motion, than in the heavier muon case. In the MIT bag model, the effect amounts to $\sim 1.6 - 1.8$ in the $K\bar{K}$ to $\pi\pi$ amplitudes. [15]

Finally, it has been suggested by many authors that "penguin" diagrams may be a source of the $K\bar{K}$ enhancement [15,18,23] as they may be the source of nonleptonic enhancement in strange particle decays. In a four-quark model, the effect is shown to be small [15,22] and unable to account for (2). The addition of extra mixing angles (in a six-quark model with color) has been shown by Holstein [15] to increase the "penguin" operator contribution significantly, perhaps providing some of the $K\bar{K}$ enhancement.

The conclusion that can be drawn from these results is that several effects can lead to significant SU(3) breaking. These in turn make it difficult to compare or determine the KM parameters from the hadronic two-body decays. The cleanest results would come from semileptonic Cabibbo suppressed decays where the final state contains only a few hadrons.

The three and four body decays which have been presented as upper limits are difficult to compare with theory since no simple relations exist among them. They do not appear anomalously large, if one makes the naïve assumption that they should be $\sim 5\%$ of the corresponding nonsuppressed mode. This latter assumption is not unreasonable considering the inclusive measurements of wrong sign kaons of Chapter VI, indicating rates of $5-7\%$ for both D^0 and $D^{\pm}$.

REFERENCES

1. Rapidis, P, et al., Phys. Rev. Lett. 39, 1301 (1977); Bacino, W., et al., Phys. Rev. Lett. 40, 526 (1977); Peruzzi, I., et al., Phys. Rev. Lett 39, 1301 (1977).
2. Eichten, E., et al., Phys. Rev. D17, 3090 (1978).
3. Fermi, E., Phys. Rev. 92, 452 (1953); Peshkin, M., Rosner, J. L., Nucl. Phys. B122, 144 (1977); Quigg, C., Rosner, J. L., Phys. Rev. D17, 239 (1978); Rosner, J. L., Orbis Scientiae, Coral Gables (1977).
4. Altarelli, G. and Cabibbo, N., Phys. Lett. 52B, 351 (1974); Gaillard, J. K. and Lee, B., Phys. Rev. Lett. 33 108 (1974).
5. Shifman, M. A., Vainshtein, A. I. and Zakharov, V. I., JETP Lett. 22, 55 (1975), Nucl. Phys. B126, 316 (1977), and Sov. Phys. JETP 45, 670 (1977).
6. Gaillard, M. K., Proceedings of the SLAC Summer Institute on Particle Physics, 1978, (ed. Zipf, M.), SLAC-Report-215, p. 397; and Ellis, J., Gaillard, M. K., and Nanopoulos, D. V., Nucl. Phys. B100, 313 (1975).
7. For excellent discussions see: Einhorn, M., Quigg, C., Phys. Rev. D12, 2015 (1977); Kingsley, R., Treiman, S. B., Wilczek, F., Phys. Rev. D11, 1919 (1975); Altarelli, G., Cabibbo, N, Nucl. Phys. B88, 285 (1975).
8. Wang, L. C., and Wilczek, F., Phys. Rev. Lett. 43, 816 (1979).
9. Rosen, S. P., "Remarks on the Differing Lifetimes of Charmed Mesons, Los Alamos preprint, and Phys. Rev. D18, 2514 (1978).

10. Prentice, J., Proceedings of the International Symposium on Lepton and Photon Interactions at High Energies, Fermilab, August 1979 (to be published).

11. Ellis, J., Gaillard, M. K., and Nanopolous, D., Nucl. Phys. B100, 313 (1975); Fakirov, D., and Stech, B., Nucl. Phys. B133, 315 (1978); Cabibbo, N., Maiani, L, Phys. Lett. 73B, 418 (1978); Jagannathan, K, Mather, V., University of Rochester, Report UR-709 (1979); and Barger, V., Pakvasa, S., Phys. Rev. Lett. 43, 812 (1979).

12. See Ref. 11, Fakirov and Stech; Barger and Pakvasa; Jagannathan and Mathur.

13. Koide, Y., Phys. Rev. D1 (1979).
Peccei, R. D., Ruckl, R., Max Plank Institute Preprint, MPI-PAE/PTH 45/79 (Sept. 1979).

14. The use of color "connected" and "disconnected" graphs is best explained in Barger, *et al*., Ref. 11.

15. Donoghue, J. F., Holstein, MIT preprint, CTP-779 (to be published, Phys. Rev. D).

16. Donoghue, J. F., Wolfenstein, L., Phys. Rev. D15, 3314 (1977).

17. Deshpande, N., Gronau, M., Sutherland, D., Fermilab-Pub-79/70-Thy.

18. Suzuki, M., Phys. Rev. Lett. 43, 818 (1979).

19. Wolfenstein, L., Carnegie-Mellon Print COO-3066-134 (1979).

20. See for example, Barger, V., Long, W., Pakvasa, S., Phys. Rev. Lett. 42, 1585 (1979), and Shrock, R. E., Treiman, S., Wang, L. L., Phys. Rev. Lett. 42, 1589 (1979).

21. See Barger, V., Pakvasa, S., Ref. 11.

22. Abbott, L., Sikivie, P., and Wise, M. B., Stanford Linear Accelerator Center, SLAC-PUB-2355 (1979).

23. Gluck, M., University of Mainz, Preprint MZ-TH-79/6 (1979).

24. Bricman, C., *et al*., Phys. Lett. 75B, 1 (1978).

APPENDIX A

Basic Track Finding and Fitting Expressions

This Appendix is meant to be a guide to aid in understanding the tracking algorithm. More complete information is available in Ref. 1, Chapter III.

d_k^m = measured distance of closest approach to a wire in layer k

σ_i^m = measurement error on d_k^m

α_μ = parameters describing a linked helical orbit (for μ=1,5 they are ϕ, κ, S, η, ξ)

d_k = predicted distance of closest approach given the orbit defined by α_μ

r_k = residual at the kth layer

$= d_k^m - d_k$

The fit seeks to minimize a χ^2 formed of

$$\chi^2 = \sum_{k=1}^{N} r_k^2/\sigma_k^2 \qquad N = \text{points in the road} \tag{1}$$

with respect to α_μ. Thus we seek a solution of

$$\frac{\partial\chi^2}{\partial\alpha_\mu} = 0 \qquad \mu=1,5 \tag{2}$$

or

$$\sum_k \left(\frac{r_k}{\sigma_k^2}\right) \frac{\partial d_k}{\partial\alpha_\mu} = 0 \tag{3}$$

These equations are linearized by expanding the orbit position d_k about its starting value, in terms of variations $\delta\alpha_\tau$ of the α_τ:

$$d_k \cong d_k^o + \sum_\tau \frac{\partial d_k}{\partial\alpha_\tau}\,\delta\alpha_\tau \tag{4}$$

The five equations then reduce to a linear system in $\delta\alpha_\tau$:

$$\sum_\tau \sum_k \frac{\partial d_k}{\partial \alpha_\tau} \frac{\partial d_k}{\partial \alpha_\mu} \delta\alpha_\tau = +\sum_k \left(\frac{r_k^o}{\sigma_k^2}\right) \frac{\partial d_k}{\partial \alpha_\mu} \tag{5}$$

Here $r_k^o = d_k^m - d_k^o$. This can be put into the matrix form by defining:

$$G_{\mu\tau} = \sum_k \frac{\partial d_k}{\partial \alpha_\tau} \frac{\partial d_k}{\partial \alpha_\mu}$$

$$F_\mu = -\sum_k \left(\frac{r_k^o}{\sigma_k^2}\right) \frac{\partial d_k}{\partial \alpha_\mu}$$

hence:

$$G_{\mu\tau}\ \delta\alpha_\tau = -F_\mu \tag{6}$$

Given the solution $\delta\alpha_\tau$ by inversion of G, the next set of orbit parameters α_τ $(= \alpha_\tau + \delta\alpha_\tau)$ is determined. The iteration proceeds by the analytic calculation of the new orbit's derivatives $\partial d_i/\partial\alpha_\tau$, exact residuals r_k, and errors σ_k. The latter two change on each iteration because a better estimate of z and incidence angle are obtained from the new orbit, and the d_k^m and σ_k are strong functions of these.

Once the solution $\delta\alpha_\tau$ in a given step is computed, an <u>estimate</u> of the d_k is available (Eq. (4)), thus allowing a precalculation of χ^2 before performing the step:

$$\chi^2_{new} = \sum_k \left(\frac{r_k^o}{\sigma_k^2}\right)^2 + \sum_\tau F_\tau\ \delta\alpha_\tau \tag{7}$$

This has the advantage of allowing a χ^2 test of different ambiguity hypotheses on many layers, with <u>only</u> the single matrix inversion and calculation of F. Ambiguities can only change d_k^m and σ_k. It is equally easy to calculate the error matrix once G is inverted.

Substituting at any step (4) into (3) using the definition of r_k, and realizing that $\frac{\partial}{\partial(\delta\alpha_\tau)} = \frac{\partial}{\partial\alpha_\tau}$ we obtain:

$$\frac{1}{2}\frac{\partial^2\chi^2}{\partial\alpha_\tau\partial\alpha_\mu} = \sum_k \frac{1}{\sigma_k^2}\frac{\partial d_k}{\partial\alpha_\tau}\frac{\partial d_k}{\partial\alpha_\mu} = G_{\tau\mu}$$

thus the error matrix Σ is given:

$$(\Sigma)_{\tau\mu} = (G^{-1})_{\tau\mu} \tag{8}$$

<u>Basic Track Finding Relations</u>

The variables θ_o, θ_j, R (= $1/\kappa$), z_i, and r_i are shown in Figure 1. The approximations follow:

$$\frac{r_i}{2R} = \sin\left(\theta_i-\theta_o \pm \alpha\frac{z_i}{R}\right) \qquad (\alpha = \text{stereo angle}) \tag{9}$$

$$r_i = \frac{z_i-z_o}{\tan\lambda} \cong 2R\left(\theta_i-\theta_o \pm \alpha\frac{z_i}{R}\right) \tag{10}$$

Solving for z_i and substituting it in (9) we can obtain:

$$\theta_i-\theta_o \approx \frac{r_i}{2R} \mp \alpha\tan\lambda \mp \alpha\frac{z_o}{r_i}$$

For tracks near the origin ($z_o < 10$ cm), the last term is ignorable, leaving:

$$\theta_i = \theta_o + \frac{r_i}{2}\kappa \mp \alpha\tan\lambda \tag{11}$$

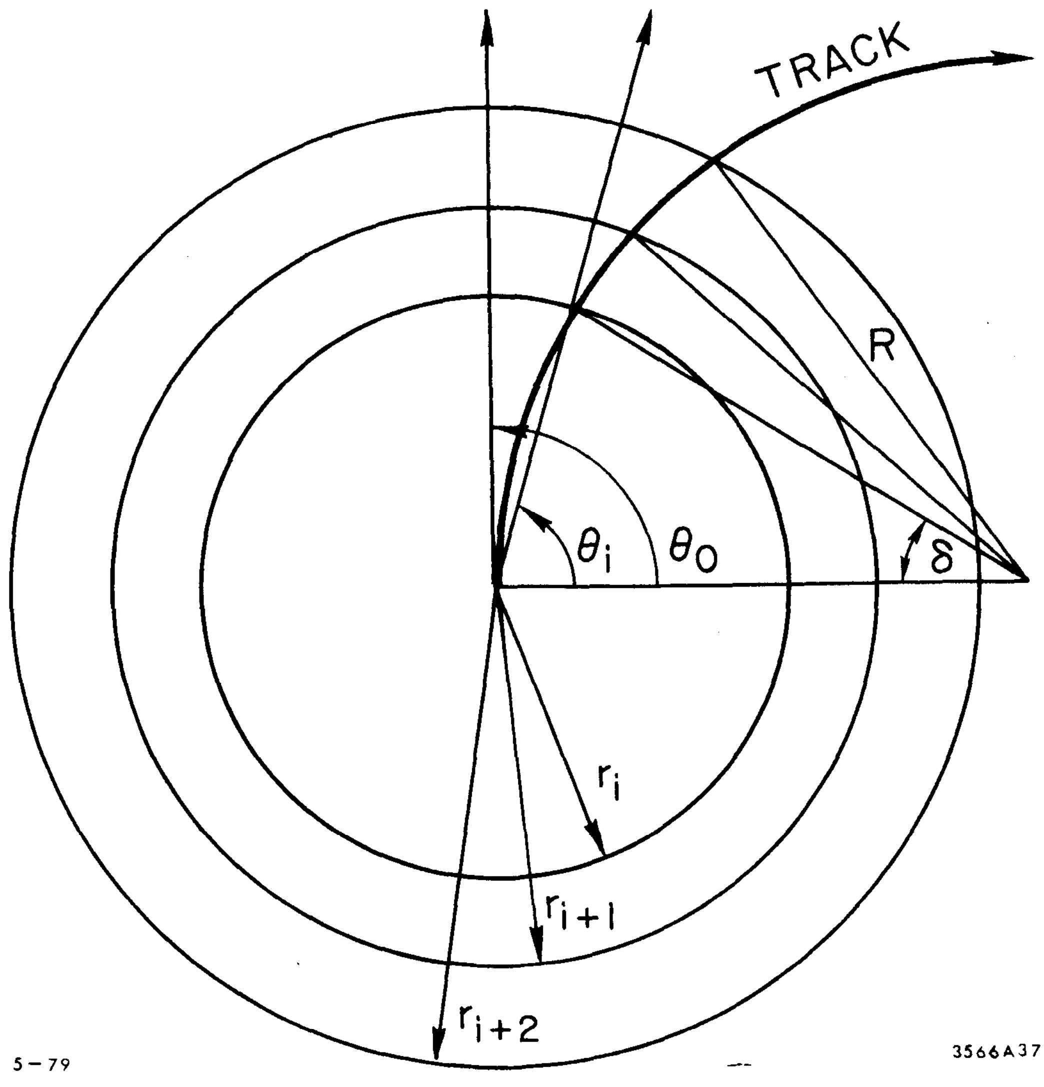

Fig. 1. Schematic showing track, and a definition of the angles θ_i and radii r_i at each drift chamber layer.

APPENDIX B

Momentum and Angular Resolution

This Appendix provides a useful summary of expressions used in estimating momentum and angular resolution resulting from finite measurement error and multi-Coulomb scattering. The following definitions are used throughout:

ε	=	the uncorrelated RMS position error
L	=	projected track length (in appropriate projection)
N+1	=	number of uniformly spaced measurements along a trajectory
ϕ	=	azimuthal angle in xy plane
θ	=	polar angle from the z axis
c	=	the curvature (1/radius)
α	=	stereo offset angle of the wires
K	=	mean-squared projected multiple scattering angle per unit thickness
H	=	mean longitudinal magnetic field (z-direction)
L_R	=	radiation length of material traversed.

Units, unless specified, will be GeV, kG, milliradians, and meters.

The following analytical results are derived (see Ref. 3, Chapter III) from performing a least-squares fit of a set of N+1 equally-spaced, measured points along a trajectory, to the polynomial:

$$y = \Delta + \phi x + \frac{1}{2} c x^2$$

For a circle in xy projection, we can relate $p_\perp$ to the curvature:

$$p_\perp = .03 \text{ H } c^{-1} \qquad (1)$$

For fixed H we have:

$$(\delta c)_m^2 = \left(\frac{\delta p}{p}\right)_m^2 \left(\frac{.03\ H}{p}\right)^2$$

The subscript m will denote measurement error, whereas, ms will denote multi-scattering error. The basic expressions are given:

$$(\delta c)_m^2 = \frac{\varepsilon^2}{L^4}\left[\frac{720\ N^3}{(N-1)(N+1)(N+2)(N+3)}\right] = \frac{A_N \varepsilon^2}{L^4} \quad (2)$$

$$(\delta\phi)_m^2 = \frac{\varepsilon^2}{L^2}\left[\frac{12(2N+1)(8N-3)\ N}{(N-1)(N+1)(N+2)(N+3)}\right] = \frac{B_N \varepsilon^2}{L^4} \quad (3)$$

$$(\delta c)_{ms}^2 = \frac{K}{L} C_N \quad (4)$$

$$(\delta\phi)_{ms}^2 = KLE_N \quad (5)$$

The correlation terms between δc and $\delta\phi$ are given in Chapter III, Ref. 3.

The coefficients A_N, B_N, C_N and E_N are given in Table I for typical values of N. An approximate expression for K is given:

$$K(\text{radians}) = \frac{\langle \phi^2_{\text{projected}} \rangle}{L} = \left(\frac{.015}{p\beta c}\right)^2 \frac{1}{L_R} \quad (6)$$

The z component of momentum derives its error from the error on the dip or polar angle θ:

$$(\delta\theta)_m^2 = \left(\frac{\varepsilon'}{L}\right)^2 \frac{12N}{(N+1)(N+2)} \quad (7)$$

$$(\delta\theta)_{ms}^2 = \frac{1}{3} KL \quad (8)$$

Here, $\varepsilon' \approx \varepsilon/\sin\alpha \approx 20\ \varepsilon$ for this experiment.

TABLE I

N	6	8	10	13	15	>>15
A_N	61.7	53.2	42.1	39.2	35.4	720/N+5
B_N	16.7	14.4	11.3	10.6	9.52	192/N+4.9
C_N	-	-	1.32	-	-	1.43
E_N	-	.18	-	.21	-	.229

Thus the total momentum and its error are given:

$$p = p_{\perp}/\sin\theta$$

$$\left(\frac{\delta p}{p}\right)^2 = \left(\frac{\delta p_{\perp}}{p_{\perp}}\right)^2 + \left(\frac{\delta(\sin\theta)}{\sin\theta}\right)^2 + \text{correlation term} \tag{9}$$

$$= \left(\frac{\delta p_{\perp}}{p_{\perp}}\right)^2 + \left(\frac{\cos^2\theta}{1-\cos^2\theta}\right)(\delta\theta)^2 + \text{correlation term} \tag{10}$$

APPENDIX C

Determination of Drift Chamber Constants

The functional form of the drift velocity is given in the text of Chapter III. Using these same variables, we linearize the equations by letting:

$$\bar{\nu}_i \rightarrow \bar{\nu}_i + \delta\bar{\nu}_i \qquad i = 1,3$$

$$\beta_i(\alpha) \rightarrow \beta_i(\alpha) + \delta\beta_i(\alpha) \qquad i = 1,2$$

$$C_{FW}(\alpha) \rightarrow C_{FW}(\alpha) + \delta C_{FW}(\alpha)$$

The equations for measured time t become (keeping first order terms):

$\underline{t < t_c}$

$$\bar{\nu} = \bar{\nu}^{old} + \delta\bar{\nu}_1(L) + \delta\bar{\nu}_2(L)(t-t_c)^2 + \delta\bar{\nu}_3(L)\beta_1(\alpha=0)(t-t_c) + \delta\beta_1(\alpha=0)\bar{\nu}_3(L)(t-t_c)$$

$\underline{t_c < t \leq t_f}$

$$\bar{\nu} = \bar{\nu}^{old} + \delta\bar{\nu}_1(L) + \delta\bar{\nu}_3(L)[\beta_1(\alpha)(t-t_c) + \beta_2(\alpha)(t-t_c)^2] + \bar{\nu}_3(L)[\delta\beta_1(\alpha)(t-t_c) + \delta\beta_2(\alpha)(t-t_c)^2]$$

$\underline{t_f < t}$

$$\bar{\nu} = \bar{\nu}^{old} + \delta\bar{\nu}_1(L) + \delta\bar{\nu}_3(L)[\beta_1(\alpha)(t-t_c) + \beta_2(\alpha)(t-t_c)^2] + \bar{\nu}_3(L)[\delta\beta_1(\alpha)(t-t_c) + \delta\beta_2(\alpha)(t-t_c)^2] + \delta\bar{\nu}_3[C_{FW}(t-t_f)^2] + \bar{\nu}_3[\delta C_{FW}(\alpha)(t-t_f)^2]$$

where $\bar{\nu}^{old}$ refers to the velocity calculated with the current parameters.

These expressions are general. As a concrete example, consider the procedure for simultaneously fitting for ν_1 and ν_3, which vary only by layer. We would use the equations above, setting the other variations $\delta\beta_1$, $\delta\beta_2$, $\delta\nu_2$, δC_{FW} to zero. This leaves:

$\underline{t \le t_c}$

$$\bar{\nu} = \bar{\nu}^{old} + \delta\bar{\nu}_1(L)(t-t_c)^2 + \delta\bar{\nu}_3\beta_1(0)(t-t_c) \qquad (1)$$

$\underline{t < t \le t_f}$

$$\bar{\nu} = \bar{\nu}^{old} + \delta\bar{\nu}_1 + \delta\bar{\nu}_3[\beta_1(t-t_c) + \beta_2(t-t_c)^2] \qquad (2)$$

$\underline{t_f < t}$

$$\begin{aligned}\bar{\nu} = \bar{\nu}^{old} &+ \delta\bar{\nu}_1 \\ &+ \delta\bar{\nu}_3[\beta_1(t-t_c) + \beta_2(t-t_c)^2] \\ &+ \delta\bar{\nu}_3[C_{FW}(t-t_f)^2] \qquad (3)\end{aligned}$$

These expressions generally can be written:

$$\bar{\nu} = \bar{\nu}^{old} + a(\alpha,L,t)\ \delta\bar{\nu}_1(L) + b(\alpha,L,t)\ \delta\bar{\nu}_3(L)$$

for each track at a particular layer. The a and b are evaluated from (1) - (3), for the appropriate measured time t. A χ^2 over all drift chamber hits can be formed from the track's fitted distance to the sense wire (using $\bar{\nu}^{old}$) and the predicted distance based on $\bar{\nu}$ given above.

$$\begin{aligned}\chi^2_L &= \sum_{\text{hits in L}} (DCA_{fit} - DCA_{pred})^2 \\ &= \sum (DCA_{fit} - t\bar{\nu}^{old} - ta\ \delta\bar{\nu}_1 - tb\ \delta\bar{\nu}_3)^2\end{aligned}$$

The first two terms clearly form a residual. In this example, we only are calculating $\delta\bar{\nu}_1$, $\delta\bar{\nu}_3$ for one particular layer L. The first two terms on the χ^2 sum are the usual residual of the fit. In seeking to converge to $\delta\bar{\nu}_1 = \delta\bar{\nu}_3 = 0$, we are seeking to reduce the χ^2 of the ARCS fit.

It is now trivial to find $\delta\bar{\nu}_1$, $\delta\bar{\nu}_3$ which minimize χ_L^2, by solving the linear system:

$$\frac{\partial\chi_L^2}{\partial\delta\bar{\nu}_1} = 2 \sum_{\text{hits in L}} (DCA_{fit} - t\bar{\nu}^{old} - ta\ \delta\bar{\nu}_1 - bt\ \delta\bar{\nu}_3)(-a)\,t = 0$$

$$\frac{\partial\chi_L^2}{\partial\delta\bar{\nu}_3} = 2 \sum_{\text{hits in L}} (DCA_{fit} - t\bar{\nu}^{old} - ta\ \delta\bar{\nu}_1 - bt\ \delta\bar{\nu}_3)(-b)\,t = 0$$

Then

$$\bar{\nu}_1 = \bar{\nu}_1^{old} + \delta\bar{\nu}_1 \qquad \text{and} \qquad \bar{\nu}_3 = \bar{\nu}_3^{old} + \delta\bar{\nu}_3$$

This gives us one set of parameters $\bar{\nu}_1$, $\bar{\nu}_3$ for each layer L. In a similar fashion, the pair $\beta_1(\alpha)$ and $\beta_2(\alpha)$, and the single parameters $\bar{\nu}_2$, $C_{FW}(\alpha)$ are determined. The complete solution is determined by alternately iterating by pairs of parameters and tracking over again.

APPENDIX D

MULTIPLICITY UNFOLD

This appendix describes the mathematical procedure used for determining a best estimate of the produced multiplicity distribution, given an observed multiplicity distribution and an estimate of the background distribution. Let:

ε_{ji} = probability of observing j particles when i are produced.

D_j = number of events with j particles observed.

P_i = fitted number of events where i particles were produced.

B_i = fitted number of background events with i particles observed.

$(B_i^o)\cdot\Delta$ = estimate of the number of background events of multiplicity i. Here B_i^o is the original distribution, and Δ is the scale factor reducing B_i to the expected number in each D_i bin.

α = $\sum_i P_i$ (total number of fitted events).

$\bar{n}$ = $\left(\sum_i iP_i\right)\Big/\alpha$ (average produced multiplicity).

The problem is to find P_i and B_i given D_j, B_j^o, ε_{ij} and Δ. The solution is to numerically minimize the -log likelihood function ($-\mathscr{L}$):

$$\mathscr{L} = \sum_j \left\{ -\left[\sum_i \varepsilon_{ji}P_i + \Delta\cdot B_j\right] + D_j \,\ell n \left[\sum_i \varepsilon_{ji}P_i + \Delta B_j\right] - \ell n\left[D_j!\right] \right\}$$

$$+ \sum_k \left\{ -B_k + B_k^o \ell n B_k - \ell n(B_k^o!) \right\} \quad . \tag{1}$$

The final $\sum_k$ allows the background to vary within the statistical errors with which it was measured before scaling by Δ. The solution is not constrained to reproduce the original number of events and background:

$$\alpha + \sum_i \Delta B_i \neq \sum_i D_i \quad . \tag{2}$$

The added constraint can be implemented with an extra term, however, the results did not change significantly (an equality in Eq. (2) can be added simply with a Lagrange multiplier to Eq. (1)). The statistical error on the resulting mean ($\bar{n}$) is calculated:

$$(\delta\bar{n})^2 = \frac{1}{\alpha^2} \sum_j \sum_i \sigma_{ij}^2 (\bar{n} - i)(\bar{n} - j)$$

where i and j correspond to the multiplicities of the particular problem and σ_{ij} is the covariance matrix from the fit. Additional error could arise from the statistical error on the elements of the (ε) matrix. Monte Carlo is used to generate the ε_{ij} with sufficient events so the errors on ε_{ij} are considerably smaller than the statistical errors in the observed distributions. As shown in the text, the model dependence of (ε) introduces a more significant effect than the statistical error from the observed distributions.